FLOW IN TEE JUNCTIONS

BY

ANDREW POLLARD

(B.A.Sc. WATERLOO)

THESIS SUBMITTED FOR THE DEGREE OF
DOCTOR OF PHILOSOPHY
IN THE FACULTY OF ENGINEERING
UNIVERSITY OF LONDON
AND
FOR THE DIPLOMA OF MEMBERSHIP OF
IMPERIAL COLLEGE

MECHANICAL ENGINEERING DEPARTMENT
IMPERIAL COLLEGE OF SCIENCE AND TECHNOLOGY
LONDON SW7

SEPTEMBER 1978

CORRIGENDA

Page No	Line	Text reads	Should read
2	8.I5,I2	compared to	compared with
3	26	existant	existent
4	2	this	these
6	2	calculate in	calculate the flow in
27	25	are	is
28	2	was	were
	22	plaque	plaques
30	5	asymetric	asymmetric
33	I0	recieve	receive
34	7	this	these
36	I0		Of both laminar and turbulent flows in geometries that resemble tee-junction.
37	I9	is	are
3B	3	to	with
4I	I7	being	which are
42	2	of this type	of a partially-parabolic flow
49	I8	there	these
50	I8	is	are
53	9	then	than
B3	I4	(p' s')	(p'' s)
B7	22	laminer	laminar
88	I5	(3.60)	(3.46)
	2I	Γ_e	Γ_{eff}
9I	2	experimetal	experimental
92	I3	plaucity	paucity
93	23	equiped	equipped
	2B	appratus	apparatus
97	I2	is	are
9B	9	succeptable	susceptible
	IB	uniformely	uniformly
I06	20	sublimition	sublimation
I07	3		naphthalene plugs
II0	I5	indentically	identically
	I7	monometer	manometer
II2	I4	"	"
	I7,I9	sublimitation	sublimation
II4	3	monometer	manometer
	20	sublimitation	sublimation
II7	4	J/kgk	j/kgK
	I7	h(Θ)	$\bar{h}(\Theta)$
	I4	longtidudinal	longitudinal
II9	3	sublimatation	sublimation
I23			C_p omitted on vertical scale
I24	I2	is	are
	I3	shows	show
I29	5	appears	appears to be
I37	II	statial	spatial
I43	7	velocites	velocities
	I3	existance	existence
I77	9	percieve	perceive
I79	II	also to observed	also observed
I79	24	Y/D_i	Y/d_i
I83	I5	combing	combining
I85	5	tubulent	turbulent
I99	I5	protion	portion
200	2	eminating	emanating
205	2,I3	to	with
206			The curves in the figure should be marked: R_3,R_2,R_1, where R_3 has the highest value
207			On the lower portion of the vertical axis change 35 to read 25
2I5	I3	veolcity	velocity
	I7	is	are
2I6	II	descrepancy	discrepancy
	I7	Krieth	Kreith
220	Caption	..circumferential heat-transfer..	..circumferential variations of heat-transfer..
22I	Caption	..longitudinal average..	..longitudinal distribution of average..
222	I2	parameter	perimeter
	23	occuring	occurring
223	I6	Here,	Secondly,
	27	is	are
224	4	denpensed	dispensed
	I3	siatuaion	situation
226	I4	capatalised	capitalised
230	42	Patankar	PATANKAR
23I	8	distribtuion	distribution
232	46	brachting	branching
235	5	circumfernetial	circumferential
24I	9	equation	equations
242	Eqn(AI=.4)	.. $\frac{\partial \sigma}{\partial x}xy + \frac{\partial \tau}{\partial y}y$..	.. $\frac{\partial \tau}{\partial x}xy + \frac{\partial \sigma}{\partial y}y$..
24B	I0	calbiration	calibration
	24	data was	data were
	25,26,2B	is	are
255	3	In Figure A3.2 is	In Figure A3.2 there is presented
	7	Burfraff	Burgraff
256	22	is	are

ABSTRACT

This thesis presents the application of a new finite-difference calculation procedure for solving the partial-differential equations governing the flow and heat and mass transfer in tee-junctions. Both laminar and turbulent flows are considered: in particular, attention is concentrated upon the combining laminar and uniformly dividing turbulent flow in tee-junctions of square and round cross-sections respectively.

The above flow situations are characterized by the appearance of only small regions of recirculating flow within the horizontal duct; surrounding this region there is a predominance to the flow direction. Such regions can be accounted for computationally in either of two ways: The whole flow may be classed as being elliptic or, alternatively, the recirculation region alone may be classified as being elliptic while the rest of the flow is considered to be partially-parabolic. In this thesis, both classifications are attended to by solving the differential equations governing each flow classification. Two distinctly different forms of one calculation procedure are used. The two forms of the calculation procedure are deemed elliptic and partially-elliptic. The elliptic procedure is described in detail; the partially-elliptic procedure being a derivative of the elliptic one and therefore only its distinquishing features are pointed out.

Turbulence is accounted for by using a two-equation model of turbulence. The time-mean momentum and continuity

equations are solved with equations describing the transport of turbulence kinetic-energy and its volumetric rate of dissipation. The turbulence model relates the turbulence to a turbulent viscosity. In the near-wall regions, wall functions are employed.

For the laminar combining flow in tee-junctions of square cross-section, two diameter ratios and up to three momentum ratios are considered. When compared to the limited experimental data, the predictions are found to agree reasonably well.

With respect to the turbulent, uniformly-dividing flow in tee-junctions of round cross-section, the predictions, when compared to the data obtained in a parallel program of study show fair agreement. In particular, the wall surface pressures and mean flow quantities are at variance with the data; the heat-transfer predictions, when compared to experimentally determined mass transfer (via the sublimation of naphthalene) shows good agreement.

The predictions of the partially-elliptic procedure were found to agree well with those predictions obtained by using the elliptic procedure. Although computational times were about the same, computer storage savings of up to 50% or more can be obtained by using the partially-elliptic procedure in lieu of the elliptic one.

The study has been made for the purposes of verifying the calculation procedure with particular reference to the three-dimensional flow in right-angled tee-junctions. Detailed parametric studies of the flow and heat-transfer characteristics of tee-junctions have not therefore been attempted.

PREFACE

This thesis presents the results of three years research on the numerical prediction of three-dimensional recirculating flows; the research commenced upon my arrival at Imperial College in October I975. Since this time, my research activities have been funded by the Science Research Council under various contracts; my supervisor was Professor D B Spalding.

Although tee-junctions are commonly encountered in many industrial applications, the detailed analysis of the flow and heat transfer phenomena has received very little attention in the literature, quite probably because the tools necessary to obtain such detailed information are not generally available. Indeed, when consideration is given to the enormous number of geometrical flow and heat-transfer variations that can be envisaged, a method capable of predicting the effects of these variations, more economically and in times much shorter than comparable experimental investigations would be of great benefit.

My research on the flow and heat-transfer characteristics of tee-junctions was first proposed by Professor Spalding. Using an existing three-dimensional code used for the prediction of recirculating flows, I embarked upon a brief investigation of the flow in a tee-junction that included an exhaustive literature survey. This survey revealed that previous work on tee-junctions was almost non-existant. It did, however, reveal a very recent (I976) publication dealing with the heat-transfer characteristics of flow-

splitting tee-junctions. By comparing a few predictions with this experimental data, confidence in the ability of the numerical procedure and the models embodied within it was partially achieved. Indeed, these predictions have now been published.

The publications revealed two main areas that required further investigation: a cheaper method had to be devised in which to obtain the predictions, and that it appeared that the case of a tee without a side (or vertical) duct was possibly one cause of the lack of agreement between the predictions and the experimental data.

It was at this point in time (March 1977) that the work presented in this thesis began to coalesce. It commenced with the further development of a new three-dimensional code, the outline of which had been developed at Combustion, Heat and Mass Transfer Limited, Wimbledon. This code was based on a proposal by Professor Spalding which in essence combined features of earlier codes developed at Imperial College. The new procedure is referred to as "NEAT". With this skeleton code, I inserted the necessary source-terms for the equations, the diffusion terms and a two-equation model of turbulence for both cartesian and cylindical polar co-ordinate systems. The finalised code was then tested by comparing the predictions against information from other sources for a variety of laminar and turbulent flows. The code was found to be cheaper in computer storage costs than earlier codes, and in most cases tested, to be cheaper in computer time.

A feature of the NEAT procedure is based on its line by line approach to solving the equations; that is, it solves the equations on a given line of finite-difference control volumes at a time, and not on the whole field basis of earlier codes (the whole field contains planes, which in turn contain lines). This feature is exploited here for it allows extensions to be made cheaply, into regions such as inlet ducts of tee-junctions. So in one stroke, the possibility existed for investigating areas directed by the initial work on tee-junctions.

At this stage, however, it appeared that the computer costs could be reduced even more. In many flow situations that are referred to as elliptic in character, the region of recirculating flow is small compared to the whole flow domain; examples include the flow around a cooling tower, and, of course, the flow in tee-junctions. It was suggested by Professor Spalding that my code should include the capability of predicting recirculating flow regions by using the elliptic form of the equations and solving the "partially-parabolic" forms elsewhere. This capability was not to be fully exploited however; the storage savings and any accuracy penalties attributable to the use of the partially-parabolic procedure were to be noted, but the actual storage manipulations were to be left for future work.

Because of the distinct lack of experimental data for the turbulent flow in tee-junctions, a parallel investigation was undertaken to obtain data suitable for the validation of the model of turbulence. An experimental rig was designed and constructed that features a pipe attached to a wedge shaped

inlet. This inlet shape permitted the numerical code to calculate in this region in a direct manner; the matching of two polar co-ordinate grids arranged at right-angles to each other is thereby side-stepped; but no matter, this complex feature can be added once confidence has been gained in the procedure's ability to predict the simplified version of a tee-junction.

In this experimental rig, air passed through the inlet and upon entering the pipe, split, to produce flows of equal mass flow rate in each of the pipe legs; only one flow Reynolds number was considered. With this flow situation, the mean velocities at a number of pipe diameters downstream of the inlet duct were obtained. The wall static pressure throughout the junction was also obtained. Because the temperature distribution is of interest in tee-junctions (e.g. thermal fatique problems), a new variation of a well-known technique was used to evaluate the heat-transfer coefficient. It involved invoking the analogy between heat and mass transfer. In this context, the mass transfer at the wall of the pipe was obtained by using the naphthalene sublimation technique. This involved developing a technique, proposed by Professor Spalding, for obtaining repeatable results from small ($^{I}/_{4}$" dia) Naphthalene embedded plugs at various locations in the pipe walls.

The results of this work is reported here. The writing of this thesis commenced in July I978.

Acknowledgements

I would now like to thank all those who have provided me with help and moral support during the course of the present study.

First, and most important of all, I express my sincerest thanks to my supervisor, Professor Spalding. I have benefited greatly from his standard of exactness in both research and comminicative skills. To have been his student I consider myself extremely fortunate. My thanks also go to Drs Sam Pun and Tony Ma for their help in many areas; their critical analysis of some of the many problems I encountered have been of considerable aid.

To Dr George Raithby at the University of Waterloo, thank you for your support and encouragement; it has been much valued.

My close association with Dr Gordon Mallinson, Professor Grahame de Vahl Davis, and Dr "Chippy" Thyagaraja and Dr A K Mujumdar during their respective short stays at Imperial College was indeed a pleasure. I thank you all for expanding my fields of interest.

During my three years at Imperial College, I came into close contact with many people who, after obtaining their Ph.D.'s have gone elsewhere. I would like to say thank-you to Drs. T T Maxwell, M A Serag Eldin, J A C Humphrey, U Svensson, A K Singhal and E E Khalil for many fruitfull scientific and philosophical discussions. For keeping Room 483 a bee-hive of activity, my thanks go to Mohammed

El-Hadidy and Amin Baghdadi. I hope that the friendship that has grown between us continues.

To Alaa Awn, Deji Demuren, Vinoth Ramachandra, Denis Skiadaressis, Ian Jennions, Ahmed Abdelmeguid, Arvind Jain, and in particular to George Carroll, I give thanks for many things, too numerous to mention.

To Colleen King, Sue Farmiloe, Maggie Dean, Christine McKenzie, thank you all for helping to sort out the administrative problems.

To the staff of the library, thank you for the trouble you all have gone to in getting the most obscure of references for me.

To Bob King, thank you for your aid and friendship in the laboratory.

Finally, I wish to express my gratitude to Betty, my wife, who has patiently and courageously suffered through all my trying moments.

To Sue Farmiloe and Sue Botter, thank-you both for doing an excellent job of typing this thesis.

The financial support for my research was provided by the Science Research Council under grants BRG/I095/0 and GR/A/4365.0, which is greatly appreciated.

IMPERIAL COLLEGE
LONDON SW7

A POLLARD
OCTOBER I978

CONTENTS OF THESIS

		Page No.
ABSTRACT		I
PREFACE		3
ACKNOWLEDGEMENTS		7
CONTENTS OF THESIS		9
LIST OF FIGURES		I6
PART I: THE PRELIMINARIES:		20
CHAPTER 1.0	INTRODUCTION	2I
1.1	NATURE OF THE PROBLEM STUDIED	2I
I.I.I	GENERAL CHARACTERISTICS	2I
I.I.2	SPECIFIC SITUATIONS INVESTIGATED	23
1.2	CONTRIBUTIONS OF THE PRESENT STUDY	26
I.2.I	THEORETICAL CONTRIBUTION	26
I.2.2	PRACTICAL CONTRIBUTION	28
1.3	REVIEW OF PREVIOUS WORK	29
I.3.I	INTRODUCTION	29
I.3.2	TEE-JUNCTIONS OF SQUARE CROSS-SECTION (a) Laminar Flow (b) Turbulent Flow	29 29 3I
I.3.3	TEE-JUNCTIONS OF ROUND CROSS-SECTION (a) Laminar Flow (b) Turbulent Flow	32 32 32
I.3.4	CALCULATION PROCEDURES (a) Introduction (b) Solution Procedures	35 35 35
1.4	OUTLINE OF THESIS	37
PART II: THEORETICAL ASPECTS		39
CHAPTER 2.0	MATHEMATICAL FRAMEWORK	40
2.1	INTRODUCTION	40
2.2	FLOW CLASSIFICATION	4I
2.3	THE CONSERVATION EQUATIONS	42
2.3.I	THE ELLIPTIC FORMS	42
2.3.2	THE PARTIALLY-PARABOLIC FORMS	43

		Page No.
2.4	THE TIME-SMOOTHED FORMS OF THE EQUATIONS	44
2.5	THE MODELLING OF TURBULENCE	46
2.5.1	INTRODUCTION	46
2.5.2	TURBULENCE MODEL CLASSIFICATION (a) Reynolds Stress (b) Eddy Viscosity Concept	46 46 47
2.5.3	MODEL SELECTION	47
2.5.4	THE MODEL OF TURBULENCE	48
2.6	BOUNDARY CONDITIONS	51
2.6.1	THE NEAR-WALL REGION - THE WALL FUNCTION (a) Motivation (b) The Wall Function Approach (c) The Wall Functions	51 51 52 52
2.6.2	OTHER BOUNDARY CONDITIONS	55
2.7	SUMMARY OF THE CHAPTER	55
CHAPTER 3.0	THE NUMERICAL SOLUTION PROCEDURES	56
3.1	INTRODUCTION	56
3.2	OUTLINE OF THE CHAPTER	57
3.3	THE FINITE-DIFFERENCE EQUATIONS	57
3.3.1	INTRODUCTION	57
3.3.2	THE FINITE-DIFFERENCE GRID	58
3.3.3	LOCATION OF FLOW VARIABLES	58
3.3.4	THE CONTROL VOLUMES	60
3.3.5	THE CONTINUITY EQUATION	62
3.3.6	THE GENERAL SCALAR VARIABLE (ϕ) EQUATION	62
3.3.7	THE MOMENTUM EQUATIONS	68
3.3.8	THE PRESSURE-CORRECTION EQUATION	69
3.4	THE PARTIALLY-PARABOLIC SIMPLIFICATIONS	72
3.5	CALCULATING ON ELLIPTIC-PARTIALLY-PARABOLIC PLANES	75

		Page No.
3.6	INCORPORATION OF BOUNDARY CONDITIONS	76
3.7	THE ELLIPTIC SOLUTION PROCEDURE	77
3.7.I	INTRODUCTION	77
3.7.2	THE SIMPLE-NEAT ALGORITHMS	77
3.7.3	THE TRI-DIAGONAL MATRIX ALGORITHM	78
3.7.4	INTEGRAL CONSERVATIONS	80
3.7.5	THE STEPS OF THE "ELLIPTIC" SOLUTION PROCEDURE	82
3.8	THE PARTIALLY-ELLIPTIC SOLUTION PROCEDURE	84
3.9	SOME MISCELLANEOUS COMPUTATIONAL MATTERS	85
3.9.I	ACCURACY OF THE PROCEDURE	85
	(a) Differential Equation errors	86
	(b) Numerical Errors	86
	(i) Discretisation errors	86
	(ii) Lack of convergence error	86
	(iii) Round-off error	87
	(iv) Numerical smearing	88
3.9.2	STABILITY OF THE NUMERICAL SCHEME	89
3.10	VERIFICATION OF THE NUMERICAL PROCEDURE	90
3.11	CLOSURE	90
PART 111: THE EXPERIMENTAL PROGRAM		9I
CHAPTER 4.0	THE EXPERIMENTAL INVESTIGATION	92
4.1	INTRODUCTION	92
4.I.I	PURPOSE OF THE EXPERIMENTS	92
4.I.2	SCOPE OF THE EXPERIMENTS	92
4.I.3	OUTLINE OF THE CHAPTER	93
4.2	DESCRIPTION OF THE MAIN APPARATUS	93
4.2.I	THE FLOW CIRCUIT	93
4.2.2	THE TEST SECTION	96

		Page No.
4.3	MEASURING TECHNIQUES	I0I
4.3.I	THE MEASUREMENT OF PRESSURE	I0I
4.3.2	THE MEASUREMENT OF VELOCITY	I0I
	(a) The Probe	I0I
	(b) The Traversing Mechanism	I0I
4.3.3	THE MEASUREMENT OF THE SUBLIMATION OF THE NAPHTHALENE	I05
	(a) Introduction	I05
	(b) The Plugs	I06
	(c) Naphthalene Plug Preparation	I09
4.4	THE EXPERIMENTAL PROCEDURES	II0
4.4.I	FLOW SYMMETRY	II0
4.4.2	INLET AND EXIT VELOCITY PROFILES	II0
4.4.3	TEST SECTION VELOCITY MEASUREMENTS	III
4.4.4	TEST SECTION PRESSURE MEASUREMENTS	II2
4.4.5	MEASUREMENT OF NAPHTHALENE SUBLIMATION RATE	II2
4.5	DATA CONVERSION	II3
4.5.I	WALL STATIC PRESSURE	II4
4.5.2	MEAN VELOCITIES	II4
4.5.3	NAPHTHALENE SUBLIMATION RATE	II4
4.6	ACCURACY AND REPEATABILITY OF THE MEASUREMENTS	II8
4.6.I	ACCURACY	II8
4.6.2	REPEATABILITY	II9
4.7	THE PRESENTATION OF THE EXPERIMENTAL DATA	II9
4.8	CONCLUDING REMARKS	I28
PART IV: THE PREDICTIONS		I30
CHAPTER 5.0	LAMINAR FLOW PREDICTIONS	I3I
5.I	INTRODUCTION	I3I
5.2	THE GENERAL PROBLEM	I3I
5.2.I	THE PHYSICAL SITUATION	I3I
5.2.2	SOME COMPUTATIONAL DETAILS	I33
	(a) Finite-Difference Grid	I33
	(b) The Computational Costs	I34
	(c) Other Boundary Conditions	I36

			Page No.
	5.3	TEE-JUNCTION OF DIAMETER RATIO 0.5	I36
	5.3.I	COMPARISON WITH EXPERIMENTAL DATA	I36
		(a) Introduction	I36
		(b) The General Flow Pattern	I37
		(c) Prediction vs Experimental data	I50
		(d) The Pressure Field	I55
		(e) Predictions obtained by using the Partially-Elliptic Procedure	I59
	5.3.2	EXTENSIONS TO THE PREDICTIONS FOR DIAMETER RATIO OF 0.5	I60
		(a) Introduction	I60
		(b) The Flow Fields	I60
		(c) The Velocity Trajectory	I60
		(d) Velocity Profile in the Plane of the Junction	I64
		(e) The Pressure Distribution	I67
		(f) The Partially-Elliptic Procedure Predictions	I67
	5.4	TEE-JUNCTION OF DIAMETER RATIO I.0	I69
	5.4.I	THE PHYSICAL SITUATION	I69
	5.4.2	THE INLET CONDITIONS	I69
	5.4.3	THE SOLUTION PROCEDURE	I69
	5.4.4	THE PREDICTED FLOW FIELDS	I76
	5.4.5	THE VELOCITY TRAJECTORY	I79
	5.4.6	VELOCITY PROFILES IN THE PLANE OF THE JUNCTION	I80
	5.4.7	THE PRESSURE DISTRIBUTION	I80
	5.5	SUMMARY OF THE CHAPTER	I83
	5.6	CONCLUDING REMARKS	I84
CHAPTER	6.0	TURBULENT FLOW PREDICTIONS	I85
	6.1	INTRODUCTION	I85
	6.2	OUTLINE OF THE CHAPTER	I86
	6.3	THE FLOW SITUATION AND SOME COMPUTATIONAL DETAILS	I86
	6.3.I	THE PHYSICAL SITUATION	I86
	6.3.2	THE COMPUTATIONAL GRID	I89

			Page No.
	6.3.3	THE INLET AND BOUNDARY CONDITIONS (a) Aerodynamics (b) Heat/Mass Transfer	I89 I90 I9I
	6.3.4	THE COMPUTATIONAL COST	I92
	6.4	THE GENERAL FLOW PATTERN	I93
	6.5	COMPARISON WITH EXPERIMENTAL DATA	205
	6.5.I	THE SURFACE STATIC PRESSURE DISTRIBUTION	205
	6.5.2	THE VELOCITY FIELD	209
	6.5.3	DISCUSSION OF THE AERODYNAMIC RESULTS	2I5
	6.5.4	THE HEAT/MASS TRANSFER DISTRIBUTION	2I6
	6.6	AN EXTENSION TO THE HEAT-TRANSFER RESULTS	2I9
	6.7	GENERAL DISCUSSION	223
	6.8	SUMMARY AND CONCLUDING REMARKS	224
CHAPTER	7.0	CONCLUDING REMARKS	225
	7.1	REVIEW OF MAIN RESULTS	225
	7.2	FUTURE WORK	226
REFERENCES			228
NOMENCLATURE			234
PART V:		THE APPENDICES	240
APPENDIX	A1	THE GOVERNING DIFFERENTIAL EQUATIONS	24I
	A1.1	INTRODUCTION	24I
	A1.2	EQUATIONS IN (X-Y-Z) COORDINATE SYSTEM	24I
	A1.3	EQUATIONS IN (θ-R-Z) COORDINATE SYSTEM	244
APPENDIX	A2	EXPERIMENTAL INFORMATION	246
	A2.1	DETAILS OF THE EQUIPMENT USED	246
	A2.2	CALIBRATION	246
	A2.2.1	MICRO-MANOMETER CALIBRATION	246
	A2.2.2	TRANSVERSE CYLINDER PROBE CALIBRATION	246

			Page No.
APPENDIX	A3	VERIFICATION OF THE NUMERICAL PROCEDURE - A FEW EXAMPLES	252
	A3.1	INTRODUCTION	252
	A3.2	THE TEST CASES	252
	A3.3	CONCLUDING REMARKS	258

LIST OF FIGURES

Section Number	Title	Page No.
I.I	Flow Distribution Classification in Tee-Junctions	22
I.2a	Geometry Considered - Square Tee-Junction	24
I.2b	Geometry Considered - Round Tee-Junction	24
I.3a	The Flow Situation Considered - Square Tee-Junction	25
I.3b	The Flow Situation Considered - Round Tee-Junction	25
3.I	Location of Dependent Variables: (a) X-Y Plane, (b) R-θ Plane	59
3.2	Location of Dependent Variables on (Y-R) (Y-R)-Z Plane A - Upmarch, B - Current, C - Downmarch	6I
3.3	Control Volume Faces: (a) X-Y Plane, (b) Y-Z Plane	63
3.4	A ϕ-Control Volume	65
3.5	W-Momentum Control Volume	73
3.6	Descretisation of Integration Domain	79
4.I	The Experimental Rig - A General View	94
4.2	Schematic Drawing of Experimental Rig	95
4.3	The Test Section	99
4.4	Schematic of Test Section	I00
4.5	Details of Static Pressure Tappings	I00
4.6	Equipment for the Measurement of Pressure	I02
4.7	The Transverse Cylinder Probe and Traversing Mechanism	I03
4.8a	$\frac{1}{4}$"- NPT Plus for Holding Naphthalene	I07
4.8b	Photograph of Four Naphthalene Plugs: (a) Ready to receive Naphthalene (b) Loaded with Naphthalene (c) Plug prepared for test, (d) Plug condition after test.	I07
4.9	Naphthalene Plug Mass Loss vs Time of Exposure	I08
4.I0	Air Temperature-Time History During a Typical Test Run for Sublimation of Naphthalene	II6

Section Number	Title	Page No.
4.II	Experimental Inlet Velocity Profiles: • Pilot Probe, X 3-Hole Cylinder Probe	I20
4.I2	Velocity Distribution at Main Duct Branch Reference Points (Z/D=40.5)	I22
4.I3	Surface Pressure Coefficient vs Distance Downstream of Inlet Duct Centre-Line;• Left X Right of Centre-Line	I23
4.I4	Axial Velocity Distribution on Pipe Diametral Symmetry Plane: • Left x Right of Inlet Duct Centre-line, O Questionable Data	I25
4.I5	Cross-Stream Velocity Profiles Note: U is Velocity Normal to Diametral Centre-Line, • Left x Right of Inlet Duct Centre-Line	I26
4.I6	Average Longitudinal Mass Transfer Coefficient • Left x Right of Inlet Duct Centre-Line	I27
5.I	The Physical Situation Considered	I32
5.2	The Finite-Difference Grid Distribution	I32
5.3	Grid Independence Test for d_i/D_m=0.5, M_i/M_m=0.25	I35
5.4a	Vector Plot on Y-Z Plane; d_i/D_m=0.5, M_i/M_m=0.25: X/D_i: (i) -0.7, (ii) -0.55, (iii) -0.45, (iv) -0.35, (v) -0.25, (vi) -0.I5, (vii) -0.05, (viii) +0.05, (ix) +0.I5, (x) +0.35, (xi) +0.35, (xii) +0.45, (xiii) +0.55, (xiv) 0.625, (xv) +0.875, (xvi) +I.I5, (xvii) +I.625, (xviii) +2.375	I38
5.5	Comparison of Experimental Data With Present Predictions (Ref Table 5.I) (—) Case I, (----) Case 2, (— —) Case 3, Case 4, ▲ Data Simitovic I977	I5I
5.6	Caption as in Figure 5.5	I52
5.7	Comparison of Experimental Data (▲) with Present Predictions, (—) Case I, (– –) Case 3, ▲ Data Simitovic (I977)	I53
5.8a	Inlet Velocity Profiles on X-Z Plane; (—···—) Case I, (— —) Case 2, (———) Case 3	I56

Section Number	Title	Page No.
5.8b	Perspective View of Inlet Duct Velocity Profile at the Junction; Case 3 Predictions	I57
5.9	Pressure Coefficient vs Main Duct Axial Distance; (— —)Case I , (—)Case 3	I58
5.I0	Longitudinal Vector Plots for Two Momentum Ratios; (a)M_i/M_m=0.I, (b) M_i/M_m=I.0, X/d_i: (i)0.0, (ii)0.5I	I6I
5.II	Cross-Stream Vectors for Two Momentum Ratios; (a) M_i/M_m=0.I, (b)M_i/M_m=I.0, Z/d_i: (i)0.0, (ii)0.2, (iii)0.3, (iv)0.6, (v) I.2	I63
5.I2	Velocity Trajectories as a Function of Momentum Ratio, d_i/D_m=0.5; — side duct l_i/d_i=2.2 -- side duct l_i/d_i=0.0	I65
5.I3	Velocity Surface at Junction; (a) d_i/D_m=0.5, M_i/M_m=0.I, $V_{max}/\overline{V}_i$=I.84 (b) d_i/D_m=0.5, M_i/M_m=0.I, $V_{max}/\overline{V}_i$=I.87	I66
5.I4	Pressure Coefficient vs Main Duct Axial Distance for Two Momentum Ratios	I68
5.I5	Main Duct Centre-Line Distribution of (a) Velocity, (b) Pressure Comparison of Procedures d_i/D_m=I.0, M_i/M_m=I.0, l_i/d_i=0.0	I70
5.I6	Longitudinal Vector Plots; d_i/D_m=I.0, m_i/M_m=0.I, X/d_i: (i) 0.07, (ii)0.I5, (iii) 0.25, (iv) 0.45	I7I
5.I7	Longitudinal Vector Plots; d_i/D_m=I.0, M_i/M_m=I.0, X/d_i= (i) 0.07, (ii) 0.I5, (iii) 0.25, (iv) 0.45	I72
5.I8	Cross Steam Vector Plots; d_i/D_m=I.0, M_i/M_m=(a) 0.I, (b)I.0 Z/d_i:(i) 0.0, (ii)0.2, (iii) 0.45, (iv) 0.55, (v) 0.7, (vi) I.3	I73
5.I9	Predicted Axial Velocity Profiles for d_i/D_m=I.0, M_i/M_m=I., Z/d_i=0.0 (— —)side duct l_i/d_i=I.I (——)side duct l_i/d_i=0.0	I74
5.20	Predicted Axial Velocity Profiles for d_i/D_m=I.0, M_i/M_m=I.0, Z/d_i=I.0 (— —)side duct l_i/d_i=I.I (——)side duct l_i/d_i=0.0	I75

Section Number	Title	Page No.
5.2I	Velocity Trajectories as a Function of Momentum Ratio for d_i/D_m=I.0 (——) side duct l_i/d_i=I.I (— —) side duct l_i/d_i=0.0	I78
5.22	Velocity Surface at Junction; (a) d_i/D_m=I.0, M_i/M_m=0.I, $V_{max}/\bar{V}_i$=3.I7 (b) d_i/D_m=I.0, M_i/M_m=I.0, $V_{max}/\bar{V}_i$= 2.47	I8I
5.23	Pressure Coefficient vs Main Duct Axial Distance for Two Momentum Ratios	I82
6.I	The Physical Situation Considered - Corresponding to the Present Experimental Situation	I87
6.2	The Finite-Difference Grid Arrangement	I88
6.3 (i to vi)	Vectors on a Dimetral R-Z Plane	I94
6.4 (i to viii)	Vectors on Axial (Cross Stream) R-θ Planes	I97
6.5a	Views of a Streamline: Particle Released at Z/L(0), y/R(I), θ(I8°)	202
6.5b	Views of a Streamline: Particle Released at Z/L(0.03), y/R(0.4),θ(45°)	203
6.6	Comparison of Data with Predictions for Pressure Distribution in the Inlet Duct	206
6.7	Circumferential Wall Pressure Variation as a Function of Axial Distance Down-Stream of Inlet Duct Centre-Line	207
6.8	Longitudinal Wall Pressures Variation in Main Legs Downstream of Inlet Duct Centre-Line	208
6.9	Axial Velocity Distribution at Z/D=+I.0	2I0
6.I0	Axial Velocity Distribution at Z/D=$\pm$2.0	2II
6.II	Axial Velocity Distribution at Z/D=$\pm$3.0	2I2
6.I2	Axial Velocity Distribution at Z/D=$\pm$5.0	2I3
6.I3	Axial Velocity Distribution Normal to 90-270 Degree Plane at Two Axial Locations	2I4
6.I4	Circumferential Mass/Heat Transfer Variation	2I7
6.I5	Longitudinal Average Mass/Heat Transfer Variation	2I7
6.I6	Predicted Circumferential Heat-Transfer Coefficient for Constant Wall Temperature	220
6.I7	Predicted Longitudinal Average Heat-Transfer Coefficient Distribution for Constant Wall Temperature	22I

- PART I -

THE PRELIMINARIES

CHAPTER 1.0: INTRODUCTION

1.1 NATURE OF THE PROBLEM STUDIED

I.I.I GENERAL CHARACTERISTICS

Duct-junctions, and in particular those junctions that are "T"-shaped, play an important role in distributing fluids. For example, they can be found in heat exchangers and in many industrial and biological piping networks.

Tee-junctions may be used to either combine or divide fluid. To illustrate this point, Figure I.I presents four sketches of the flow situations usually encountered in tees; the arrows on the sketches indicate the flow directions.

In the tee-junction flow distribution classification presented above, there are two common characteristics of the flow that require especial mention. The first of these characteristics is the existance of one or more regions containing recirculating fluid. The second characteristic is that surrounding these recirculation regions, there is a predominance to the flow direction; it would appear then that regardless of how fluid enters and leaves the junction the flow within the geometry is complex in nature and three-dimensional in its extent.

To calculate local values of velocity etc., in recirculating flows, the complete forms of the Navier-Stokes equations must be solved; these equations are usually termed "elliptic". In areas outside these elliptic regions, the predominant flow direction ensures that flow properties are convected only from upstream regions to downstream. Also, if the Reynolds number is high enough, the molecular actions in

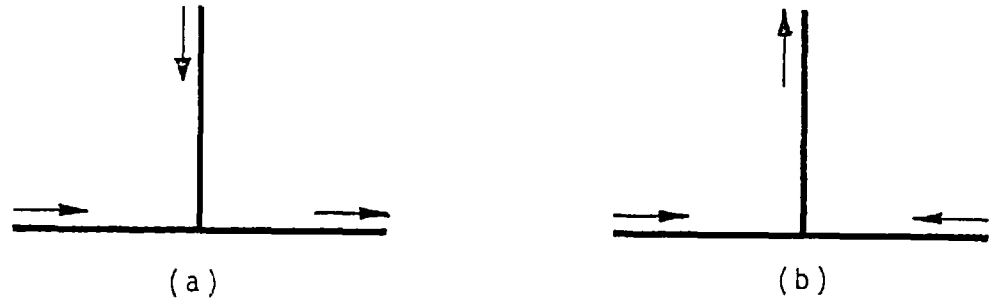

(a) (b)

COMBINING FLOW

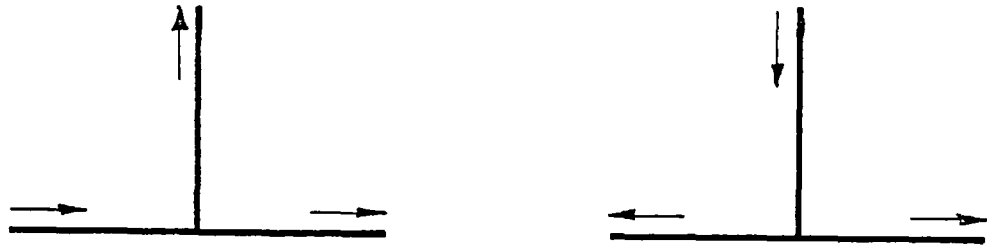

(c) (d)

DIVIDING FLOW

FIGURE I.I: FLOW DISTRIBUTION CLASSIFICATION IN TEE-JUNCTIONS

the predominant direction are of a magnitude that can be neglected. These predominant flow characteristics allow simplifications to be imposed upon the elliptic form of the equations, thereby making them easier to solve.

1.1.2 SPECIFIC SITUATIONS INVESTIGATED

In the present study, both the laminar and turbulent flow in tee-junctions is investigated.

For laminar flows, a tee-junction of square cross-section is used; the geometry is shown in Figure I.2(a). The flow situation considered and the expected flow pattern is illustrated in Figure I.3(a); it is observed that this flow is of the combining type.

For turbulent flows, a tee-junction of round cross-section is used, as shown in Figure I.2(b). The inlet duct is noticed to be not round, but of wedge shape. The flow situation considered and the expected flow pattern for a uniformly dividing flow is shown in Figure I.3(b).

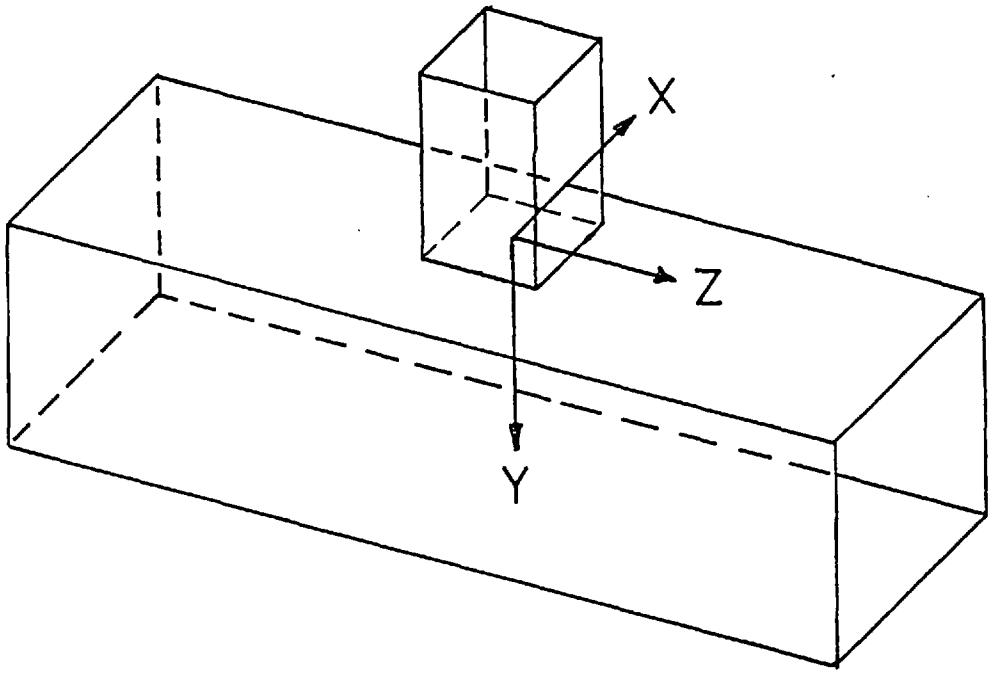

FIGURE I.2a: GEOMETRY CONSIDERED - SQUARE TEE-JUNCTION

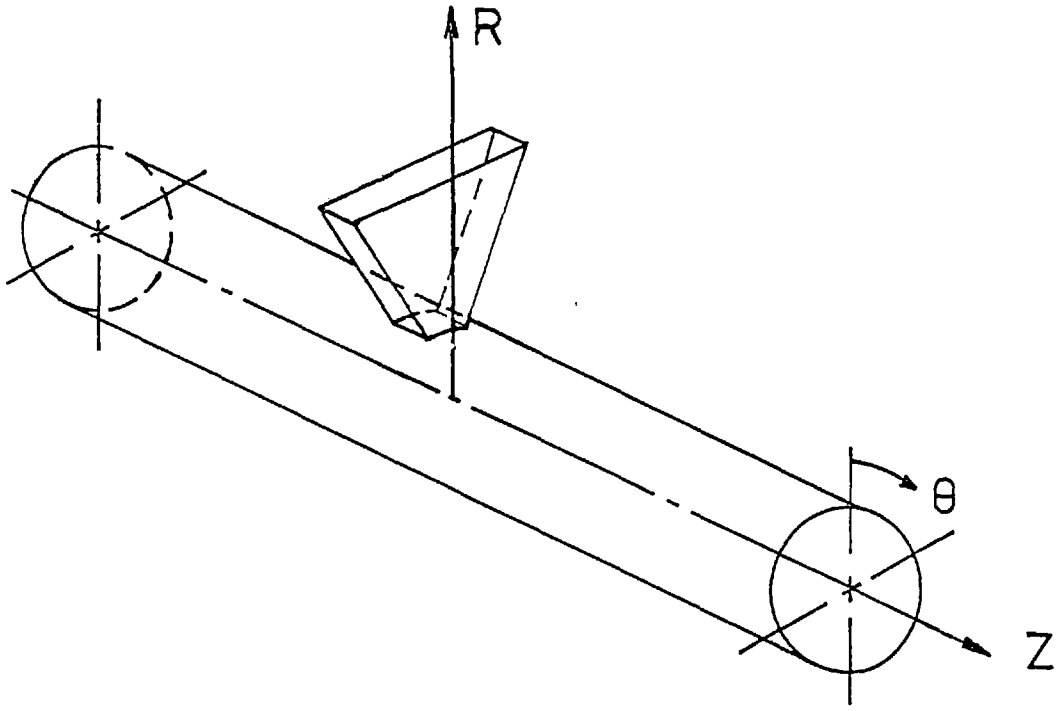

FIGURE I.2b: GEOMETRY CONSIDERED - ROUND TEE-JUNCTION

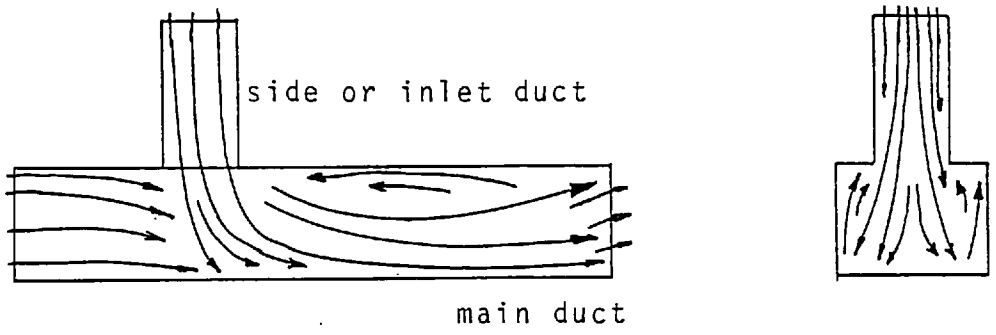

FIGURE I.3a: THE FLOW SITUATION CONSIDERED - SQUARE TEE-JUNCTION

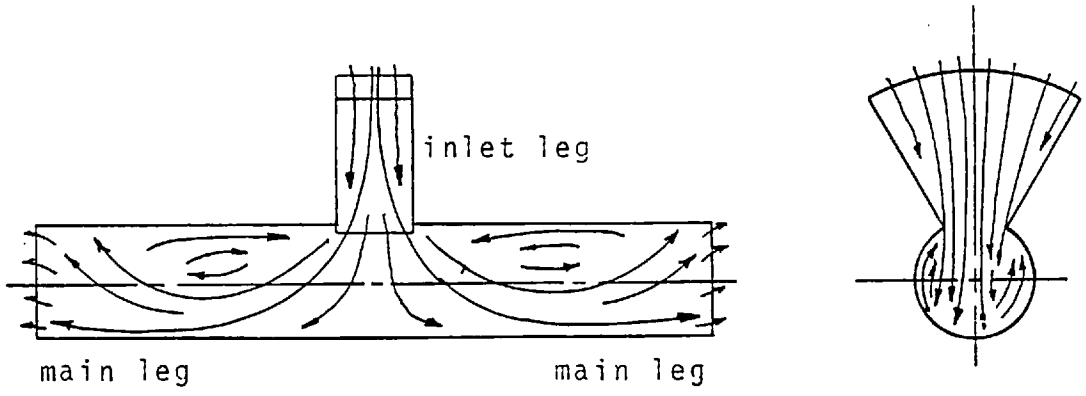

FIGURE I.3b: THE FLOW SITUATION CONSIDERED - ROUND TEE-JUNCTION

1.2 CONTRIBUTIONS OF THE PRESENT STUDY

I.2.I THEORETICAL CONTRIBUTION

The theoretical calculations for the flow and heat and mass transfer in tee-junctions involve the simultaneous solution of a set of non-linear partial-differential equations describing the transport processes in three dimensions. For turbulent flow, the additional stresses arising from the turbulence require additional inputs to the equations. The complexity of the equations has until recently been such as to hinder all but approximate analysis.

In the present study, these equations have been solved using two forms of a new finite-difference calculation procedure. First, the basic procedure is of the iterative type devised by Patankar and Spalding (I972), and utilises the NEAT (Nearly Exact Adjustment of Terms) idea of Spalding (I976). This procedure in its most general form calculates three-dimensional "elliptic" flows. The second procedure is a derivation of the first; it solves the "elliptic" forms of the equations in areas containing recirculating fluid, while outside these areas, it solves the equations that describe "partially-parabolic" flow. Briefly, a "partially-parabolic" flow is classified as having a predominant direction in which downstream events are transmitted upstream, but only through the action of pressure; further details may be found in Pratap (I975). This second procedure is referred to here as being "partially-elliptic".

In the numerical calculation of these flow types, the "elliptic" regions require full three-dimensional storage of all variables, while the "partially-parabolic" requires only three-dimensional storage for pressure; the other variables require only two-dimensional storage. The "partially-elliptic" flow classification economises on otherwise large (and therefore expensive) storage requirements. For example, in the laminar predictions presented in this thesis, the main variables in the elliptic procedure used about 100,000 storage locations, while the "partially-elliptic" predictions would have used only about 50,000.

The purpose of using both the "elliptic" and "partially-elliptic" procedures in the present study is to determine, by comparison, the potential storage savings, the increase (or decrease) in computational cost, and the accuracy penalties associated with solving the "partially-elliptic" forms of the equations in lieu of the "elliptic" forms. This assessment is to include the calculations of laminar and turbulent flows; it is to the turbulence that attention is now turned.

Turbulence is accounted for by way of a mathematical model in which the turbulent stresses are related to a turbulent viscosity. The turbulent viscosity (or turbulent diffusivity for the transport of a scalar variable) are evaluated by solving equations describing the local variation of the turbulent kinetic energy k, and its volumetric rate of dissipation ε. The comparison of the predictions with experimental data then allows an assess-

ment to be made of the turbulence model. The data used for this purpose was obtained in experiments carried out in a parallel program of study.

The experimental investigation of the turbulent flow in a round cross-sectioned tee-junction (see Figure I.I(b)) was confined to determining, for one Reynolds number, the following:-

i) the mean velocity profiles;

ii) the wall static-pressure distribution;

iii) the wall mass-transfer distributions via the technique of naphthalene sublimation.

I.2.2 PRACTICAL CONTRIBUTION

In industrial applications, the large variations in the rate of heat transfer provided by tee-junctions (relative to straight-duct values) can give rise to thermal fatique problems. This problem is particularly troublesome in power-generation plants. Other areas where tee-junctions are found are in gas turbines (for blade cooling) and dilution ports in combustors.

From a physiological point of view, the interaction of the fluid (blood) with arterial or venous branching causes the formation of athero-sclerosis plaque and thrombi; this can result in blood-clot formation.

It would appear that the ability to predict the detailed nature of the transfer processes in tee-junctions would therefore lead to improved design capabilities for industrial equipment and to the better understanding of the transfer phenomena.

1.3 REVIEW OF PREVIOUS WORK

I.3.I INTRODUCTION

In this section, a brief review is made of the relevant literature so as to relate the present work to that which has been done previously. The chapter is divided into three main parts: the first reviews the previous work on the laminar and turbulent flow, including heat transfer in tee-junctions constructed from ducts that are rectangular (or square) in cross-section; the second complements the first by concentrating attention on tees constructed of circular pipes; the final section of the review concentrates upon examining the generalised calculation procedures which are suitable for predicting the flow in tee-junctions.

I.3.2 TEE-JUNCTIONS OF SQUARE CROSS-SECTION

(a) LAMINAR FLOW

Because of the limited industrial application of the laminar flow in "square-tees", few data are available. Indeed, the work of Simitovic (I977) appears to be the only one. Using a square main duct butted to a square side duct in a combining flow situation (drawing (a) of Figure I.I), Simitovic obtained the mean axial velocity distribution at various main duct cross-stream locations. The data, obtained via Laser Doppler Anemometry, revealed the extent to which the incoming side fluid disturbs the main stream. For a main duct inlet Reynolds number of I00, and a momentum ratio (ω)of 0.25($\omega=\frac{\rho_i A_i \bar{V}_i^2}{\rho_m A_m W_m^2}$, where i's refer to inlet or side duct, and m's to the main duct; ρ,A are

density and cross-sectional area respectively, and $\bar{V}$,$\bar{W}$ are the inlet velocities to the side or inlet and main duct respectively). This disturbance extended to at least 10 inlet duct diameters downstream of the inlet duct centre-line. The data also revealed that the flow was asymetric by as much as 20% and that the near-wall measurements appear unreliable.

Simitovic obtained data for the sole purpose of validating a three-dimensional elliptic procedure. The predictions, when compared to his data, showed reasonable agreement. This is a particularly noteworthy point considering that in his predictions he neglected the inlet duct (i.e. he used a square duct with a hole in the side); at the hole, he prescribed a uniform velocity profile. Simitovic extended his predictions by calculating in the same geometry, the effects of changing the main duct Reynolds number and the inlet fluid magnitude to produce varying momentum ratios. This parametric study revealed that with increasing momentum ratio, there is an increase in the side fluid penetration into the main stream and an increase in the length of recirculation zone located in the upper half of the main duct and downstream of the inlet "hole".

From a physiological point of view, the laminar flow in tees is worthy of investigation, because a junction localises atherotic plaques and thrombi (blood clots), see for example, Fernandez et al (1976). Most of the work in this area has been confined to two-dimensional studies, that are not necessarily restricted to right-angled

junctions; the flow is usually of the dividing type and is not therefore directly applicable to the present investigation. Further information on pulmonary fluid mechanics can be found in O'Brien et al (I977), Erlich et al (I977) and Pedley (I977).

(b) TURBULENT FLOW

The previous work on the turbulent flow in tee-junctions has been restricted to jets issuing into a confined co-flowing stream. Stoy and Ben Haim (I973), Kamotani and Greber (I972) and Bouchez and Goldstein (I975), Tatchell (I975) and Simitovic (I977) to name only a few, have looked at the problem. In all cases, the geometries used were similar in shape; and each researcher examined the effects of varying the momentum ratio on either the flow or the heat transfer in the main duct.

The results of these studies indicate several common features: (i) the existence of a recirculation zone located downstream of the jet and between the injection wall and the jet centre-line; the re-attachment length of the recirculation zone increases with injection ratio; (ii) the jet produces a pair of counter-rotating vortices in the main duct, the strengths of which first increase with downstream distance, then decrease because of viscous and turbulent diffusion; (iii) as the injection ratio $R \equiv \frac{\overline{V}_i}{\overline{W}_m}$ increases, the depth of penetration of the jet into the main stream also increases; indeed, impingement upon the wall opposite the jet inlet may occur.

With respect to heat transfer, Bouchez and Goldstein (I975) determined the heat-transfer coefficient distribution along the wall opposite the jet. They found that as the injection ratio increases, so does the maximum heat-transfer coefficient. Indeed, for an injection ratio of about I2, the maximum heat-transfer coefficient was I5 times the fully-developed value.

Kamotami and Greber (I972) and (I974) measured the velocity and temperature trajectories (the locus of the maximum velocity or temperature on the symmetry plane parallel with the jet axis) of the incoming jet of fluid; they found that the temperature trajectory was located closer to the injection wall than the corresponding velocity trajectory.

I.3.3 TEE-JUNCTIONS OF ROUND CROSS-SECTION

(a) LAMINAR FLOW

Kried et al (I975) performed a small experimental investigation into the laminar flow in a tee-junction; the flow arrangement was of the dividing type, illustrated by drawing (d) in Figure I.I. At the junction the fluid split to produce a "split ratio" of about I5. The split ratio S is defined as $S \equiv \frac{\dot{M}_{LEG2}}{\dot{M}_{LEGI}}$. The average velocity profiles on the diametral plane parallel with the inlet duct axis for the leg carrying the least amount of fluid (LEGI) showed the existence of a recirculation zone in the upper half of the leg, while at the bottom, the maximum velocity was 9 times the average velocity in the leg.

Liepsch (I974) used a flow situation depicted by

drawing (c) of figure I.I. For various flow ratios, Liepsch determined, using laser - doppler anemometry, the average velocities in the horizontal duct; the diametral plane containing these velocities was normal to the exit duct (vertical) axis.

(b) TURBULENT FLOW

An exhaustive literature survey did not reveal any detailed data on the turbulent flow in round cross-sectioned tee-junctions. It would appear, however, that this type of junction has, and indeed is continuing to recieve a large amount of attention to determine its flow rate-pressure drop characteristics. Further information can be found in Villemonte (I977), Miller (I97I) or the publications of the Engineering Sciences Data Unit (I973).

From a theoretical viewpoint, the turbulent flow in a uniformly dividing tee-junction (split ratio of I.) has been predicted using a finite-difference scheme, Pollard and Spalding (I977a). The predictions, when coupled with heat transfer, show good agreement with available heat transfer data, Pollard and Spalding (I977b). The flow predictions are, however, in doubt for a number of reasons not least of which is the use of an assumed inlet velocity profile in lieu of an inlet duct.

With respect to heat transfer, the experiments of Wesley and Sparrow (I976) provide what is quite probably the most comprehensive data available. Using dividing flow for a number of split ratios, they determined the longitudinal average and circumferential local heat-transfer variation in one of the "horizontal" legs of a tee-junction. (This data was employed by Pollard et al (I977b)).

The data of Wesley et al indicated the following:-

(a) for increasing Reynolds number, but constant split ratio, the maximum Nusselt number increased slightly. For a fixed Reynolds number, the maximum Nusselt number increased markedly with split ratio.

(b) for a fixed split ratio the circumferential variation of the heat-transfer coefficient was found to be weakly dependent upon Reynolds number, and the circumferential variations reduced to zero within 6 or 7 diameters downstream of the inlet axis.

Note that the above two points relate to data taken in LEGI (i.e. $S=\frac{\dot{M}_{LEG2}}{\dot{M}_{LEGI}}$) .

Mozharov et al (I972) determined the temperature trajectory in a combining flow situation (drawing (a) of Figure I.I); the side fluid was heated. For various momentum ratios their data indicated that the cross-stream temperature variations diminished to zero in about 5 main duct diameters.

Rathegeber et al (I977), using a geometry and flow situation similar to Mazharov et al (I972) obtained concentration measurements in the jet stream for various

momentum ratios.

Mills (I962) used a tee-junction as an inlet constriction to evaluate its effects on the heat transfer in a pipe downstream of the tee. Immediately downstream of the tee, the heat-transfer coefficient was found to be large when compared to the fully-developed pipe flow heat-transfer coefficient; however, the tee orientation was not specified.

I.3.4 CALCULATION PROCEDURES

(a) INTRODUCTION

The previous two sections of this Chapter present a brief review of the investigations relevant to the flow and heat transfer in tee-junctions. This review revealed that the processes involved in tee-junctions are three-dimensional requiring numerical procedures for their prediction.

In this section, a review is made of the calculation procedures that may be employed for the analysis of three-dimensional processes occurring in tee-junctions.

(b) SOLUTION PROCEDURES

Pracht et al (I976) employed a version of the ALE (Arbitrary-Lagrangean-Eulerian) procedure of Hirt et al (I974) to demonstrate its capability in calculating laminar flow in a bifurcation. That this procedure can be extended to tee-junctions there can be no doubt; however, to do so in a general manner that maintains computer economy is doubtful.

Kandarpa et al (I976) used a finite element procedure to calculate the two-dimensional laminar flow in a dividing flow situation. Its extension to three dimensions with particular emphasis on turbulent flow is, however, not yet available.

It would appear that the finite-difference procedures based on the SIMPLE (Semi-Implicit-Method for Pressure-Linked Equations) algorithm of Patankar and Spalding (I972) is the most common method that has been used for the calculation of both laminar and turbulent flows in tee-junctions.

Tatchell (I975) used a "parabolic" version of SIMPLE for predicting the turbulent flow of a jet issuing into a rectangular duct containing a co-flowing turbulent stream. Simitovic (I977) used an "elliptic" version to predict the same flow situation as Tatchell (I975), but with different momentum ratios. Pollard and Spalding (I977a) used a version of Simitovic's code for predicting the turbulent flow in a tee-junction of round cross-section.

In comparing predictions to experimental data, Tatchell found gross disagreement, while Simitovic found the agreement to be better; this indicates that the flow in tee's is not "parabolic". Pollard et al (I977a) did not compare with velocity data. In all these cases, the predictions used an assumed inlet flow profile in lieu of a side duct. This fact could account for the lack of agreement observed by Simitovic.

The "partially-parabolic" scheme of Pratap (I975) can be employed for the prediction of flow in tee-junctions;

however, provision for flow recirculation must be included. This provision, proposed by Spalding (I976) is developed in this thesis, and is referred to as the "partially-elliptic" version of SIMPLE.

1.4 OUTLINE OF THE THESIS

The remaining sections of this thesis describe the application of two numerical procedures for the prediction of the laminar and turbulent flows in all legs of a tee-junction.

In Chapter 2, the partial-differential equations governing the flow in tee-junctions are presented and classified for steady flows. This Chapter also presents an account of how turbulence is to be handled. Chapter 3 provides details of the numerical calculation procedures that are employed to obtain solutions to the equations presented in Chapter 2.

An experimental program is outlined in Chapter 4. The test rig, the measuring devices and the procedures employed for obtaining the data are also described. Some of the data so obtained is presented and discussed.

In Chapter 5, the predictions, obtained from the use of both numerical procedures, for the laminar combining flow in tees of square cross-section are presented. Predictions for two-diameter ratios and three momentum ratios are displayed and for one case, the predictions are compared with experimental data.

Chapter 6 presents the predictions for the turbulent

dividing flow in a tee-junction of round cross-section. These predictions are obtained using both numerical procedures, the results of which are compared to the experimental data presented in Chapter 4.

Chapter 7 terminates the thesis by summarising the main results obtained from the present study and suggests areas requiring future work.

There is also a set of appendices that provide details of the partial-differential equations, together with some information regarding the calibration of the experimental apparatus. Also presented are four test cases that illustrate the predictive abilities of the numerical procedures when applied to flows that are simple relative to the flow in tee-junctions.

- PART II -

THEORETICAL ASPECTS

CHAPTER 2: MATHEMATICAL FRAMEWORK

2.1 INTRODUCTION

This Chapter deals with the mathematical description of the flow processes occurring in tee-junctions. Assembled here are the partial-differential equations that govern the conservation of mass, momentum and any general scalar variable for both laminar and turbulent flows. The equations are given in cartesian tensor notation; the specific forms used in the present work are provided in Appendix AI.

Presented here also is the method by which the fluid turbulence is handled. It is well-known that the solution of the time-dependent equations governing turbulent flow cannot be accomplished, particularly in three dimensions, because the time scale and size of the fluctuating motions are so small: a finite-difference solution would require both excessive grids and short time steps in order to adequately resolve the details of the turbulence.* It is therefore necessary to solve the time-smoothed equations; the turbulence effects entering into the equations via the time-averaged products of the fluctuating quantities. These products, commonly referred to as "turbulent fluxes" are the focus of the attention of turbulence modellers. A good example of the scope of how these fluxes may be attended to is given by Launder and Spalding (1972). It is one of the models described by Launder and Spalding

*FOOTNOTE:
A good example of the magnitude of the problem is given by Leslie (1973), page 12.

(1972) that is employed here.

The chapter is divided into a further five sections. In Section 2.2, steady flows are classified, from a computational viewpoint, into two categories: elliptic and partially-parabolic; each category is then examined to point out their mathematical features. Next, the elliptic form of the conservation equations are stated in Section 2.3; these equations are then transformed into their time smoothed counter-parts in Section 2.4. The fluctuating components arising from the transformation are further modified so as to provide closure to the time smoothed set of equations: the closure is provided by the model of turbulence described in Section 2.5. Finally, Section 2.6 presents an account of the near-wall boundary conditions used in the computation of turbulent flows.

2.2 FLOW CLASSIFICATION

Strictly speaking, all flows except those being wholly supersonic are such that perturbations of conditions at one point in the flow, can effect changes in the conditions at any other point. These flows are usually classified as being elliptic. There are, of course, situations where some of the mechanisms (i.e. convection, diffusion and pressure) may be weak enough to be ignored. Parabolic flows for example, are characterised by the uni-directional effects of all the above mechanisms; for example, straight duct flows are of this type. Partially-parabolic flows on the other hand, are mid-way between being elliptic and parabolic: pressure is not uni-

directional, but may transmit its effect in the upstream direction. An example of this type is the flow in strongly curved ducts, see Pratap (1975).

There are two main consequences of the above classification system. First, the partially-parabolic partial -differential equations are simpler in form than the elliptic equations. Secondly, both the computational resources and effort required in solving the partially-parabolic equations are smaller than those for the elliptic equations. The first consequence is examined in this Chapter, while the second is attended to in Chapter 3.

2.3 THE CONSERVATION EQUATIONS

2.3.I THE ELLIPTIC FORMS

The equations describing the steady incompressible flow in three-dimensions are given below in cartesian tensor notation. The detailed expansion of these equations in both cartesian and cylindrical polar coordinates can be found in Appendix AI.

The Continuity Equation:

$$\frac{\partial}{\partial X_i}(\rho u_i) = 0 \qquad . (2.1)$$

The Momentum Equations:

$$\frac{\partial}{\partial X_j}(\rho u_i u_j) = -\frac{\partial}{\partial X_i} p + \frac{\partial}{\partial X_j} \tau_{ij} \qquad . (2.2)$$

The Equation for a General Scalar Variable, ϕ

$$\frac{\partial}{\partial X_j}(\rho u_j \phi) = \frac{\partial}{\partial X_j} J_{\phi,j} + S_\phi \qquad . (2.3)$$

where,

u_i, u_j - instantaneous velocities

X_i, X_j - coordinate directions

$\tau_{ij}, J_{\phi,j}$ - stress tensor and flux of ϕ respectively

ρ, p - instantaneous density and pressure respectively

$S\phi$ - source/sink of ϕ

The stress tensor and the flux of ϕ can be related to the gradients of the dependent variables of the equations in which they appear through

$$\tau_{ij} = \mu\{\frac{\partial u_i}{\partial X_j} + \frac{\partial u_j}{\partial X_i}\} \qquad ,(2.4)$$

and

$$J_{\phi,j} = \frac{\mu}{\sigma_\phi} \frac{\partial \phi}{\partial X_j} \qquad ,(2.5)$$

where μ is the laminar viscosity and σ_ϕ is the laminar Prandtl/Schmidt number of the fluid, both of which are taken as constants in the present work.

2.3.2 THE PARTIALLY-PARABOLIC FORMS

The equations given above are the general forms of the conservation equations for steady, incompressible flow. The equations take cognisance of the fact that convection, diffusion and pressure effects are transmitted in all three coordinate directions. Partially-parabolic flows, classified briefly in the previous section, are governed by the following characteristics: (to quote Pratap (1975))

" (a) absence of recirculation so that convection operates only in a single (downstream) direction,

(b) high Reynolds number, so that diffusion is significant only normal to streamlines, and

(c) significant curvature of the streamlines, rendering pressure the dominant transmitter of influences in an upstream direction. "

Flows characterised by (a-c) above allow the elliptic forms of the equations to be simplified, omitting those terms that are weak enough to be ignored. For flows along the Z coordinate direction, for example, we can write:

$$\tau_{i,Z} = J_{\phi,Z} = 0.0 \qquad .(2.6)$$

It is for the sake of clarity that the complete forms of the partially-parabolic equations are not given here; a complete account is provided in Appendix AI.

2.4 THE TIME-SMOOTHED FORMS OF THE EQUATIONS

In this Section, the elliptic form of the instantaneous equations, presented in Section 2.3 are presented in their time-mean form. The partially-parabolic forms are not given for they can be easily inferred from those that are presented.

The time-mean equations for the dependent variables are derived from those previously presented by introducing the following relationships (Hinze (1959)):

$$u_i = U_i + u_i' \qquad ,(2.7)$$

$$p = P + p' \qquad .(2.8)$$

where U_i, P are average values and the primed (') variables are their fluctuating components.

Introducing equation (2.7) and (2.8) into equations (2.I), (2.2) and (2.3) and time averaging, results in the following equations for a steady incompressible flow:

Continuity:

$$\frac{\partial}{\partial X_i}(\rho U_i) = 0 \qquad ,(2.9)$$

Momentum:

$$\frac{\partial}{\partial X_j}(\rho U_i U_j) = -\frac{\partial P}{\partial X_i} + \frac{\partial}{\partial X_j}\left\{\mu\frac{\partial U_j}{\partial X_i} - \rho\overline{u_i' u_j'}\right\} \qquad ,(2.I0)$$

where the overbars indicate time-averaged quantities and the stress tensor has been replaced by equation (2.4).

General Scalar, ϕ

$$\frac{\partial}{\partial X_i}(\rho U_i \phi) = \frac{\partial}{\partial X_i}\left\{\frac{\mu}{\sigma_\phi}\frac{\partial \phi}{\partial X_i} - \rho\overline{u_i'\phi'}\right\} + S\phi \qquad ,(2.II)$$

where $\phi = \phi + \phi'$,(2.I2)

and equation (2.5) has been introduced; and $S\phi$ is now the source/sink of time-averaged quantities.

Appearing in equations (2.I0) and (2.II) are two terms, namely $-\rho\overline{u_i' u_j'}$ and $-\rho\overline{u_i'\phi'}$. These terms or correlations between fluctuating quantities are called "Reynolds stresses" and "turbulent flux" of a scalar variable respectively. These terms must be composed of quantities that are either known or calculable in order that the

equations may be solved. It is the task of the turbulence modeller to provide these quantities; it is to that sphere that attention is now focussed.

2.5 THE MODELLING OF TURBULENCE

2.5.I INTRODUCTION

In this Section, the mathematical model of turbulence employed in the present work is outlined. The choice of models available are diverse as shown by, for example, Launder and Spalding (I972). However, there are two common approaches for modelling the velocity-velocity and velocity-scalar correlations pointed out in the previous section. The approaches are usually referred to as the Reynolds or turbulent-stress concept, and the eddy or turbulent viscosity concept.

2.5.2 TURBULENCE MODEL CLASSIFICATION

(a) REYNOLDS STRESS CONCEPT

The Reynolds or turbulent-stress concept evaluates the stress components (e.g. $\rho\overline{u_i' u_j'}$) directly from differential equations that describe the transport of such stresses. For a turbulent flux (e.g. $\rho\overline{u_i' \phi'}$) other differential equations are solved. Proposers of such models see, for example, Launder, Reece and Rodi (I975), show that for three-dimensional flow, at least seven differential equations (six for stresses, and one for dissipation) together with additional equations for the transport of a scalar variable need to be solved, together with the

momentum and continuity equations. Obviously, the computer requirements of such a model are large indeed.

(b) THE EDDY-VISCOSITY CONCEPT

The eddy-viscosity concept relates the correlations between velocity fluctuations to the gradient of the mean velocities via a turbulent viscosity, i.e.:

$$\rho\overline{u_i' u_j'} = \mu_t \left(\frac{\partial U_i}{\partial X_j} + \frac{\partial U_j}{\partial X_i} \right) \qquad ,(2.I3)$$

where μ_t is the eddy or turbulent-viscosity that is a property of the flow and not of the fluid.

In a similar manner, the turbulent flux of a scalar is related to its own turbulent viscosity or exchange coefficient, via:

$$\rho\overline{u_j' \phi'} = \Gamma_{t,\phi} \frac{\partial \phi}{\partial X_j} = \frac{\mu_t}{\sigma_{t,\phi}} \frac{\partial \phi}{\partial X_j} \qquad ,(2.I4)$$

where $\Gamma_{t,\phi}$ is the turbulent exchange coefficient, μ_t the turbulent viscosity and $\sigma_{t,\phi}$ is the turbulent Prandtl/ Schmidt number.

2.5.3 MODEL SELECTION

From the above brief statements regarding turbulence model classification, it is apparent that the Reynolds stress model is more soundly based than the eddy viscosity approach to the modelling of turbulence. However, even in the former case, there comes a stage in the derivation

when rigor must be abandoned and some hypothesis put forward to effect closure.

In an attempt to provide evidence of the superiority of the Reynolds stress model over a model based on the eddy viscosity concept, Pope and Whitelaw (1976) studied the two-dimensional flow behind a disk. They showed, however, that, when compared to experimental data, the results obtained using the Reynolds stress model were of no better accuracy than those obtained using a two-equation model based on the eddy-viscosity concept. It is because of these findings, coupled with the large computer resources required by a Reynolds stress model for solving a three-dimensional flow situation, that an eddy-viscosity model was chosen for the present work.

2.5.4 THE MODEL OF TURBULENCE

The eddy-viscosity approach to the modelling of turbulence is to relate the local turbulent viscosity, μ_t to one or more properties of the turbulent flow; this viscosity is allowed to vary from one location in the flow domain to another, but at any point, it is assumed to be isotropic. Here, the distribution of the eddy viscosity is calculated from the value of two turbulence quantities, for which partial-differential equations of transport are solved. The two quantities solved for are the turbulence kinetic energy, k, and its volumetric rate of dissipation, ε.

The "k-ε" model of turbulence was first suggested by Harlow and Nakayama (1968); it has been subsequently used in the

form presented by Launder and Spalding (I974) by, for example, Pratap (I975), Tatchell (I975), Serag-Eldin (I977), Simitovic (I977), Pollard and Spalding (I977a,b), and Vasilic-Melling (I976).

Below, the model of turbulence is briefly described; full details of the model can be found in Launder and Spalding (I974). The turbulent viscosity is related to the kinetic energy of turbulence and its volumetric rate of dissipation by the following:-

$$\mu_t \alpha \rho k^2/\varepsilon \qquad ,(2.I5)$$

where

$$k \equiv \overline{\tfrac{1}{2}u_i'^2} \qquad ,(2.I6)$$

$$\varepsilon \equiv \frac{\mu}{\rho}\overline{\left(\frac{\partial u_i'}{\partial X_j}\right)^2} \qquad ,(2.I7)$$

or,

$$\mu_t \equiv C_\mu \rho k^2/\varepsilon \qquad ,(2.I8)$$

where C_μ is a constant.

The partial-differential equations governing the transport of k and ε are stated below; using cartesian tensor notation there are (Launder and Spalding (I974)):-

Transport Equation for k

$$\frac{\partial}{\partial X_i}(\rho U_i k) = \frac{\partial}{\partial X_i}\left(\Gamma_{e,k}\frac{\partial k}{\partial X_i}\right) + \mu_t G_k - \rho\varepsilon \qquad .(2.I9)$$

Transport Equation for ε

$$\frac{\partial}{\partial X_i}(\rho U_i \varepsilon) = \frac{\partial}{\partial X_i}\left(\Gamma_{e,\varepsilon}\frac{\partial \varepsilon}{\partial X_i}\right) + \frac{C_1 \mu_t \varepsilon G_k}{k} - \frac{C_2 \varepsilon^2 \rho}{k} \qquad .(2.20)$$

where C_1, C_2 are constants, $\Gamma_{e,\phi}$ represents the effective exchange coefficients and the generation of turbulence kinetic energy G_k is defined as:

$$G_k \equiv \frac{\partial U_j}{\partial X_i}\left(\frac{\partial U_j}{\partial X_i} + \frac{\partial U_i}{\partial X_j}\right) \qquad .(2.21)$$

The turbulence model involves the use of three constants. The values ascribed to them are given below and are the same as those recommended by Launder and Spalding (1974); they are:-

$$C_1 = 1.44;\ C_2 = 1.92,\ C_\mu = 0.09 \qquad .(2.22)$$

The effective exchange coefficients $\Gamma_{e,\phi}$ relates the combined laminar and turbulent fluxes to the gradients of the flow variables. The exchange coefficient may be expressed by:-

$$\Gamma_{e,\phi} = \frac{\mu_t}{\sigma_{t,\phi}} + \frac{\mu}{\sigma_\phi} \qquad ,(2.23)$$

where $\sigma_{t,\phi}$,σ_ϕ are the turbulent and laminar Prandtl/Schmidt numbers respectively, for the variable ϕ. The laminar Prandtl/Schmidt numbers are dependent upon properties of the fluid and is equal to unity for the momentum, k and ε equations. $\sigma_{t,\phi}$ on the other hand, is dependent upon the turbulence phenomena; the values assigned to these are (Launder and Spalding (1974)):-

$\phi\rightarrow$	u	v	w	k	ε	T,M
$\sigma_{t,\phi}$	1	1	1	1	1.3	0.9

,(2.24)

where T,M denotes temperature or mass transport.

The equations given above are expanded in both cartesian and cylindrical polar coordinates in Appendix AI.

2.6 BOUNDARY CONDITIONS

2.6.I THE NEAR-WALL REGION - THE WALL FUNCTION

(a) MOTIVATION

The turbulence model presented here is valid only for turbulent flows where laminar viscosity effects are negligible when compared to its turbulent counterpart. As a wall is approached, however, both these viscosities begin to influence the transport processes occurring there; in addition, the dependent variables vary steeply in this region. Consequently, extremely fine finite-difference grid distributions are necessary in this region if good accuracy is to be obtained.

At the present time (I978), there appears to be only two ways of accounting for the near-wall region in the numerical calculation of turbulent flow: the wall function method of Launder and Spalding (I972), and the low Reynolds number model for the near-wall region, proposed by Jones and Launder (I973). In the present work, the wall function approach has been adopted chiefly because of its economy from the point of view of computer storage and time. The wall function has been reviewed by Launder and Spalding (I974) where it was found satisfactory for two-dimensional flows; it is the forms recommended by them that are used here.

(b) THE WALL FUNCTION APPROACH

The main idea behind the use of wall functions relates to the spacing of the near-wall finite-difference grid node to its wall neighbour. The position of the near-wall node must be such that it lies within the logarithmic layer: then the near-wall node is related to the wall node by the full implications of the logarithmic profile that is assumed to exist between them. That is, a region of uniform stress where the generation and dissipation of the turbulence energy is locally in balance.

(c) THE WALL FUNCTIONS

The velocity variation in the near-wall region is assumed to obey a logarithmic law; see, for example, Hinze (1959). The log-law is:

$$U^+ = \frac{I}{\kappa} \ln(Ey^+) \qquad ,(2.25)$$

where,

$$U^+ = \vec{U}_p/\vec{U}_\tau = \vec{U}_p/(\tau/\rho)^{\frac{1}{2}} \qquad ,(2.26)$$

and,

$$y^+ = \rho y_p \vec{U}_\tau/\mu \qquad .(2.27)$$

The constants E and κ are assigned the values 9.0 and 0.4 respectively. The terms in the above equations relate the location of the resultant near-wall velocity vector, $\vec{U}_p$ (parallel to the wall) to the distance y_p from the wall.

The shear velocity, $\vec{U}_\tau$ and the non-dimensional distance y^+ are related to the local values of the turbulent kinetic energy by solving the kinetic energy equation with convection and diffusion neglected; this results in:-

$$\vec{U}_\tau = (k_p \, C_\mu^{\frac{1}{2}})^{\frac{1}{2}} \qquad ,(2.28)$$

and,

$$y^+ = y_p \, k_p^{\frac{1}{2}} \, C_\mu^{\frac{1}{4}} / \mu \qquad .(2.29)$$

Inserting equations (2.28) and (2.29) into (2.25), gives the wall-functions for the velocities. It is:-

$$U^+ = \frac{\vec{U}_p}{(\tau/\rho)_p} C_\mu^{\frac{1}{4}} k_p^{\frac{1}{2}} = \frac{I}{\kappa} \ln\left(\frac{E y_p \, C_\mu^{\frac{1}{4}} k_p^{\frac{1}{2}} \rho}{\mu}\right) \qquad .(2.30)$$

where the subscript "p" refers to the values at the near-wall node.

The turbulence properties, k and ε, are treated differently then the momentum equations in the near-wall region. The rate of turbulence dissipation equation (ε) near the wall is fixed by reference to the requirement that the length scale ℓ, varies linearly with distance from the wall; the value of of ε_p is determined from:

$$\ell_m = \kappa y_p \qquad ,(2.3I)$$

where ℓ_m is Prandtl's mixing length, and from the definition (Launder and Spalding (I972)):-

$$\varepsilon = k^{3/2}/\ell \qquad ,(2.32)$$

which leads to:-

$$\varepsilon_p = \frac{C_\mu^{3/4} k_p^{3/2}}{\kappa \, y_p} \qquad .(2.33)$$

The quantity k_p is calculated from the regular balance equations but with the following modifications: the diffusion of kinetic energy to the wall is set equal to zero; the generation terms in the k equation are modified

to account for the near-wall stress (calculated from equation (2.30)). The dissipation term is also modified in light of equation (2.33) and is prescribed as an average value over the near-wall control volume (see next Chapter for control volume definitions); therefore:-

$$\varepsilon\rho = \frac{I}{y_c} \int_0^{y_c} \rho\varepsilon \, dy = \frac{C_\mu^{3/4} k_p^{3/2}}{y_c} \int_0^{y_c} \frac{dy}{\kappa y} \qquad ,(2\text{-}34)$$

where y_c is the distance from the wall to the face of the control volume, parallel with the wall.

For a general scalar variable ϕ, the wall functions are derived in a manner similar to equation (2.30). The near-wall variation of ϕ is also assumed to be logarithmic, so:-

$$\phi^+ = \sigma_{e,\phi} \, (U^+ + P) \qquad ,(2.35)$$

where ϕ^+ is defined in terms of the local (ϕ_p) and boundary (ϕ_w) values of ϕ and the boundary or wall flux J_w through:

$$\phi^+ = \frac{(\phi_p - \phi_w)\rho C_\mu^{1/4} k_p^{1/2}}{J_w \quad \sigma_{e,\phi}} = U^+ + P \qquad ,(2.36)$$

where $\sigma_{e,\phi}$ is the effective Prandtl/Schmidt number, and where P is commonly called the "P"-function which takes cognisance of the resistance of the laminar sub-layer, Jayatillaka (1969); for the present work, P is taken from Launder and Spalding (1974); it is:-

$$P = \sigma_{e,\phi} \frac{\pi/4}{SIN(\pi/4)} \left(\frac{A}{\kappa}\right)^{\frac{1}{2}} \left(\frac{\sigma_\phi}{\sigma_{e,\phi}} - 1.0\right) \left(\frac{\sigma_{e,\phi}}{\sigma_\phi}\right)^{\frac{1}{4}} \qquad ,(2.37)$$

where for the present work, $\sigma_{e,\phi} = 0.9$ and $\sigma_\phi = 0.7$, both of which are taken as constants, and A is Van Driest's

constant, A = 26.0.

2.6.2 OTHER BOUNDARY CONDITIONS

The previous section dealt with the near-wall boundary conditions for turbulent flow. The boundary conditions for other areas of the domain of interest, for example, symmetry planes, will be described as each particular geometry is attended to.

2.7 SUMMARY OF THE CHAPTER

In the present Chapter, the details of the mathematical description of the flow in tee-junctions has been described. For turbulent flows, a two-equation model has been described that effects a closure for the time-averaged equations: two additional equations are solved, the transport equation for the turbulent kinetic energy and its volumetric rate of dissipation. Also, special practices have been outlined for the treatment of near-wall regions whereby wall fluxes are calculated from empirical relationships and not from gradient-type laws.

CHAPTER 3.0: THE NUMERICAL SOLUTION PROCEDURES

3.1 INTRODUCTION

The equations of the previous chapter were presented in their general elliptic form which, when suitably modified, reduce in complexity to produce the partially-parabolic versions. This chapter provides details of the numerical solution procedure employed for the solution the elliptic form of the equations, together with details of how this solution procedure is capable of solving both the elliptic and partially-parabolic forms of the equations in a simultaneous manner. Both procedures are a development of the present investigation, and are described here in detail for the first time.

The two calculation procedures are similar in their approach, and they share many common features; for example, in calculating the flow using both sets of equations, it is the pressure field that is the common link between each set of equations. They differ however in that the partially-parabolic portion of the solution procedure employs marching integration, while the elliptic portion does not. It is through the use of marching integration, instead of calculating elliptically, that substantial storage savings may be obtained. Of course, the justification of using a marching integration in certain regions of the flow will depend upon how well the predictions (from the two procedures) compare with information from other sources.

3.2 OUTLINE OF THE CHAPTER

First, the general elliptic form of the equations are put into their finite-difference form; thereafter, these finite-difference equations are examined so as to indicate what modifications are required to obtain the partially-parabolic forms; in particular, attention is placed upon the modifications to the finite-difference equations in areas that lie midway between elliptic regions and partially parabolic regions of the flow (i.e. moving from a region of recirculating fluid to a region that has none). Thereafter, a detailed account of the general solution procedure is given; the partially parabolic marching integration procedure is then described by reference to the general elliptic procedure. Finally, an account is given of the accuracy of the numerical procedures together with some other computational matters.

3.3 THE FINITE-DIFFERENCE EQUATIONS

3.3.I INTRODUCTION

In this section the finite-difference forms of the general three-dimensional elliptic equations are derived, together with their partially-parabolic counterparts. Although there are fundamental differences in the equations they are derived from a common datum:

(a) The flow domain is subdivided into smaller volumes by a finite-difference grid; this grid is common to both sets of equations and procedures.

(b) Each finite-difference equation is then derived based on the integration of the partial-differential equations over the finite-difference control volumes.

(c) Subsequently, the solution procedures then solve the equations resulting from step (b).

3.3.2 THE FINITE-DIFFERENCE GRID

The finite-difference grid consists of orthogonal, intersecting lines (grid lines) mapped over the flow domain; they are parallel with the three coordinate axes. The points of intersection of these grid lines, usually referred to as grid nodes, form a set of reference locations that identify the location of the flow variables. The grid arrangement does not need to be uniform; it may be varied to locate more grid nodes in regions where steep gradients are expected, as for example near solid boundaries. The grid density can be chosen, after experimentation, so as to make the results of the computations independent of grid refinement; the density selected is, of course, dictated by both economic restraints and the available computer storage.

3.3.3 LOCATION OF FLOW VARIABLES

Figures 3.I (a), (b) and 3.2 show the manner in which the dependent variables are distributed within a finite-difference grid. Figures 3.I(a) and 3.I(b) show an X-Y and R-θ plane respectively, while Figure 3.2 shows a Y-Z (or R-Z) plane. The pressure and any scalar variable such as temperature are stored at the grid nodes, while the velocity

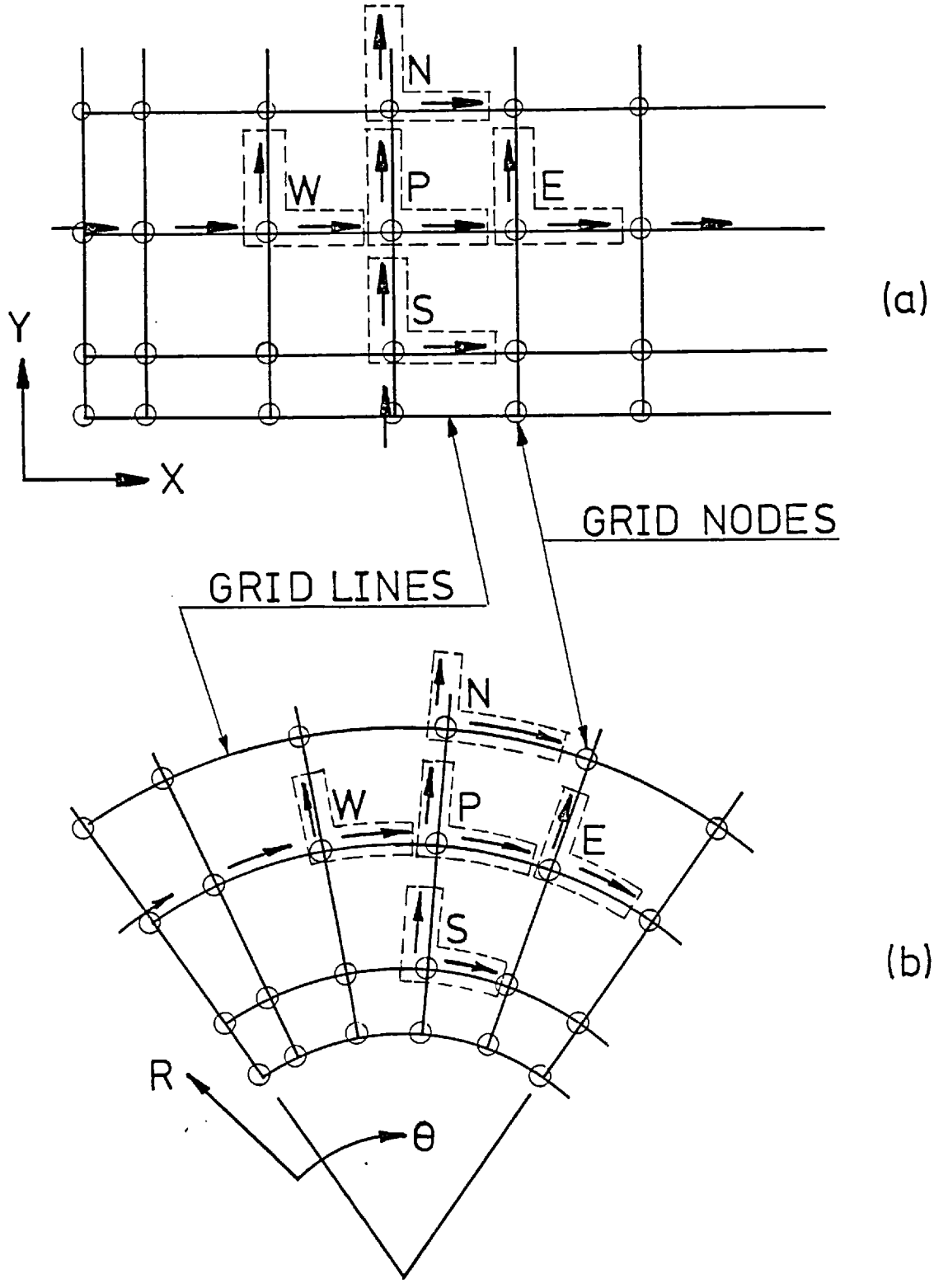

FIGURE 3.I: LOCATION OF DEPENDENT VARIABLES
(a) X-Y PLANE; (b) R-θ PLANE

components are stored midway between adjacent nodes. This staggered arrangement is adopted from Harlow et al (1965).

The velocity components are enclosed in dotted lines in the figures; the purpose of these lines is to denote an identification system for accessing the velocity component synonymous with the grid node. Note that each velocity component is placed ahead of their respective grid nodes, and is located midway between the grid points.

In Figure 3.2, the grid lines (they are really planes made up of X-Y grid lines) marked A, B and C are referred to as the upmarch, current and downmarch planes respectively.* This is done so as to allay any confusion regarding the flow direction: the term upstream in regions of flow recirculation, is somewhat confusing.

3.3.4 THE CONTROL VOLUMES

The term "control-volume" refers to those regions over which the partial differential equations are integrated so as to derive their finite-difference counterparts. These control volumes are different for each dependent variable. Figure 3.3(a) show the control volume faces for the velocity components and a general variable ϕ on an X-Y plane (an R-θ plane can be inferred easily from that given), while Figure 3.3(b) shows the control volumes on a Y-Z, or R-Z plane.

Note that the interfaces of the control volumes always pass through locations at which the normal velocities are stored.

*FOOTNOTE:
The term "march" means the marching integration direction or the direction in which the numerical solution procedure sweeps the integration domain. This is explained further in Section 3.7.5.

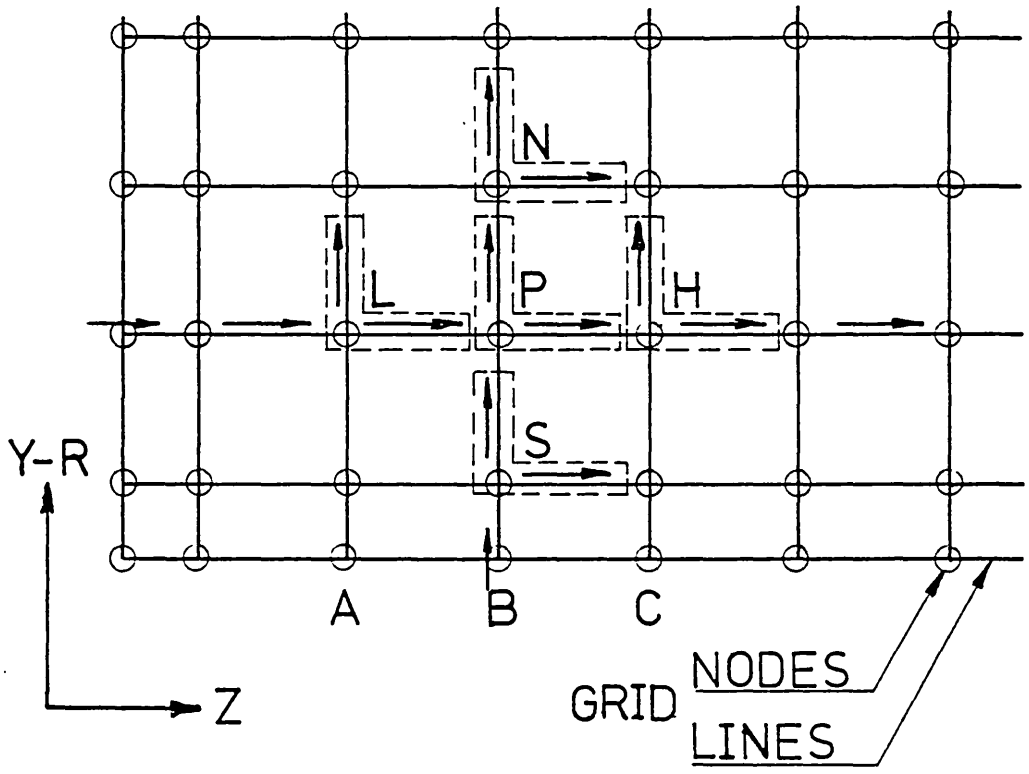

FIGURE 3.2: LOCATION OF DEPENDENT VARIABLES ON (Y-R)-Z PLANE
A-UPMARCH B-CURRENT C-DOWNMARCH

In Figures 3.3(a),(b), the control volumes at the boundaries are shown to be slightly different to those existing at internal grid or velocity locations. The practice adopted is to cause the boundary node, the control volume side and the normal velocity all to coincide with the boundary itself.

3.3.5 THE CONTINUITY EQUATION

The mass continuity equation (Equation 2.I) is integrated over a control volume, the limits of the integration being the control volume sides. The result is:

$$\{\rho_e U_e - \rho_w U_w\}\ \Delta y \Delta z + \{\rho_n V_n - \rho_s V_s\}\ \Delta x \Delta z$$

$$+ \{\rho_h W_h - \rho_l W_l\}\ \Delta x \Delta y = 0 \qquad ,(3.I)$$

where the velocities represent average values over the control volume cell faces and the terms in the equation are illustrated in Figure 3.4. The interface values of densities are evaluated as an arithmetic mean of the appropriate grid node values, e.g.: $\rho_e = \frac{1}{2}(\rho_E + \rho_P)$.

3.3.6 THE GENERAL SCALAR VARIABLE (ϕ) EQUATION

Equation (2.3), given in expanded form in Appendix (A.I) is integrated over a control volume (see Figure (3.4)) in a manner similar to that used for the continuity equation (Equation 3.I) above. Before doing so, the equation can be re-cast in a different form; for a Cartesian coordinate system it is: (where U, V, W are the velocity components in the X, Y, Z coordinate directions):

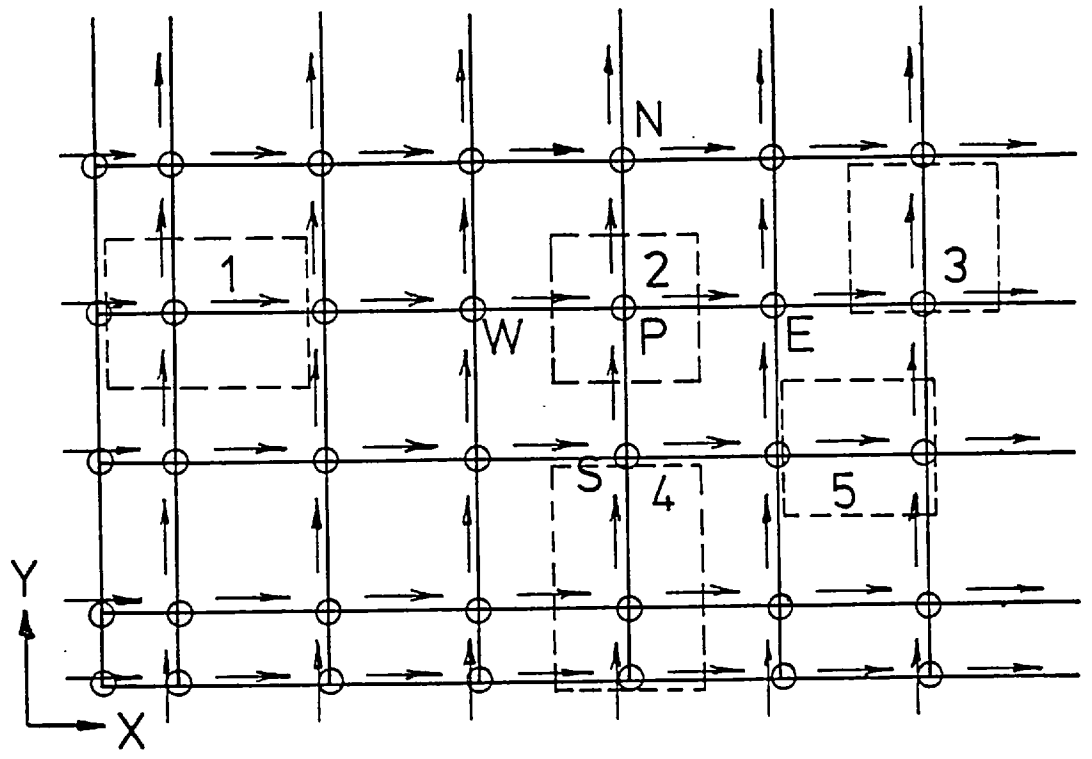

(a)

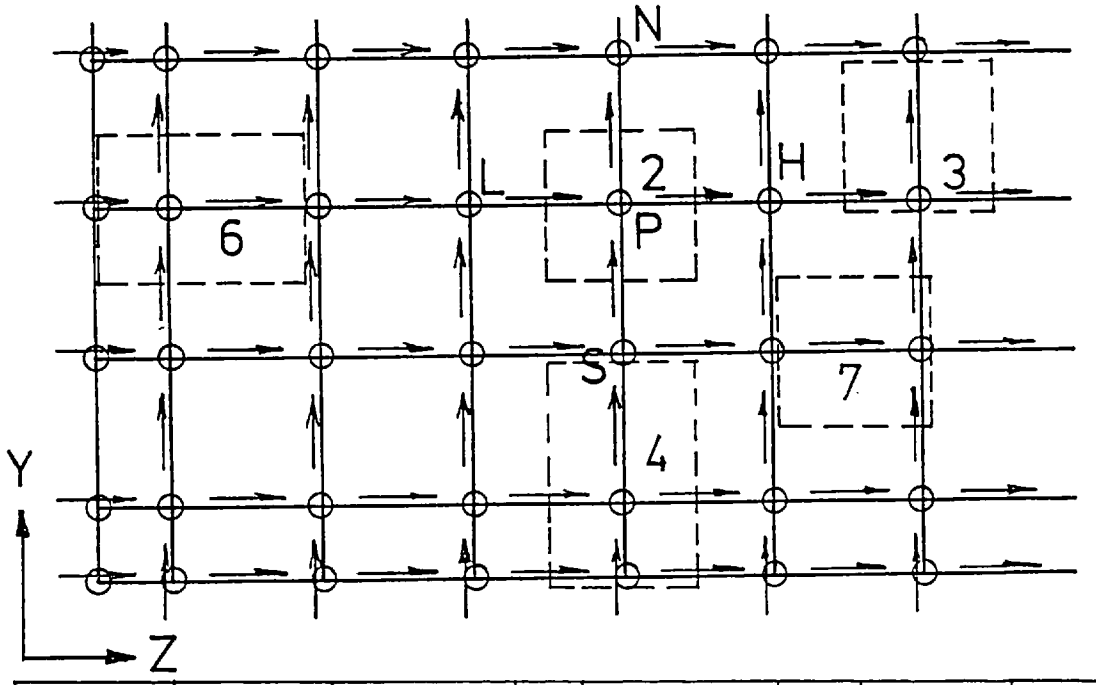

(b)

Number	I	2	3	4	5	6	7
Control Volume Type	U Bound'y	ϕ and Contin'ty	V	V Bound'y	U	W Bound'y	W

FIGURE 3.3: CONTROL VOLUME SPECIFICATION
(a) Y-X PLANE (b) Y-Z or R-Z PLANE

$$\frac{\partial}{\partial x}\left(\rho U\phi - \Gamma_{e,\phi}\frac{\partial\phi}{\partial x}\right) + \frac{\partial}{\partial y}\left(\rho V\phi - \Gamma_{e,\phi}\frac{\partial\phi}{\partial y}\right)$$

$$+ \frac{\partial}{\partial z}\left(\rho W\phi - \Gamma_{e,\phi}\frac{\partial\phi}{\partial z}\right) + S_\phi = 0 \qquad ,(3.2)$$

where the symbols are as before and S_ϕ contains the remainder of the terms from Equation (2.3). Integration of this equation leads to (see Patankar and Spalding (I972))

$$\rho_e U_e \Delta y\Delta z \{f_e\phi_P+(I-f_e)\phi_E\} - \rho_w U_w \Delta y\Delta z \{f_w\phi_W+(I-f_w)\phi_P\}$$

$$+ \rho_n V_n \Delta x\Delta z \{f_n\phi_P+(I-f_n)\phi_N\} - \rho_s V_s \Delta x\Delta z \{f_s\phi_S+(I-f_s)\phi_P\}$$

$$+ \rho_h W_h \Delta y\Delta x \{f_h\phi_P+(I-f_h)\phi_H\} - \rho_l W_l \Delta y\Delta x \{f_l\phi_L+(I-f_l)\phi_P\}$$

$$+ S_U^\phi + S_P^\phi \phi_P = 0 \qquad ,(3.3)$$

where the geometrical terms ($\Delta x,\Delta y,\Delta z$) are defined in Figure (3.4); the subscripts refer to the values at the control volume interfaces (lower case letters) and grid points (upper case letters). The source term S_ϕ has been integrated over the control volume and linearised, i.e.:

$$S_\phi \Delta x\Delta y\Delta z = (S_u^\phi + S_P^\phi \phi_P) \qquad .(3.4)$$

The f's are weighting factors that take cognisance of what properties are convected and diffused across the control volume faces; it is to the evaluation of these weighting factors that attention is now briefly turned.

(a) CENTRAL DIFFERENCING SCHEME (CDS)

As the name implies, the CDS linearly interpolates between grid nodes to obtain the value at the control volume interface. When put in terms of the grid Peclet number ($Pe=\frac{\rho W\delta}{\Gamma}$)

$$N - n - P = \delta y_n$$
$$S - s - P = \delta y_s$$
$$E - e - P = \delta x_e$$
$$W - w - P = \delta x_w$$
$$L - l - P = \delta z_l$$
$$H - h - P = \delta z_h$$

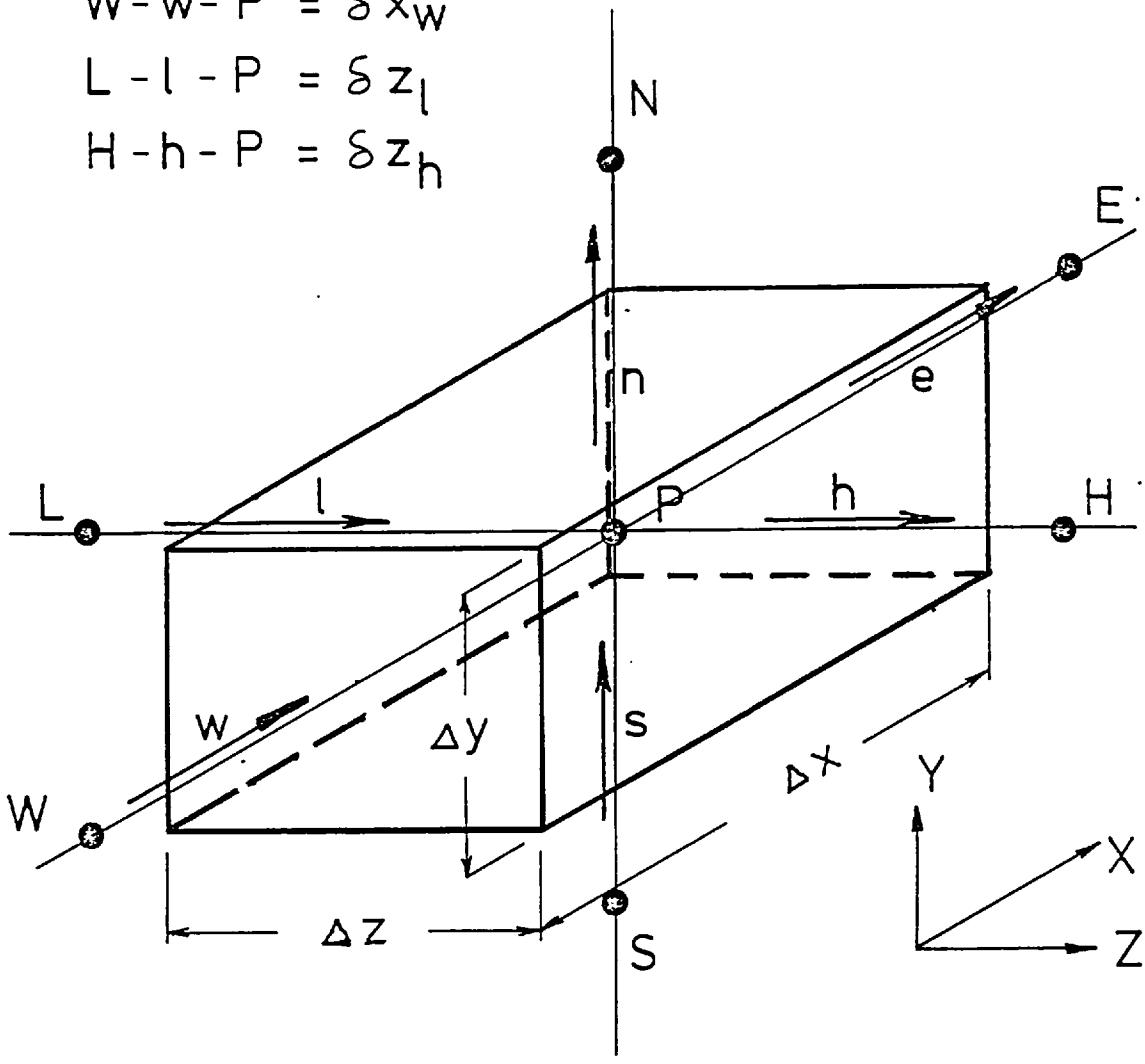

FIGURE 3.4: A ϕ-CONTROL VOLUME

the weighting factor for the h face (for example) is given by:

$$f_h = \frac{I + 2/Pe_h}{2} \qquad ,(3.5)$$

where

$$Pe_h = \rho_h W_h \delta Z_h / \Gamma_h \qquad ,(3.6)$$

and f_n, f_s, f_e, f_w and f_ℓ are defined similarly.

It is well known that when applied to problems where the Peclet number is high, the CDS gives unrealistic results, see, for example Spalding (I972); it is because of the defects of CDS that upstream differencing was formulated.

(b) UPSTREAM DIFFERENCING SCHEME (UDS)

In evaluating the flux across a control volume face, the UDS takes account of the flux direction. That is, a linear variation between grid nodes is presumed for the diffusive flux, while for the convective contribution the value of ϕ convected across a cell face is taken to be the nodal value prevailing on the upwind side of the face; the weighting factor becomes in this case (Spalding (I976))

$$f_h = I + \frac{I}{Pe_h} \qquad Pe_h \geq 0 \qquad ,(3.7)$$

$$f_h = \frac{I}{Pe_h} \qquad Pe_h < 0 \qquad .(3.8)$$

The UDS has been shown to be, see for example Spalding (I972), superior to the CDS when $|Pe_h| > 2$, but slightly inferior otherwise.

(c) THE HYBRID DIFFERENCE SCHEME (HDS)

Realising the discrepancies in both the CDS and UDS, Spalding (I972) proposed a scheme that used the favourable properties of these two schemes. That is, for small Peclet number $|Pe|<2$, CDS is used, while for regions outside this Peclet number range, UDS is used and the diffusive flux is neglected altogether. Therefore, the weighting functions are:

$$f_h = \frac{I+2/Pe_h}{2} \quad \text{for} \quad |Pe_h|<2 \qquad ,(3.9)$$

and $$f_h = I \quad \text{for} \quad Pe_h \geq 2 \qquad ,(3.I0)$$

and $$f_h = 0 \quad \text{for} \quad Pe_h \leq -2 \qquad .(3.II)$$

In the present work, the upstream differencing scheme has been employed simply because of the lower programming complexity; indeed the advantages gained through the use of the hybrid scheme are small, particularly at high Peclet numbers; further details may be found in Spalding (I976).

Returning to Equation (3.3), this equation can be easily rearranged to prepare the equation for solution. Manipulating Equation (3.3) for ϕ_P gives:

$$C_P^\phi \phi_P = (C_E^\phi \phi_E + C_W^\phi \phi_W) + (C_N^\phi \phi_N + C_S^\phi \phi_S) + (C_H^\phi \phi_H + C_L^\phi \phi_L) + S_u^\phi \qquad ,(3.I2)$$

where $$C_E^\phi = \rho_e \Delta y \Delta z U_e (f_e - I)$$

$$C_W^\phi = \rho_w \Delta y \Delta z U_w f_w \qquad .(3.I3)$$

etc.

and $$C_P = C_E^\phi + C_W^\phi + C_N^\phi + C_S^\phi + C_H^\phi + C_L^\phi + S_P^\phi$$

This completes the derivation of the finite-difference equation for a general scalar variable ϕ; attention is now turned to the momentum equations.

3.3.7 THE MOMENTUM EQUATIONS

The elliptic form of the momentum equations are derived in a manner that follows closely the derivation of the scalar variable (ϕ) equation. It must be remembered however that allowances are to be made for the change in control volume appropriate to the velocities, and that special attention is paid to the pressure gradient terms. With this in mind, the momentum equations can be stated as:

U-MOMENTUM

$$C_P^u U_P = C_E^u U_E + C_W^u U_W + C_N^u V_N + C_S^u V_S + C_H^u W_H + C_L^u W_L + S_U^u + \Delta y \Delta z \, (P_P - P_E) \qquad .(3.I4)$$

V-MOMENTUM

$$C_P^v V_P = C_E^v U_E + C_W^v U_W + C_N^v V_N + C_S^v V_S + C_H^v W_H + C_L^v W_L + S_U^v + \Delta x \Delta z \, (P_P - P_N) \qquad .(3.I5)$$

W-MOMENTUM

$$C_P^w W_P = C_E^w U_E + C_W^w U_W + C_N^w V_N + C_S^w V_S + C_H^w W_H + C_L^w W_L + S_U^w + \Delta x \Delta y \, (P_P - P_H) \qquad .(3.I6)$$

Where the C's are evaluated as in Equation (3.I3) and the grid Peclet number has the significance of a grid Reynolds number.

Note that in the above three equations, and from now on, the velocity subscripts refer to their respective storage locations, and not grid location.

The formulation of the equations is now complete; however, no attention has been paid to the pressures except to say that special attention is required. If the pressures were known, there would be little difficulty in solving the resulting uncoupled momentum equations; they are not known a priori, so a method must be found by which the pressure may be obtained. It is the purpose of the "pressure-correction" equation to effect this closure, to which attention is now turned.

3.3.8 THE PRESSURE-CORRECTION EQUATION

The momentum equations allow a velocity field to be calculated for a given pressure field, but because the velocities obtained using this pressure field will not necessarily also satisfy the continuity equation, a method must be found to link the momentum equations to the continuity equation. The method, briefly described below, is the SIMPLE (Semi-Implicit-Method for Pressure-Linked-Equations) method of Patankar and Spalding (I972).

The starting point of the SIMPLE method is to begin with a "guessed" pressure field, the "guess" being either an initial guess or from information obtained from another source. Using this pressure field, the momentum equations can be solved to obtain new velocities. Let the pressure, and the new velocities be represented by P*, U*, V* and W*.

Corrections, P', U', V' and W' are now required whose purpose is to bring the continuity and momentum equations into balance (there is of course only one relative pressure field that will produce velocities that simultaneously satisfy both the momentum equations and the continuity equations).

The corrected velocities can be represented by:

$$\begin{aligned} U &= U^* + U' \\ V &= V^* + V' \\ W &= W^* + W' \\ P &= P^* + P' \end{aligned} \qquad .(3.I7)$$

Now, by subtracting the "stored" form of the momentum equations (equations 3.I4, 3.I5, 3.I6 with U = U*, V = V* etc.), from Equation (3.I4), (3.I5), (3.I6), the corrected form of the velocities and pressures are obtained. For example, the V-momentum equation becomes,

$$C_P^V V_P' = C_E^V U_E' + C_W^V U_W' + C_N^V V_N' + C_S^V V_S' + C_H^V W_H' + C_L^V W_L' + \Delta x \Delta z \, (P_P' - P_N') \qquad ,(3.I8)$$

by neglecting* the first six terms on the right-hand side of Equation (3.I8) results in:

$$V_P' = \frac{\Delta x \Delta z}{C_P^V} (P_P' - P_N') \qquad ,(3.I9)$$

or

$$V_P = V_P^* + \frac{\Delta x \Delta z}{C_P^V} (P_P' - P_N') \qquad .(3.20)$$

---

*FOOTNOTE

This approximation will be attended to shortly.

By introducing expressions like that indicated by Equation (3.20) into the continuity equation (Equation (3.I)), the pressure-correction equation is obtained; it is, for the pressure correction at point P:

$$C_P P'_P = C_E P'_E + C_W P'_W + C_N P'_N + C_S P'_S + C_H P'_H + C_L P'_L + Su \quad ,(3.2I)$$

where

$$C_P = C_E + C_W + C_N + C_S + C_H + C_L \quad ,(3.22)$$

$$C_E = \rho_e \ (\Delta y \Delta z)^2 / C_P^{U_E} \quad ,(3.23)$$

$$C_W = \rho_w \ (\Delta y \Delta z)^2 / C_P^{U_W} \quad ,(3.24)$$

$$C_N = \rho_n \ (\Delta x \Delta z)^2 / C_P^{V_N} \quad ,(3.25)$$

$$C_S = \rho_s \ (\Delta x \Delta z)^2 / C_P^{V_S} \quad ,(3.26)$$

$$C_H = \rho_n \ (\Delta x \Delta y)^2 / C_P^{W_H} \quad ,(3.27)$$

$$C_L = \rho_\tau \ (\Delta x \Delta y)^2 / C_P^{W_L} \quad ,(3.28)$$

and the source term S_u which is defined by:

$$S_u = (\rho_n V_N^* - \rho_s V_S^*) \ \Delta x \Delta z + (\rho_e U_E^* - \rho_w U_W^*) \ \Delta y \Delta z + (\rho_h W_H^* - \rho_\tau W_L^*) \ \Delta x \Delta y \quad .(3.29)$$

It is the purpose of the pressure-correction equation to reduce this mass source term to zero. It is obvious that as a solution reaches the converged state, both the pressure corrections and the mass source are approaching zero, and therefore the solution is actually independent of approximations that entered into the derivation of the equation. This fact has been employed in reducing the complexity of Equation (3.I8) to that shown in Equation (3.I9).

3.4 THE PARTIALLY-PARABOLIC SIMPLIFICATIONS

In the previous section, the finite-difference form of the three-dimensional elliptic equations of Chapter 2 were presented. The finite-difference form of the momentum and general ϕ equations can be put in the following form:

$$\phi_P = \frac{C_N\phi_N + C_S\phi_S + C_E\phi_E + C_W\phi_W + C_H\phi_H + C_L\phi_L + S_U^\phi}{C_N + C_S + C_E + C_W + C_H + C_L - S_P^\phi} \quad .(3.30)$$

The purpose of this section is to examine what effect the partially-parabolic concepts have on the terms comprising Equation (3.30) and in particular, to determine what adjustments are necessary to allow elliptic-partially-parabolic regions to be calculated.

As a first step, consider the W-momentum control volume shown in Figure (3.5). Located on Figure (3.5) are some control volume faces, and velocities, whose subscripts denote the computer storage convention. (i.e. W_P is stored at P.) A, B and C on the figure denote the upmarch, current, and downmarch plane (see Section 3.3.3).

Calculating W_P using the elliptic form of the equations is straightforward for all the velocities are in store; for example C_N^W would look like (see Spalding (I975)):

$$C_N^W = \left[\!\left[\frac{\Gamma_{e,w}\delta z_h \Delta x}{\delta y_n} \; ; \; \frac{\Gamma_{e,w}\delta z_h \Delta x}{\delta y_n} - \rho_k \delta z_h \Delta x \bar{V} \right]\!\right] \quad ,(3.3I)$$

where $\rho_k = \frac{1}{4}(\rho_P + \rho_N + \rho_H + \rho_{NH})$

(and similarly for Γ)

$\bar{V} = \frac{1}{2}(V_P + V_H)$,(3.32)

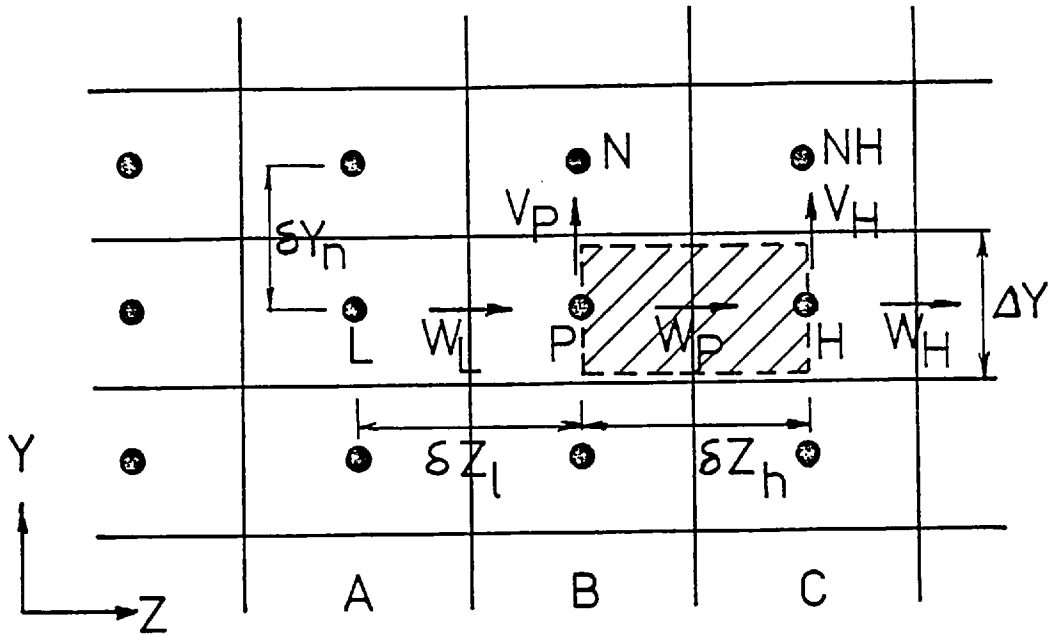

ΔX IN THIRD DIRECTION

FIGURE 3.5: W-MOMENTUM CONTROL VOLUME

and δy, δz, Δx are control volume dimensions. The brackets ($[\![\ ]\!]$) imply that C_N^W takes on a value that is the maximum of the two expressions within the brackets.

Now, let the z direction be that direction where there is a predominant flow direction (Section 2.3.2) for the partially-parabolic procedure. C_N^W would be of the same form as Equation (3.3I) but $\overline{V}$ would equal the upstream value ($\overline{V} \doteq V_P$), and ρ_k would equal $\frac{1}{2}$ ($\rho_N + \rho_P$), because the values on plane C would be unknown (i.e. they would not be in store).

The predominant flow direction velocities, (i.e. the W velocities) coefficients, from an "elliptic" point of view would again be of the same form as Equation (3.3I); whereas, because diffusion in the predominant flow direction is neglected, the "partially-parabolic" coefficient would look like the following:

$$C_H^W = [\![\, 0 \;;\quad 0 - \rho_P \Delta y \Delta x W_P \,]\!] = 0 \qquad .(3.33)$$

Introducing these concepts into Equation (3.30), the equation for W_P would take the following form for calculating in a partially-parabolic manner:

$$W_P = \frac{C_N W_N + C_S W_S + C_E W_E + C_W W_W + C_L W_L + S_U^W}{C_N + C_S + C_E + C_W + C_L - S_P^W} \qquad ,(3.34)$$

where C_N, C_S, C_E, C_W follow from Equation (3.3I)(remembering that values on downmarch plane C, are not available), and C_L takes the form:

$$C_L = [\![\, 0 \;;\quad 0 + \rho_P \Delta y \Delta x \overline{W}_B \,]\!] \qquad ,(3.35)$$

$$= \rho_P \Delta y \Delta x \overline{W}_B$$

where $\overline{W}_B$ is the value of velocity on the plane B.

It should also be pointed out that the source terms must also reflect the partially-parabolic nature of the flow.

3.5 CALCULATING ON ELLIPTIC-PARTIALLY-PARABOLIC PLANES

Attention will now be turned to examining the form of the coefficients that lie on either side of a plane containing say, the reattachment point of a recirculation zone. This plane will be referred to as a plane of transition. A plane of transition is chosen to be located at that point in the flow over which a change in the sign of the march direction velocities is detected. On the upmarch side of the plane, the flow is considered to be elliptic in nature, while on the downmarch side, the flow is considered to be partially parabolic.

With the above definition of the plane of transition, attention is directed to Figure (3.5), where it will be assumed that, W_L in the figure is now pointing towards the upmarch plane and not towards the current plane as indicated; plane B is now considered to be the plane of transition with plane "A" in a wholly "elliptic" region (inside a recirculation zone) and plane "C" in the wholly "partially-parabolic" region. For demonstration purposes, it will be assumed that we are solving a scalar transport equation for ϕ, so that the control volume under consideration is bounded by the velocities normal to its faces.

With reference to the form of the coefficients for elliptic (see Equation (3.3I)) and partially-parabolic (see Equation

(3.35)) flow classification, the coefficients C_N, C_S, C_E and C_W of Equation (3.30) would be as usual for an "elliptic" flow classification, while C_L and C_H are as follows:

$$C_L = \left[\left[\frac{\Gamma_{e,\phi}\Delta y\Delta x}{\delta z_1} \; ; \; \frac{\Gamma_{e,\phi}\Delta y\Delta x}{\delta z_1} + \rho_1 \Delta y\Delta x \, (-W_L) \right]\right] \qquad ,(3.36)$$

$$C_H = \left[\left[0 \; ; \; 0 - \rho_h \Delta y\Delta x W_H \right]\right] = 0$$

where $\Gamma_{e,\phi}$ is evaluated via $\frac{1}{2}(\Gamma_L + \Gamma_P)$.

It should be remarked here that the total volume containing reversed flow, bounded by two planes of transition (i.e. partially-parabolic to elliptic and elliptic to partially-parabolic) and the boundaries of the integration domain, are calculated "elliptically"; extensions to calculate "elliptically" that volume bounded by the reversed flow itself (i.e. a "bubble" of reversed flow) has been left for future work.

3.6 INCORPORATION OF BOUNDARY CONDITIONS

The boundary conditions for the finite-difference equations are usually of two types: either Dirichlet (specified boundary value) or Neumann (specified boundary gradient). In either case, these conditions are easily imposed by coefficient or source term manipulation. For example, at planes of symmetry, the gradients normal to the boundary are zero; this is achieved by setting to zero the coefficient linking the near wall node to that node located on the boundary. In turbulent flows, the wall region is treated via the wall functions whose effect on the equations is felt through the source terms.

3.7 THE ELLIPTIC SOLUTION PROCEDURE

3.7.I INTRODUCTION

The finite-difference equations were formulated in the previous sections. The task is now to solve these equations in an efficient a manner as possible. In this connection, the NEAT algorithm, Spalding (I976) is explained which, when coupled with the well known tri-diagonal matrix algorithm (see for example Roache (I976)) will procure a solution to the equations.

3.7.2 THE SIMPLE-NEAT ALGORITHMS

In extending the range of the SIMPLE procedure, Patankar (I973) devised a general three-dimensional elliptic code that has been used with good success by Pollard and Spalding (I977a,b), Serag-Eldin (I977), Vasilic-Melling (I976) and Simitovic (I977). The exact forms of the procedure vary slightly in their approach; however the common thread is based upon solving over the whole of the calculation domain, each equation in succession until the required level of convergence is reached* In many of the flow situations investigated by the authors quoted above, and indeed, for the flow situations investigated here, the flow is characterised by the fact that only small regions of the calculation domain contain recirculating flow. The implication of the above statement is that undue attention is placed on regions that depend on upmarch conditions.

---

*FOOTNOTE

Convergence will be attended to shortly.

The NEAT algorithm (Nearly Exact Adjustment of Terms) was devised by Spalding (I976) as an aid in overcoming the defects of the whole field approach; the philosphy behind the NEAT procedure can be found in Spalding (I976). All that needs to be said here is that, instead of concentrating attention on the whole field, only one line of control volumes are attended to at any one time, (see Figure (3.6)); and while concentrating attention on a line, all variables are solved for in a successive manner.

3.7.3 THE TRI-DIAGONAL MATRIX ALGORITHM

The finite-difference equations are formulated as mentioned above on a line of control volumes. The solution of the resulting set of equations is achieved through the use of the TDMA; the TDMA will now be described.

For a line orientated in say the y-direction, equation (3.20) can be written as:

$$C_P\phi_P = C_N\phi_N + C_S\phi_S + S_u \qquad ,(3.37)$$

where the C's are as before but S_u now contains all the other terms of Equation (3.30); these other terms are considered constants while the TDMA is performed. For the purposes of explaining the TDMA, Equation (3.37) can be rewritten in terms of the index j; the equation becomes:

$$D_j\phi_j = \overline{A}_j\phi_{j+I} + \overline{B}_j\phi_{j-I} + \overline{C}_j \qquad ,(3.38)$$

or

$$\phi_j = A_j\phi_{j+I} + B_j\phi_{j-I} + C_j$$

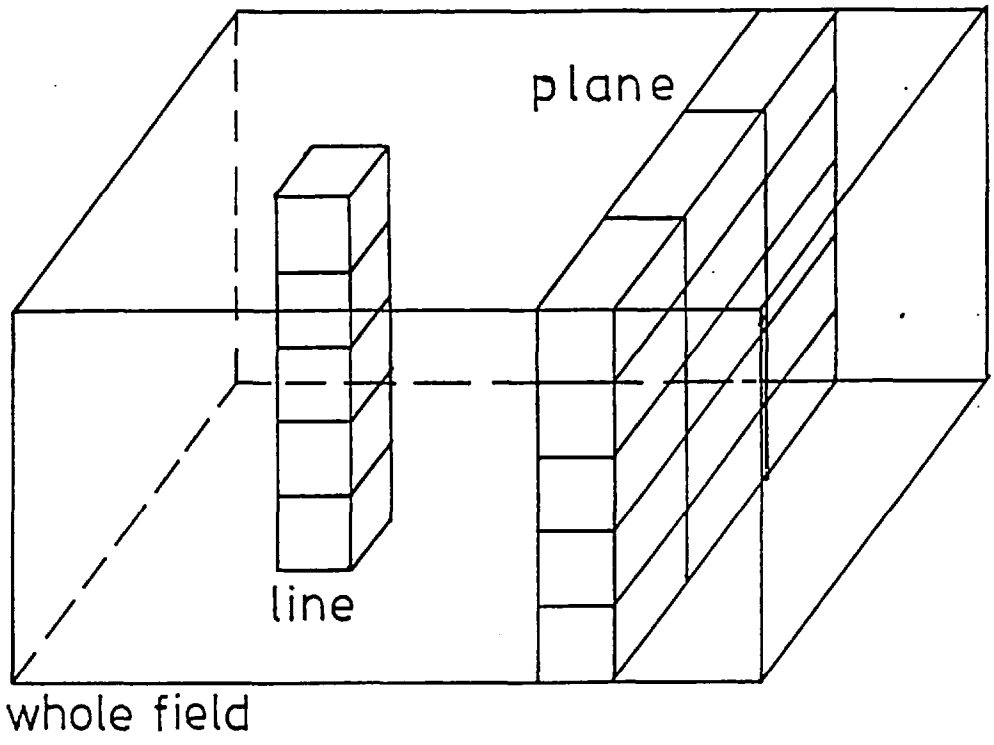

FIGURE 3.6: DISCRETISATION OF INTEGRATION DOMAIN

where $2 \leqslant j \leqslant NY-I$ (the limits of the y-line being I and NY), and A, B, C and D follow directly from Equation (3.37). The values of the ϕ's can now be obtained by:

$$\phi_j = A'_j \phi_{j+I} + B'_j \qquad ,(3.39)$$

where the primed values are given by the recurrence relations:

$$A'_j = \frac{A_j}{I-B_j A'_{j-I}} \quad ; \quad B'_j = \frac{C_j + B'_{j-I} B_j}{I-B_j A'_{j-I}} \qquad ,(3.40)$$

where $A'_2 \equiv A_2$, $B'_2 \equiv B_2 \phi_I + C_2$.

By back-substition, i.e.

$$\phi_{NY-I} = A'_{NY-I} \phi_N + B'_{NY-I} \text{ etc.} \qquad ,(3.4I)$$

the new values of the variables on the line are obtained.

The above TDMA sequence can be used in the calculation of all variables; however, there is evidence to suggest that, when applied to the pressure-correction equation, the rate of convergence can be increased greatly if a "two-dimensional" TDMA is employed, Spalding (I978). In essence, the two-dimensional TDMA solves for the pressure corrections on a plane of cells by using a modified form of the above "one-dimensional" or line TDMA. A two-dimensional TDMA is used here. For details of this form of the TDMA, the reader is referred to, for example, Pratap (I975).

3.7.4 INTEGRAL CONSERVATIONS

NEAT is a semi-implicit numerical procedure which starts from guessed values and converges to the solution of the finite-difference form of the governing equations with their

relevant boundary conditions. As an aid in achieving this goal, certain operations can be performed; these operations can be referred to as block or integral conservation techniques. In the calculations reported in this thesis a plane-wise mass adjustment has been employed. Others are available such as SNIP (Start with a New Integration for Pressure), details of which can be found in Spalding (I976).

The mass adjustment takes the form of a constant pressure adjustment on both sides of the current plane (see Section 3.3.3); in particular, the pressures on the upmarch and downmarch planes are adjusted to effect changes in the velocities entering and leaving the current plane. The adjustment is derived with particular reference to the upmarch pressures and velocities; starting from the linearised momentum equation (see Equation (3.20), i.e.

$$W'_L = DWL\ (\overline{P}'_{LOW} - \overline{P}'_P) \qquad ,(3.42)$$

and

$$ALL \sum_{i,j} (W^*_L + W'_L)_{ij} \rho_{ij} A_{ij} = \dot{M}_{UPMARCH} \qquad ,(3.43)$$

where W'_L - upmarch velocity correction required to satisfy planewise continuity

DWL - pressure correction coefficient (Equation (3.28))

$\overline{P}'_{LOW}$ - the "block" pressure correction required on the upmarch plane

$\overline{P}'_P$ the "block" pressure correction required on the current plane; this is taken as zero

W_L^* - in store velocities

ρ_{ij} - density at each grid node

A_{ij} - area of each control volume face

$\dot{M}_{UPMARCH}$ - the mass flow rate into the upmarch plane, a known quantity.

Solving for $\overline{P}'_{LOW}$ from (3.42) and (3.43) gives the required pressure adjustment,

$$\overline{P}'_{LOW} = \frac{\dot{M}_{UPMARCH} - \sum_{ij} W^*_{L_{i,j}} \rho_{ij} A_{ij}}{\sum_{ij} DWL_{ij} \rho_{ij} A_{ij}} \qquad .(3.44)$$

This average pressure ($\overline{P}'_{LOW}$) is applied directly to all the upmarch direction pressures, while the upmarch velocities are adjusted via Equation (3.42). In a similar manner a $\overline{P}'_{HIGH}$ can be derived and applied to all downmarch direction pressures. Note that, as with the pressure correction, as a converged solution is reached, these corrections go to zero.

Armed with the above information, attention can now be turned to the sequence of steps that make up the solution procedure.

3.7.5 THE STEPS OF THE "ELLIPTIC" SOLUTION PROCEDURE

The main steps in the "elliptic" calculation procedure are as follows:

(a) The flow domain in which the distributions of velocity, turbulence quantities etc., are to be calculated is divided into smaller control volumes via the finite-difference grid.

(b) Consider a plane of control volumes and in particular a line of control volumes located within this plane; calculate the coefficients of the finite-difference equations using in store values of velocity and pressure.

(c) Solve each equation in turn on the line via the TDMA and obtain U*, V*, W*.

(d) Proceed across the plane calculating at each new line, new values of U*, V*, W*.

(e) Using this plane-wise array of "starred" velocities, calculate the coefficients of the pressure-correction equation; solve this set of coefficients using the "two-dimensional" TDMA, for the pressure corrections, (p' s').

(f) Apply these pressure-corrections to the pressures and velocities, in Equations (3.I7), so as to bring both the continuity and momentum equations into alignment.

(g) Apply integral conservations on upmarch and downmarch planes.

(h) Solve, if required, other ϕ equations line by line across the plane.

(i) Repeat steps (b) to (h) until the equations have been satisfied to within a predetermined level.

(j) Move to the next plane, and repeat steps (b) to (i).

(k) Continue until all planes that make up the calculation domain have been visited; this constitutes a domain "sweep".

(l) Perform as many "sweeps" as necessary until all the equations have reached the necessary level of convergence.

3.8 THE PARTIALLY-ELLIPTIC SOLUTION PROCEDURE

The partially-parabolic portion of the solution procedure is fundamentally different from its elliptic counterpart in that it is a marching integration type of procedure. The marching integration is so called because, as the solution domain is traversed, the variables in store are continually being over-written so that the exit conditions of one plane become the inlet conditions for the next. It is apparent that large savings of computer storage can therefore be obtained through the use of marching integration techniques. It must be stressed however that in the predictions to be presented later in this thesis, the overwriting of variables has not been performed; it is the potential storage savings and accuracy penalties of the partially-elliptic procedure that are being assessed here.

It is therefore, the elliptic solution procedure that is used for calculating in a partially-elliptic manner; by specifying that the coefficients are to be formulated in a partially-parabolic manner, the procedure marches in the downmarch direction until a plane of transition is detected.

Then, switching to the "elliptic" form of the coefficients, continue to march until the end of the reversed flow is reached. The march continues from there to the end calculation domain using the partially-parabolic form of the coefficients. The domain is "swept" in this manner, continually checking for a diminution or growth in the volume of reversed flow, until the required level of convergence is reached.

For the flow situations examined in this thesis, it may occur that during the "sweeping" process, no axial recirculation is encountered. However, a minimum region was forced to exist where the flow was calculated using the elliptic form of the coefficients. This region coincided with the planes parallel with the upmarch and downmarch sides of the side (or vertical) duct of the tee-junction (relative to the side duct axis). This was done because the neglect of the march direction diffusion in the side duct, means neglecting the cross-stream diffusion in this duct; this is not in keeping with the partially-parabolic concept.

3.9 SOME MISCELLANEOUS COMPUTATIONAL MATTERS

3.9.I ACCURACY OF THE PROCEDURE

The degree of accuracy of the predictions obtained using the present procedures are governed by two factors: these are firstly, errors in the differential equations, and secondly, numerical errors (i.e. given a differential equation, how well does the numerical solution compare to the exact solution of the differential equation). These are discussed below.

(a) Differential Equation Errors

These errors will arise in two ways: firstly the introduction of the partially-parabolic concept; secondly, in the modelling of turbulence. The level of the error arising out of these approximations is assessed by comparison with experimental data in later chapters of the thesis.

(b) Numerical Error

The numerical error has many components; each component is briefly discussed below.

i) Discretization Error

This error is a result of representing the continuous distribution of a quantity (as described by the differential equations) by finite, discontinuous lumps of that quantity at finite-difference grid nodes, with interpolation formulae between them. The magnitude of the error is determined by the grid distribution; it is reduced by making the grid non-uniform, so as to concentrate nodes in regions of steep gradients, and by systematically increasing the number of grid points until the solutions obtained using these grids are the same within acceptable levels.

ii) Lack of Convergence Errors

The elliptic and partially-elliptic solution procedures both employ iteration using successively updated values of the dependent variables to

obtain a final solution where these values change negligibly with additional sweeps of the domain. The criteria used in all of the prediction work to be presented was determined by two factors. These are:

(a) The normalised residuals of any equation, evaluated via

$$RESIDUAL_{\phi} = \frac{\sum_{ALL\ CELLS} (CONVECTION+DIFFUSION+SOURCE)}{\sum_{ALL\ INLETS} J_{\phi}} \quad ,(3.45)$$

must be less than 0.0I.

(b) The values of the dependent variables at any point in the field do not change by more than I% during successive iterations.

Lack of convergence errors are, therefore small in the solutions to be presented.

iii) Round-off Error

This error is due to computer truncation error. The predictions to be presented were performed on an IBM 360-I95 computer; this machine works to 8 figure accuracy (whereas a CDC 7600 works to I6 figure accuracy).

In an attempt to quantify the round-off-error associated with using the IBM machine, a test run was made for the laminer flow in a square duct, using both the CDC and IBM machines. The grid used consisted of 20,000 grid points, and the solutions were taken to within the convergence criterion outlined above. The maximum difference in the fully-developed velocity obtained was about I%. Of course,

this error would be expected to increase as the number of arithmetic operations are increased, as in for example, the fine(er) grid results to be presented (28000 grid points); even so, the error quoted above is almost insignificant.

iv) Numerical Smearing

Numerical smearing is primarily associated with using one sided, or upwind differencing schemes applied to the convection terms in the equations. The numerical smearing of the results has the effect of introducing an additional, but false, viscosity into the calculations. The magnitude of this false viscosity may be represented by, (Wolfstein (1968)):

$$\Gamma_{false} \tilde{\simeq} 0.36\ \rho V h \sin(2\alpha) \qquad ,(3.46)$$

or, with reference to the actual viscosity, (3.60) may be easily transformed into,

$$\frac{\Gamma_{false}}{\Gamma_{eff}} \simeq .36 Re_h \frac{\mu}{\mu_e} \sigma_e \sin(2\alpha) \qquad ,(3.47)$$

$$\simeq .36 Re_L \frac{h}{L} \frac{\mu}{\mu_e} \sigma_e \sin(2\alpha)$$

where,

Γ_{false} - "false" diffusion coefficient

Γ_e - "actual" diffusion coefficient

$Re_{h,L}$ - grid Reynolds number ($\equiv \frac{\rho V h,L}{\mu}$)

α - angle the velocity vector makes with the grid

h - grid spacing

L - some typical length of the problem considered

V - local velocity.

It is apparent from the list of possible errors associated with the numerical evaluation of differential equations, that the magnitude of these errors can be minimised by using as fine a grid distribution as possible. The grid independence tests to be presented later in the thesis, reflect the attention that has been paid to this area.

3.9.2 STABILITY OF THE NUMERICAL SCHEME

The non-linear, coupled partial-differential-equations employed in the present work are solved by an iterative process. This technique depends therefore upon previous iteration values so as to obtain new ones. In performing this task values of a particular variable will vary, in a strong manner, from iteration to iteration. If violent enough, this fluctuation may cause the procedure to diverge. In order to counteract such behaviour, it is often found judicious to employ an under-relaxation technique so as to effect a slower variation in the dependent variables, i.e.:

$$\phi = \alpha\phi^{N} + (I-\alpha)\phi^{N-I} \qquad ,(3.48)$$

where ϕ is the resulting value obtained from the newly calculated value ϕ^{N} and the previous value ϕ^{N-I}; α is the under-relaxation factor.

An additional technique used as an aid in maintaining a stable, converging procedure, is to linearise the source terms. This technique has been used here also; see Equation (3.4).

3.10 VERIFICATION OF THE NUMERICAL PROCEDURE

As with any new computational procedure, confidence in its accuracy and ability is based upon comparing the predictions against analytical and experimental information; thereby, constructing a firm foundation from which tentative steps into the unknown can be made. In Appendix A3 four test cases are presented to illustrate the accuracy and ability of the present code. The test cases include the laminar flow in a round pipe, the laminar flow in a square duct, the laminar flow in a sudden enlargement, the laminar flow in a square cavity with a sliding top. In the Appendix, it is concluded the predictions agree well with data from other sources.

3.11 CLOSURE

This chapter has presented the derivation of the finite-difference forms of the partial differential equations, and has also presented two methods by which these equations may be solved. One of these methods is capable of calculating flows that contain recirculating fluid embedded in a "partially-parabolic" main stream,thus demanding less computer storage than its purely "elliptic" counterpart.

The calculation procedures are general and flexible, and may be applied to calculate various flow situations governed by different boundary conditions; four test cases, presented in Appendix A3 support this view. The results of more complex flows obtained using these procedures will be presented in Chapters 5 and 6.

- PART III -

THE EXPERIMETAL PROGRAM

CHAPTER 4.0: THE EXPERIMENTAL INVESTIGATION

4.1 INTRODUCTION

4.I.I PURPOSE OF THE EXPERIMENTS

The purpose of the experimental investigation was to provide data for the validation of the numerical scheme and the model of turbulence.

The experiments involved the measurements of the flow and wall mass transfer in a round pipe into which air enters from a square hole located on the wall at the mid-point of the pipe axis: the air splits in a symmetrical manner between the two legs of the pipe.

The motivation for this particular geometry was provided by the plaucity of data for the turbulent flow in tee-junctions of round cross-section and by the need to provide an inlet duct geometry that could be modelled easily by the calculation procedure.

4.I.2 SCOPE OF THE EXPERIMENTS

The investigation was carried out in a limited time frame; this restriction allowed only one flow situation to be examined: the specific geometry and the flow conditions will be examined shortly.

The experiments embodied two measuring techniques to obtain three types of data. Through the use of pressure measurements, the wall static pressures and the mean velocity profiles were obtained at various locations throughout the tee-junction region. The second technique employed the sublimation of

naphthalene to obtain the local mass transfer rates at various locations downstream of the tee-junction.

4.I.3 OUTLINE OF THE CHAPTER

The chapter describes the flow circuit together with brief remarks concerning its construction; this is provided in Section 4.2. In Section 4.3, the measuring techniques are described in detail; thereafter, in Section 4.4 the procedures employed in obtaining the data are presented and discussed. The raw data obtained by the techniques and procedures, are then converted into non-dimensional parameters, and the accuracy and repeatability of the experimental data are discussed. Then in Section 4.7, some of the converted data are presented, and a summary of the main findings is made in the final section (4.8).

4.2 DESCRIPTION OF THE MAIN APPARATUS

4.2.I THE FLOW CIRCUIT

The experimental system, shown photographically in Figure 4.I and in schematic form in Figure 4.2, will now be described.

Air is supplied to the system by a constant speed blower* located some distance away from the rig so as to eliminate vibrational effects. From the blower, the air passes through a flexible pipe to a settling chamber equiped with honeycomb flow straighteners. At the exit of the settling chamber, there is located a contraction section which has a

---

*FOOTNOTE

Details are given in Appendix A.2 of the particular items mentioned in the description of the appratus.

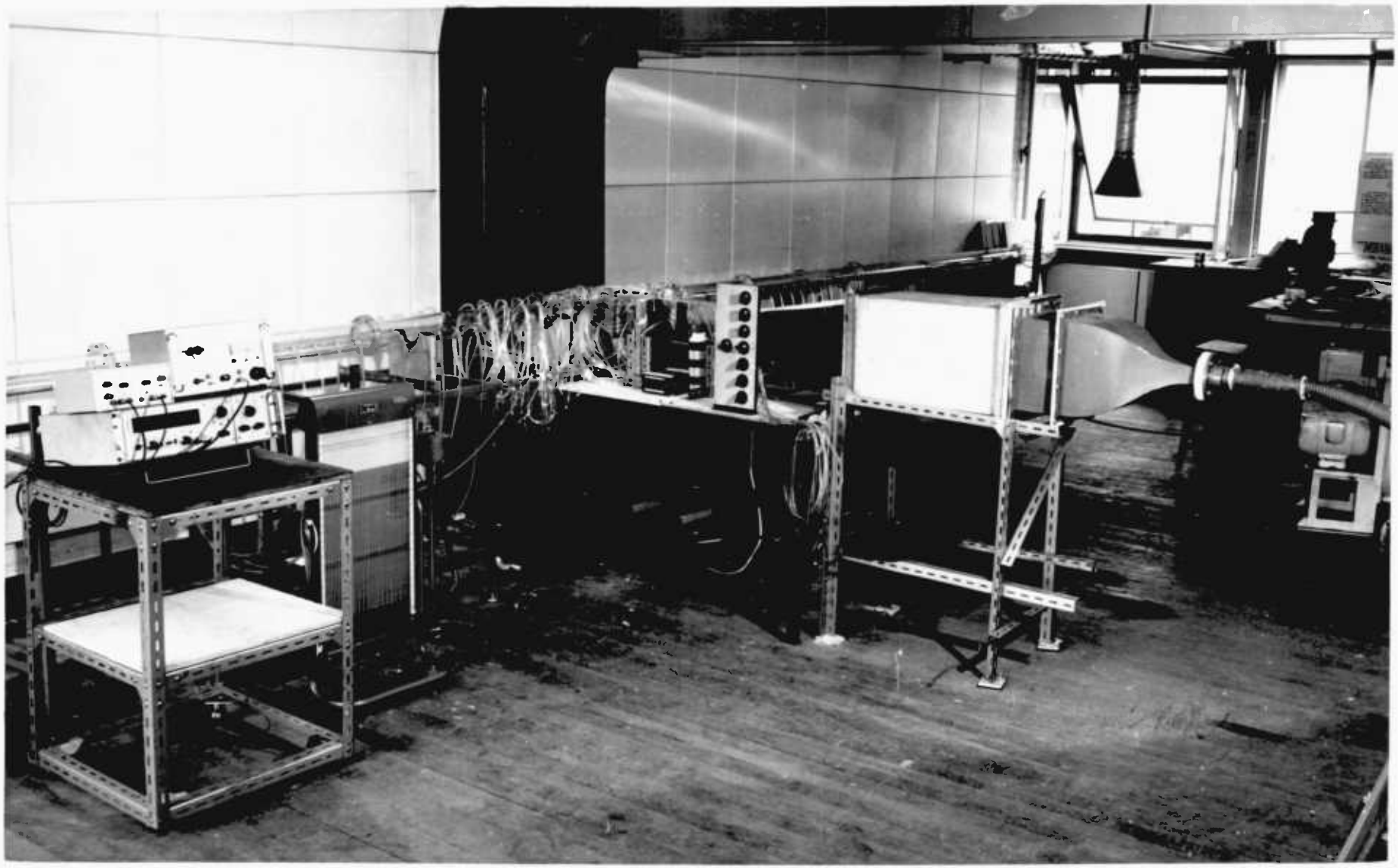

FIGURE 4.I: THE EXPERIMENTAL RIG - A GENERAL VIEW

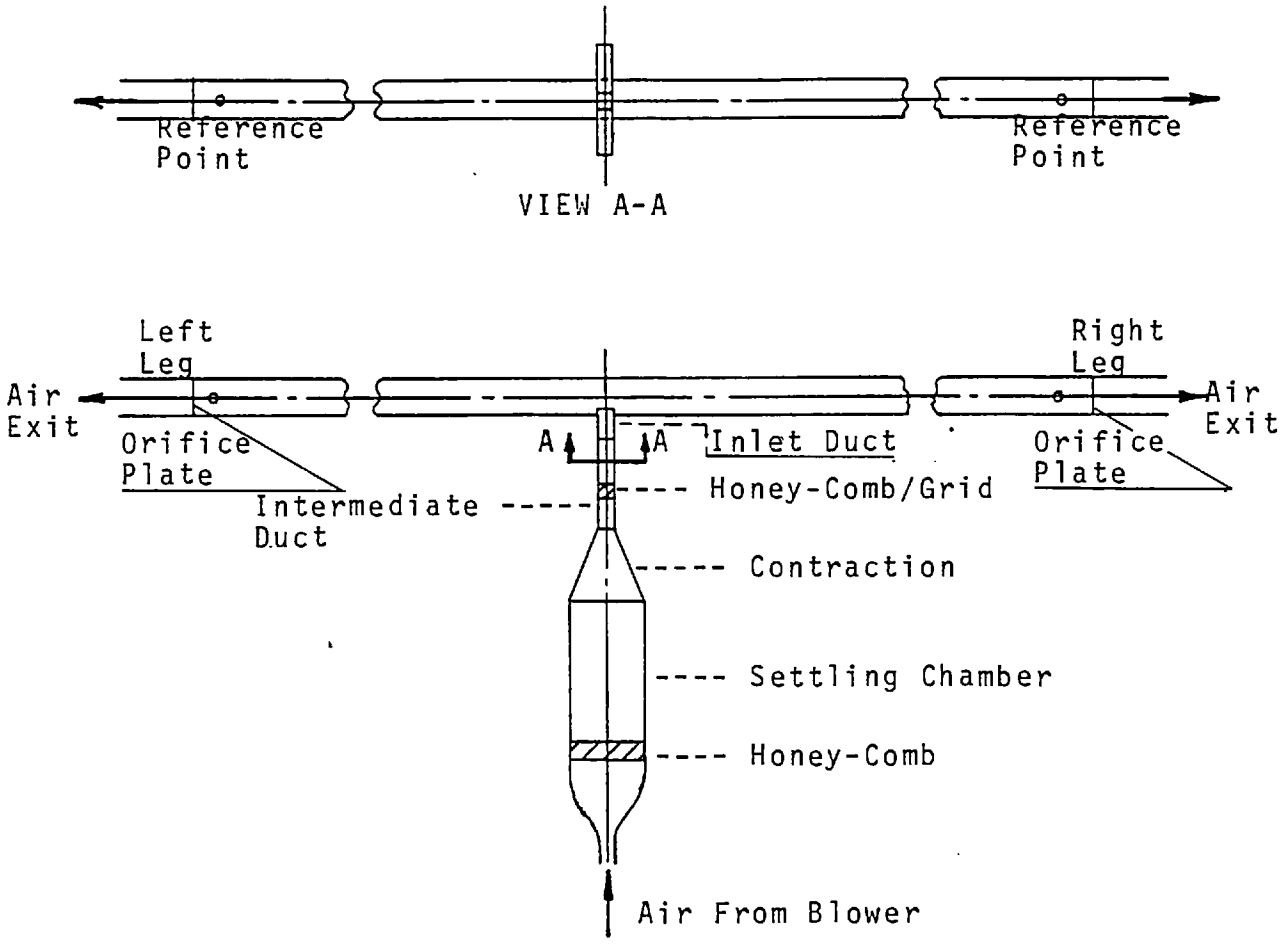

ITEM	DIMENSIONS
Settling Chamber	30x32x80 cm.
Contraction	30x32 to 3.4xI6 cm.
Intermediate Duct	3.4xI6x70 cm.
Diameter of Junction Legs	8.9 cm.
Length of Junction Legs (Inlet-Duct Centre-Line to Reference Points)	360.45 cm.

FIGURE 4.2: SCHEMATIC DRAWING OF EXPERIMENTAL RIG

vertical aspect ratio of 2.0 and a horizontal aspect ratio of 9.4 (area ratio of I8.8). Attached to the contraction is a rectangular "perspex" duct, (0.034m wide x 0.I6m high x 0.8m long) that functions as an intermediate duct between the test section and the contraction. This duct contains a honeycomb flow straightener and two mesh screens whose purpose is to provide a uniform velocity profile at the inlet of the junction; the honeycomb-grid arrangement was designed in accordance with Loehrke (I976). After passing through the grid and honeycomb, the air travels through the inlet duct of the tee-junction; the inlet duct is of wedge shape and with a 45^{o} included angle, a vertical aspect ratio of 4.7, a horizontal aspect ratio of I, and a centre-line length of about 0.I5 meters; this gives a square end of 0.034m to the inlet duct, which is butted onto the pipe. Once the flow has passed through the inlet duct, it splits symmetrically between the two legs of the main pipe (nominal internal diameter = 0.089m) and then exits from the system by passing through orifice plates located about 45 pipe diameters downstream of the inlet duct centre-line. The orifice plates, designed according to British Standards (BS I042, Pt I, (I964)), allowed the mass flow rates in each leg of the junction to be measured.

4.2.2 THE TEST SECTION

The test section is defined as that part of the flow circuit located between the beginning of the inlet duct and points located about 6 pipe diameters downstream of the inlet duct centre-line. This region is shown photographically in

Figure 4.3 and schematically in Figure 4.4. It is observed that all ducts are made of clear "perspex".

Downstream of the honeycomb grid arrangement but 0.045m upstream of the intersection between the rectangular and wedge-shaped ducts there is located 7 plugs, whose purpose is to allow the insertion of probes (the details of which will be described shortly) to measure the inlet velocity profiles; the positioning of these holes is indicated in Figure 4.4.

The wedge-shaped inlet section, shown in Figure 4.3 and 4.4, contains 48 static pressure taps; the positions of these taps is indicated in Figure 4.4; (for specific details refer to Figure 6.6 in Chapter 6). These tappings, and indeed all others, were designed according to Shaw (1960). The physical dimensions are shown in Figure 4.5.

The inlet duct (the wedge shaped one) butted onto the main duct (the pipe) and before joining, all ridges were removed to leave a clean, smooth, flush surface; the joining was accomplished by the use of "TENSOL-6" acrylic glue; this gave a smooth finish to the joint.

The legs of the tee-junction (two legs make up the main duct) are made up of 9 sections of "perspex" tubing: a central portion 0.27m long that was attached to the inlet duct, and 4 sections of various lengths on either side of the central portion of the main duct. The joints between the various sections were carefully manufactured and subsequently very carefully aligned to eliminate any lips. The central

portion of the main duct, together with its Im (II dia.) long neighbours are of cast "perspex", while the remainder of the tubing is of extruded "perspex". The cast tubing is of higher quality than the extruded tubes in that the manufacturer's tolerance levels for ovality, diametrical consistency and wall thickness are guaranteed to be within I% of the mean diameter; the extruded tubing is within 5%. The cast tubing has the additional advantage of being annealed and is therefore, less succeptable to cracking. It is in the cast portion that the majority of measurements were made.

On either side of the inlet duct centre-line the cast sections of tubing contain I0 rows of static pressure taps; each row containing up to I2 taps each, arranged at 30^{o} intervals around the pipe circumference. The positioning of these taps can be obtained from Figure 4.4; although not shown in Figure 4.4, there are I6 additional pressure taps positioned in a uniformely spaced manner between $7 \leqslant \frac{Z}{D} \leqslant 23.6$.

Interspersed between the I0 rows of static pressure tappings, there is located 48 $\frac{1}{4}$"-NPT threaded holes (6 rows of 8, arranged at 45^{o} intervals around the pipe circumference). These holes, plugged with flush fitting brass plugs when not in use, served a dual purpose. First, they allowed access for the pressure probe (a cylindrical type, to be described later), and secondly, they allow for the positioning of plugs that, when filled with naphthalene permits mass transfer measurements to be made. The actual location of these holes is indicated in Figure 4.4.

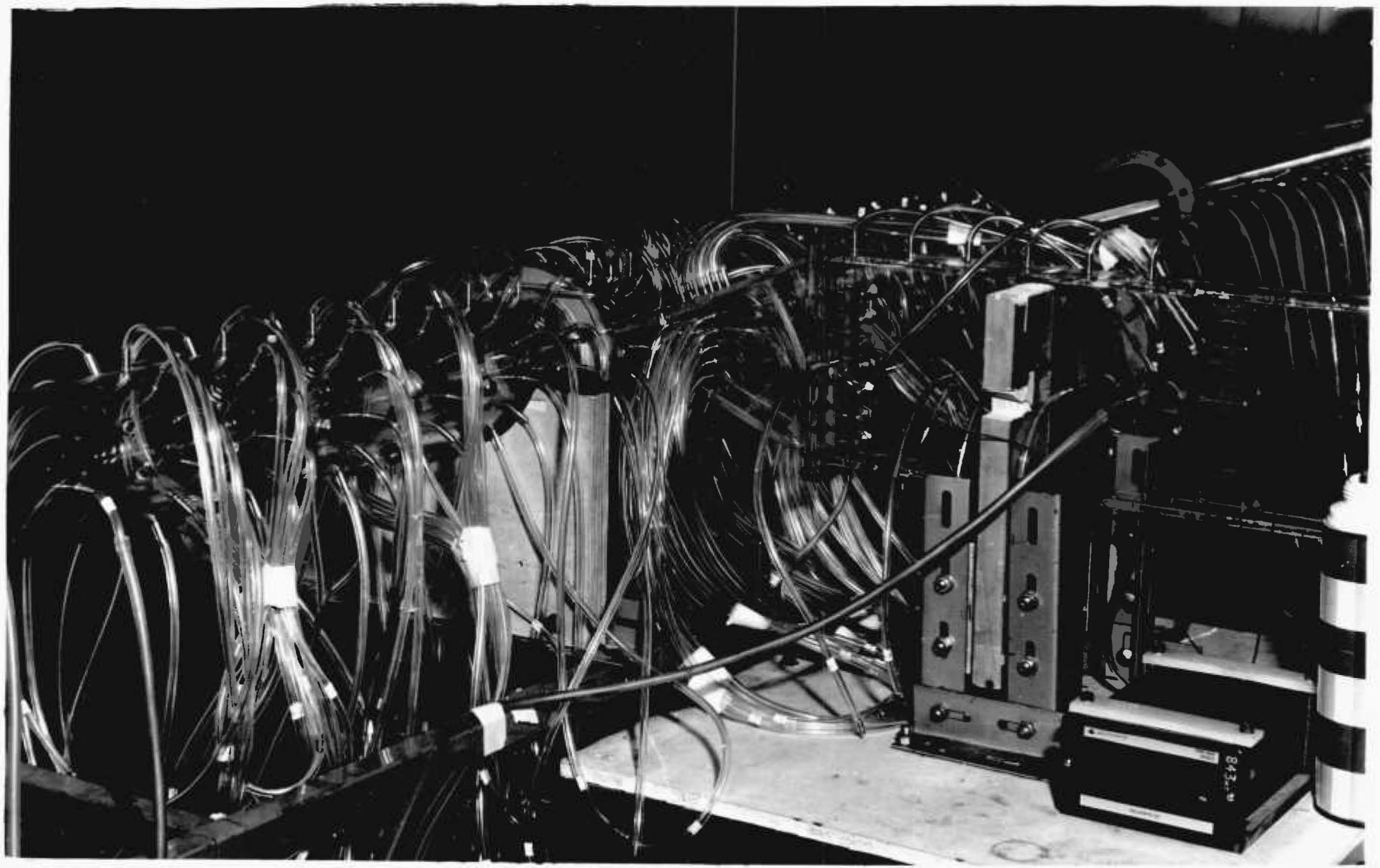

FIGURE 4.3: THE TEST SECTION

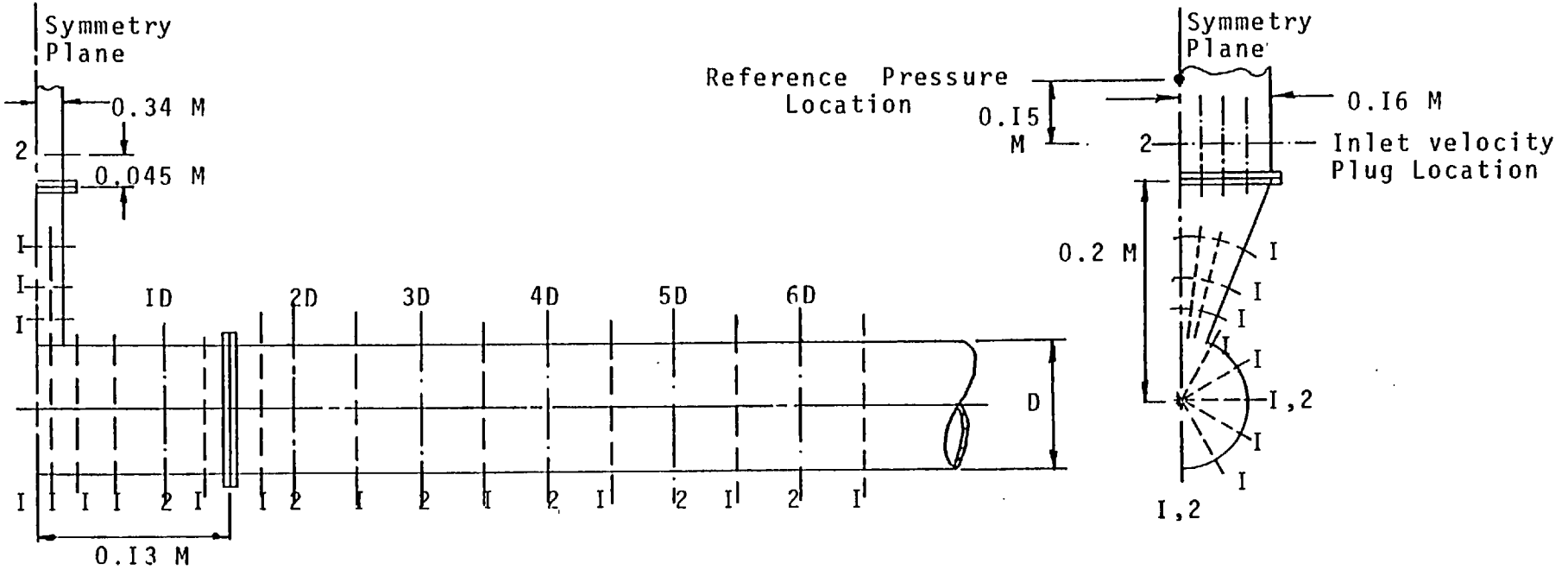

I - STATIC PRESSURE TAPPINGS (30 deg. SPACING IN MAIN LEGS)

2 - HOLES FOR NAPTHALENE PLUGS AND PROBE (45 deg. SPACING IN MAIN LEGS)

FIGURE 4.4: SCHEMATIC OF TEST SECTION

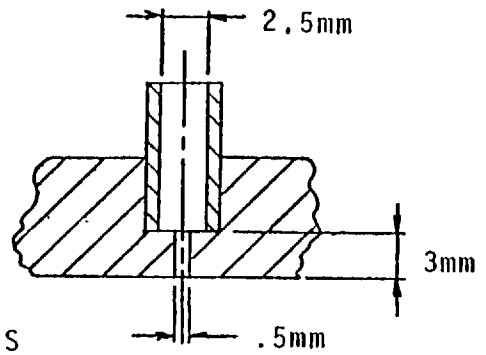

FIGURE 4.5: DETAILS OF STATIC PRESSURE TAPPINGS

At 40.5 diameters downstream of the inlet duct centre-line there is located an additional ¼"-NPT threaded hole, the purpose of which is to allow reference values of velocity and mass transfer to be obtained. These holes (one on each side of the junction) are located approximately 5 diameters upstream of the orifice plates.

4.3 MEASURING TECHNIQUES

4.3.1 THE MEASUREMENT OF PRESSURE

The wall static pressures were obtained using an electronic pressure-transducer (i.e. a micro-monometer). The output of this transducer was fed via a voltage-time integrator into a digital voltmeter (DVM). The output registered by the DVM was then converted into pressures, via a calibration curve; this calibration curve along with others to be mentioned, can be found in Appendix A2 . The equipment used in the measurement of pressure is shown in Figure 4.6.

4.3.2 THE MEASUREMENT OF VELOCITY

(a) THE PROBE

The measurement of the mean velocity was obtained using a three-hole transverse cylinder probe; the probe is shown in Figure 4.7 and details of its construction can be found in Hiett and Powell (1962).

The probe is direction sensitive; it contains 3 pressure sensing holes, arranged in an "L" shaped pattern. The differential pressure readings from any two of the three holes, when coupled with the probes calibration curve, allows the three mean velocity

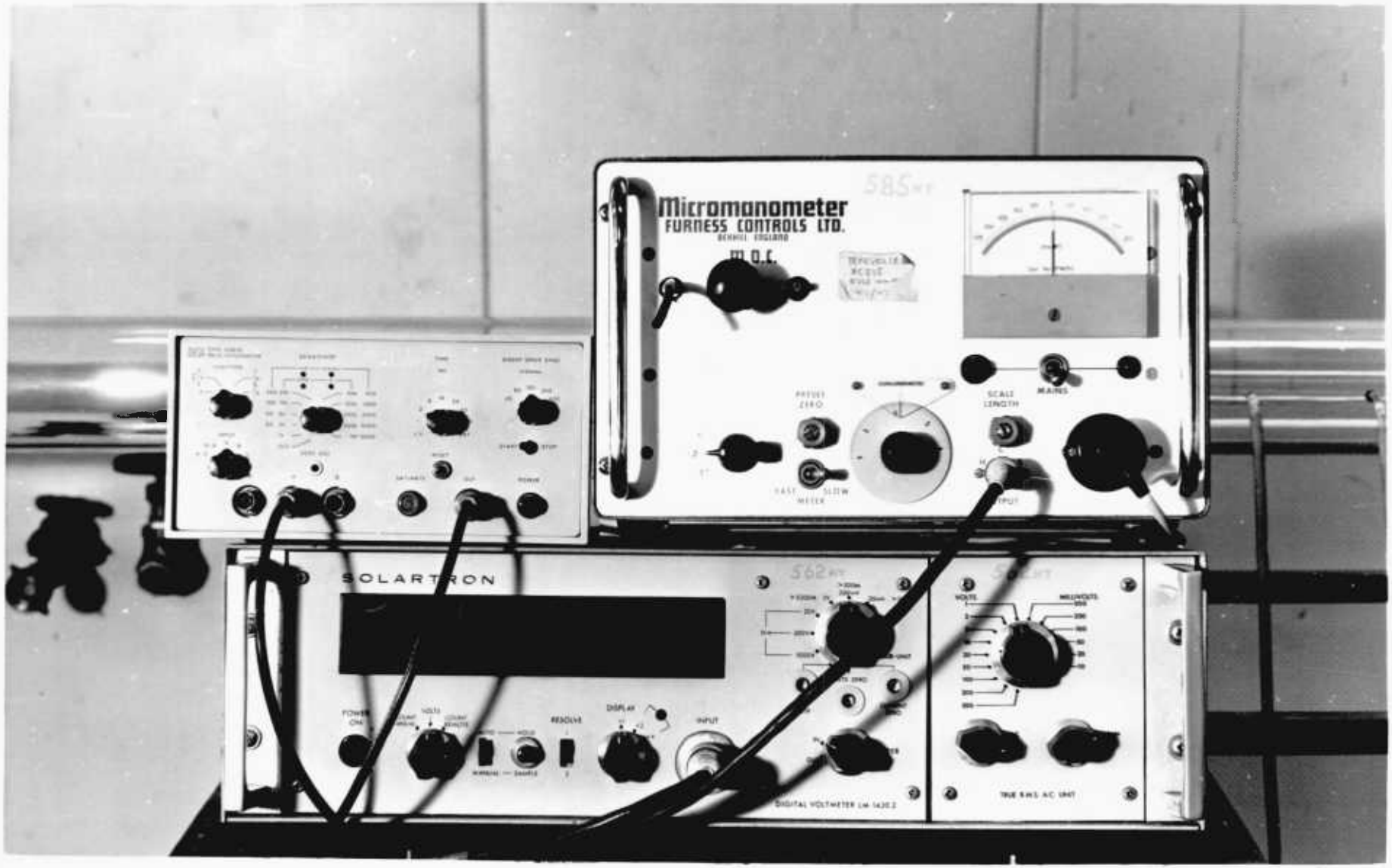

FIGURE 4.6: EQUIPMENT FOR THE MEASUREMENT OF PRESSURE

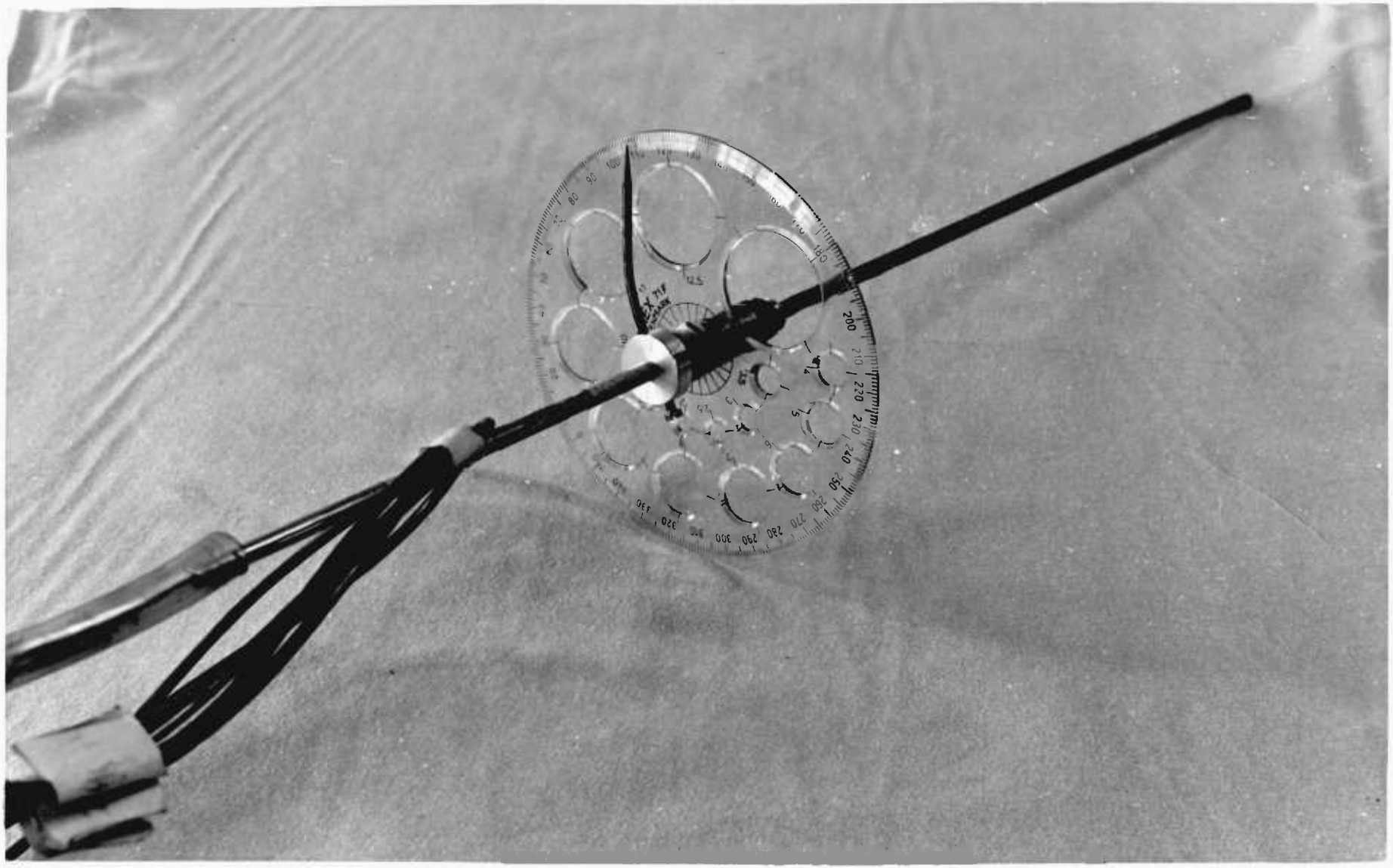

FIGURE 4.7: THE TRANSVERSE CYLINDER PROBE AND TRAVERSING MECHANISM

components of the flow to be determined. The differential pressures were measured using the pressure measuring equipment described in the previous section of this chapter. The calibration curves, together with a discussion regarding the limits of applicability of the probe is given in Appendix A2 , (Section A2.2.2).

(b) THE TRAVERSING MECHANISM

The mechanism employed to traverse the cylinder probe in the main duct radial direction and to obtain readings of yaw angle is shown (with the probe) in Figure 4.7.

The mechanism consisted of a hollow shaft, which, when the probe was introduced, produced a tight, but sliding fit. At one end of the hollow shaft there is located a $\frac{1}{4}$"-NPT thread that permits the positioning of the shaft into the test-section walls. At the other end there is located a 360^{o} protractor; the protractor is rotatable about the shaft axis but is provided with a locking nut to firmly secure it in place. Above the protractor, a threaded cap is located, which, with the addition of an "O" ring allows the probe to be fixed into a secure position and also prevents the leakage of air from the test section.

An additional piece of the traversing mechanism is a pointer; the pointer is attached to the probe via a moveable collar containing a locking screw. The pointer is positioned by aligning to accurately machined scribe lines on the collar with two similar

lines on the probe shaft. This arrangement allows the yaw angle to be measured to within one half a degree.

The radial positioning of the probe was obtained by using a toolmakers scale, that allowed the positioning of the probe to an accuracy of within 0.5mm.

4.3.3 THE MEASUREMENT OF THE SUBLIMATION OF NAPHTHALENE

(a) INTRODUCTION

The sublimation of naphthalene can be used as an indicator of surface mass transfer rates; indeed it may be used in preference to the measurement of temperature because there are situations in which a mass transfer process can be set up and studied both more easily and accurately than the corresponding heat transfer process; examples include the experiments on finned cylinders in cross-flow, Owen (I967), plate fin and tube heat exchanger configuration, and corrugated wall channel flows, Sparrow (I977). In all these examples, the geometries were themselves made of naphthalene; to construct a naphthalene tee-junction or for that matter a cylinder of naphthalene for insertion into a pipe is extremely difficult, Sparrow (I976). The thin film naphthalene technique of Neal (I975) may be used, but requires an elaborate "tooling-up" process. It was decided therefore to try a new approach that involved the positioning of naphthalene plugs to fit flush with the inner wall of the main pipe. By noting the mass diminution over specific time periods, the mass transfer coefficient distribution can be obtained.

(b) THE PLUGS

A typical plug is shown schematically in Figure 4.8(a) and photographically in Figure 4.8(b); indeed Figure 4.8(b) shows a sequence of pictures depicting the stages of plug development. Each plug is bored out to a depth of approximately 0.4cm and subsequently filled with naphthalene ((b) in Figure 4.8(b)); the naphthalene is then smoothed so as to be flush with the plug face (by a process to be described later) ((c) in Figure 4.8(b)); the plug resulting after a test run is shown in (d) of Figure 4.8(b).

The surface of the naphthalene, during a test, becomes irregular; the irregularities increase with time due to continuing mass loss to the air stream. To determine the mass diminution with time characteristics of the naphthalene filled plugs, a few tests were performed in which some plugs (filled with naphthalene) were located in the tee-junction's pipe wall; the weight-time characteristics are shown in Figure 4.9. The data of Figure 4.9 shows that the sublimitation rate is uniform within the time frames and mass loss range investigated. During the data collection phase of the experiments, every attempt was made to ensure that no plug sublimated away more naphthalene than that covered in this test.

The rate at which naphthalene sublimes is strongly dependent on temperature; a variation of $I^{o}C$ can change the sublimitation rate by about I0%, see

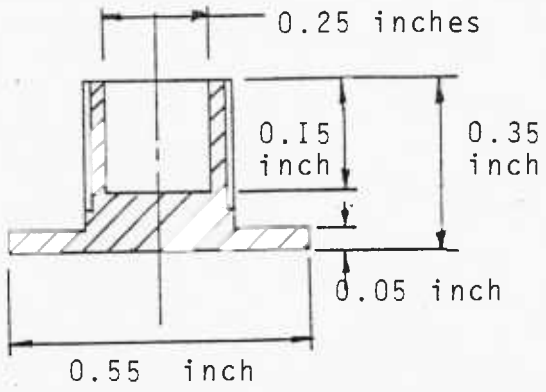

FIGURE 4.8(a) $\frac{1}{4}$ INCH NPT PLUG FOR HOLDING NAPHTHALENE

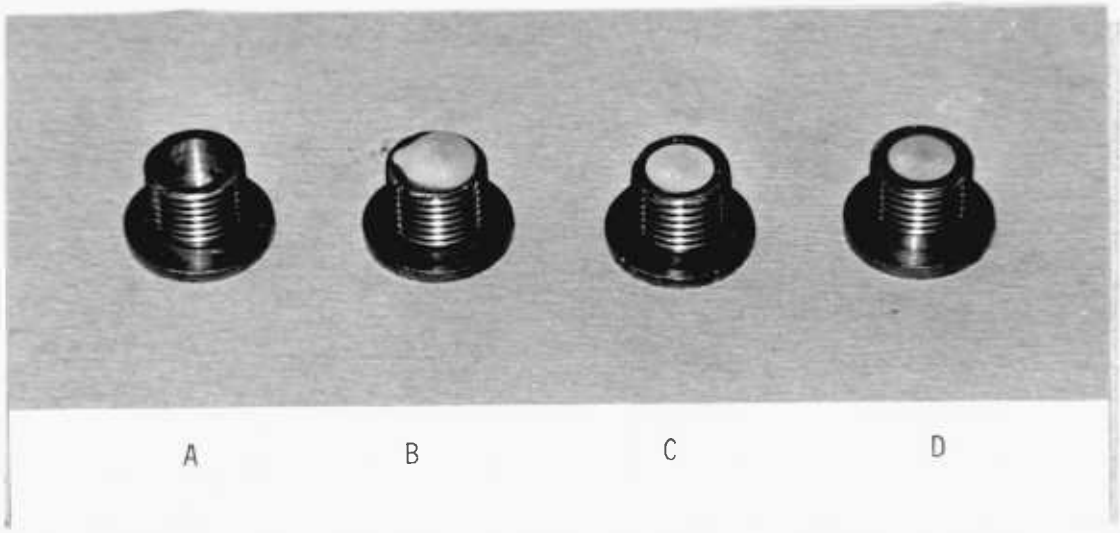

FIGURE 4.8(b) PHOTOGRAPH OF 4 NAPHTHALENE

(a) READY TO RECIEVE NAPHTHALENE
(b) LOADED WITH NAPHTHALENE
(c) PLUG PREPARED FOR TEST
(d) PLUG CONDITION AFTER A TEST

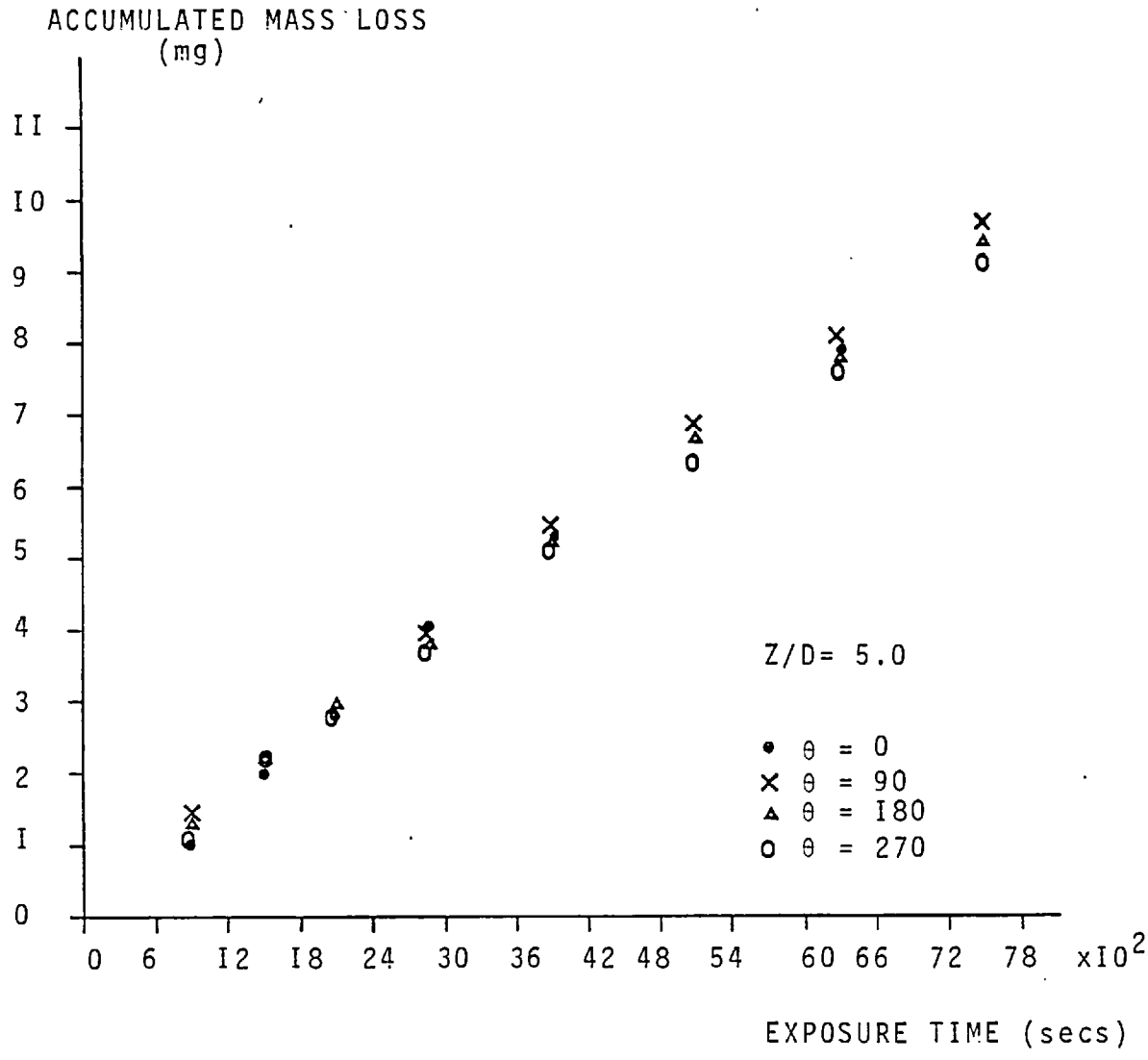

FIGURE 4.9: NAPHTHALENE PLUG MASS LOSS vs TIME OF EXPOSURE

Section 4.5.3. During the test runs, the air temperature was very closely monitored using calibrated copper-constantan thermocouples; it was found that during all test runs, the air temperature never varied by more than $0.5^{o}C$. Indeed it is because the naphthalene temperature was not measured directly that the plugs used were made of brass, the high thermal conductivity of which, it was presumed, would maintain the naphthalene at the temperature of the measured air stream.

(c) NAPHTHALENE PLUG PREPARATION

The preparation of the plugs for each test run was performed in two stages.

The first stage was to melt reagent grade crystalised naphthalene in a crucible. Each plug was then filled to overflowing with liquid naphthalene and allowed to solidify. This stage produced plugs like that shown in Figure 4.7(b), picture (b).

The second stage was to very carefully scrape away the excess naphthalene to produce a very smooth surface that was flush with the plug face. A plug resulting from this stage is shown in Figure 4.7(b), picture (c). The scraping was performed using a very sharp, new razor blade. As each plug passed through this second stage, it was placed in a naphthalene rich environment.

4.4 THE EXPERIMENTAL PROCEDURES

4.4.I FLOW SYMMETRY

The following preliminary tests were performed to ascertain the symmetry of the flow. There are two planes of symmetry; the first is on a plane parallel with the inlet duct axis so that the flow in one leg of the main duct is the mirror image of the flow in the other; the second symmetry plane is the diametral centre plane of the two legs, parallel with the inlet duct axis.

To check the mass flow ratio of the legs, the pressure drops across the orifice plates were compared. This comparison indicated that a split ratio $(\frac{\text{mass flow of left leg}}{\text{mass flow of right leg}})$ of 0.978 had been achieved. The 2% discrepancy was deemed acceptable in view of the fact that by taking the differential pressure between two indentically located pressure taps (relative to the inlet duct centre-line) gave a null reading on the micro-monometer.

The diametral symmetry was checked (for both legs) by measuring the differential wall pressures between taps located in the same position on either side of the symmetry plane. The differences indicated that, on average, there was about a 4% æsymmetry.

4.4.2 INLET AND EXIT VELOCITY PROFILES

The velocity profile at the start of the inlet duct were measured using the transverse cylinder probe. The measurements indicated that the flow contained peaks. Because the transverse cylinder probe could not reach the side opposite

the access holes in the duct, it was decided to employ a pitot probe (tip dia. = 0.0022m) to investigate the duct velocity-profile. The data obtained via the pitot probe confirmed, to within 5%, the readings obtained by the cylinder probe. The inlet profiles, together with other data will be presented shortly.

The exit profiles, (located at the reference locations) were determined in a manner similar to that used for the inlet profiles. The measurements indicate that at least as far as the mean velocity is concerned, the flow at these locations is very close to being fully developed, as will be seen shortly.

The Reynolds number in each leg of the pipe based on the mean velocities is Re_{LEFT} = 27300 and Re_{RIGHT} = 27900.

4.4.3 TEST SECTION VELOCITY MEASUREMENT

The procedure for the measurement of velocity is simple and straightforward. It involves the systematic and patient positioning of the probe at each axial and angular location and the recording of the various parameters such as voltage, yaw angles, etc.

At each location around the circumference of the pipe, the probe holder was inserted and locked into place. The protractor was then aligned with the pipe axis by reference to lines accurately scribed onto the pipe outer wall. The probe was inserted to the required depth. In this location the probe was aligned with the local velocity vector and the differential pressures and yaw angle were noted.

At each positioning of the probe, ten readings were taken, the average of which was used to determine the velocity vector. At each angular location around the pipe, 9 radial positions were attended to. The velocities were obtained at Z/D = I,2,3 and 5 on both sides of the inlet duct centre line.

4.4.4 TEST SECTION PRESSURE MEASUREMENTS

The static pressure at the walls of the test section were taken relative to the pressure at the beginning of the inlet duct. The specific location of this relative pressure point is indicated in Figure 4.4. The pressures were straightforward to obtain, the magnitudes being recorded as a voltage. Post-processing of this voltage (via the calibration curves for the micro-monometer, see Appendix A.2) gave the relative pressures. At each location, ten readings were taken, the average of these ten are presented here.

4.4.5 THE MEASUREMENT OF NAPHTHALENE SUBLIMITATION RATE

The experimental technique for determining the mass transfer via the sublimitation of naphthalene is outlined below.

The flow circuit was first allowed to achieve a constant temperature condition. This process took up to five hours, during which time the air temperature was monitored; stable conditions were assumed to be achieved when the air temperature did not change by more than $0.25^{o}C$ within a thirty minute time frame. Each (suitably numbered) plug was then removed from the naphthalene rich environment and weighed to within 0.0001gms where upon it was immediately replaced in the naphthalene environment.

Once the necessary number of plugs had been accurately weighed, the plugs were carefully inserted into the appropriate downstream location of the test section. The plugs were positioned so that the face of the naphthalene was flush with the pipe inner surface. As only one downstream location was attended to for any one test run, this positioning process was accomplished very quickly, usually within two minutes. During each test run there was located also a plug at the reference locations. A stopwatch was started as the first plug was inserted; the time-temperature history of the air was recorded.

At the end of the test, the stopwatch was stopped as the plugs were removed in the order of their insertion. As each plug was removed, it was placed into the naphthalene rich environment, where upon each plug was reweighed and the change in mass noted.

At five locations downstream of the inlet duct centreline (on both sides), four tests were run; this gave 8 data points for each location together with 40 reference point values of the mass transfer.

4.5 DATA CONVERSION

The data conversion procedure consisted of obtaining the distributions of pressure, velocity and mass-transfer from the "raw" experimental data. The steps followed will now be outlined.

4.5.I WALL STATIC PRESSURE

The differential wall static pressures were converted from the raw data via the micro-monometer calibration curve shown in Appendix A2 . The pressures are presented as non-dimensional pressure coefficients defined as:

$$C_p = \frac{P - P_{ref}}{\frac{1}{2}\rho \bar{V}_i^2} \qquad ,(4.I)$$

where P is the local pressure, P_{ref} the reference pressure (see Figure 4.4), ρ is the density, and $\bar{V}_i$ is the mean velocity at the beginning of the inlet duct.

4.5.2 MEAN VELOCITIES

The velocity distributions were obtained from the raw data by obtaining the pitch angle from the calibration are shown in Appendix A2. Using this pitch angle, a pressure coefficient could be obtained from the other calibration curve, also shown in Appendix A2. This pressure coefficient allowed the velocity vector to be obtained that, when coupled with the measured yaw angle, permitted the velocity components to be deduced.

4.5.3 NAPHTHALENE SUBLIMATION RATE

The raw data for the sublimitation of naphthalene consisted of a mass change, the time over which this mass changed, and the temperature-time history of the air during the test run. This information was evaluated for each test run using the following method.

The temperature-time curve was integrated to give the temporal average temperature over the test run; a typical curve is shown in Figure 4.IO which indicates that during the tests, the air temperature was constant to within $0.5^{o}C$.

The temporal average temperature was then employed to evaluate the mass transfer coefficient using the following relationship from Sogin (I958)

$$h = \frac{\Delta M/(At)}{(C_{V,W}-C_{V,O})} \qquad ,(4.2)$$

where
- h - mass transfer coefficient
- A - surface area of naphthalene exposed to air stream
- t - time
- $C_{V,W}$ - concentration of naphthalene vapour at the wall
- $C_{V,O}$ - concentration of naphthalene vapour in the free stream
- ΔM - mass sublimated

and $C_{V,O}$ is assumed zero since the naphthalene plugs were prepared in a room well away from the test area. The concentration of naphthalene at the wall was evaluated assuming that the vapour at the surface of the plug is saturated at the temporal mean air temperature $\overline{T}$, and that the partial pressure of the naphthalene vapour is small compared to that in the air stream; with these assumptions, the vapour is supposed to behave like a perfect gas, therefore:

$$\rho_{V,W} = C_{V,W} = \frac{P_{V,W}}{R_V \overline{T}} \qquad ,(4.3)$$

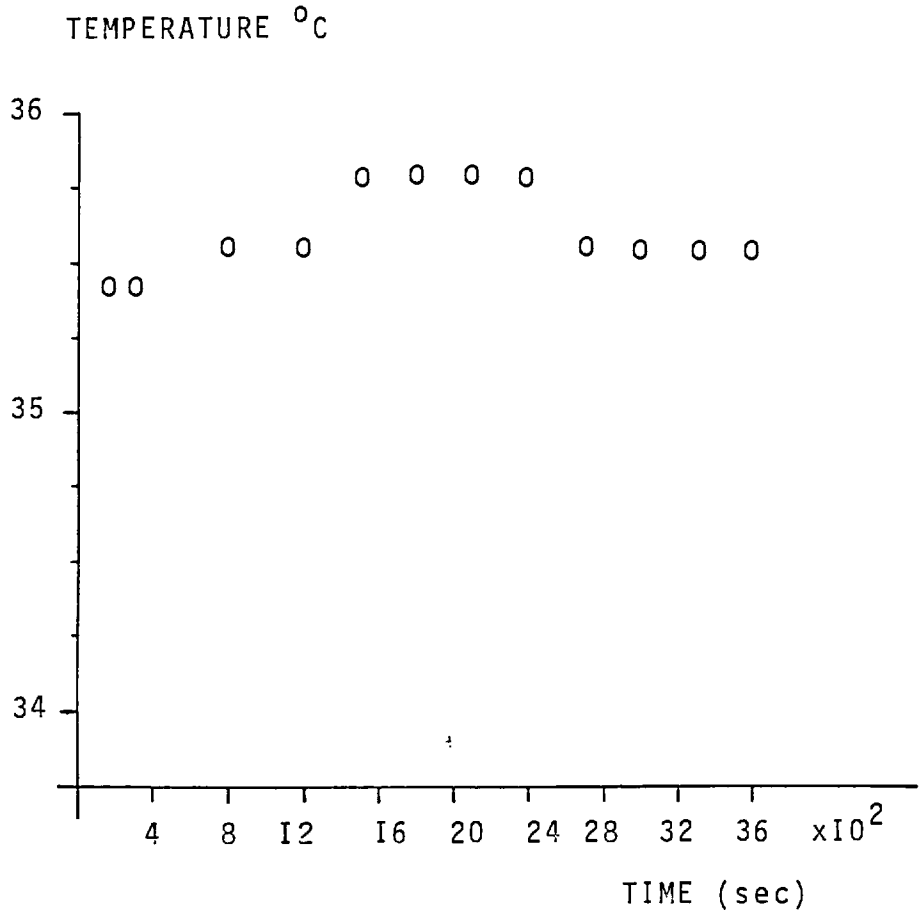

FIGURE 4.IO: AIR TEMPERATURE - TIME HISTORY DURING A TYPICAL TEST RUN FOR SUBLIMATION OF NAPHTHALENE

where $p_{V,W}$ is the saturated vapour pressure of the naphthalene vapour at the wall, $\rho_{V,W}$ is the density of the vapour at the wall, $\overline{T}$ is the temporal average temperature, and R_V is the naphthalene gas constant (R_V = 64.96 J/kgk). The vapour pressure, $p_{V,W}$ can be evaluated using the expression recommended by Sherwood and Trass (I960); it is

$$\log_{IO} p_{V,W} = II.55 - \frac{3765}{\overline{T}} \qquad ,(4.4)$$

where $p_{V,W}$ is expressed in mm Hg and $\overline{T}$ in ^{O}K.

Each data point was evaluated separately and upon completion of all test runs, the average of the data points were plotted in terms of non-dimensional mass transfer coefficients. For the circumferential variation,

$$\tilde{h} = \frac{h(\Theta)}{\overline{h}(\Theta)} \qquad ,(4.5)$$

and for the longtidudinal average variation:

$$\tilde{h}_R = \frac{\overline{h}(\Theta)}{h_R} \qquad ,(4.6)$$

where $h(\Theta)$ - local mass transfer coefficient

$\overline{h}(\Theta)$ - average of $h(\Theta)$ at a given axial location

h_R - mass transfer coefficient at the reference location.

Incidently, the mass Stanton number is defined by:

$$S_t = \frac{Sh}{Re\ Sc} = \frac{h}{\overline{W}} \qquad ,(4.7)$$

where h - mass transfer coefficient

Sh - Sherwood Number

$(= hd/\lambda$, λ - diffusion coefficient)

Re - Reynolds Number

$(= \rho\overline{W}D/\mu)$

Sc - Schmidt Number $(= \frac{\mu}{\rho\lambda})$

where the Schmidt Number can be calculated via (Sherwood and Trass (I960))

$$Sc = 7.0\overline{T}^{-0.I85} \qquad .(4.8)$$

4.6 ACCURACY AND REPEATABILITY OF THE MEASUREMENTS

4.6.I ACCURACY

Before presenting the data, the accuracy of the data will be examined.

The limiting factor regarding the measurement of pressure is the uncertainty in the calibration of the micro-monometer (see Appendix A2). The error in such measurement is therefore likely to be less than I%.

With regard to the velocity measurements, the accuracy with which the probe could be positioned is estimated to be within 0.5mm in the radial direction and to within 0.5 degrees in the angular determination of the yaw angle. The reader is referred to Appendix A2 for information regarding the limits of applicability of the probe.

The volumetric flow rate, as measured by the orifice plates, has an error that is estimated to be within ±5%.

The sublimitation rate of naphthalene, as pointed out in Section 4.3.3, is highly dependent upon temperature. It is therefore estimated that the error in determining the mass transfer coefficients is within 7%.

4.6.2 REPEATABILITY

As a test of the repeatability of the results, a practice was adopted whereby measurements were selectively checked on different days; the agreement between the results was within the above quoted limits.

4.7 THE PRESENTATION OF THE EXPERIMENTAL DATA

In this section of the chapter, a few results are presented which describe the general flow pattern observed in the present flow situation. The complete data obtained in the present experimental investigation will be presented in Chapter 6 where they will be compared with the predictions from the calculation procedures.

In Figure 4.II the profiles of the mean velocity at the entrance to the inlet duct are shown; the orientation of the velocities relative to the inlet duct is shown in the accompanying sketch, and the velocities are non-dimensionalised with the mean inlet velocity $\overline{V}_i$. The profiles indicate that the velocity is, for the most part, of "plug" shape, but two distinct features are noticeable. First, each profile exhibits a dip at the centre-line, and

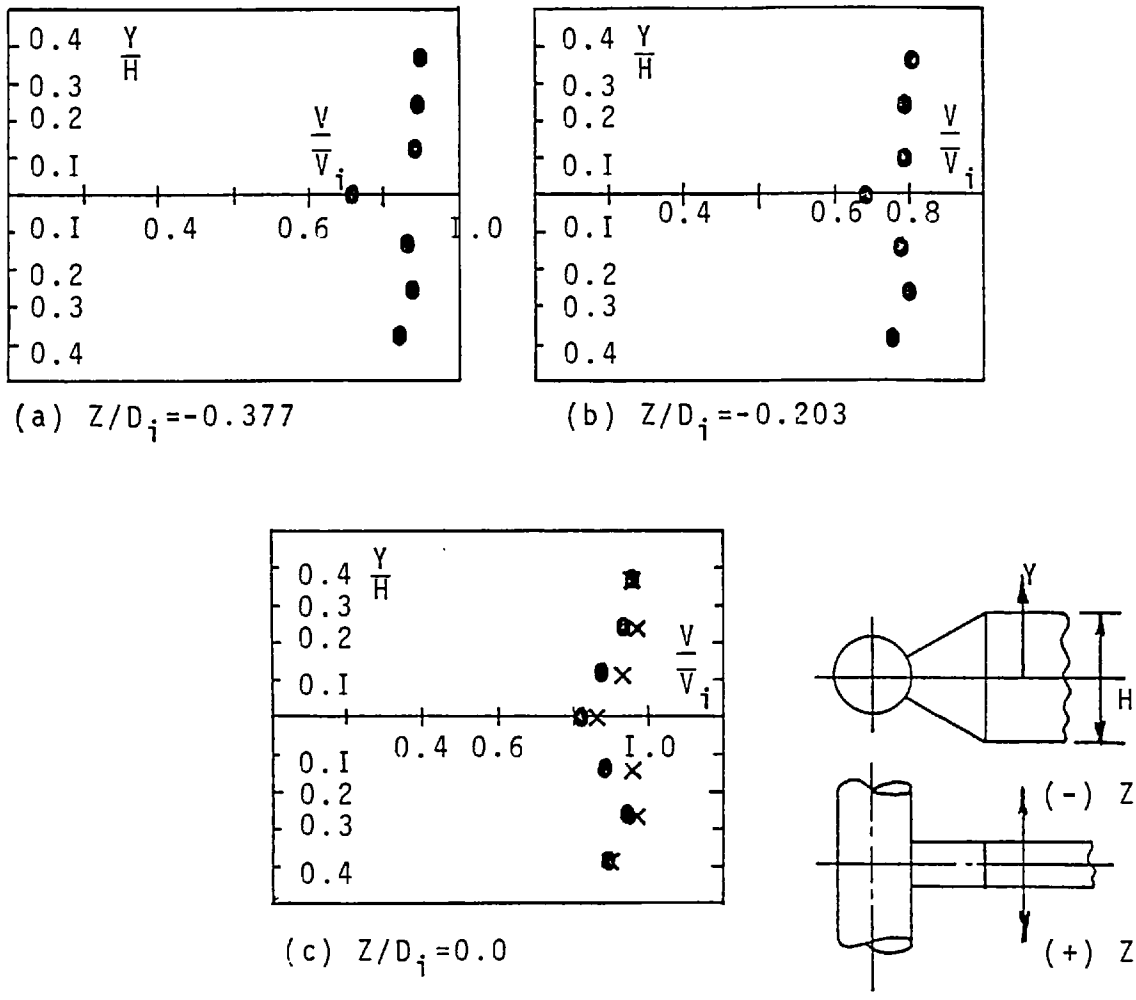

FIGURE 4.II: EXPERIMENTAL INLET VELOCITY PROFILES
(•) PITOT PROBE (X) 3-HOLE CYLINDER PROBE

secondly, the results obtained using the cylinder probe and pitot probe are within 5% of each other. Further, it is noticed that in plot (e) there is a distinct peak in the profile. The inlet profile is a result of the grid-honeycomb arrangement (see Section 4.2.I) orientation within the duct.

Figure 4.I2 shows the velocity profiles at the reference locations at the end of each leg of the tee-junction. At each radial location, there are four data points, two of which refer to the left leg of the tee and two to the right leg; each pair is composed of the results obtained using the cylinder probe and the pitot probe. It is observed that, when compared to the information supplied by Schlichting (I968), the data is in acceptable agreement. The results from the two probes are also in good agreement.

Figure 4.I3 shows the wall static-pressure coefficient along the pipe wall downstream of the inlet duct centre-line; the pressure coefficients obtained from the left and right legs of the junction are shown. From the figure it is observed that the highest pressure is located at the point of impingement of the inlet fluid on the wall opposite to the inlet duct, and that the pressure coefficient falls rapidly as the fluid leaves the junction region. The data from both the left and right legs show good symmetry. At the Θ=0 location (the wall adjacent to the inlet duct) a gap in the data is observed to exist; this is due to the presence of the inlet duct. The pressures at this location do not exhibit the large gradients observed at the Θ=I80^{o} position.

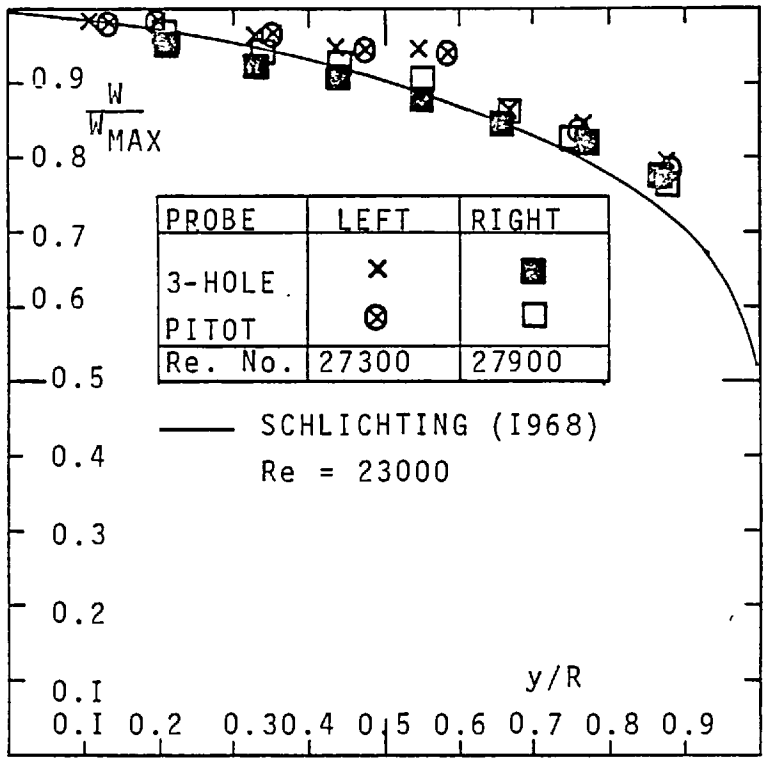

FIGURE 4.I2: VELOCITY DISTRIBUTION AT MAIN DUCT BRANCH(S) REFERENCE POINTS (Z/D=40.5)

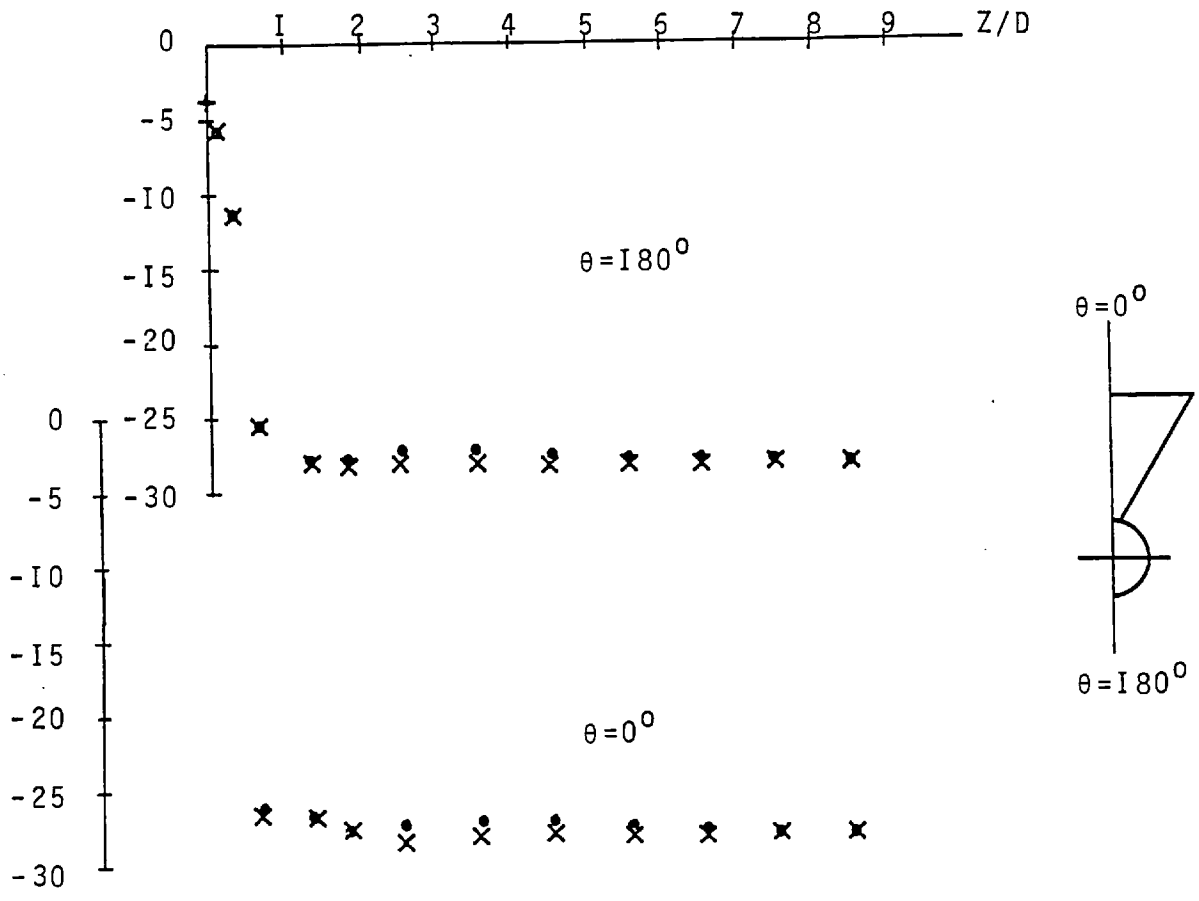

FIGURE 4.I3: SURFACE PRESSURE COEFFIENT vs DISTANCE DOWNSTREAM OF INLET DUCT CENTRE-LINE
• LEFT OF CENTRE-LINE
X RIGHT OF CENTRE-LINE

From these data the pressures become quite uniform within 2 or 3 diameters downstream of the inlet duct centre-line.

Figure 4.I4 presents the mean axial velocity profiles on a diametral plane parallel with the inlet duct centre-line. Data obtained from both the left and right legs of the junction are shown. The data enclosed by circles are questionable; also, the gap in the data, particularly at the Z/D=I location, is because the flow in this region is presumably of a character that the measuring device is unable to detect it accurately; these points are elaborated upon in Appendix A2. Nevertheless the data that is considered to be reliable, shows that the velocity is featured by a large peak in the lower portion of the tee-junction legs, and that this peak diminishes to zero in about four leg diameters. Around the centre-line of the pipe there is indicated a region of reversed flow; this region is seen not to exist at $Z/D \geq 2$.

In Figure 4.I5, the velocity profiles along a plane normal to the inlet axis are presented. In part (a) of the figure, the velocities are for a Z/D=I; while in (b), for a Z/D=2. Note that the velocities shown ($U/\overline{W}_m$) are not angular velocities, but rather U velocities in a Cartesian coordinate reference frame. The data indicates that the fluid leaving the junction region does so by "climbing" the walls of junction legs; the magnitude of these cross-stream velocities is seen to diminish quite rapidly, the maximum dropping from $U/\overline{W}_m \simeq 5$ to $U/\overline{W}_m \simeq I,5$ within one diameter.

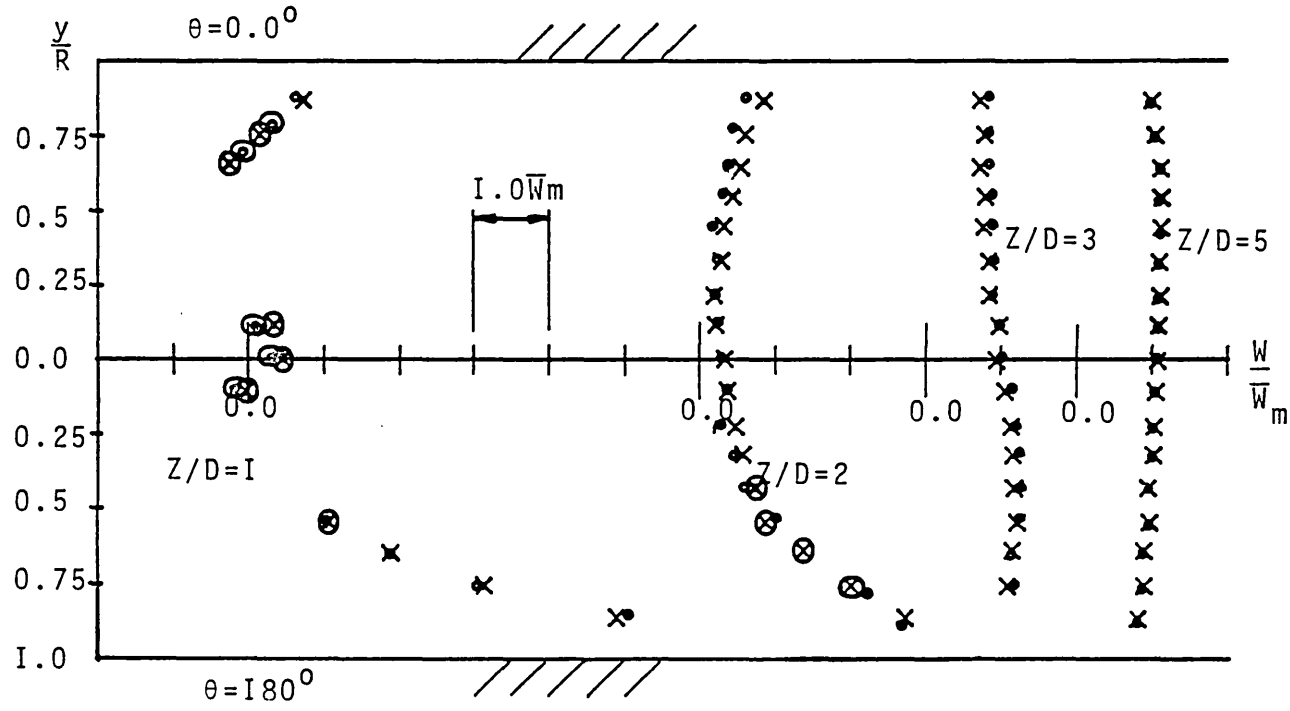

FIGURE 4.I4: AXIAL VELOCITY DISTRIBUTION ON PIPE DIAMETRAL SYMMETRY PLANE

• LEFT OF INLET DUCT CENTRE-LINE

X RIGHT OF INLET DUCT CENTRE-LINE

O QUESTIONABLE DATA

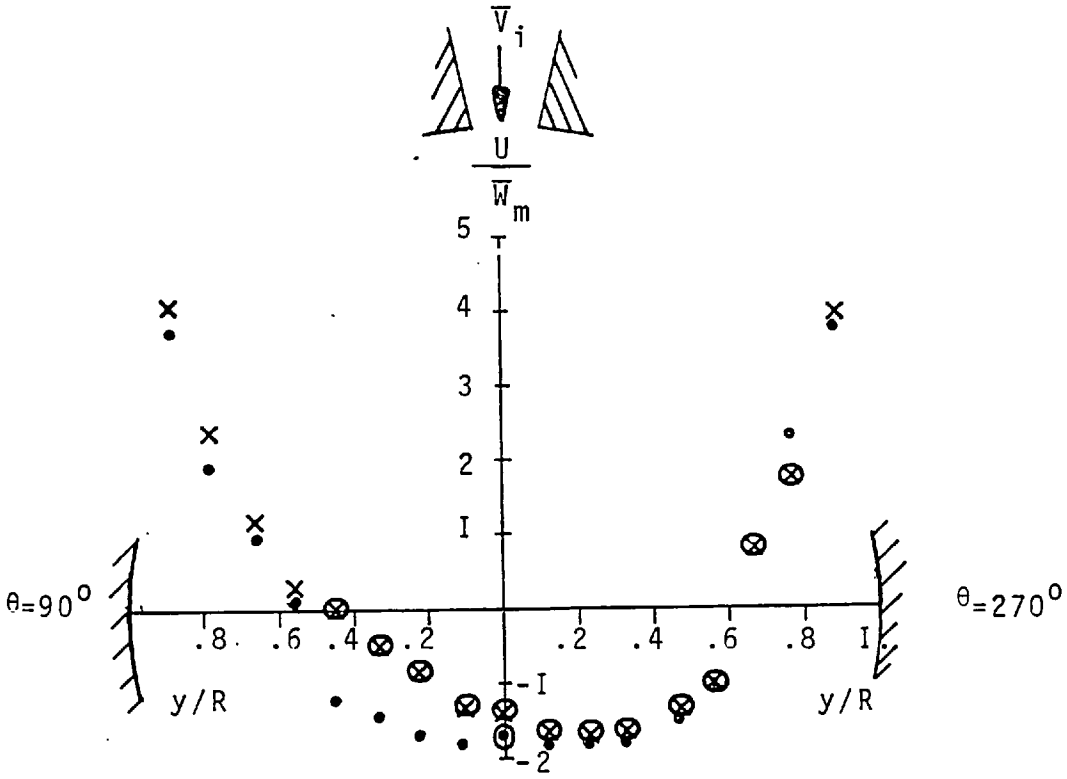

(a) Z/D=I.0

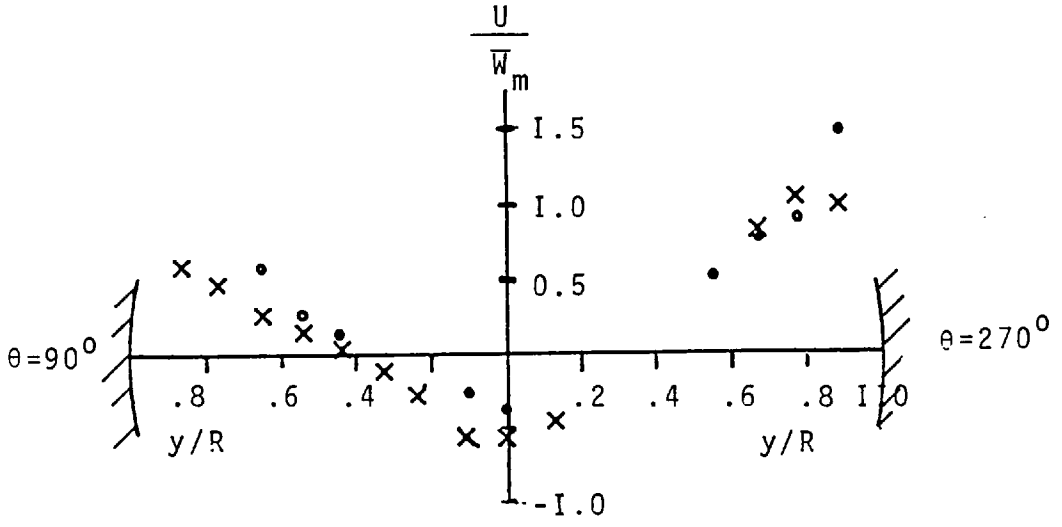

(b) Z/D=2.0

FIGURE 4.I5: CROSS - STREAM VELOCITY PROFILES

NOTE: U IS VELOCITY NORMAL TO DIAMETRAL CENTRE-LINE

• LEFT OF INLET DUCT CENTRE-LINE

X RIGHT OF INLET DUCT CENTRE-LINE

O QUESTIONABLE DATA

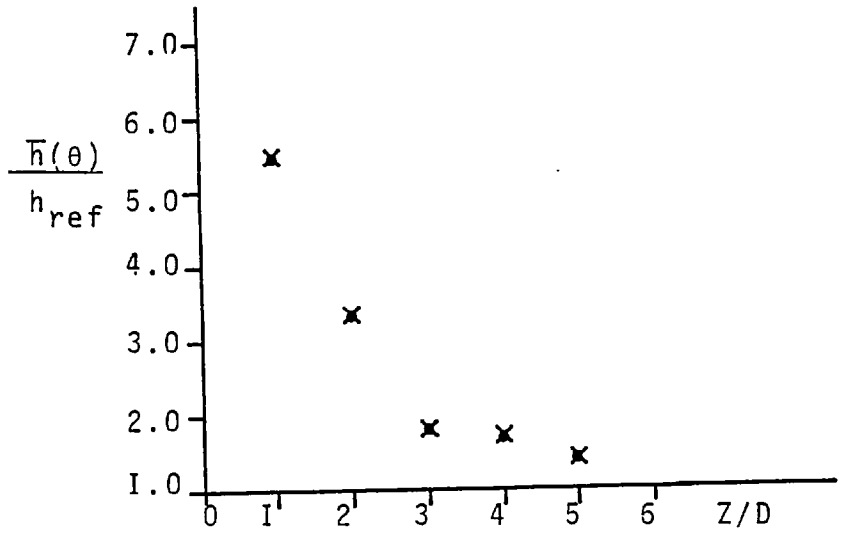

FIGURE 4.I6: AVERAGE LONGITUDINAL MASS-TRANSFER COEFFICIENT

● LEFT OF INLET DUCT CENTRE-LINE

X RIGHT OF INLET DUCT CENTRE-LINE

The experimental data presented above lead to three main observations. First, there is a region of recirculating fluid around the centre-line of the junction legs; it is between I and 2 pipe diameters in length. Second, the inlet fluid first impinges on the wall opposite the inlet duct; the high pressures generated by this impingement force the fluid to move in both the axial and circumferential directions; the majority of the fluid passing downstream does so in the near-wall region. This wall-jet behaviour is however quickly nullified as the two wall flows, on either side of the symmetry plane ($\Theta=0^{o}$ to $\Theta=I80^{o}$), meet at the top of the pipe ($\Theta=0$); thereafter the flow appears to be plug-like. The final main observation is that the flow in this particular tee-junction, operating under the previously discussed flow conditions exhibit regions of flow that may be classified as being elliptic and partially-parabolic in nature.

In Figure 4.I6, the longitudinal average mass transfer coefficient at five axial locations are presented. The data show that at one diameter downstream, the mass transfer is 5½ times as great as the reference values; this maximum falls rapidly to about I.5 that of the reference value within five junction leg diameters.

4.8 CONCLUDING REMARKS

In the present chapter, the details of the experimental program have been described. The experimental rig, and both the experimental techniques and devices have been described,

together with an outline of the sequence and scope of the measurements. The brief set of experimental data has shown that the flow is very complex in nature, particularly in the junction region; as the fluid leaves the junction region, the flow appears partially parabolic in nature.

- PART IV -

THE PREDICTIONS

CHAPTER 5: LAMINAR FLOW PREDICTIONS

5.1 INTRODUCTION

The laminar flow in tee-junctions of square cross-section have been predicted using both the elliptic and partially-elliptic versions of the calculation procedure presented in Chapter 3. Calculations have been made in tee-junctions of square cross-section in which fluid in the "horizontal" portion of the tee combines with fluid entering from the "vertical" portion; indeed, this "vertical" portion, in some circumstances, has been neglected so as to illustrate its need when considering the flow in tee-junctions. Some of the predictions have also been compared to the available experimental data.

Briefly, the chapter is divided in the following manner. First, predictions are presented, using both calculation procedures, for a tee-junction of diameter ratio of 0.5; by employing various inlet duct boundary conditions, the predictions so obtained are compared to experimental data. Using the same geometry, the effect of varying the momentum ratio is investigated. Then, by employing a tee-junction of a diameter ratio of I.0, the predictions for various momentum ratios are presented and discussed. Finally, a summary is made of the findings and some concluding remarks are made.

5.2 THE GENERAL PROBLEM

5.2.I THE PHYSICAL SITUATION

The geometry and flow situation is shown in Figure 5.I.

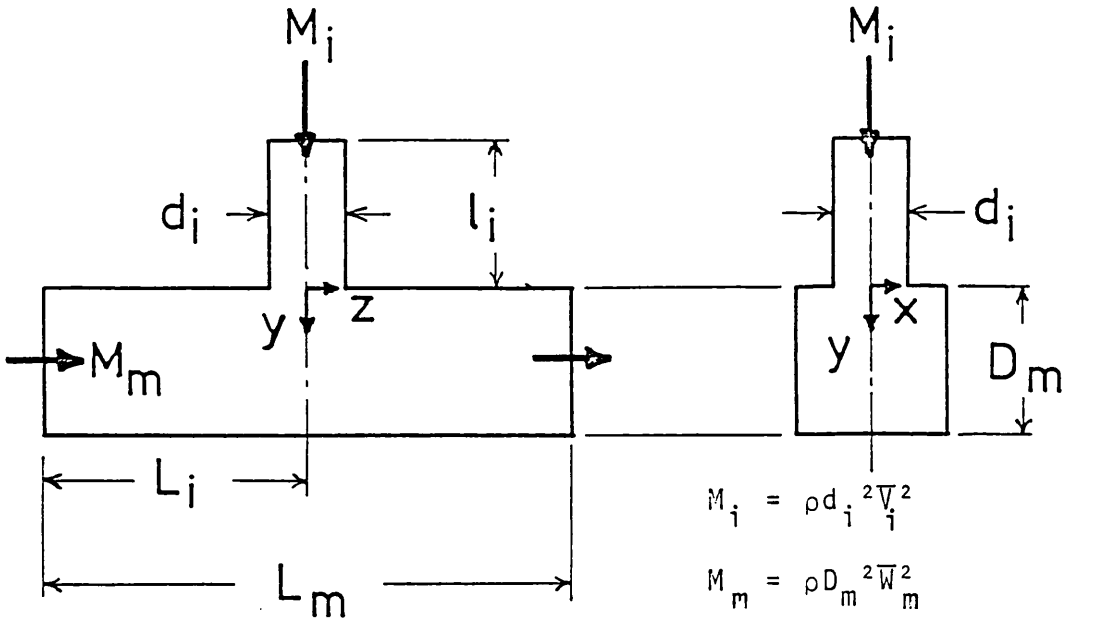

FIGURE 5.I: THE PHYSICAL SITUATION CONSIDERED

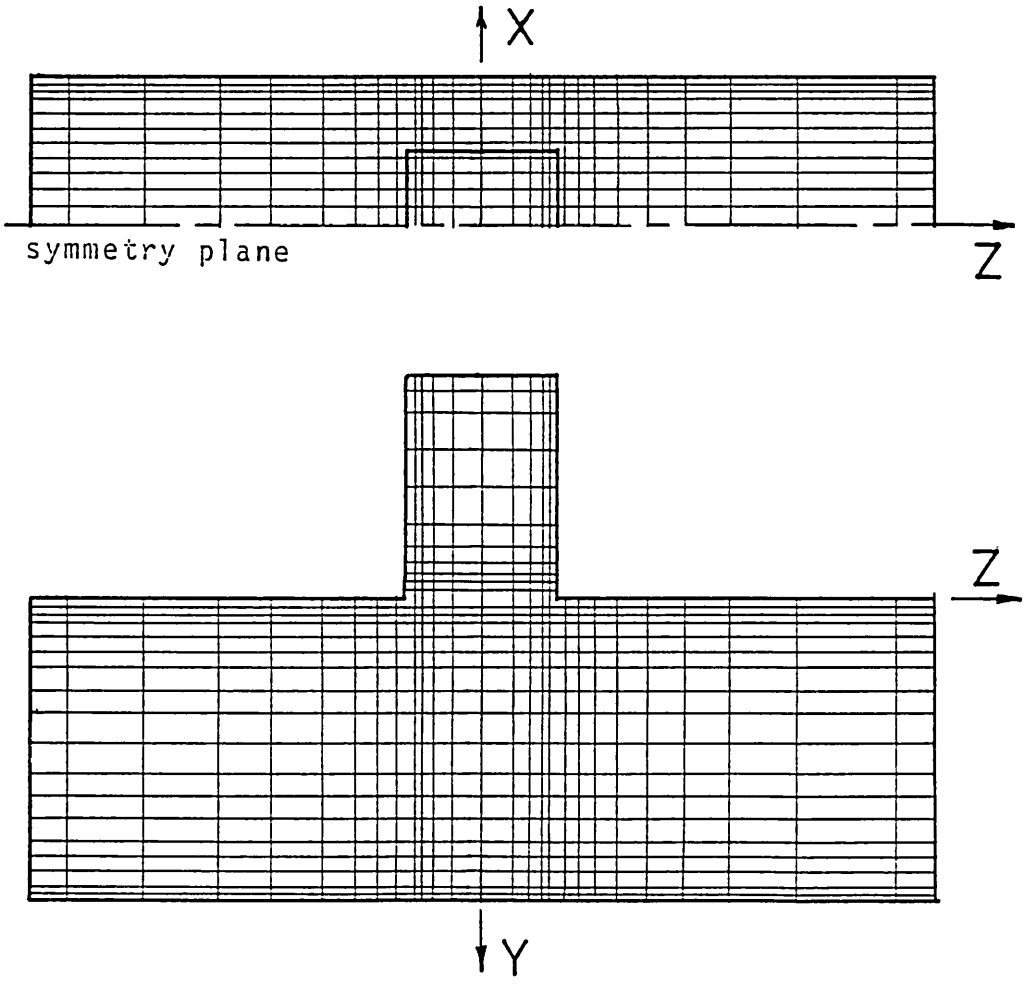

FIGURE 5.2: THE FINITE-DIFFERENCE GRID DISTRIBUTION

Note that the geometrical quantities indicated in the figure may be varied to produce any diameter ratio ($d_i \leq D_m$, where d_i, D_m are the hydraulic diameters). Fluid enters the junction from both the "vertical" and "horizontal" ducts; the combined mass flow then leaves the junction via the remaining leg. The momentum ratio ($\omega = \frac{M_i}{M_m}$) may be varied also. The specific geometry and momentum ratios used here are given below:

$$\frac{d_i}{D_m} = 0.5 \quad ; \quad \omega = 0.1, 0.25, 1.0$$

$$\frac{d_i}{D_m} = 1.0 \quad ; \quad \omega = 0.1, 0.25, 1.0$$

where for all cases, the main duct inlet Reynolds number = 100 ($Re = \rho \frac{D_m \bar{W}_m}{\mu}$, where $\bar{W}_m$ is the main duct bulk inlet velocity), and where for $\frac{d_i}{D_m} = 0.5$, $\omega = 0.25$ corresponds to the experimental conditions of Simitovic (1977).

5.2.2 SOME COMPUTATIONAL DETAILS

(a) FINITE-DIFFERENCE GRID

The typical finite-difference grid distribution is shown in Figure 5.2. A feature of the physical situation is the symmetry exhibited by the flow about the central Y-Z plane; the computations have, therefore, been restricted to cover only half the (X-Y) cross-section, and gradients of variables normal to this plane are prescribed to be zero. The non-uniformly distributed finite-difference grid was composed of 20 grid points in the X-direction, 40 in the Y-direction and 25 in the Z-direction. That this grid distribution (20,000 grid nodes) gave sufficient accuracy was confirmed by repeating the calculations with coarser

(9375 grid nodes) and finer (28,000) grids*; the results of one such grid independence test is illustrated in Figure 5.3.

(b) THE COMPUTATIONAL COSTS

The "elliptic" computational procedure, in the finest grid case, required 28,000 storage locations per variable; for four variables, this amounts to II2,000 storage locations. On the other hand, the "partially-elliptic" procedure, if storage manipulations had been undertaken (see Section 3.8), would have required only about 50,000 storage locations; this figure is based on an average of I5 X-Y planes in regions requiring three-dimensional storage of velocities.

The computer execution time required to satisfy the convergence criteria of Section 3.9, again for the finest grid case, was of the order of one hour on an IBM 360/I95 computer (using Fortran H-level Extended Compiler). For a similar flow situation, but which used only 9375 grids, the computer time shrinks dramatically to about ten minutes.

In all the cases tested, the computer time required for the same convergence level, by the partially-elliptic version of the code, was about the same as that used by its elliptic counterpart.

---

*FOOTNOTE:
The integration domain used was, in fact, a rectangular box, interspersed with grid lines in numbers and directions listed. The tee itself was formed as indicated (Fig.5.2) within this rectangular box. Although up to 28,000 grid points were provided, only about 20,000 were used in the calculations. This selective calculation is enabled by the NEAT procedure, as pointed out in Section 3.7.2.

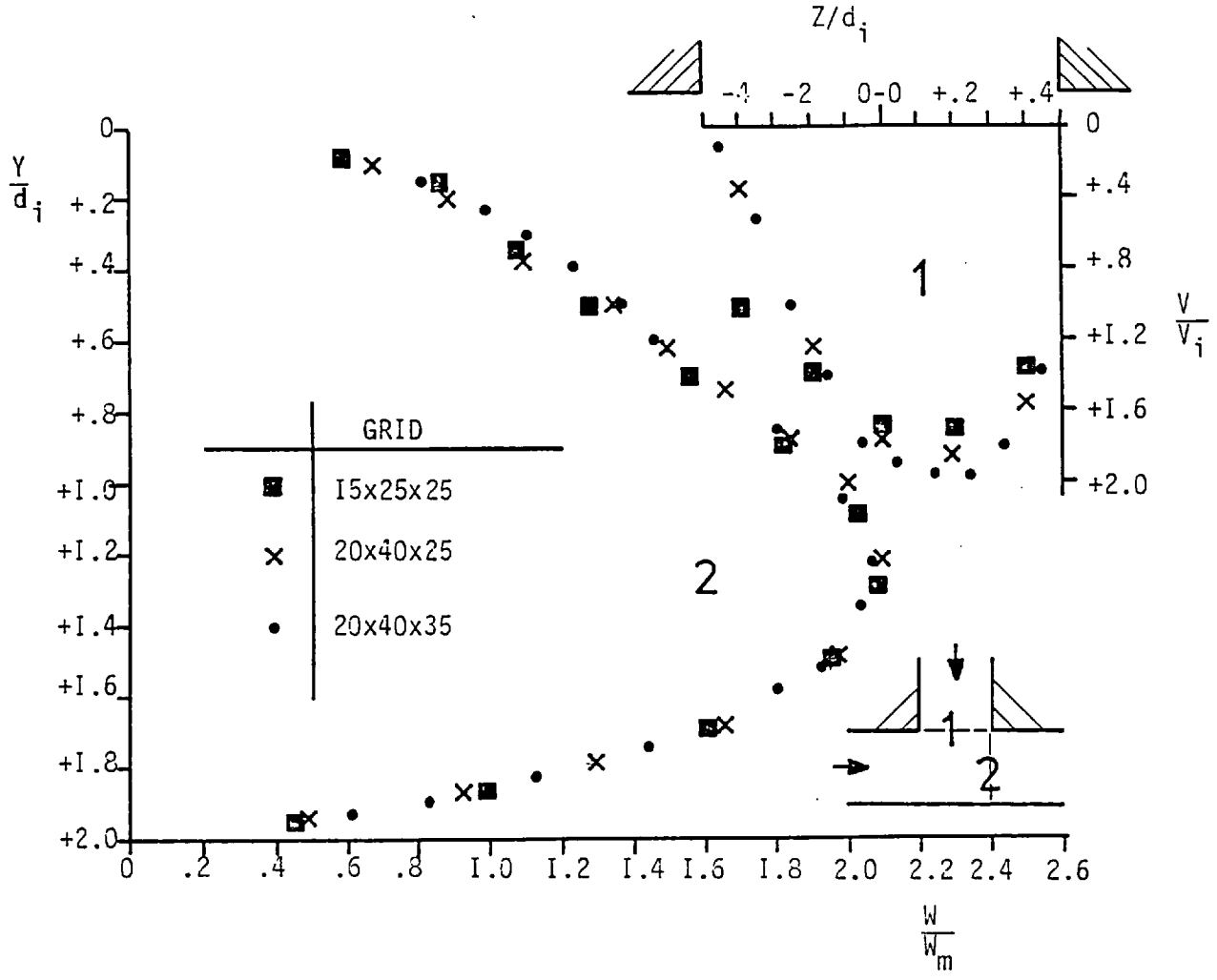

FIGURE 5.3: GRID INDEPENDENCE TEST FOR

$$\frac{d_i}{D_m} = 0.5, \quad \frac{M_i}{M_m} = 0.25$$

(c) OTHER BOUNDARY CONDITIONS

As mentioned in (a) above, the symmetry plane is characterised by a zero normal gradient and zero normal velocity. The inlet conditions are specified with a given velocity distribution; the specific distributions employed will be attended to shortly. At the exit of the calculation domain, the cross-stream velocities are set to zero while the axial velocity is prescribed to be a zero axial gradient. These exit conditions may not be strictly correct, but their influence is felt only a very short way upstream of the exit.

5.3 TEE-JUNCTION OF DIAMETER RATIO 0.5

5.3.I COMPARISON WITH EXPERIMENTAL DATA

(a) INTRODUCTION

The experimental data of Simitovic is used here to validate further the computational procedures. The validation does, of course, depend upon how well the geometry and both the inlet(s) and boundary conditions model the experimental situation. Indeed, it is because of the lack of experimental evidence that three inlet boundary conditions at the beginning of the side duct are employed here; the predictions are subsequently compared with the data that is available. These boundary conditions together with some geometrical quantities relating to the physical situation (see Figure 5.I) are listed below in Table 5.I. The fully-developed profile was evaluated from White (I974).

Case No.	Inlet Velocity Profiles		l_i/d_i
	main duct	side duct	
I	plug	plug	0.0
2	plug	plug	2.2
3	plug	fully devel.	2.2
4	experiment	fully devel.	2.2

TABLE 5.I: GEOMETRICAL FACTORS AND INLET CONDITIONS ($l_i=4.5D_m$, $L_m=9.5D_m$)

(b) THE GENERAL FLOW PATTERNS

Before comparing the present predictions with the available experimental data, the general flow patterns obtained, via Case 3 in Table 5.I, will be described; that these flow patterns agree with experimental observation will be confirmed shortly.

Figures 5.4a and 5.4b present the velocity vectors located in a number of Y-Z and X-Y planes respectively. In Figure 5.4a, the total length of the calculation domain is shown in only one plot, while the other six have been cropped for statial economy.

In Figure 5.4a, there is presented seven planes of velocity vectors; the orientation of the planes is such as to traverse the main duct from the symmetry plane ($\frac{X}{D_m} = 0.0$) to near the wall ($\frac{X}{D_m} = 0.36$).

From the plots of Figure 5.4a, it is observed that as both fluid streams approach the junction, the velocity profiles are fully-developed (or parabolic) in shape; the fluid

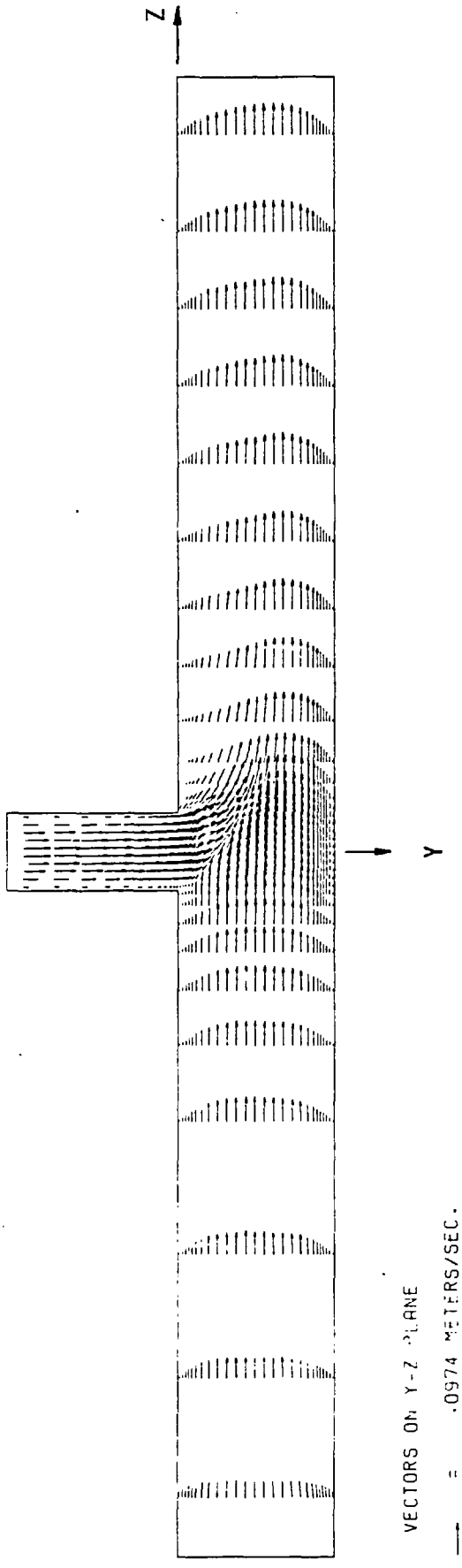

FIGURE 5.4a(i): VECTOR PLOT ON Y-Z PLANE

$$\frac{d_i}{D_m} = 0.5, \quad \frac{M_i}{M_m} = 0.25 \qquad \frac{X}{d_i} = 0.0$$

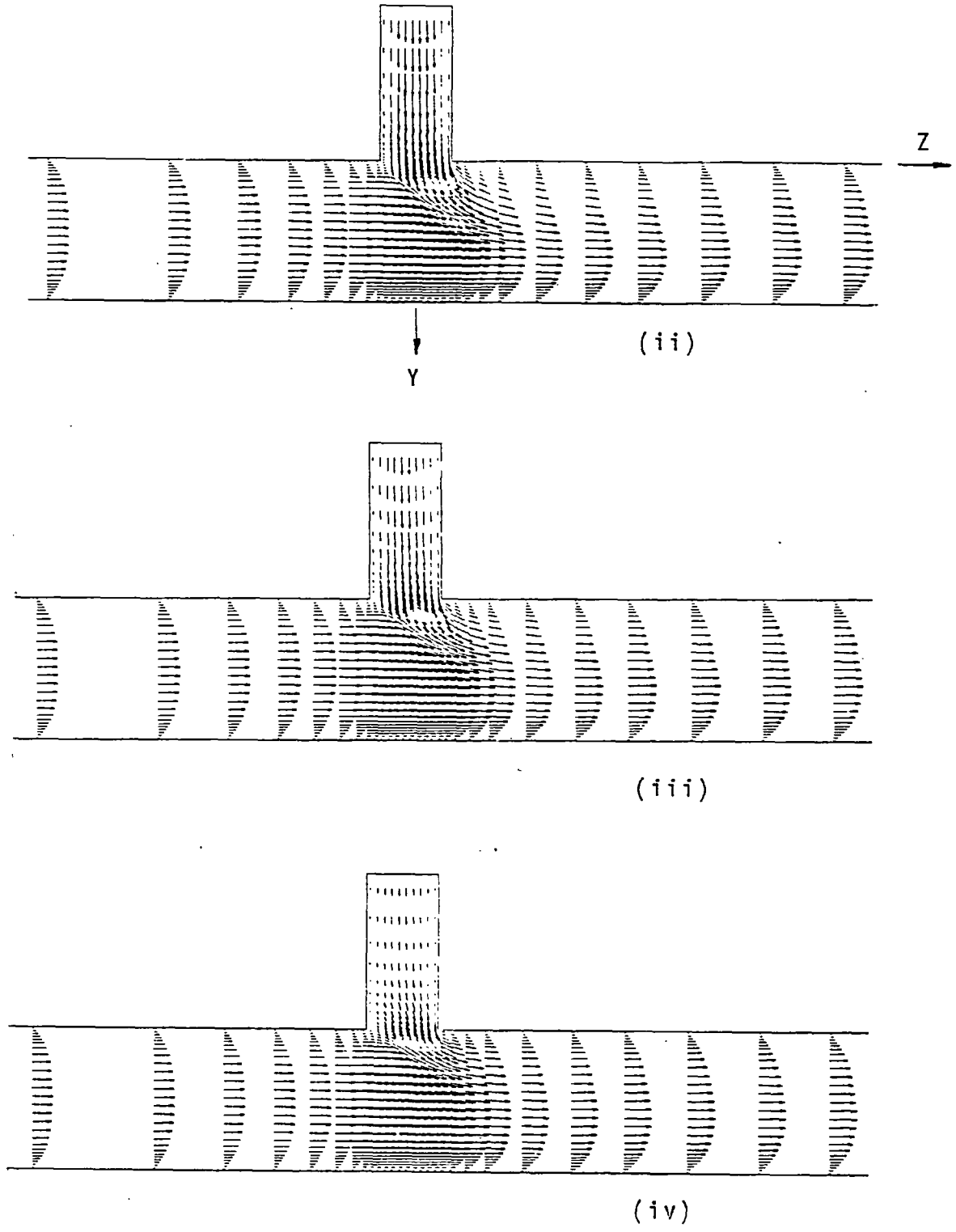

— 0.0974 M/Sec

FIGURE 5.4a: VECTOR PLOTS IN Y-Z PLANE
(Continued) $\frac{d_i}{D_m} = 0.5$, $\frac{M_i}{M_m} = 0.25$, $\frac{X}{d_i}$: ii(0.I4), iii(0.30), iv(0.42)

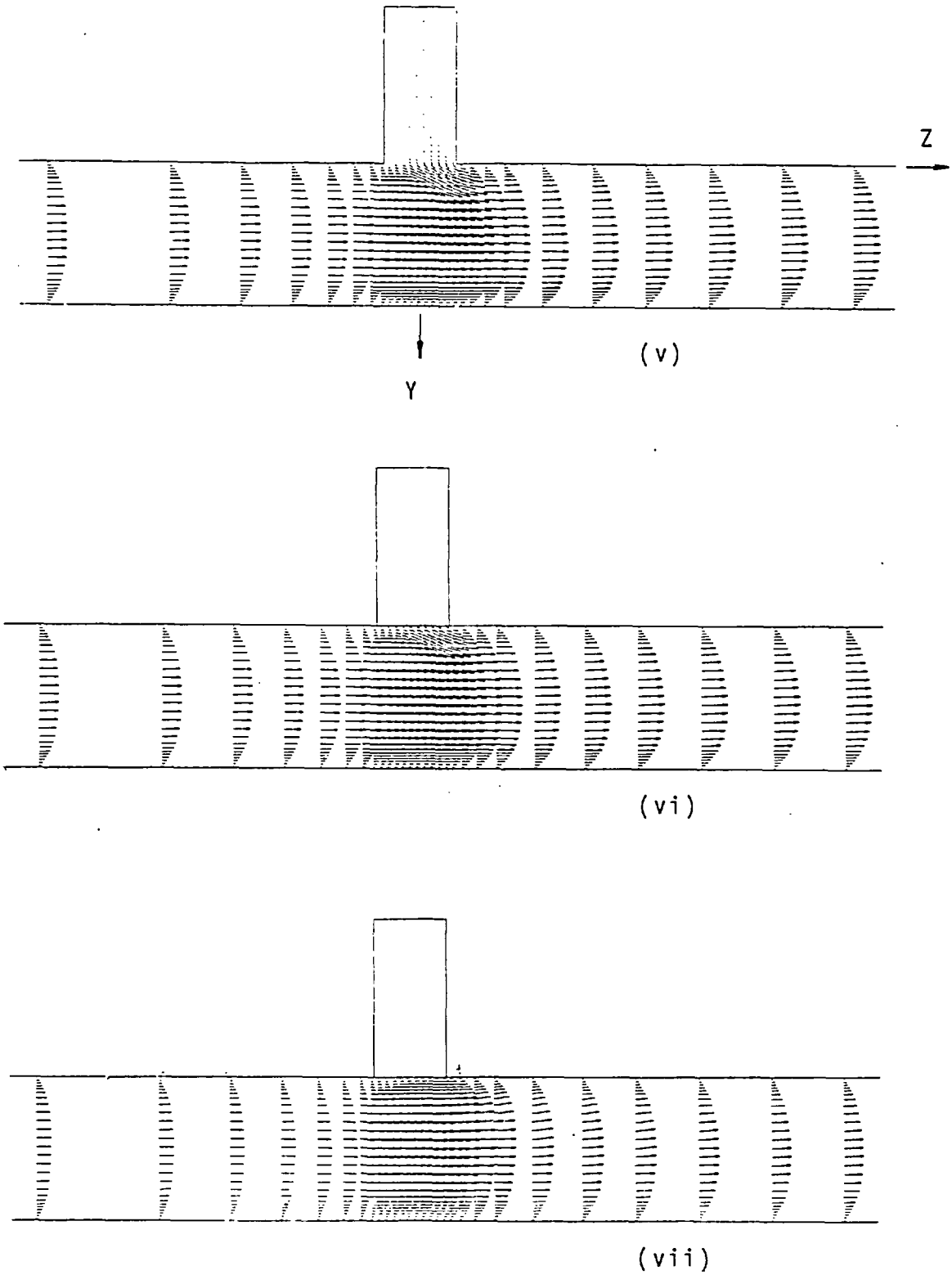

FIGURE 5.4a: VECTOR PLOTS ON Y-Z PLANE
(Continued) $\frac{d_i}{D_m} = 0.5$, $\frac{M_i}{M_m} = 0.25$ $\frac{X}{d_i}$: v(0.49), vi(0.5I), vii(0.72)

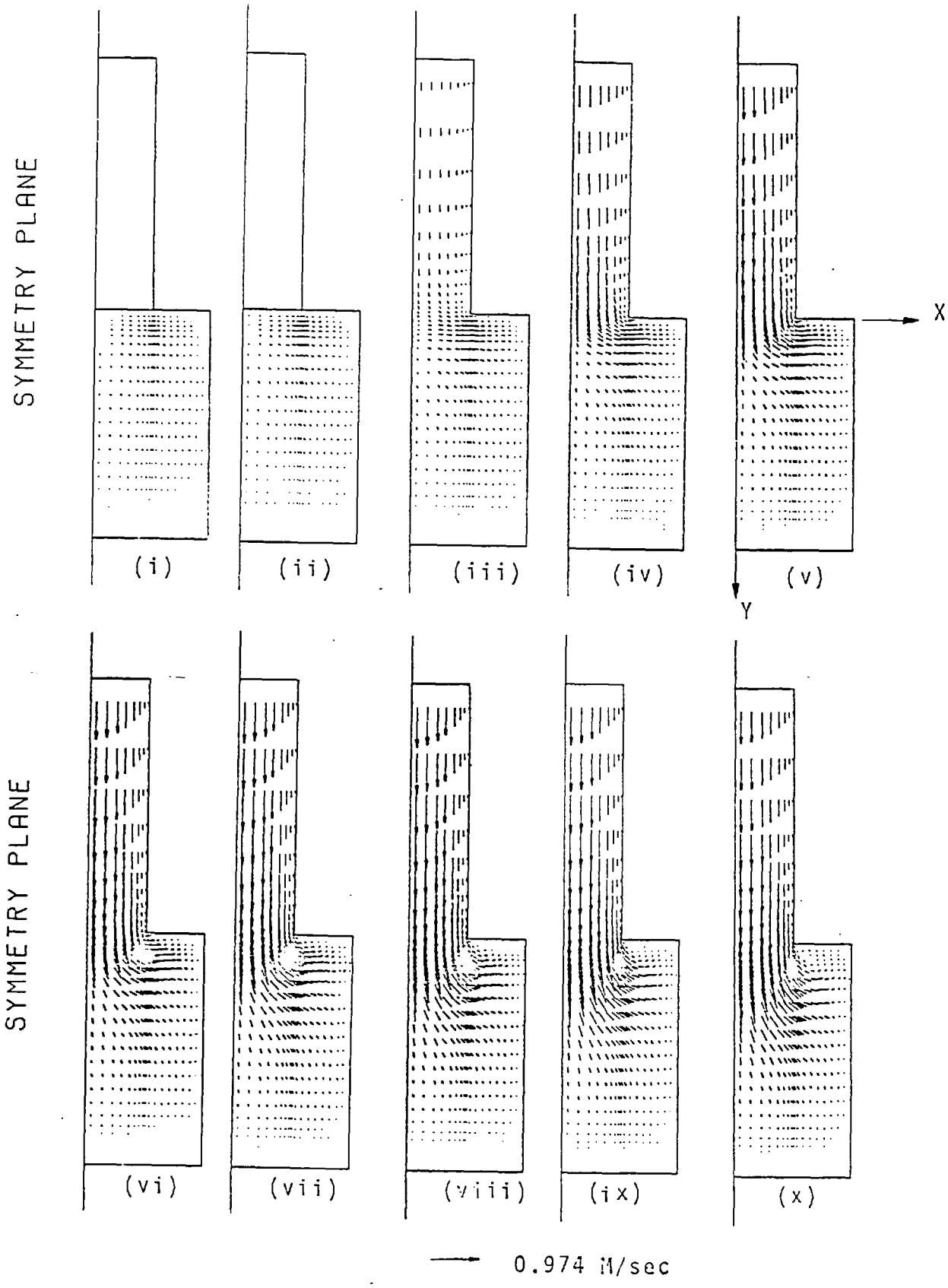

FIGURE 5.4b: VECTOR PLOTS ON X-Y PLANES

d_i/D_m = 0.5, M_i/M_m =0.25

$\frac{Z}{d_i}$: (i)-0.7, (ii)-0.55, (iii)-0.45 (iv)-0.35
(v)-0.25, (vi)-0.I5, (vii)-0.05, (viii)+0.05,
(ix)+0.I5, (x)+0.25

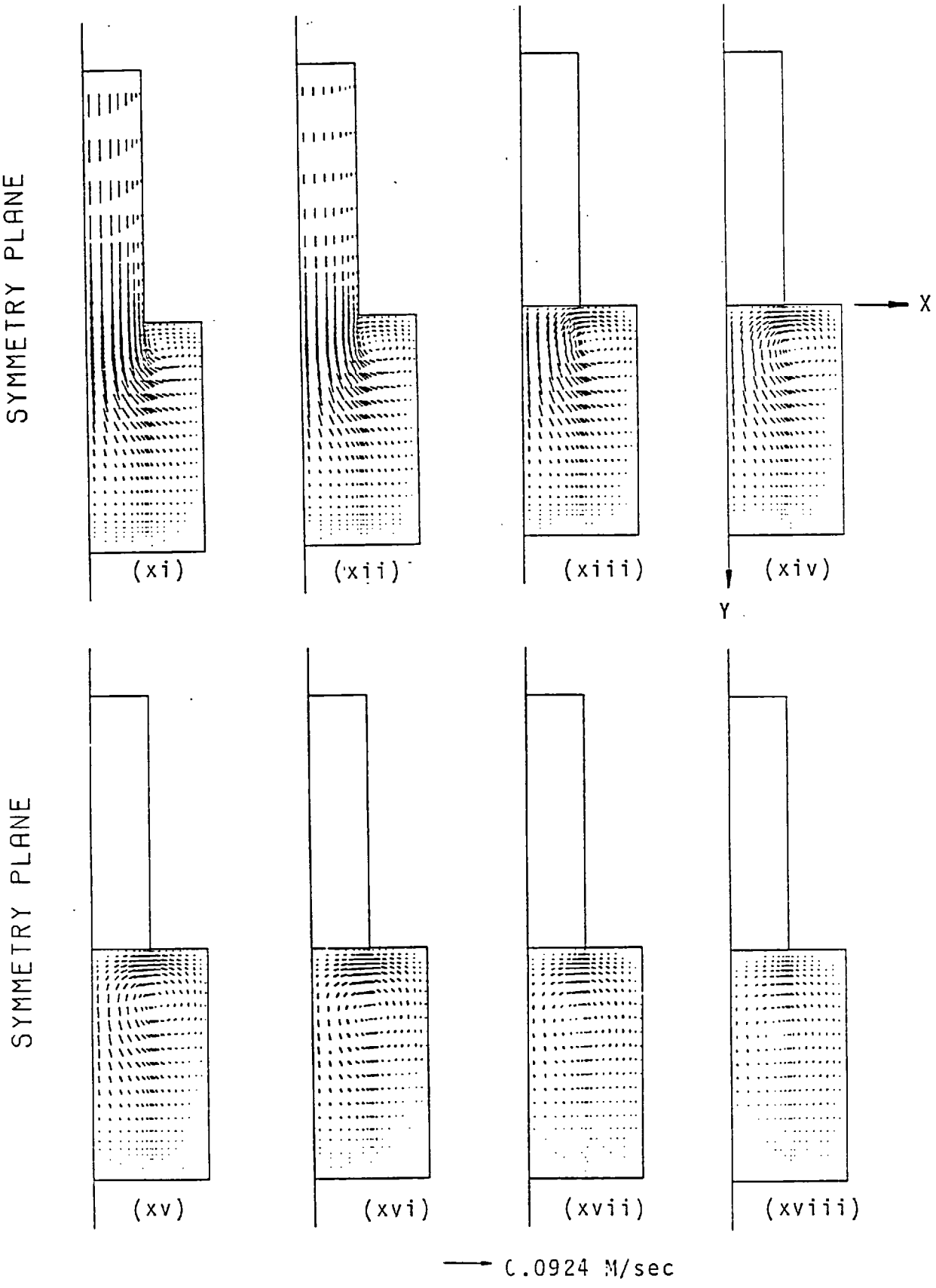

FIGURE 5.4b: VECTOR PLOTS ON X-Y PLANE

$\frac{Z}{d_i}$ = (xi)+0.35, (xii)+0.45, (xiii)+0.55, (xiv)0.625, (xv)+0.875, (xvi)+I.I5, (xvii) +I.625, (xviii)+2.375

upon leaving the junction region is also observed to be of a somewhat fully-developed nature, but features a small wall jet-like bulge; this is particularly noticeable in the first plot (Figure 5.4a(i)). This bulge in the velocity profile is observed to become insignificant as the duct is traversed towards the wall opposite the symmetry plane, but at the same time, the magnitudes of the velocites first increase and then decrease as the final plane presented is reached. These features of the flow indicate that the inlet fluid acts somewhat like a barrier in that it diverts the main duct fluid towards the bottom and side walls of the main duct.

A feature of the flow in tee-junctions is the existance of recirculating fluid. In particular, in a region adjacent to the downstream edge of the junction, there exists such a region of fluid. This region is only faintly observable in the figures presented; it is at the most only 0.5 d_i in length and about 0.I d_i in depth. As the edge of the junction is approached (Figure 5.4a(v)), this region ceases to exist quite possibly due to the main stream fluid "washing" it away as the main fluid re-establishes itself from interacting with now lower momentum inlet fluid. The lower inlet momentum is, of course, a consequence of viscous action in the down-march corner of the side duct.

An additional feature of the flow is again caused by the main stream interacting with the side flow. The predominantly "vertical" momentum of the inlet fluid interacting with the predominantly "horizontal" momentum main duct fluid generates secondary velocities in a plane normal to those

shown in Figure 5.4a. To observe these velocities, attention is now focussed onto the velocity vectors located in planes depicted in Figure 5.4b.

Figure 5.4b presents eighteen planes of velocity vectors ranging from $Z/d_i = -0.7$ to $Z/d_i = 2.375$. As the main duct is traversed from a region upstream to a region downstream of the inlet duct centre-line, there are at least five distinct features to the flow. These features are presented and discussed below.

The first feature encountered is in the region upstream of the inlet duct centre-line (panel i); although of a magnitude to appear indistinguishable, the vectors in this region are pointing away from the inlet duct toward the "bottom" wall of the main duct, indicating that the entering side fluid transmits its effects (via pressure) in the upstream main duct direction. (Although not shown, these effects could be detected at about 4 d_i upstream of the inlet duct centre-line.)

The second feature is located in the inlet duct. In panels (iii) through (xii), it is observed at the entrance to the side duct, the velocity profiles are uniform about the inlet duct centre-plane (the central X-Y plane). However, as the side duct is traversed from its inlet to the junction with the main duct, it is noticed that there is a distinct shift in symmetry: the fluid velocity at $Z/d_i = + 0.45$ (panel xii) is much higher than that at $Z/d_i = - 0.45$ (panel iii) indicating that the mainstream fluid tends to push the side fluid towards the down-march side of the inlet duct.

The third feature is also associated with the inlet fluid. As this fluid enters the main duct, it is observed to spread in the main duct cross-stream direction. This lateral spreading is quite probably due to the side fluid entraining fluid from the main stream. The effect of the incoming side fluid on the main stream lateral velocities is seen to be small, particularly in the lower half of the main duct.

The next feature to be observed is the creation of a pair of counter-rotating vortices in the main stream; only one of the pair is shown, the other is located on the opposite side of the symmetry plane. The vortex motion is seen to begin at the edge of the junction at $Z/d_i = -0.45$, and continues to grow between the $X/D_m = 0.25$ and $X/D_m = 0.5$ planes (planes parallel with the inlet duct axis) until the downstream corner of the junction is reached, $Z/d_i = 0.45$. As the fluid passes through the $Z/d_i = 0.5$ point, the vortex driving force (the incoming side fluid) is no longer directly present; the vortex strength, however, appears to first grow and then die away. This feature has been observed by Kamotani and Greber (I972), and Simitovic (I977).

The fifth and final feature is concerned with the recirculation zone in the upper half of the main duct and downstream of the inlet duct. In discussing the previous figure, (5.4a), it was mentioned that this recirculation is "washed" away by the mainstream fluid as it tries to re-establish itself after the encounter with the inlet fluid. This appears to be confirmed by the cross-stream vector plot in Figure 5.4b(xiii).

(c) PREDICTIONS vs EXPERIMENTAL DATA

Figures 5.5a-d, 5.6a-d and 5.7a-b present a comparison between the experimental data of Simitovic (I977) and the present predictions for the first three of the prediction cases outlined in Table 5.I. Predictions for Case 4 of Table 5.I are not shown specifically in the figures for they correspond very closely to those of Case 3 and would, therefore, only confuse the presentation of the remaining cases.

Figure 5.5a-d present the profiles of axial velocity in X-Z planes as the main duct is traversed from the inlet duct to the wall opposite the inlet duct; all the figures are for an axial location corresponding to the inlet duct centre-line (i.e. $Z/d_i = 0$); Figure 5.6a-d presents similar information as that in Figure 5.5a-d, but for an axial location of $Z/d_i = I$.

Finally, in Figure 5.7a and b, there is presented a comparison between the experimental data and the predictions for Case I and 3 of Table 5.I, for main duct axial locations of $Z/d_i = 5$ and $Z/d_i = 9.5$; at these locations, the comparison has been selected to be along the "horizontal" (X-Z) plane at $Y/d_i = I.0$.

The information presented in Figures 5.5, 5.6 and 5.7 confirms the general trends of the flow outlined in the previous section.

From these figures, it is seen that the predictions agree reasonably well with the experimental data of Simitovic (I977).

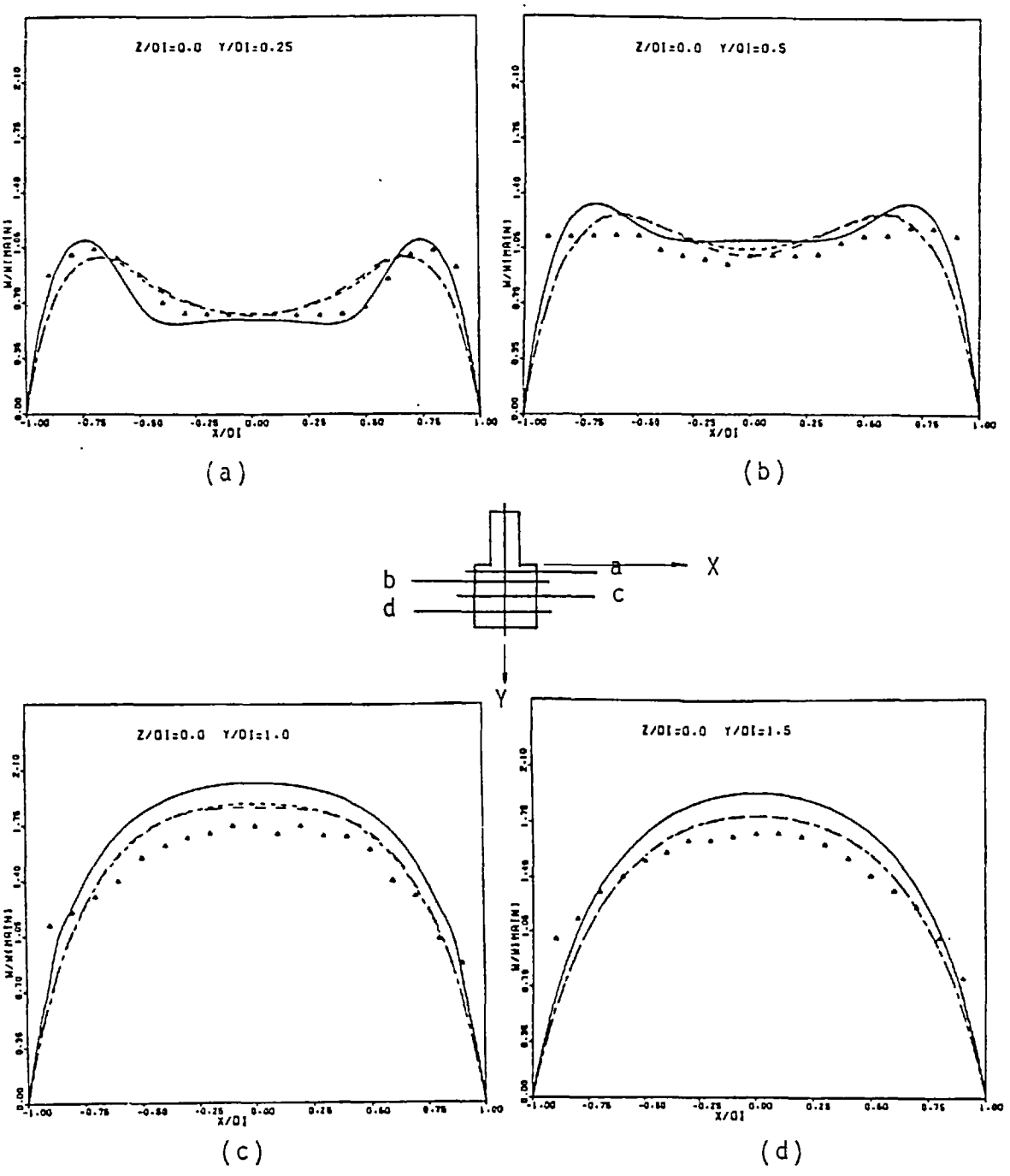

FIGURE 5.5: COMPARISON OF EXPERIMENTAL DATA
(▲) WITH PRESENT PREDICTIONS

——— Case I
------ Case 2
— — Case 3, Case 4
▲ Data Simitovic (I977)

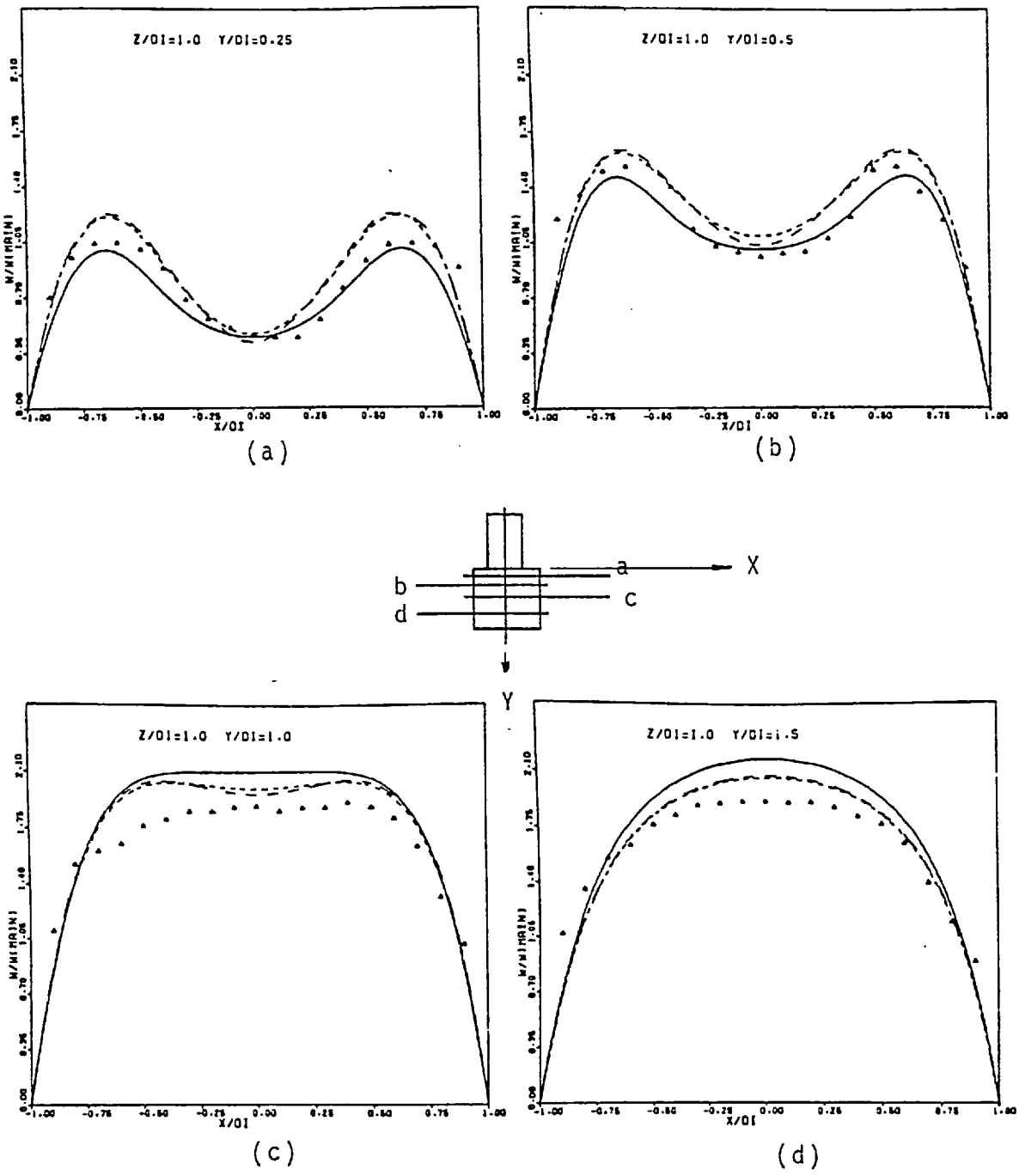

FIGURE 5.6: COMPARISON OF EXPERIMENTAL DATA (▲) WITH PRESENT PREDICTIONS

——— Case I
- - - - - Case 2
— — Case 3, Case 4
▲ Data Simitovic (I977)

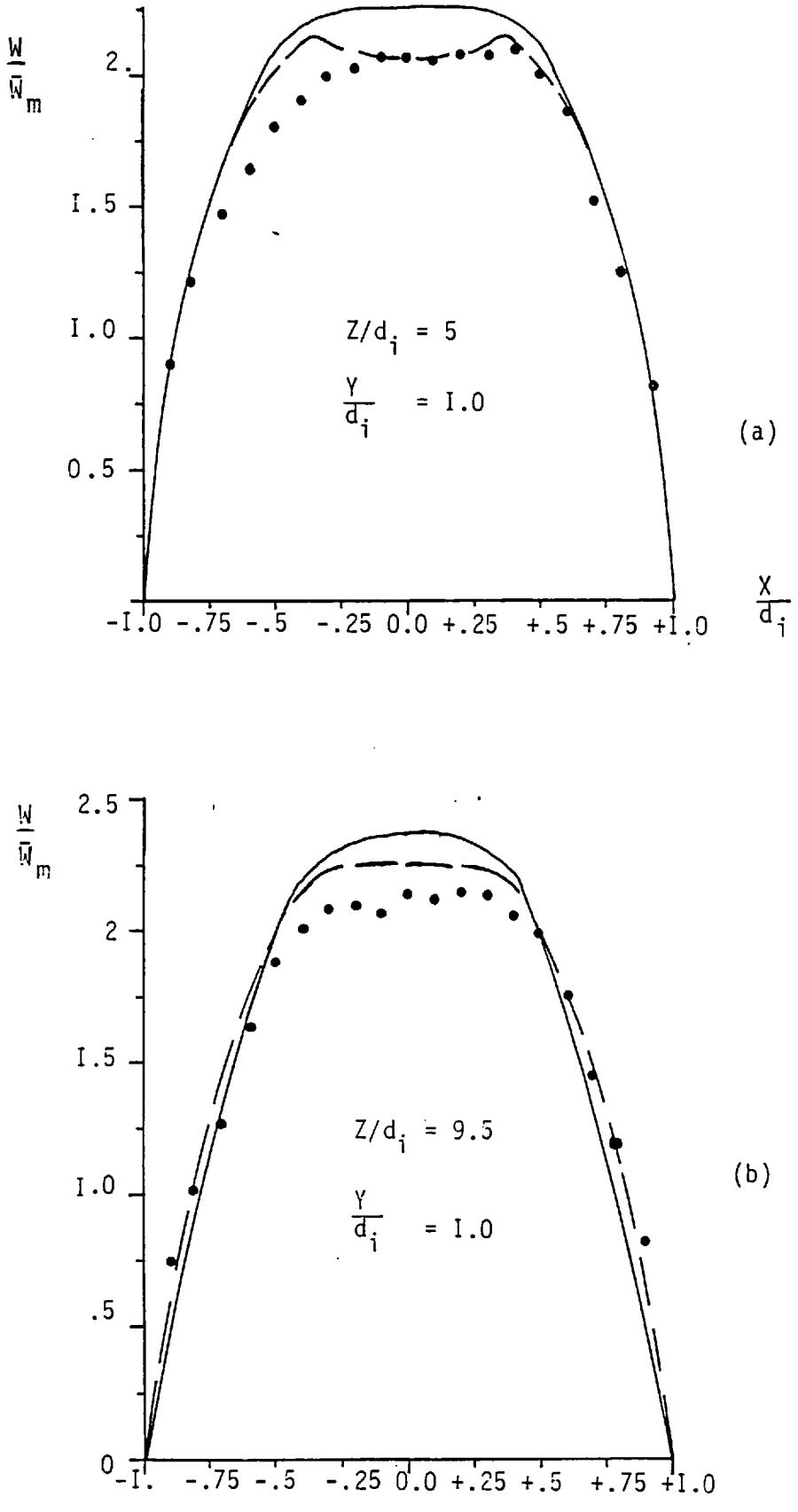

FIGURE 5.7: COMPAPISON OF EXPERIMENTAL DATA WITH PRESENT PREDICTIONS

——— Case I
— — - Case 3
• Data Simitovic (I977)

There are differences in the predictions obtained using different inlet duct boundary conditions. It is to an examination of these differences that attention is now turned.

In Figure 5.5a it is seen that the lack of an inlet duct (Case I) produces a more flattened profile in the axial velocity at this section than either of the other three cases. This is as expected since at the hole vacated by the inlet duct, the "top-hat" velocity profile presents a broader blockage than the other cases. The more fully-developed profile of the other three cases gives the main stream fluid an opportunity to exert its influence on the slower moving fluid entering the main duct from the inlet duct near-wall region. As the $Z/d_i = 0$ axial station is traversed from the inlet duct to the wall opposite the inlet, (panels b to d) the predictions for Cases 2 to 4 show less penetration and better agreement with the experimental data than the Case I predictions. The lower penetration appears to be due to the main flow affecting the inlet flow within the inlet duct itself.

At $Z/d_i = I.0$ (Figure 5.6), the trends observed in Figure 5.5 are evident here also; the magnitudes of the normalised velocities are different, however, because of the increased mass flow rate past this axial location. From the figures, the predictions for Case I show remarkable agreement with the data in the upper half of the main duct (panels a and b), while the other predicted cases indicate slightly higher velocities, particularly in panel a. In panel c, however, the predictions obtained using an inlet duct (Cases 2-4)

show a feature that is not present for Case I: the velocity profile exhibits a slight "dip" indicating that the inlet fluid influences this region of the flow.

Turning attention to Figure 5.7, there is noticed that even at $Z/d_i = 5$, the inlet fluid effects are still noticeable as reflected by the predictions and experiments. No such effects are observed for the Case I predictions. By the time the combined fluid flow reaches about 9 d_i downstream of the inlet duct, all traces of the inlet fluid distorting influences have disappeared.

Although not mentioned specifically in the above discussion, it is apparent that when using an inlet duct, the inlet condition at the start of the inlet duct has little effect on the resulting main duct axial flow field. Indeed, in Figure 5.8 there is plotted the velocity parallel with the inlet duct axis, for Cases I, 2 and 3 of Table 5.I. The velocities are located in the plane that joins the two ducts. The plots indicate the results of the main stream effecting changes in the inlet velocity profile in the plane of the junction.

As an aid in the visualising of the shape of the three-dimensional velocity surface of the junction of the two ducts, there is presented in Figure 5.8b a computer-generated perspective view of this surface; the surface is generated from the predictions corresponding to Case 3.

(d) THE PRESSURE FIELD

Figure 5.9 presents the pressure distribution in both the

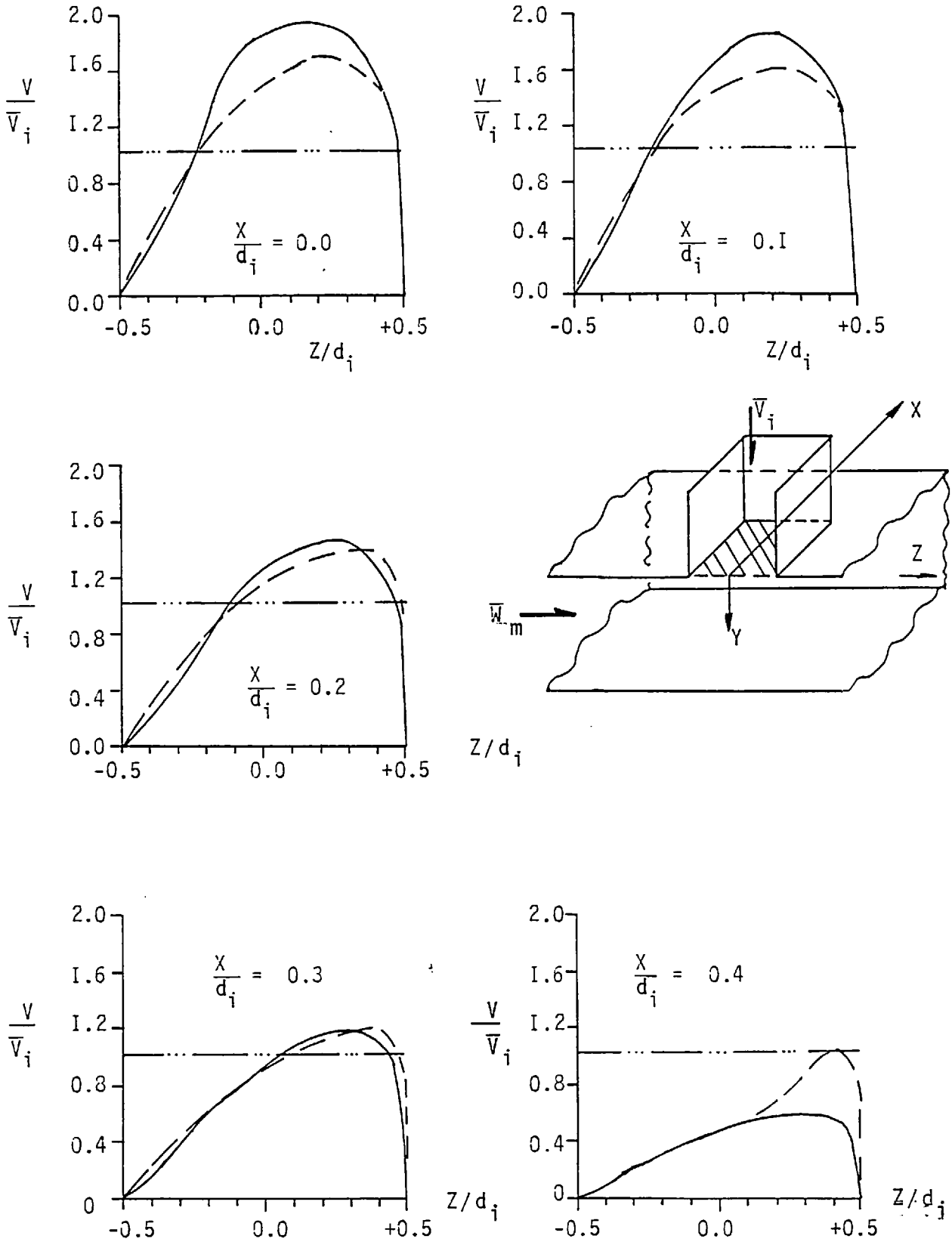

FIGURE 5.8a: INLET VELOCITY PROFILES ON Y-Z PLANES
—·—·— Case I; — — Case 2;
——— Case 3.

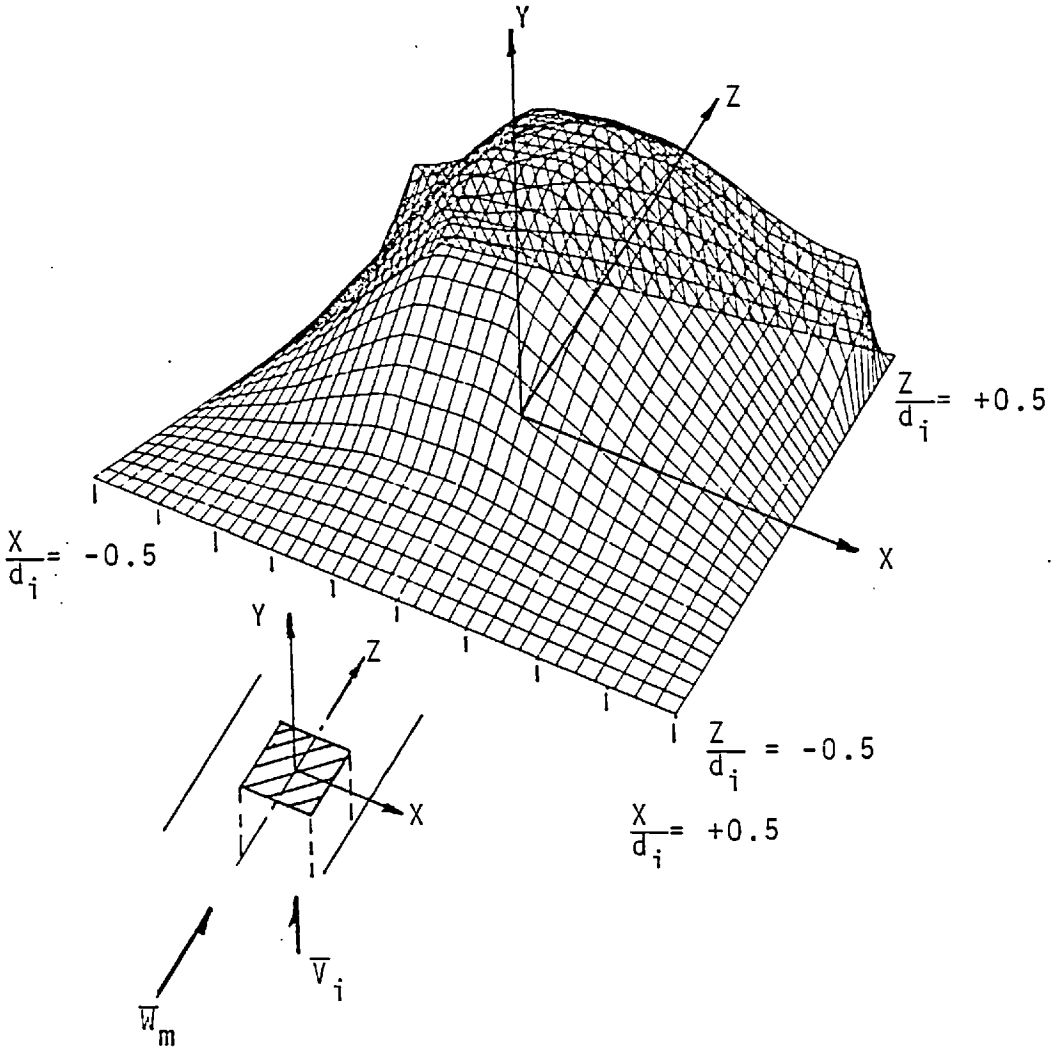

FIGURE 5.3b: PERSPECTIVE VIEW OF INLET DUCT VELOCITY PROFILE AT THE JUNCTION; CASE 3 PREDICTIONS.

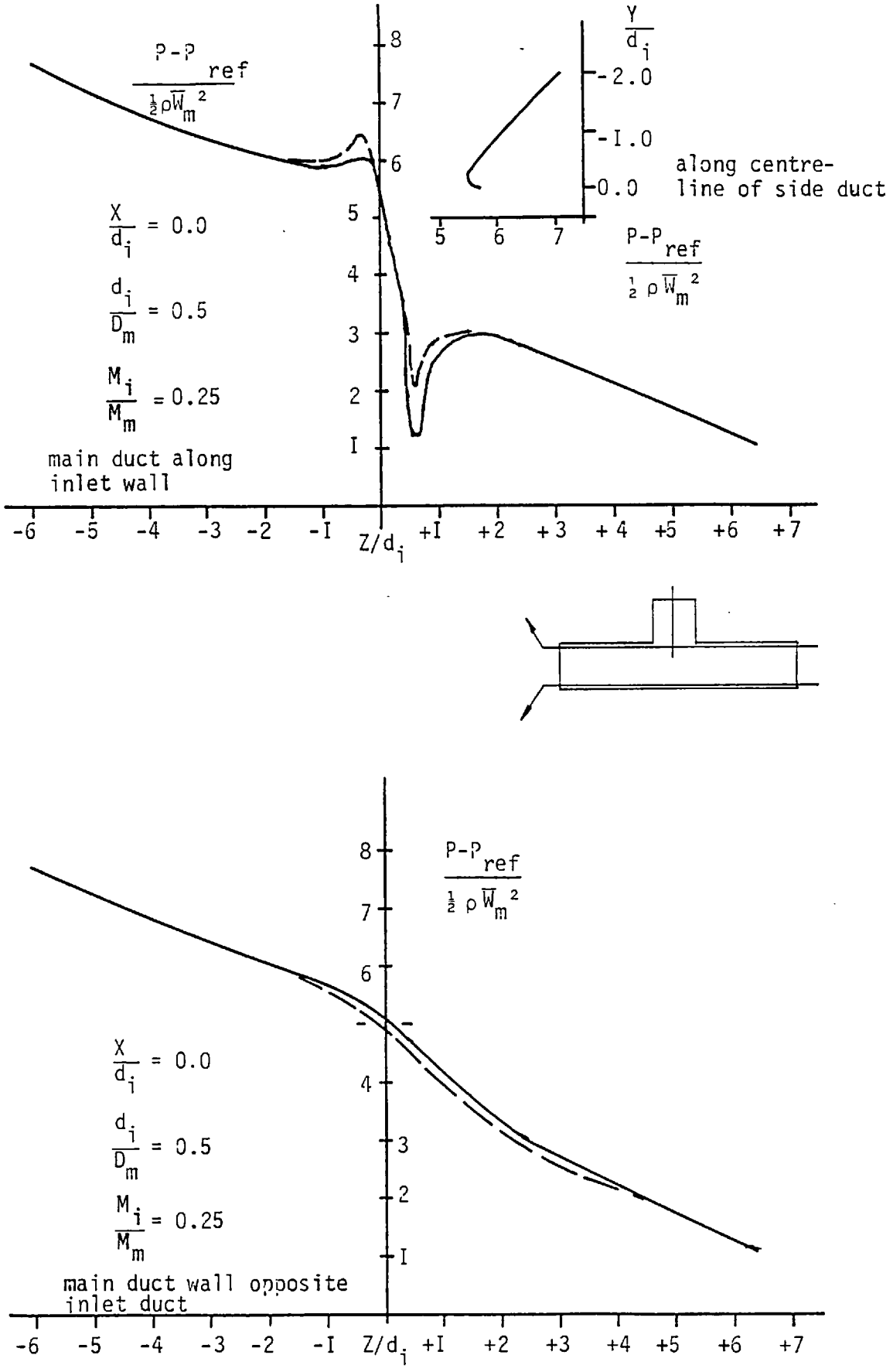

FIGURE 5.9: PRESSURE COEFFICIENT vs MAIN DUCT AXIAL DISTANCE

— — Case I

——— Case 3

main and side ducts. The upper plot depicts the axial pressure gradients along the side duct centre-line and along the wall of the main duct that contains the inlet duct, while the lower plot presents the pressure gradient along the main duct wall that faces the inlet. Eash plot presents two curves; the solid curve corresponds to Case 3, while the dotted one corresponds to Case I of Table 5.I.

From these curves, it is seen that the use of an inlet duct produces a pressure distribution similar in shape, but of different values to those obtained without an inlet duct particularly in the junction region.

(e) PREDICTIONS OBTAINED USING THE PARTIALLY-ELLIPTIC PROCEDURE

The predictions presented in the last few sections of this Chapter were obtained using the "elliptic" version of the computational code. Here, a few comments are made concerning the predictions produced by its "partially-elliptic" counterpart, with particular reference to the accuracy penalties incurred through the use of this procedure. No mention is made here regarding the storage savings; reference to such savings have been made in Section 5.2.2.

The predictions obtained using the partially-elliptic procedure have been carefully compared to those obtained using the elliptic version; the differences between the predictions was found to be small. Both procedures predicted the same axial length of the recirculation zone;

indeed, in the cross-stream plane containing the re-attachment point, individual comparisons between the pressures and velocities at the re-attachment point produced a disparity of less than 3%. This level of disagreement appeared to be the maximum.

5.3.2 EXTENSIONS TO THE PREDICTIONS FOR DIAMETER RATIO OF 0.5

(a) INTRODUCTION

The previous sub-section dealt with comparing against limited experimental data, the predictions for the laminar flow in tee-junctions with a momentum ratio of 0.25. It was also shown that by the use of various inlet duct boundary conditions, the predictions were slightly different. However, of the four cases examined, the third case was found to be in best agreement with the experimental data.

Here, using the same geometry and flow inlet conditions corresponding to Case 3, the predictions are extended by varying the magnitude of the inlet duct velocity to produce momentum ratios of 0.I and I.0. The main duct inlet Reynolds number remains unaltered at I00.

(b) THE FLOW FIELDS

Figure 5.I0 presents vector plots located in planes parallel to the main duct symmetry plane for two momentum ratios; plot (a) corresponds to a momentum ratio of 0.I, while plot (b) is for a ratio of I.0.

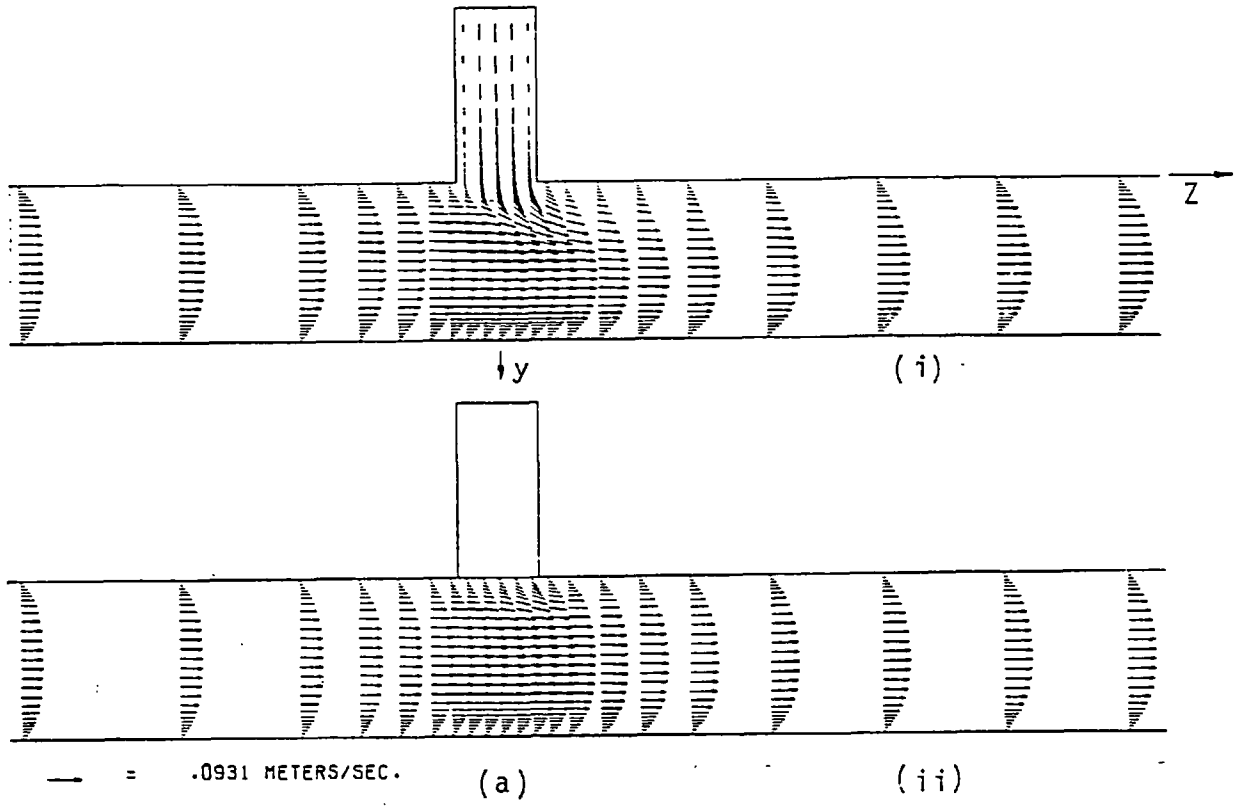

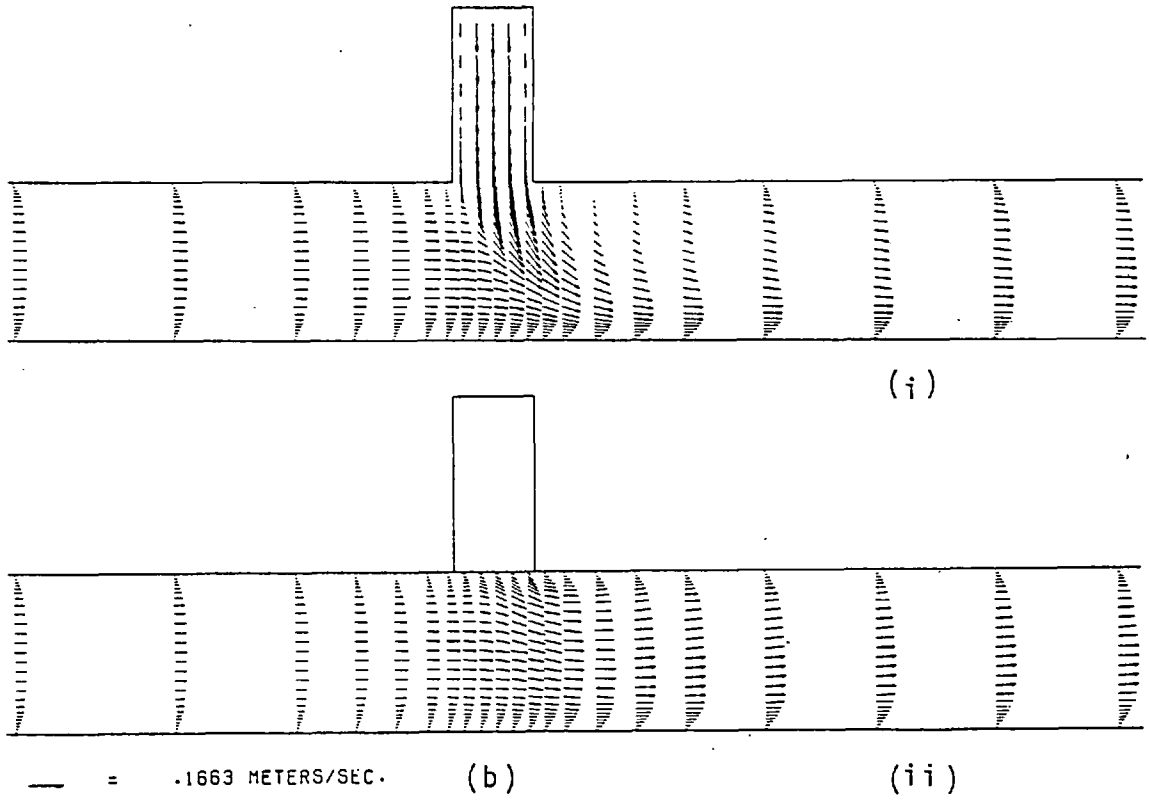

FIGURE 5.IO: LONGITUDINAL VECTOR PLOTS FOR TWO MOMENTUM RATIOS

(a) $\frac{M_i}{M_m}$ = 0.I, (b) $\frac{M_i}{M_m}$ = I.0, $\frac{X}{d_i}$:(i)=0.0, (ii)=0.5I

Comparison of these plots reveals four main features. First as the momentum ratio is increased, the main duct fluid appears to affect the incoming inlet fluid less, as evidenced by the increased parallel nature (with respect to the inlet duct axis) of the vectors in the junction region. Secondly, as the momentum ratio is increased, the disturbance created by the side duct fluid upon the main stream increases; this is evidenced by the increased penetration of the side duct fluid into the main stream. Next, as the momentum ratio is increased, the size of the recirculation zone in the upper part of the main duct, downstream of the junction, increases also. Finally, as the momentum ratio is decreased, the main duct fluid appears to recover faster after its encounter with the inlet duct fluid.

In Figure 5.II, there is presented some plots of vectors located in various main duct cross-stream planes; these plots correspond to a momentum ratio of 0.I (plots a) and I.0 (plots b).

The features of the flow displayed by these plots (Fig. 5.II) are similar to that previously explained in reference to the momentum ratio of 0.25 case (Section 5.3.Ib); it is evident, however, that as the momentum ratio is increased, the strength of the cross-stream fluid motion increases. Also, as plot iv (for both series(a) and (b)) clearly indicates, as the momentum ratio increases, do does the persistence of the cross-stream fluid motion.

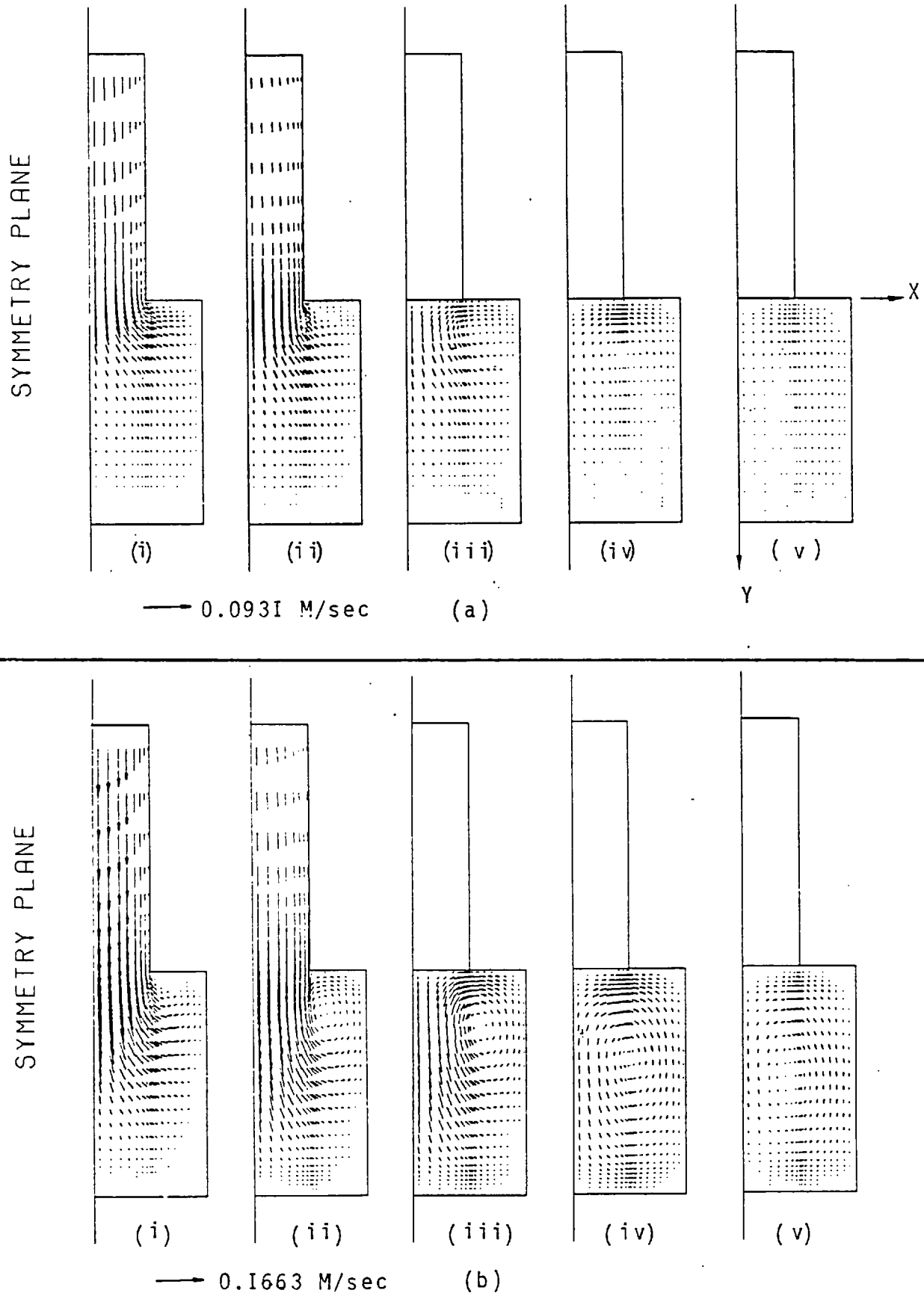

FIGURE 5.II CROSS STREAM VECTORS FOR TWO MOMENTUM RATIOS
(a) M_i/M_m = 0.I, (b) M_i/M_m = I.0
Z/d_i: (i)0.0, (ii)0.2, (iii) 0.3, (iv)0.6, (v)I.2

(c) THE VELOCITY TRAJECTORY

In Figure 5.I2, the velocity trajectories are plotted versus axial distance downstream of the inlet duct centre-line. The velocity trajectory, it will be remembered, is defined as the locus of the maximum velocity on the main duct symmetry plane. The plot shows the trajectories for three momentum ratios (ω= 0.I, 0.25, I.0). The solid curves correspond to the Case 3 situation of Table 5.I, while the dotted one corresponds to Case I.

From the figure, the depth of penetration is seen to increase with momentum ratio; this, it will be recalled is a feature observed in both laminer and turbulent flows in tee-junction geometries, see for example, Simitovic (I977) or Kamotani et al (I974).

It is also interesting to note that the trajectory corresponding to a uniform velocity profile at the junction (Case I) is not as deep as the trajectory for the situation corresponding to Case 3.

(d) VELOCITY PROFILES IN THE PLANE OF THE JUNCTION

Figure 5.I3 presents a computer-generated perspective view of the predicted velocity surfaces located in the junction region; the plane is orientated in the manner indicated by the sketch accompanying the surfaces. The flow situation corresponding to each surface is indicated in the figure caption.

Although only of a qaulitative nature, the surfaces show the extent to which the main stream distorts the side duct

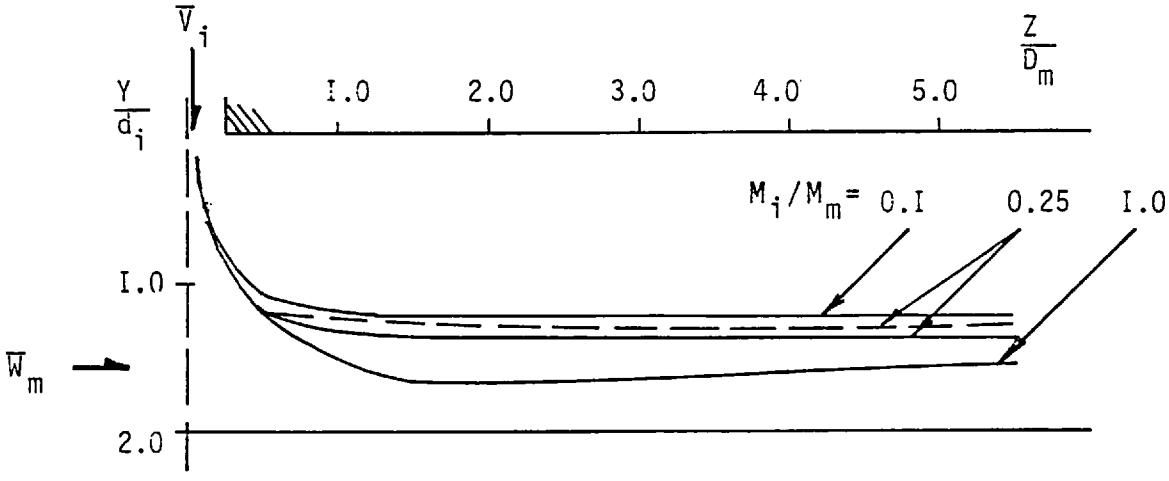

FIGURE 5.I2: VELOCITY TRAJECTORIES AS A FUNCTION OF MOMENTUM RATIO

—— side duct l_i/d_i = 2.2

— — side duct l_i/d_i = 0.0

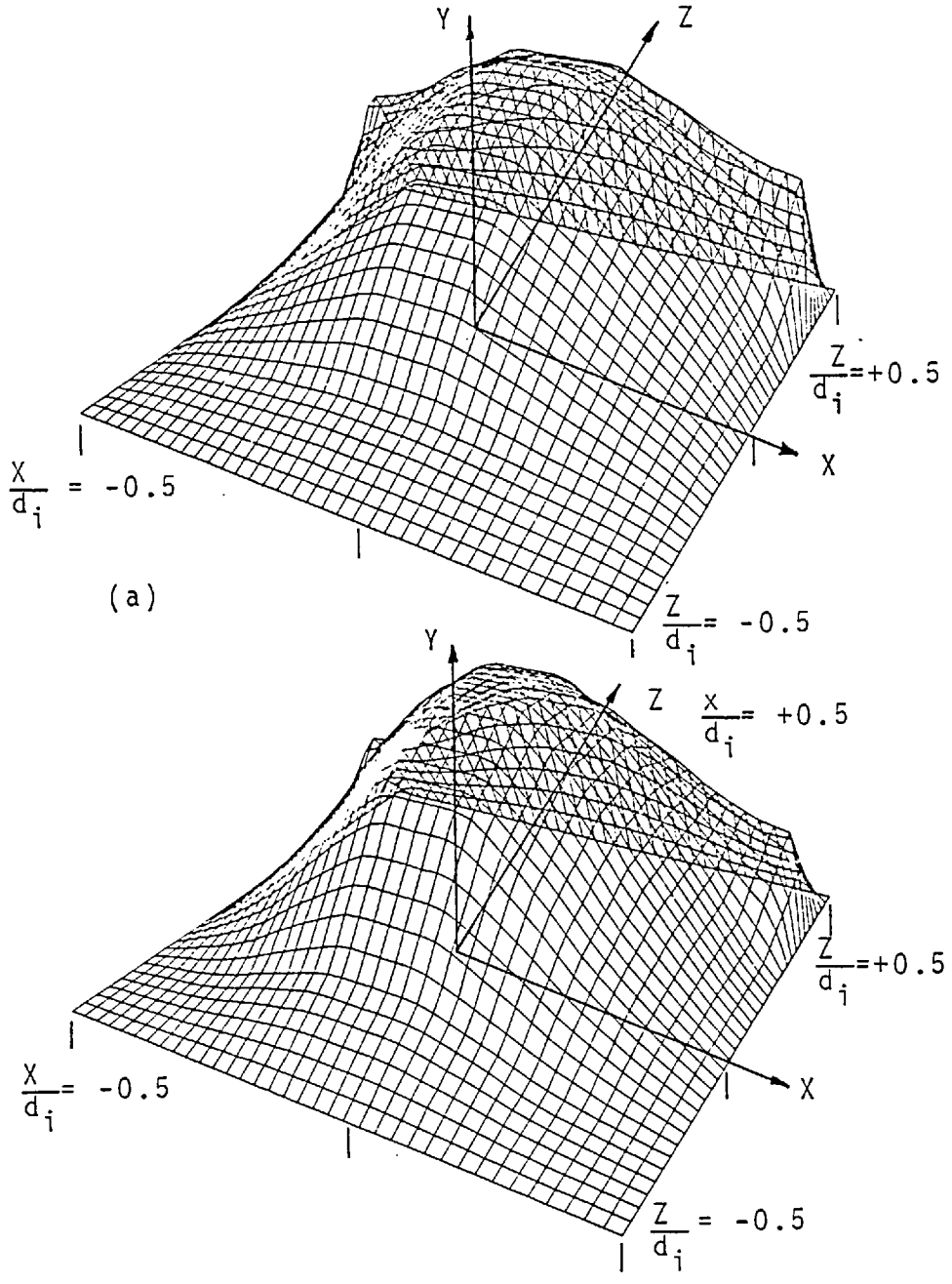

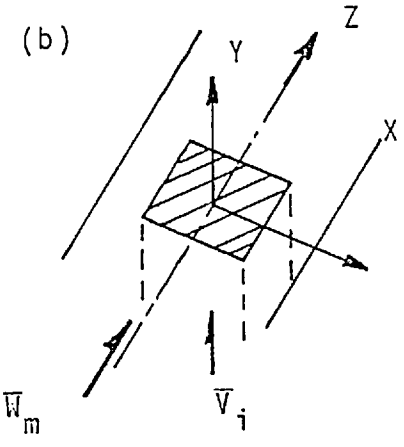

$\frac{X}{d_i}$ = +0.5

FIGURE 5.I3:
VELOCITY SURFACE AT JUNCTION

(a) $\frac{d_i}{D_m} = 0.5 \quad \frac{M_i}{M_m} = 0.I$

$V_{max}/\overline{V}_i = I.84$

(b) $\frac{d_i}{D_m} = 0.5 \quad \frac{M_i}{M_m} = I.0$

$V_{max}/\overline{V}_i = I.87$

velocity profile. For a diameter ratio of 0.5, the maximum velocity normal to the plane of the junction is about the same for the range of momentum ratios predicted.

(e) THE PRESSURE DISTRIBUTION

In Figure 5.I4, the pressure-distribution along the main duct upper and lower walls (i.e. the wall containing and the wall opposite the inlet respectively); also shown is the side duct centre-line pressure-distribution. The solid and dotted curves corresponds to a momentum ratio of I.0 and 0.I respectively.

Although appearing the same in shape as that discussed previously (Figure 6.9), it is observed that the magnitudes are substantially different. An additional feature is seen by comparing the curves in the upper diagram. It is observed that the blockage effects of the inlet duct fluid are transmitted farther upstream in the main duct as the momentum ratio is increased. Additionally, it is observed that a region of negative pressure is predicted near the downstream face of the junction. The pressure, after the inlet duct has been passed is seen to recover: the length of duct required to achieve the maximum recovery increases with momentum ratio. This pressure recovery is, of course, due to the main duct fluid decelerating as it begins to fill the duct in as uniform a manner as possible.

(f) PARTIALLY-ELLIPTIC PROCEDURE PREDICTIONS

The predictions presented above were obtained using the

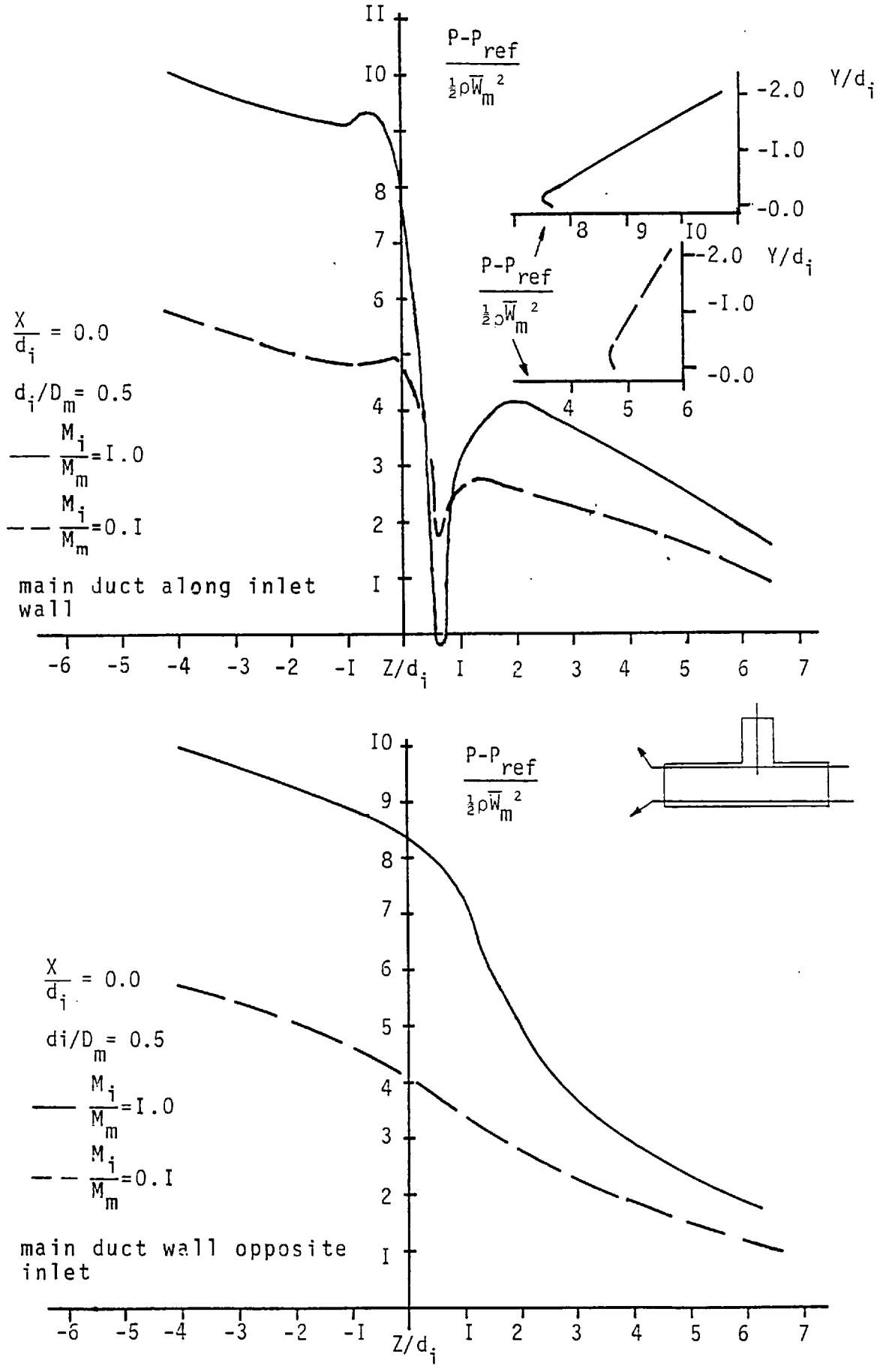

FIGURE 5.I4: PRESSURE COEFFICIENT vs MAIN DUCT AXIAL DISTANCE FOR TWO MOMENTUM RATIOS

"elliptic" form of the procedure. Predictions, using the "partially-elliptic" procedure produced effectively the same results as the "elliptic" code: the maximum difference was found to be about 3%.

5.4 TEE-JUNCTION OF DIAMETER RATIO I.0

5.4.I THE PHYSICAL SITUATION

With reference to the geometry depicted in Figure 5.I, the diameter ratio considered in this Section corresponds to $d_i = D_m$. The flow situation is of the combining type; this is as before. The momentum ratios considered here are ω=0.I, 0.25 and I.0. The other variables that describe the geometry considered are as follows:

$$L_i = 4.5\ D_m,\ L_m = 9.50\ D_m \text{ and } l_i/d_i = I.I.$$

5.4.2 THE INLET CONDITIONS

The inlet conditions used for the flow situations investigated here correspond to a plug inlet profile at the start of the main duct, and a fully-developed square duct (laminar) profile at the start of the inlet duct. It will be remembered that this corresponds to Case 3 of the previous section, which was found to agree best with the experimental data.

5.4.3 THE SOLUTION PROCEDURE

The predictions for the cases to be presented here are those obtained using the "elliptic" form of the solution

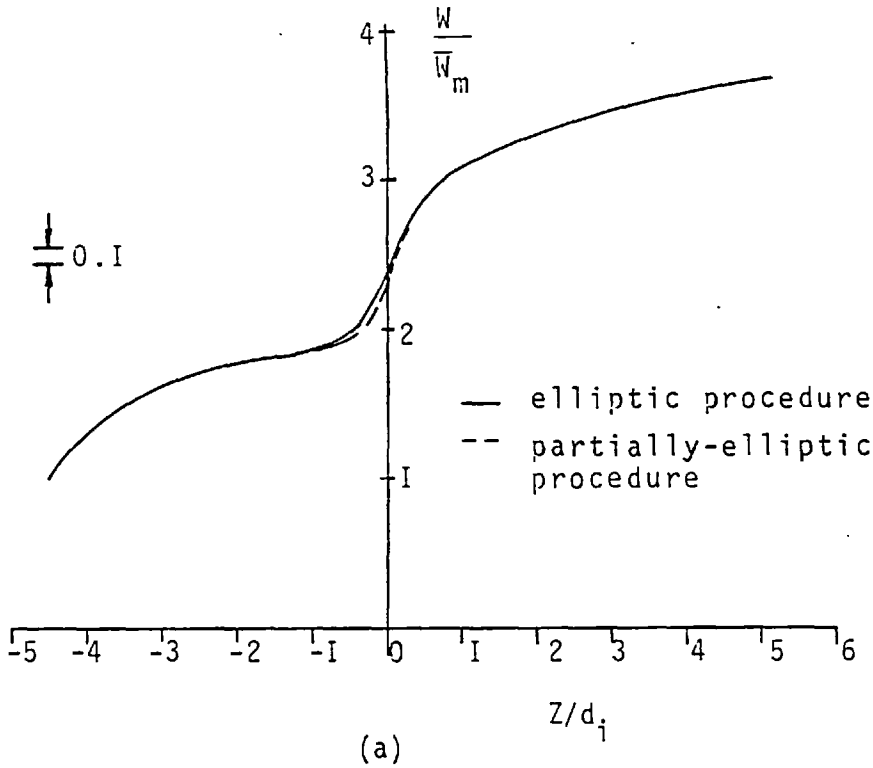

(a)

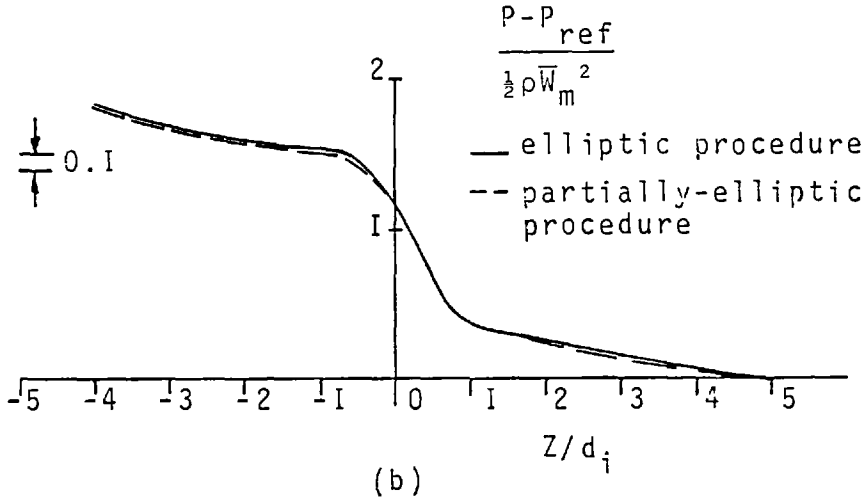

(b)

FIGURE 5.I5: MAIN DUCT CENTRE-LINE DISTRIBUTION OF (a) VELOCITY , (b) PRESSURE COMPARISON OF PROCEDURES d_i/D_m=I.0 M_i/M_m=I.0, l_i/d_i=0.0

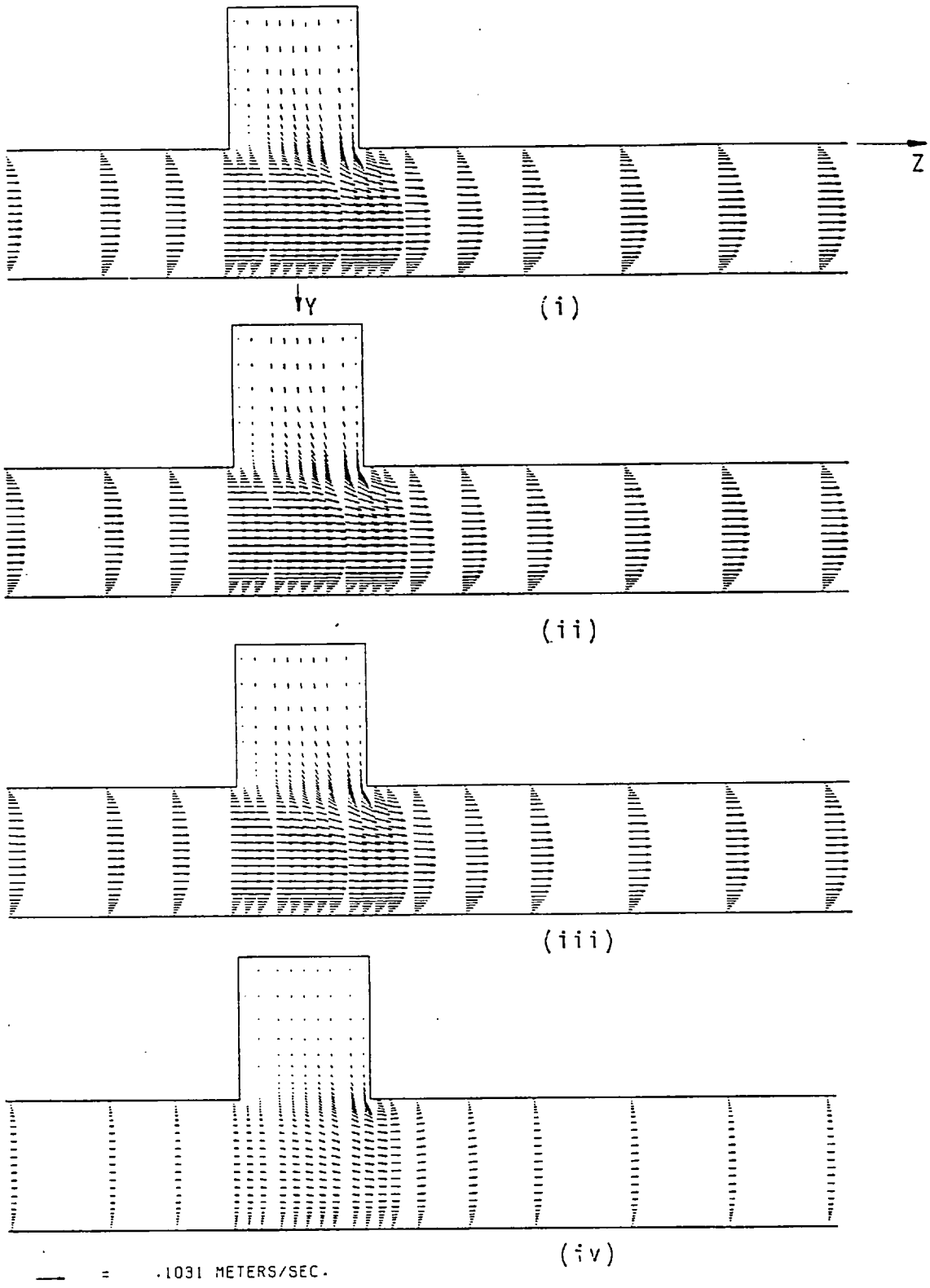

FIGURE 5.I6: LONGITUDINAL VECTOR PLOTS
d_i/D_m = I.0, M_i/M_m = 0.I

X/d_i: = (i) 0.07, (ii) 0.I5, (iii) 0.25
(iv) 0.45

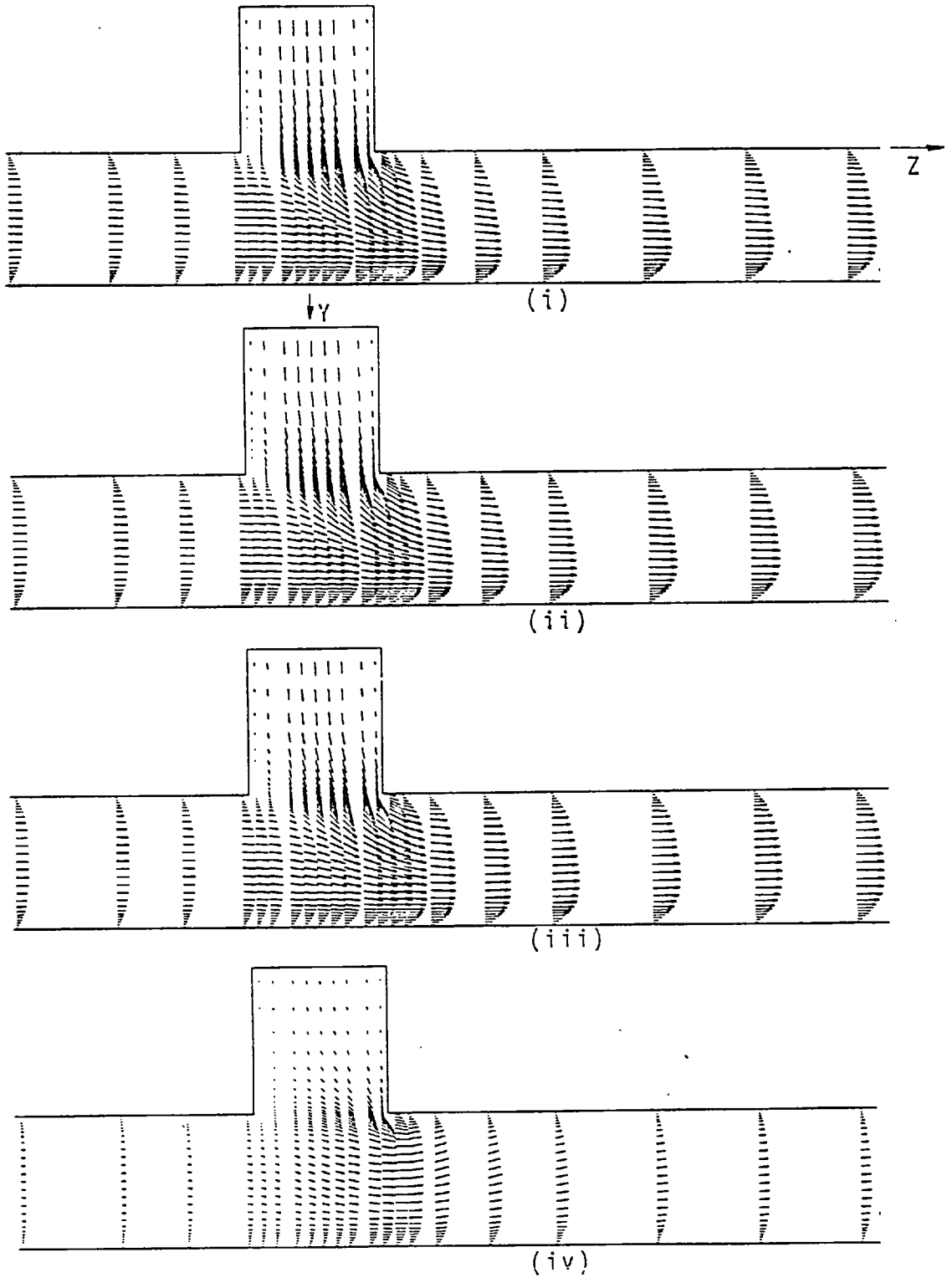

FIGURE 5.I7: LONGITUDINAL VECTOR PLOTS
d_i/D_m = I.0, M_i/M_m = I.0
X/d_i:=(i)0.07, (ii)0.I5, (iii)0.25. (iv) 0.45

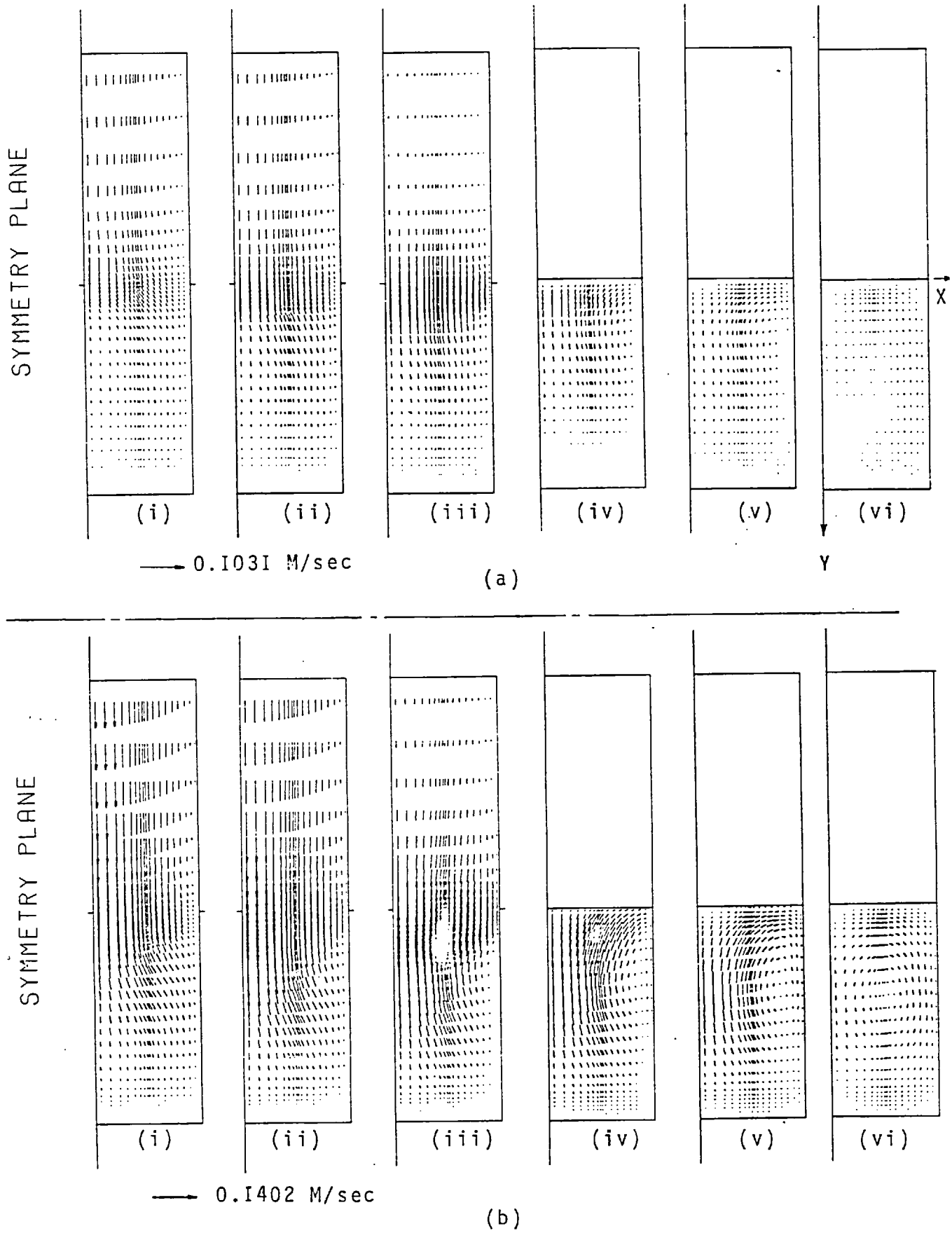

FIGURE 5.I8: CROSS STREAM VECTOR PLOTS
d_i/D_m = I.0, M_i/M_m = (a) 0.I, (b) I.0

Z/d_i: (i)0.0, (ii)0.2, (iii)0.45, (iv)0.55
(v) 0.7, (vi)I.3

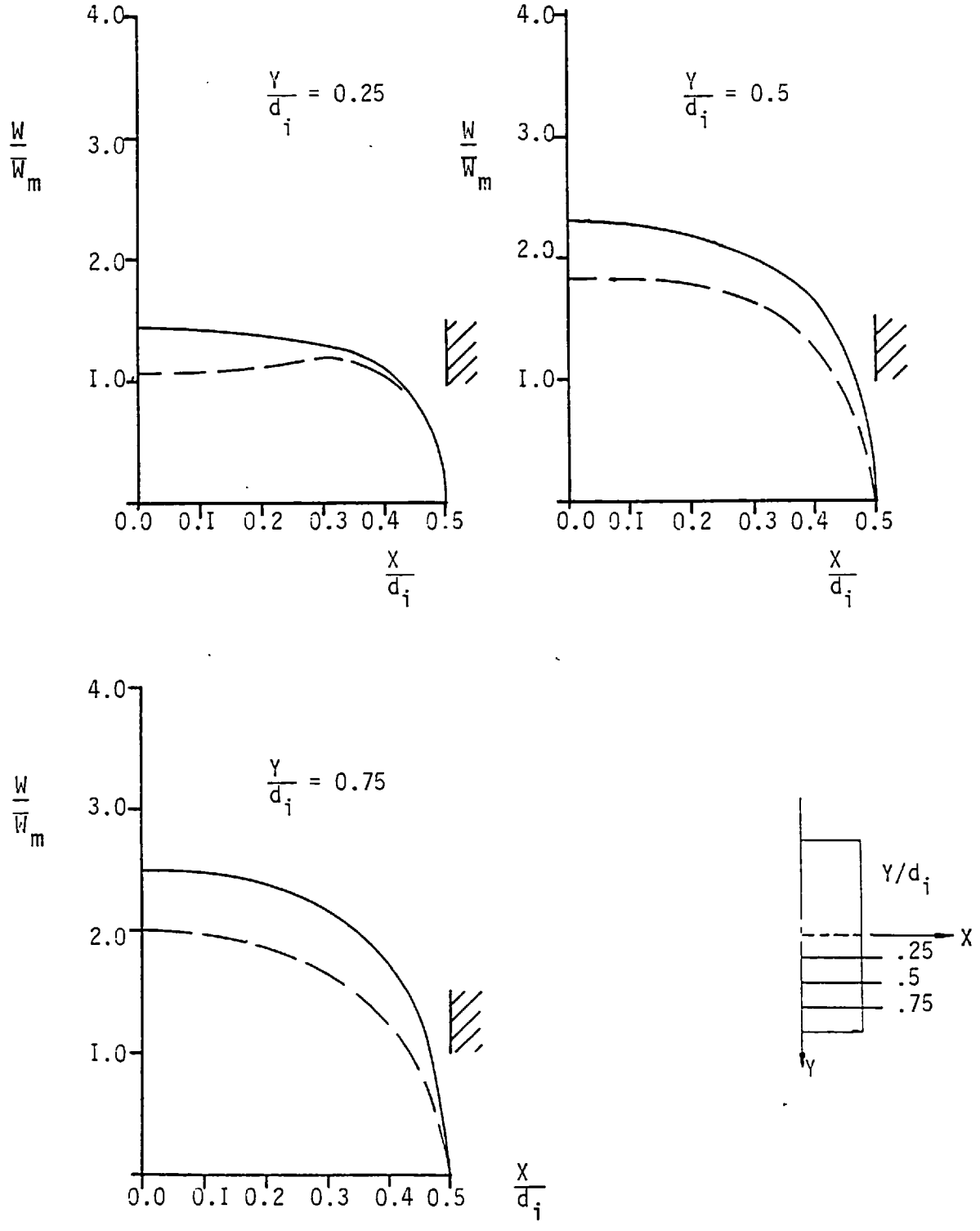

FIGURE 5.I9: PREDICTED AXIAL VELOCITY PROFILES FOR $\frac{d_i}{D_m}$ = I.0, $\frac{M_i}{M_m}$ = I.0, $\frac{Z}{d_i}$ = 0.0

— — side duct l_i/d_i = I.I

—— side duct l_i/d_i = 0.0

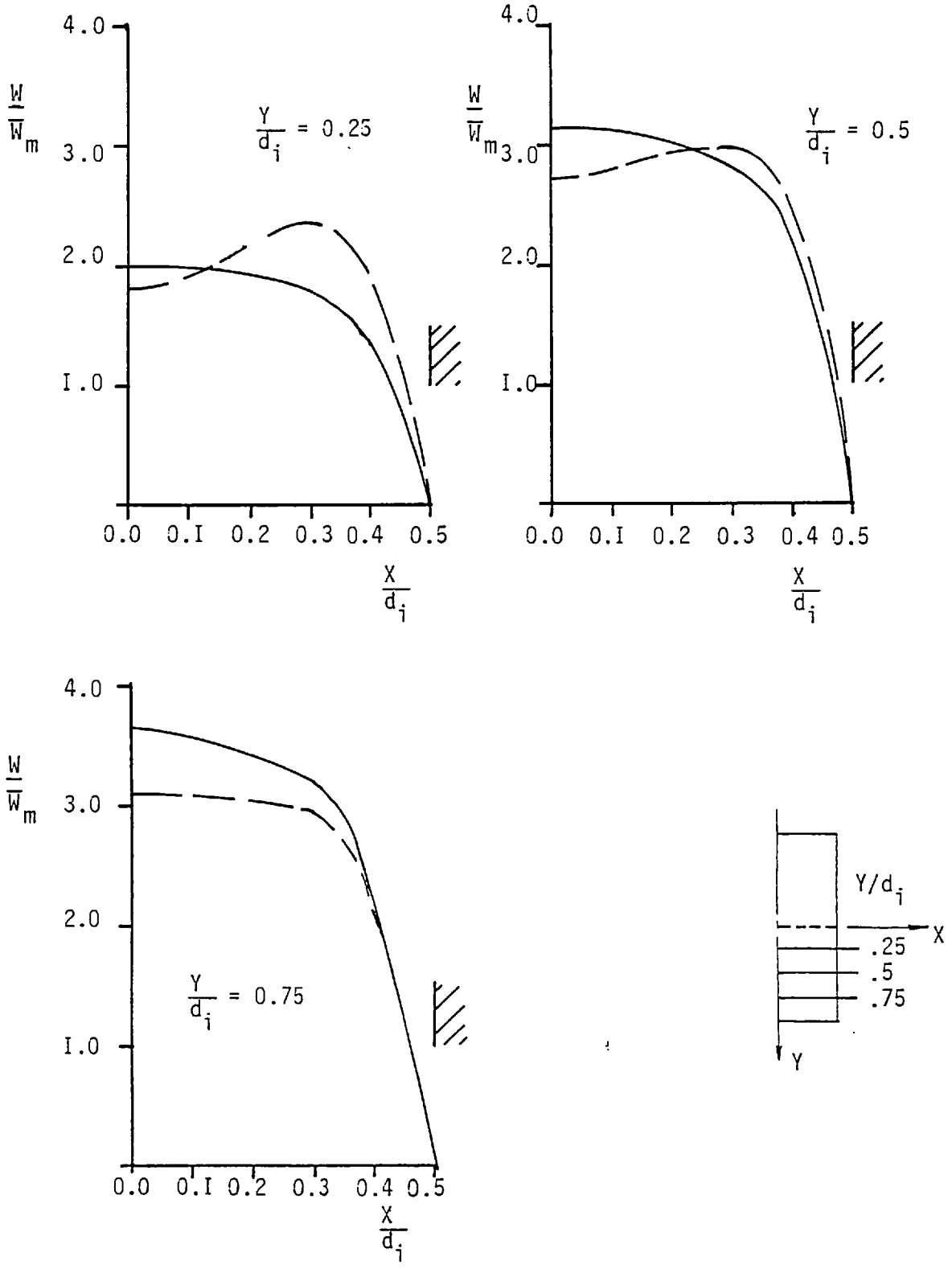

FIGURE 5.20: PREDICTED AXIAL VELOCITY PROFILES FOR $\frac{d_i}{D_m}$ = I.0, $\frac{M_i}{M_m}$ = I.0, $\frac{Z}{d_i}$ = I.0

— — side duct, l_i/d_i = I.I

—— side duct, l_i/d_i = 0.0

procedure. The predictions using the "partially-parabolic" form of the computational code, when compared with those from the "elliptic" form are in almost complete agreement. This is illustrated in Figure (5.I5) where, for M_i/M_m=I.0 and l_i/d_i= 0.0, the main duct centre-line velocity and pressure distribution obtained from the two procedures are compared. The disagreement is seen to be within 3% or 4%.

5.4.4 THE PREDICTED FLOW FIELDS

In Figure 5.I6 and 5.I7, there is presented some vector plots in various longitudinal (Y-Z) planes for momentum ratios of 0.I and I.0. The total length of the main duct is not shown for reasons of spatial economy. In Figure 5.I8, vectors in various (X-Y) planes are presented; note that the plots originate at the centre-plane of the inlet duct. In Figures 5.I9 and 5.20, the main duct axial velocity profiles at Z/d_i = 0.0 and Z/d_i = I.0 are presented for the M_i/M_m = I.0 case; for comparison purposes, the velocity profiles resulting from a uniform velocity profile at the junction of the ducts, (i.e. like case I of the previous Section) are also shown.

Concentrating attention on the plots presented in Figure 5.I6, it is observed that the profiles are of similar shape as the main duct is traversed from the centre-line to the wall of the main duct. Indeed, the profiles are as one would expect from a two-dimensional plane tee-junction. Moreover, it is only as the wall (in the plane of the vector plots) is approached that the viscous action tends to slow the fluid down. An additional feature highlighted in Figure 5.I6 is the interaction of the two fluid streams, particularly in

that segment of the junction bounded by the inlet duct centre-line and the upmarch (Z/d_i= -0.5) edge of the side duct. In the d_i/D_m=0.5 case, the main stream was deflected from this area by the incoming side duct fluid. For this case (d_i/D_m=I.0), however, the main duct fluid actually enters the side duct before joining the side fluid; together the combined flow then leaves the inlet duct. The magnitude of the main duct fluid velocity entering the side duct is small and it is therefore difficult to percieve in the figures.

Turning our attention of Figure 5.I7, (ω=I.0) it is seen that the trends described above for the ω=0.I case are apparent here also; only the magnitude of the velocities have changed. The infusion of main stream fluid into the side duct appears to be present only in the near wall region, panel (iv).

Figure 5.I8 presents a variety of vector plots in an (X-Y) cross-stream plane for momentum ratios of 0.I and I.0. The plots in (a) correspond to the same main duct axial location as those in the lower collection, (b).

From these plots, it is interesting to note the development of the vortex motion in the main duct. As the flow patterns in Figure 5.I8 are very similar, attention will be concentrated on the lower collection of plots; these are marked panel "b".

It is observed that in the first three plots, fluid enters the main duct from the side duct; the entering side duct fluid is parabolic in profile, that, upon meeting the main-

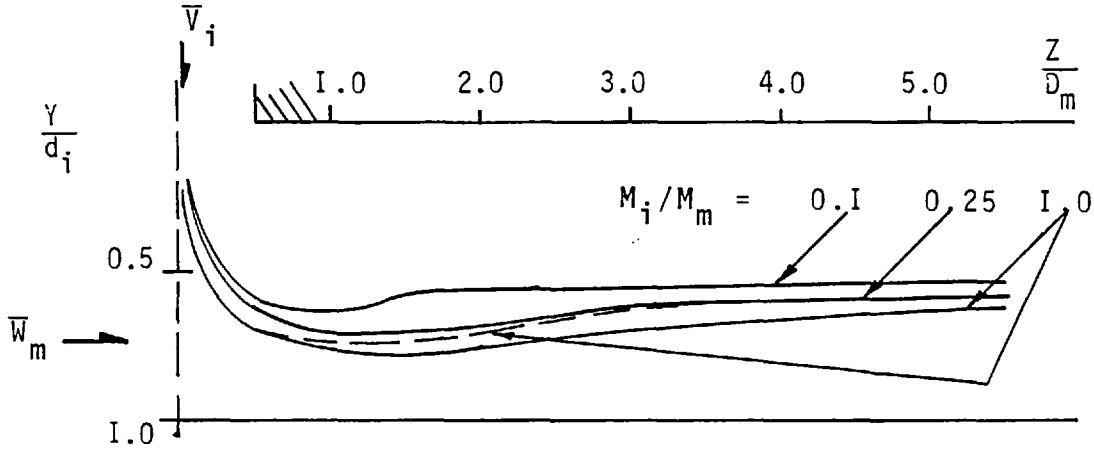

FIGURE 5.2I: VELOCITY TRAJECTORIES AS A FUNCTION OF MOMENTUM RATIO FOR $\frac{d_i}{D_m}$ = I.0

—— side duct, l_i/d_i = I.I

— — side duct, l_i/d_i = 0.0

stream, "fans" out in an attempt to fill the main duct. It would appear that it is this process that gives rise to the generation of the main duct vortex; the location of which is noticed to be next to the wall (the vertical wall, opposite to the symmetry plane). In plot (iv) this vortex is seen to move away from the wall; indeed, in the subsequent cross-streams that are presented, the vortex centre is observed to move towards the centre of the main duct. As the last plane of vectors shows, the cross-stream fluid motion is distributed quite uniformly across the duct; the strength of the vortex is also to observed to increase and then to decay with axial distance; this feature was noticed previously in the d_i/D_m = 0.5 situation. From the upper sequence of vector plots in Figure 5.I8, the fluid motions are all the same as that just described, but as is clearly noticeable, the magnitudes of the velocities are lower.

In Figure 5.I9 and 5.20 the main duct axial velocity profiles exhibit two noteworthy features. First, there is the gross disagreement in the magnitude, and indeed in some cases the direction of the flow predicted by the change in inlet duct boundary conditions. Differences in magnitude of up to 50% can be detected. The second feature is the "bulging" of the velocity profiles, particularly noticeable at Y/D_i = 0.25 of Figure 5.20; this bulging is a consequence of the cross-stream pressure gradients generated by the incoming side fluid.

5.4.5 THE VELOCITY TRAJECTORY

Figure 5.2I presents a plot of the inlet duct fluid velocity trajectories for

three momentum ratios in a tee-junction of diameter ratio of I.0. There is also presented, for comparison purposes, the trajectory for the ω = I.0 and l_i/d_i = 0.0 case.

From the figure, it is seen that the inlet fluid penetration increases with momentum ratio. The penetration is also seen to increase when an inlet duct of some length is used.

5.4.6 VELOCITY PROFILES IN THE PLANE OF THE JUNCTION

Figure 5.22 presents a computer-generated perspective view of the predicted velocity surfaces located in the junction region; the plots are presented in a manner similar to those presented for d_i/D_m = 0.5, (see Figure 5.I3), and are as such qualitative in nature.

The surfaces in Figure 5.22 do however, illustrate two features not seen previously. With a diameter ratio of one, the inlet fluid profile is almost two-dimensional: it is almost triangular in profile in the y-Z plane that persists from X/d_i = 0 to X/d_i = ± 0.5. The other feature is that the maximum velocity normal to plane of the junction decreases with increasing momentum ratio. Although not shown in the figure, the predictions for a momentum ratio of 0.25 predicted a maximum velocity ratio ($V_{MAX}/\overline{V}_i$) of 2.6I.

5.4.7 THE PRESSURE DISTRIBUTION

Figure 5.23 presents the predictions for the main duct axial pressure distribution; the curves represent pressures

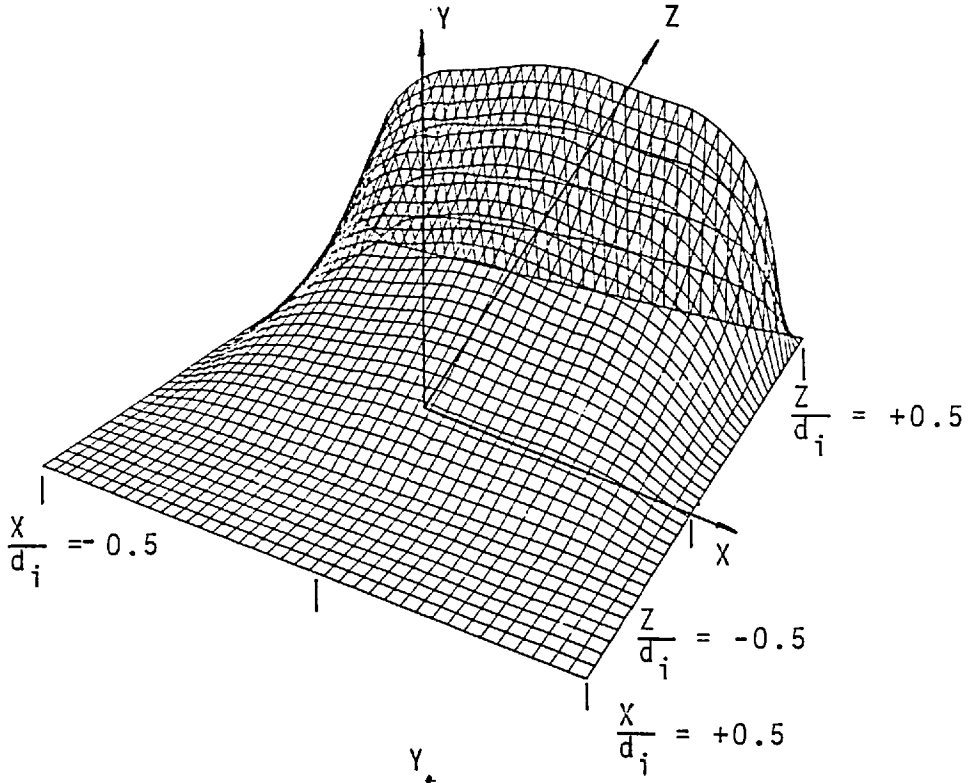

(a)

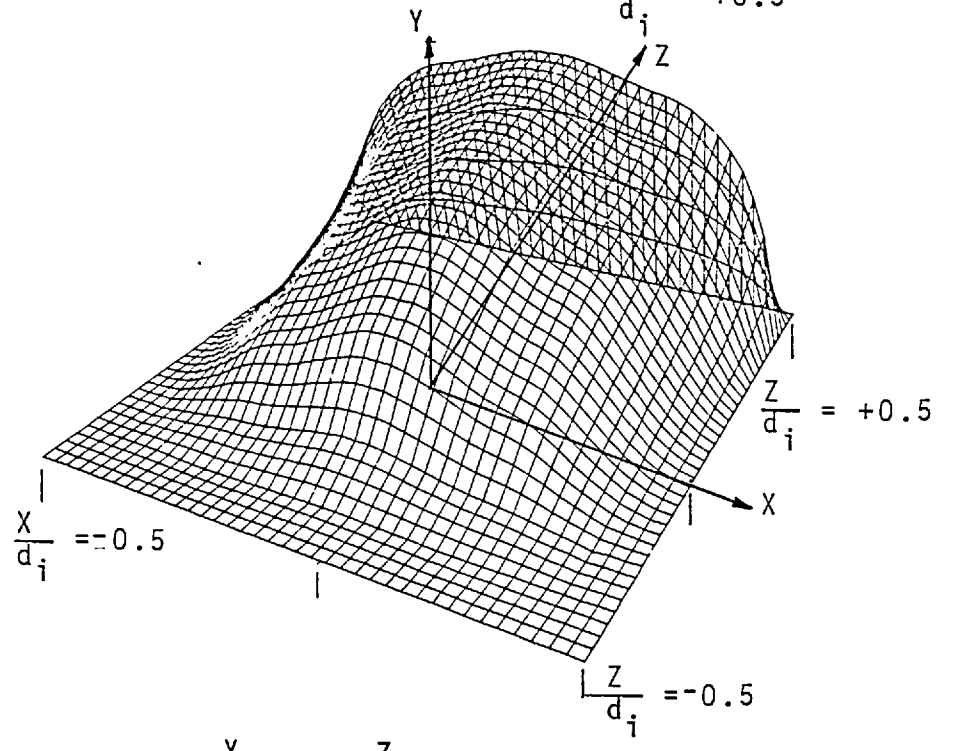

(b)

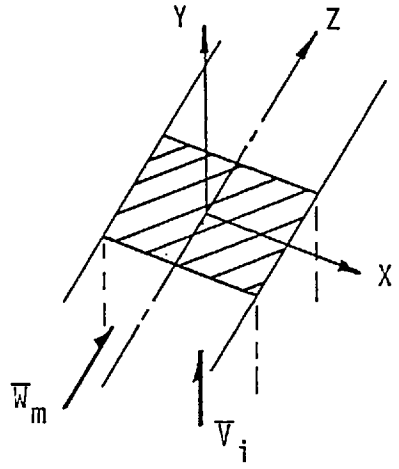

FIGURE 5.22:
VELOCITY SURFACE AT JUNCTION

(a) $\frac{d_i}{D_m}$ = I.0, $\frac{M_i}{M_m}$ = 0.I

$V_{max}/\overline{V}_i$ = 3.I7

(b) $\frac{d_i}{D_m}$ = I.0, $\frac{M_i}{M_m}$ = I.0

$V_{max}/\overline{V}_i$ = 2.47

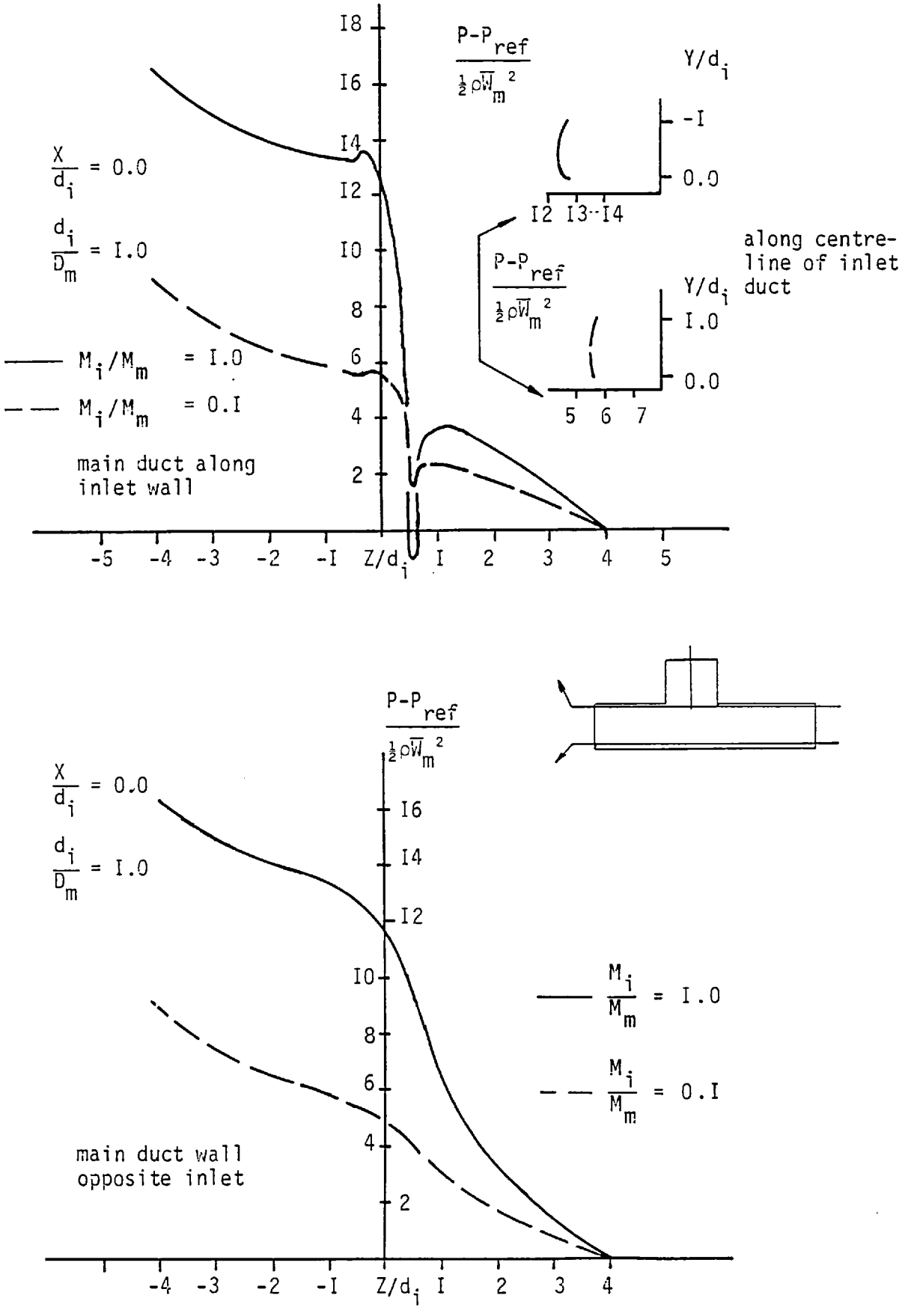

FIGURE 5.23: PRESSURE COEFFICIENT vs MAIN DUCT AXIAL DISTANCE FOR TWO MOMENTUM RATIOS

along the walls adjacent to the symmetry plane. The pressure gradient along the side duct centre-line is also presented.

By comparison with Figures 5.I4, it is seen that by increasing the diameter ratio has but a slight effect on the shape of the main duct axial pressure distribution. It is noticed, particularly for the $\frac{M_i}{M_m} = I.$ case that the predictions indicate that the pressure rise (at $Z/d_i = -I.0$) are transmitted further upstream (-ve Z direction) as the diameter ratio is increased. Additionally, it is observed that for a given momentum ratio, the overall pressure drop across the junction increases with diameter ratio.

5.5 SUMMARY OF THE CHAPTER

The previous sections of this Chapter presented some predictions of the laminar combing flow in tee-junctions. Two prediction procedures were used; a three-dimensional elliptic procedure, and a three-dimensional partially-elliptic procedure. In all the cases presented, the predictions obtained using these two procedures were found to be in very good agreement: a maximum discrepancy of about 3% between the predictions was noted; this error penalty may be acceptable in view of the potential storage savings (about 50%) incurred through the use of the partially-elliptic procedure. The computer time used by the proceduresw as about the same.

The predictions concentrated attention upon the flow in tee-junctions of two diameter ratios and up to three

momentum ratios. In the case of a diameter ratio of 0.5 and momentum ratio of 0.25, the predictions, employing various inlet duct boundary conditions were compared with available experimental data. The predictions showed varying levels of agreement with the data. It was found, however, that with the use of a side duct with a fully-developed velocity profile at its entrance produced the best agreement with the experimental data.

For a given diameter ratio, it was found that with an increase in momentum ratio there occurs the following trends: (i) an increase in the penetration of the side fluid into the main stream; (ii) an increase in the transmittal of pressure distrubances in the main duct upstream direction; (iii) an increase in the strength of the secondary motion of the fluid in regions downstream of the inlet duct; (iv) a decrease in the effects transmitted in the upstream direction of the side duct; and finally, (v) a decrease in the maximum velocity normal to the plane of the junction, but only for the di/Dm=I.0 case.

For a fixed momentum ratio, but with an increase in diameter ratio, the following trends are observed: (i) there is an increase in the transmittance of disturbances into the side duct; (ii) there is a decrease in the penetration of the side flow into the main stream; (iii) an increase in the pressure drop across the junction; (iv) an increase in the maximum velocity normal to the plane of the junction.

5.6 CONCLUDING REMARKS

The elliptic and partially-elliptic procedures have been successfully applied to predict the laminar flow in tee-junctions of square cross-section.

CHAPTER 6: TURBULENT FLOW PREDICTIONS

6.1 INTRODUCTION

The object of this Chapter is to assess the ability of both prediction procedures, presented in Chapter 3, to predict the tubulent flow and heat and mass transfer in tee-junctions of round cross-section.

The predictions reported here are for the case of inlet fluid (in the "vertical" duct) entering and dividing uniformly within the "horizontal" duct that makes up the other two legs of the junction. The predictions are compared against the experimental data obtained during the course of the present investigation; furthermore, other heat transfer predictions are presented whose purpose is to increase the scope of the investigation.

From the previous chapter, it will be recalled that up to 28,000 grid points per dependent variable were used to obtain laminar flow solutions. These solutions were substantially grid independent, and both procedures used the same amount of computer storage (this is in keeping with the objectives in Section I.2.I). For turbulent flow, the storage requirements almost double, which, from an economic standpoint, restricts severely the maximum size of grid one can use*.

Therefore, grid independence tests of the order described in Chapter 5, have not been performed for the predictions presented here. Two grid densities are used: a coarse

---

*FOOTNOTE:
Indeed, it is precisely for this reason that the partially-elliptic procedure shows its true potential.

(θ(I5), R(I5), Z(30) or 6750 grid points) and a fine (θ(23), R(24), Z(30) or I6560 grid points). Of course, results based on two tests are inconclusive; but, by increasing the grid size by a factor of $2\frac{1}{2}$, the variations in the results have been found on average not to change by more than about I0% (see Section 6.5).

6.2 OUTLINE OF THE CHAPTER

The remaining sections of this Chapter are six. In Section 6.3, the physical situation, as a reminder, is presented; thereafter the computational aspects are attended to. In the next section, Section 6.4, the general flow patterns are presented using vector plots and other methods. This is followed, in Section 6.5, by comparing the predictions obtained by using both numerical procedures, to the experimental data of Chapter 4. In Section 6.6, the heat transfer predictions are extended to observe the effects of heating the whole junction. In Section 6.7, a brief discussion is made regarding the predictions. Finally, in Section 6.8, a summary of the chapter is outlined together with some concluding remarks.

6.3 THE FLOW SITUATION AND SOME COMPUTATIONAL DETAILS

6.3.I THE PHYSICAL SITUATION

To serve as a reminder of the physical situation attended to in the present experimental investigation, Figure 6.I is provided. The tee-junction is composed of a "horizontal" pipe of diameter D, to which is butted a wedge-shaped inlet duct. Fluid enters the junction via the inlet duct,

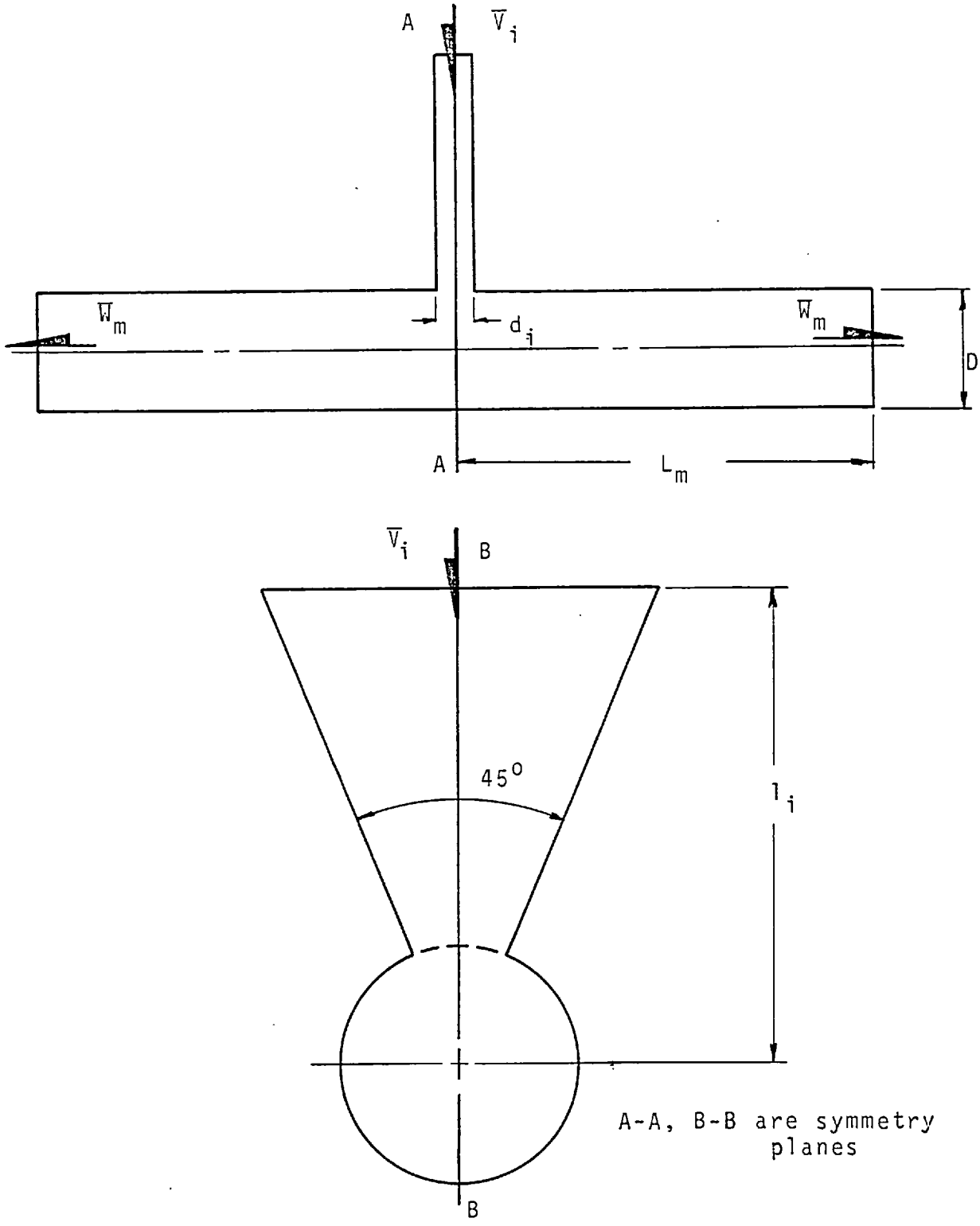

FIGURE 6.I: THE PHYSICAL SITUATION CONSIDERED - CORRESPONDING TO THE PRESENT EXPERIMENTAL SITUATION

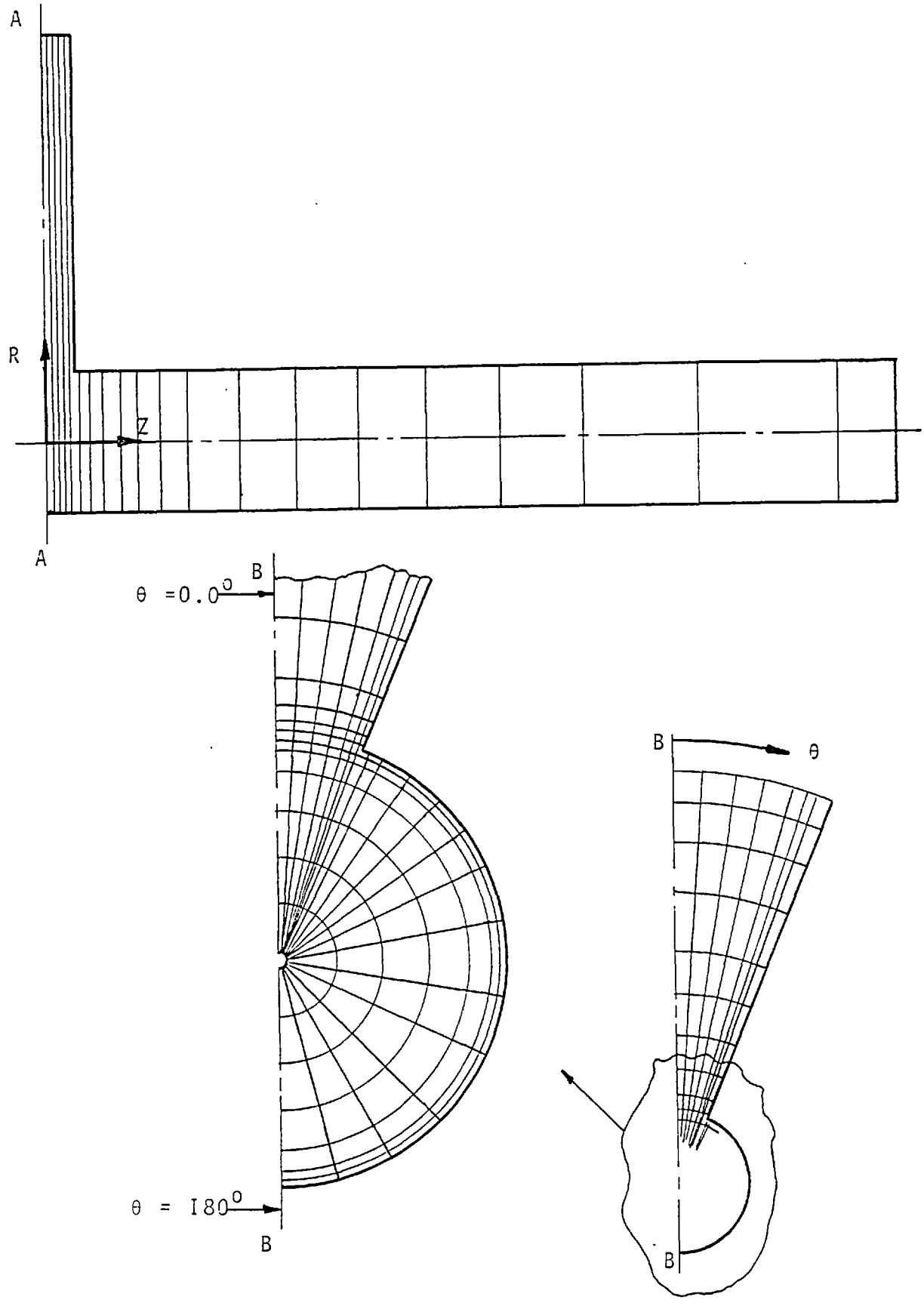

A-A, B-B are symmetry planes

FIGURE 6.2: FINITE-DIFFERENCE GRID ARRANGEMENT

and divides uniformly between the horizontal legs; this produces a split ratio of one. It is noticed that this flow situation is symmetric about those planes indicated in Figure 6.I, thereby allowing computations to be performed in only one-quarter of the geometry illustrated.

6.3.2 THE COMPUTATIONAL GRID

A quarter section of the geometry shown in Figure 6.I is overlaid with a finite-difference grid as shown in Figure 6.2. The grid is a non-uniform one, with more grid points being located in those regions where gradients of the dependent variables are expected to be large, e.g. near walls. The actual fine grid distribution may be deduced from the vector plots, to be presented shortly.

6.3.3 THE INLET AND BOUNDARY CONDITIONS

From Figure 6.2, it will be noticed that the finite-difference grid features three symmetry-planes. At these planes, normal gradients of the variables are set to zero, except for the normal velocity, which are prescribed to be zero. At the walls, the wall functions, outlined in Chapter 2, are used. The exit boundary condition is specified to be of a zero gradient type for all variables except for the cross-stream velocities, whose values are set instead to zero. The exit condition is discussed further in Section 6.7.

The predictions presume that the flow is of uniform density

and of constant properties*. Therefore, the energy equation may be treated separately once the aerodynamic field has been obtained; (i.e. the equations are "uncoupled"). The other boundary conditions are stated below in view of this uncoupling.

(a) Aerodynamics

At the entrance to the inlet duct, a uniform velocity field is imposed. This does not correspond exactly to the experimental situation as a quick glance at Figure 4.II will reveal. However, this slight discrepancy is not expected to affect the predictions because of the relatively large aspect ratio of the inlet duct (i.e. about 5.I)† . The turbulence field was specified to be uniform also.

The specific values of the inlet values of the velocities and turbulence quantities are given below. They are:

$$\begin{aligned} V &= \overline{V}_i \cos(\theta) \\ U &= \overline{V}_i \sin(\theta) \\ k &= 0.005\ \overline{V}_i^{\,2} \\ \varepsilon &= 0.062\ \overline{V}_i^{\,3/2} \end{aligned} \qquad (6.I)$$

where θ is measured positive from the plane of the junction. The constants appearing in the values for k and ε

FOOTNOTES:

*This restriction is not really necessary; the two procedures incorporate the machinery necessary to take account of both variable properties and density.

†It may be argued here that if the known boundary condition is not used, why use an inlet duct? The answer is that guidance is available to set the inlet condition at the start of the inlet duct, but such guidance is not available at the junction of the two ducts.

take cognisance of the inlet duct width.

(b) Heat/Mass- Transfer

Once the aerodynamic field has been calculated, it is but a simple matter to calculate the heat/mass transfer at the walls of the junction. Remembering that a constant wall temperature is analogous to a constant wall concentration, the boundary conditions for calculating the heat transfer are:

$$\begin{aligned} T_{in} &= T_{wall} = \text{Constant, say } C_1 \\ T_{i,j} &= \text{Constant, say } C_2 \end{aligned} \qquad (6.2)$$

where T_{in} and T_{wall} are the air and junction wall temperatures respectively. $T_{i,j}$ is the temperature of the junction wall at the locations i and j that correspond to the axial and circumferential locations of the naphthalene plugs in the experimental investigation (see Section 4.2.2).

As mentioned in Chapter 4 (Section 4.3.3), the naphthalene plugs were positioned at different axial locations (while maintaining an angular symmetry of the plugs) until the test section had been traversed ($1 \leqslant \frac{Z}{D} \leqslant 5$). The predictions followed the same procedure, thereby requiring one solution of the energy equation for the whole domain for each change in the location of the "plugs". In this manner the heat-transfer coefficient distribution is related to the mass transfer coefficient distribution via:

$$h(\theta) = \frac{\dot{q}''}{T_{in} - T_{i,j}} \qquad (6.3)$$

which, it will be recalled, is directly analogous to the mass transfer coefficient $h(\theta)$ defined in Section 4.5.3 (equation 4.2). The heat flux is calculated from the wall functions described in Chapter 2. That the wall functions of Chapter 2 are applicable for comparing the heat transfer predictions with the experimental mass transfer, is confirmed by noting that the laminar Prandtl and Schmidt numbers (i.e. σ_ϕ) for air and naphthalene respectively, are about the same. Also, since a very small amount of naphthalene is sublimated away from the plugs (as shown in the experimental chapter), the properties of the air should be altered very little.

6.3.4 THE COMPUTATIONAL COST

By using the "elliptic" procedure for the physical situation attended to in this Section, the fine grid predictions required about I,050,000 bytes of storage on an IBM 360/I95 computer. To obtain solutions that satisfied the convergence criteria of Section 3.9.I required the expenditure of about I½ hours of IBM 360 computer time. This large amount of time was due to the extremes in flow conditions that exist within the tee-junction; moreover, certain adjustments to the code, such as optimization of the under-relaxation factors, that may result in increased convergence rates, were not carried out. By contrast, the coarse grid predictions required only about 30 minutes to reach the same level of convergence.

The large computer resources required by the elliptic procedure can be seen to be lowered by reference to the

costs associated with using the partially-elliptic procedure. The fine grid predictions would have used only about 550,000 bytes of storage, or just over half the elliptic procedure's requirments. Alas, the computer time required was about the same because the residuals of the equations (Section 3.9.I) in the "elliptic" region of the partially-elliptic domain governed whether the convergence criteria had been satisfied.

In solving the energy equation, the computational cost was minimal; times of less than one minute being required to satisfy the convergence criteria.

6.4 THE GENERAL FLOW PATTERN

Here the fine-grid predictions, obtained by using the "elliptic" version of the calculation procedure, are displayed through the use of vector plots; in addition to these plots, and as a flow visualisation aid, several views of streamlines are presented*. The predictions correspond to the experimental flow situation outlined in Chapter 4. The Reynolds number in the horizontal leg is 26,700, which is just slightly below the average experimental Reynolds number of 27,600.

Figure 6.3 presents vector plots located in various R-Z planes; the actual orientation of which, relative to the $\theta=0^{o}$ location (see Figure 6.2), is shown on each figure.

---

*FOOTNOTE:
These streamlines are based on the coarse grid data because of computer storage limitations.

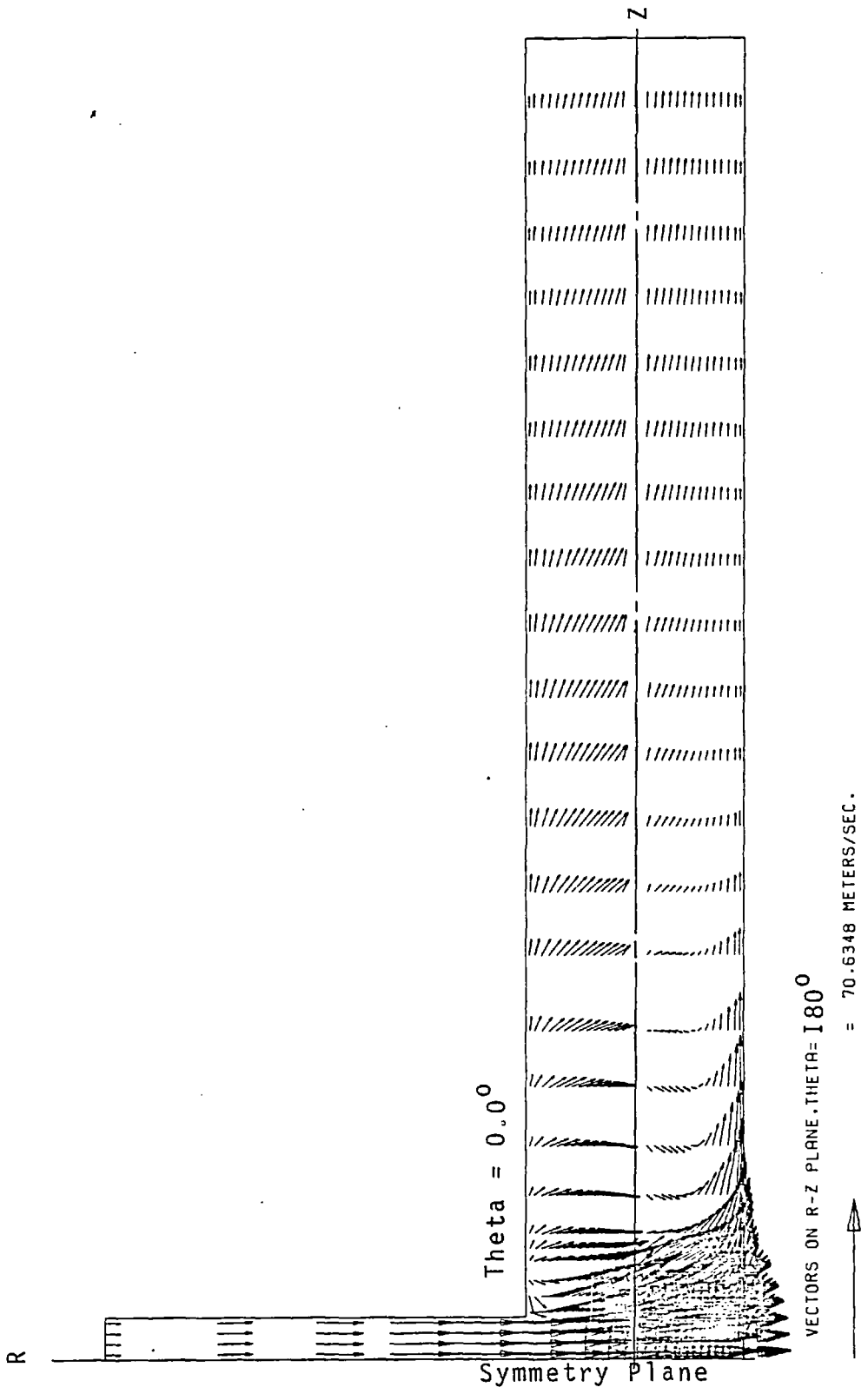

FIGURE 6.3(i): VECTORS ON DIAMETRAL R-Z PLANES

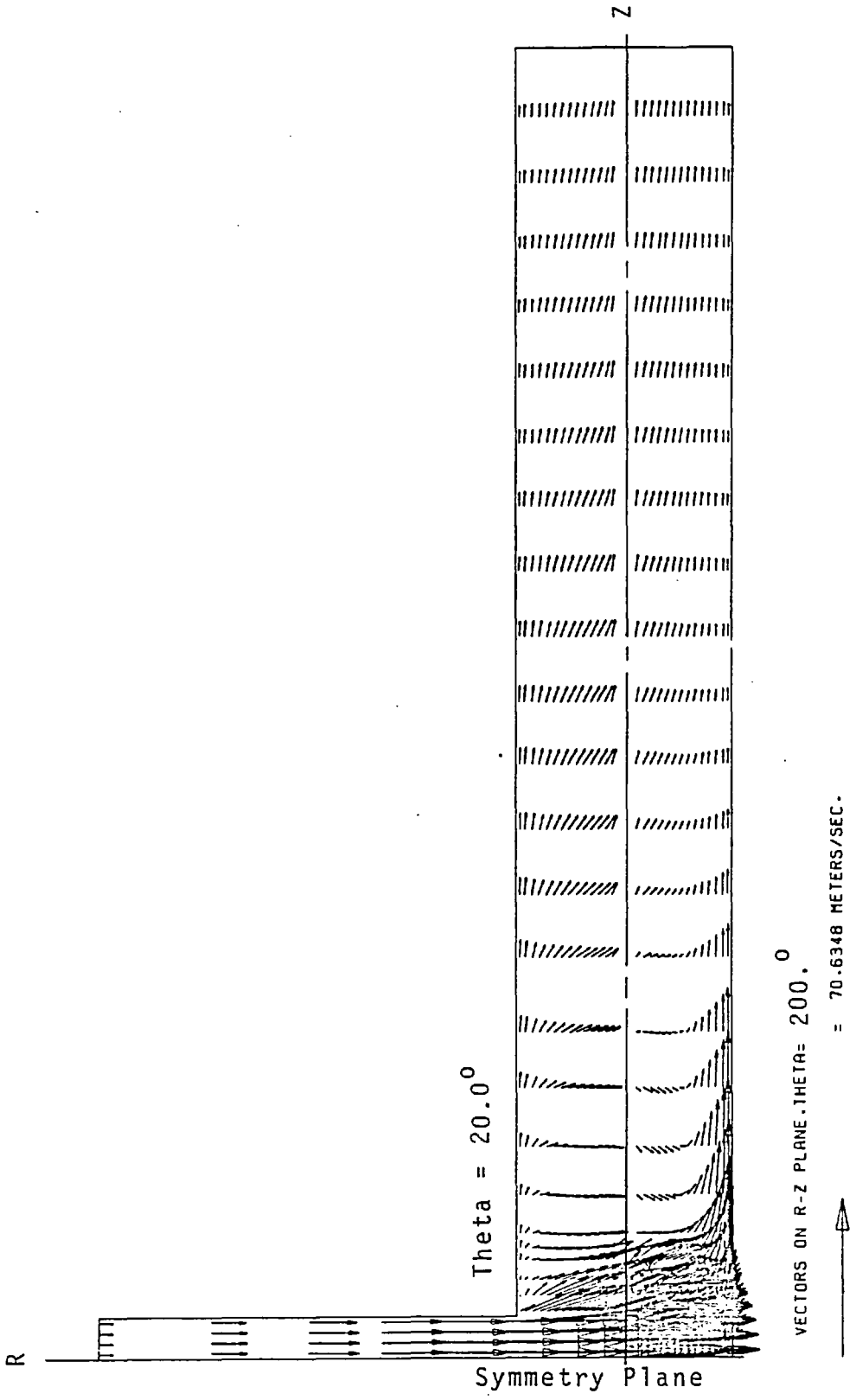

FIGURE 6.3(ii): VECTORS ON DIAMETRAL R-Z PLANE

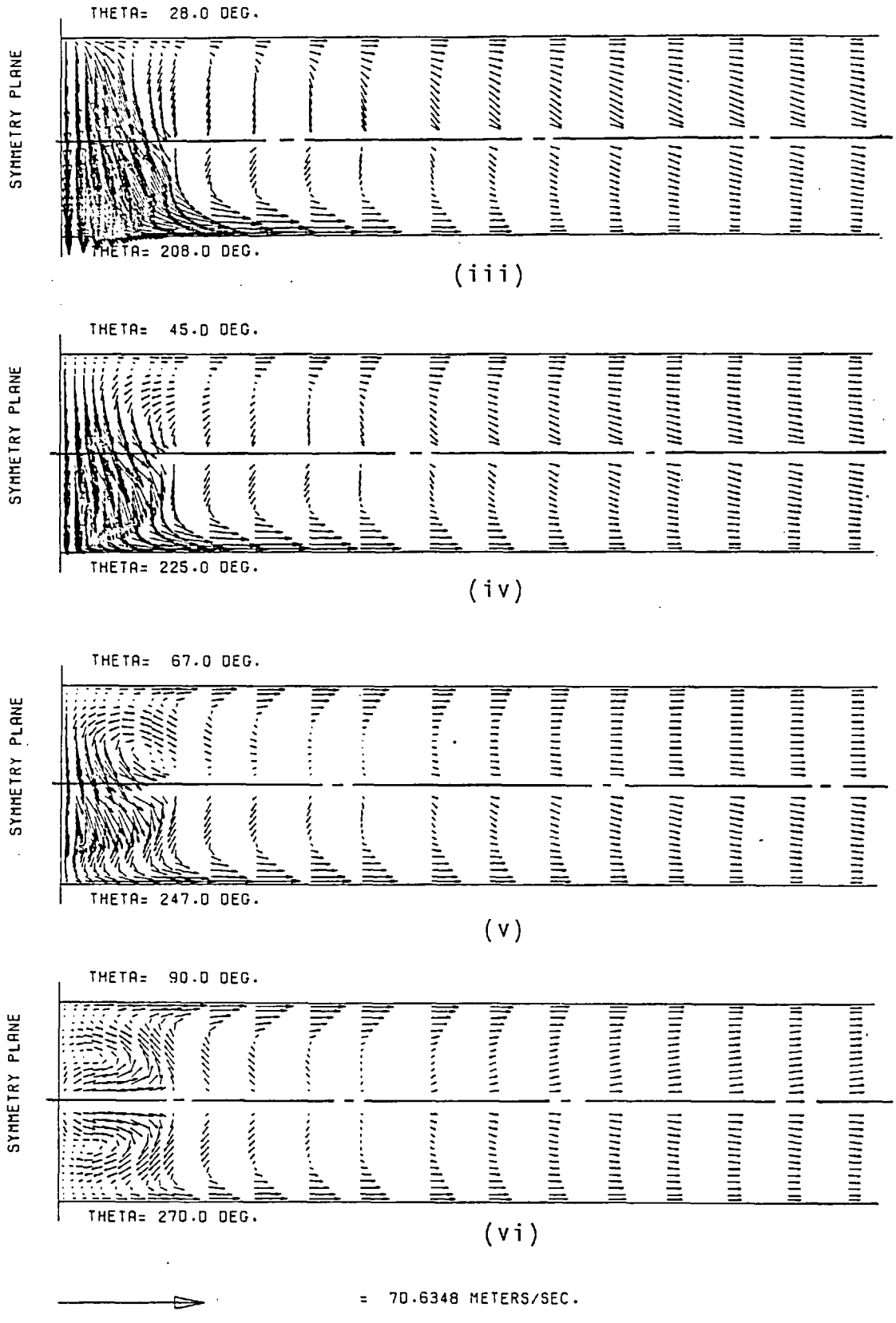

FIGURE 6.3: VECTORS ON DIAMETRAL R-Z PLANE
(Continued)

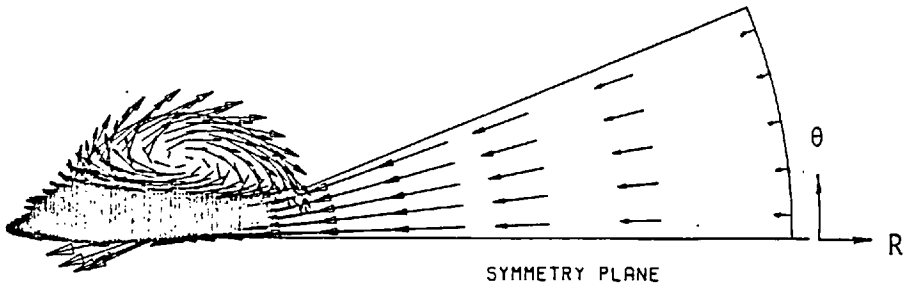

SYMMETRY PLANE

VECTORS ON R-THETA PLANE Z/D= .0

= 70.6348 METERS/SEC.

(i)

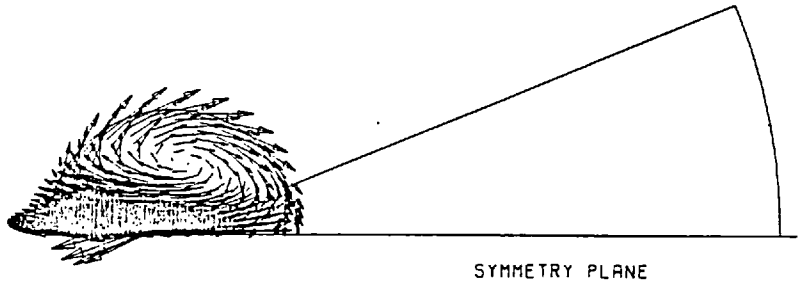

SYMMETRY PLANE

VECTORS ON R-THETA PLANE Z/D= .21

= 70.6348 METERS/SEC.

(ii)

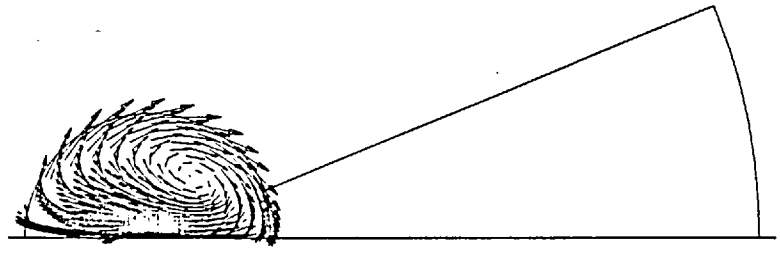

SYMMETRY PLANE

VECTORS ON R-THETA PLANE Z/D= .45

= 70.6348 METERS/SEC.

(iii)

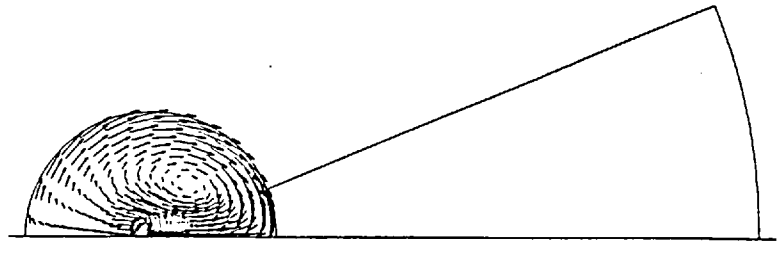

SYMMETRY PLANE

VECTORS ON R-THETA PLANE Z/D= .98

= 70.6348 METERS/SEC.

(iv)

FIGURE 6.4: VECTORS ON AXIAL (CROSS-STREAM) R - θ PLANES

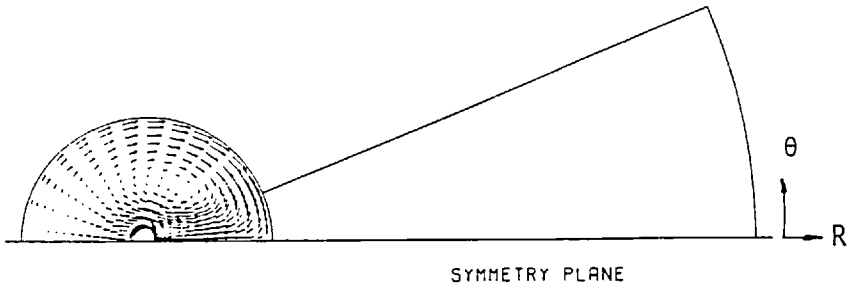

SYMMETRY PLANE

VECTORS ON R-THETA PLANE Z/D= 2.1

= 70.6348 METERS/SEC.

(i)

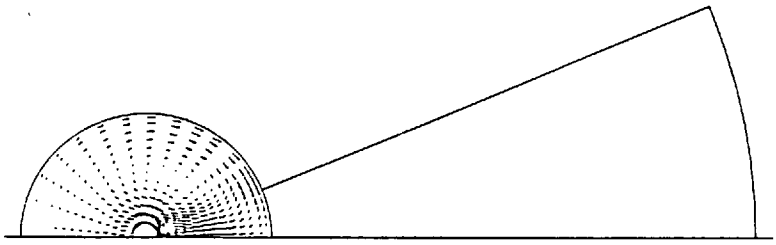

SYMMETRY PLANE

VECTORS ON R-THETA PLANE Z/D= 3.3

= 70.6348 METERS/SEC.

(ii)

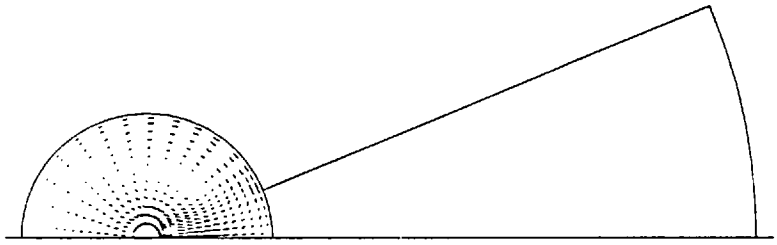

SYMMETRY PLANE

VECTORS ON R-THETA PLANE Z/D= 4.0

= 70.6348 METERS/SEC.

(iii)

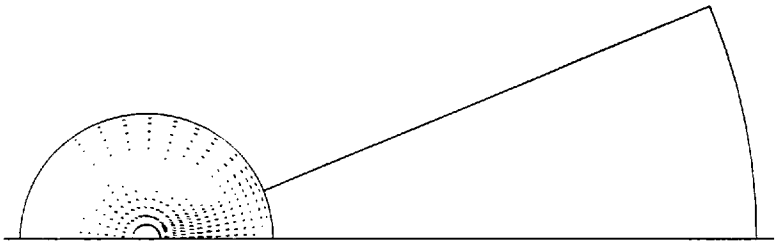

SYMMETRY PLANE

VECTORS ON R-THETA PLANE Z/D= 4.6

= 70.6348 METERS/SEC.

(iv)

FIGURE 6.4: VECTORS ON AXIAL (CROSS-STREAM) (Contined) R - θ PLANES

Note that each figure presents a diametral plane of vectors. Figure 6.4 presents, on the other hand, cross-stream vector-plots, at various horizontal leg axial locations.

In Figure 6.3, and concentrating attention upon panel(i) in particular, fluid is observed to enter the tee via the inlet duct, located on the left-hand side of the horizontal pipe. The inlet fluid is seen to accelerate as it nears the junction itself; this is, of course, a consequence of the inlet duct which, it will be recalled, is of a wedge shape. Upon leaving the inlet duct, the inlet fluid expands and impinges on the wall opposite the inlet. The large pressures generated in the impingement region (as will be seen shortly) force the fluid away from the junction, apparently along the lower protion of the leg. However, as a quick glance at Figure 6.4 will reveal, the impingement deflects fluid in a circumferential direction as well. Indeed, at small $X/D(\leq 2)$, fluid is transported largely in this direction rather than axially.

The relatively low pressures situated in the upper half of the main pipe (as will be seen shortly), particularly near the corner of the main and inlet ducts, gives rise to a region of axially reversed flow. This negative flow is seen to feed the inlet fluid. The region of reversed flow in the upper half of the leg is also observed to be quite short. This, it is believed, is a consequence of the recirculation zone existing in the lower half of the horizontal pipe.

The recirculation zone in the lower half of the horizontal duct feeds the fluid eminating (and expanding) from the impingement region. The fluid from the impingement region travels circumferentially near the wall of the pipe, and it is this fluid that is drawn into the recirculation region; this is particularly noticeable at about X/D=I. Once the fluid clears this region of reversed flow, it is seen to flow towards the main duct centre-line in an attempt to produce flow of a more uniform character.

Attention is now focussed on the other panels in Figure 6.3. Note that panels (iii) to (vi) have been cropped for spatial economy. The flow features two recirculation zones (particularly noticeable in panels (iv) and (vi)); the first is an extension of the one located in the lower portion of the horizontal leg; this has been previously referred to. The other is seen to exist midway between the horizontal centre-line and the wall of the pipe, at the Z/D=0.25 position (approximately). This latter recirculation zone is, in fact, composed of fluid with a velocity component directed normally to the plane of recirculation (i.e. a helical motion); this motion is a result of the inlet fluid entraining fluid from a region located between, but parallel to the inlet duct centre-line and the wall of the main pipe.

Turning attention now to Figure 6.4, the sequence of cross-stream plots of vectors show the development of the "helical" motion of the fluid in the horizontal leg. The

plot is situated at Z/D=0.0 (i.e. a plane within the inlet duct). The large concentration of vectors along the symmetry plane is because of the high grid density used in this region.

From the sequence of cross-stream plots, the vortex centre and strength are seen to change with distance downstream of the inlet duct centre-line. Indeed, the vortex centre begins(panel(i)) at about θ=90 and moves in the negative angular and radial directions (i.e. towards the symmetry plane and centre of the leg respectively). At about Z/D=I, the centre then moves back towards its original position. The vortex strength is seen to diminish with increasing Z/D. This feature is different from the laminar flow in a square tee-junction (Chapter 5) where, it will be recalled, the vortex strength first increased and then decreased with distance downstream of the inlet.

In Figure 6.5, there is presented various perspective and orthogonal views of "particle-tracks" or streamlines. These streamlines are generated by introducing a mass-less particle into the calculation domain and the resulting motion is plotted*. It is important to note here that the coarse grid predictions have been used to generate these plots and that the whole calculation domain has not been used; in fact, the inlet duct has been removed, together with over half of the original length of the pipe, i.e. L=I.5D. This restriction is imposed by the computer

*FOOTNOTE:
The computer program used for this purpose is called "GRAFFIC", Mallinson (I977). Additional information can be found in Majumdar and Pollard (I977).

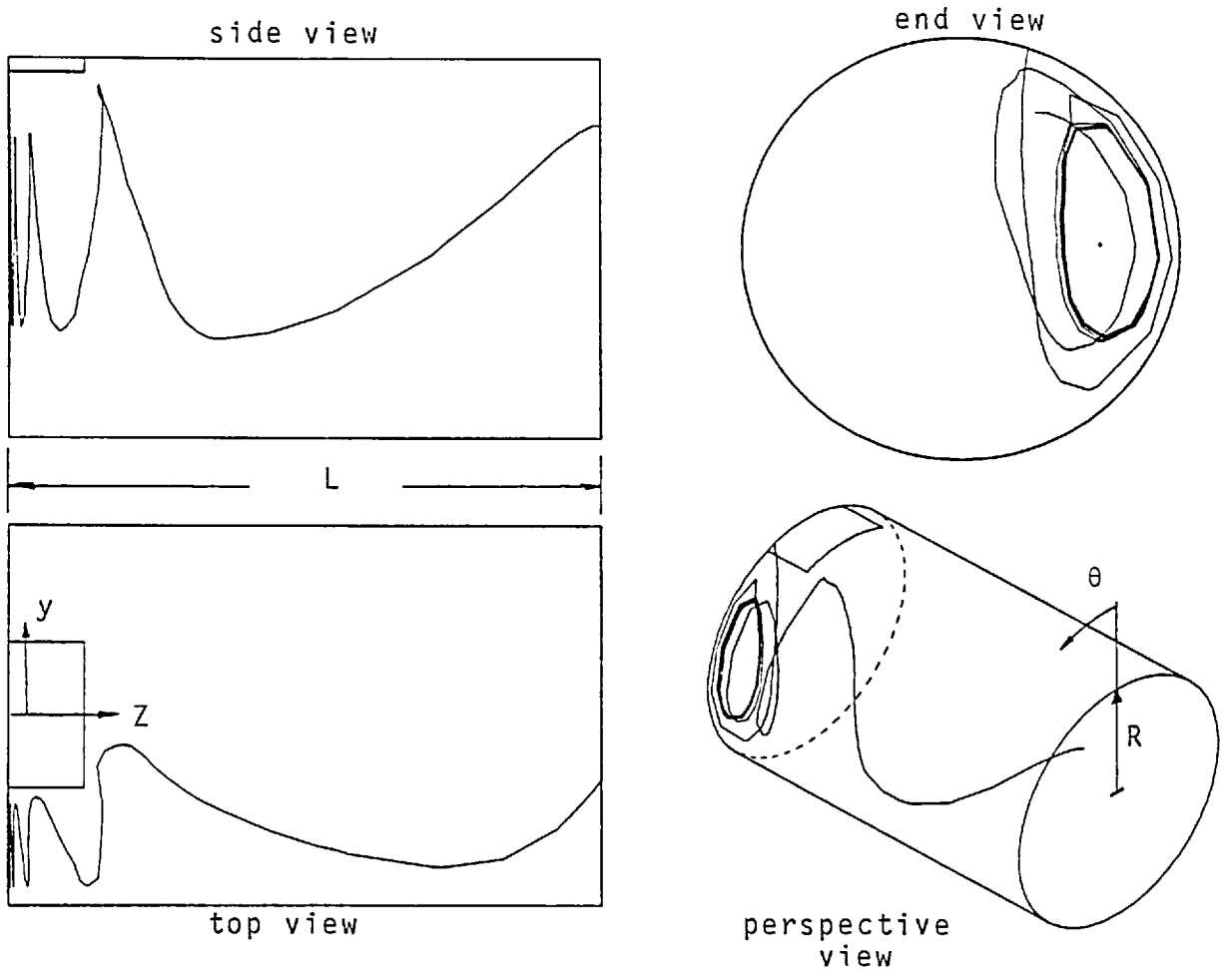

FIGURE 6.5a: VIEWS OF A STREAMLINE: PARTICLE RELEASED AT Z/L(0), y/R(I), θ(I8^{o})

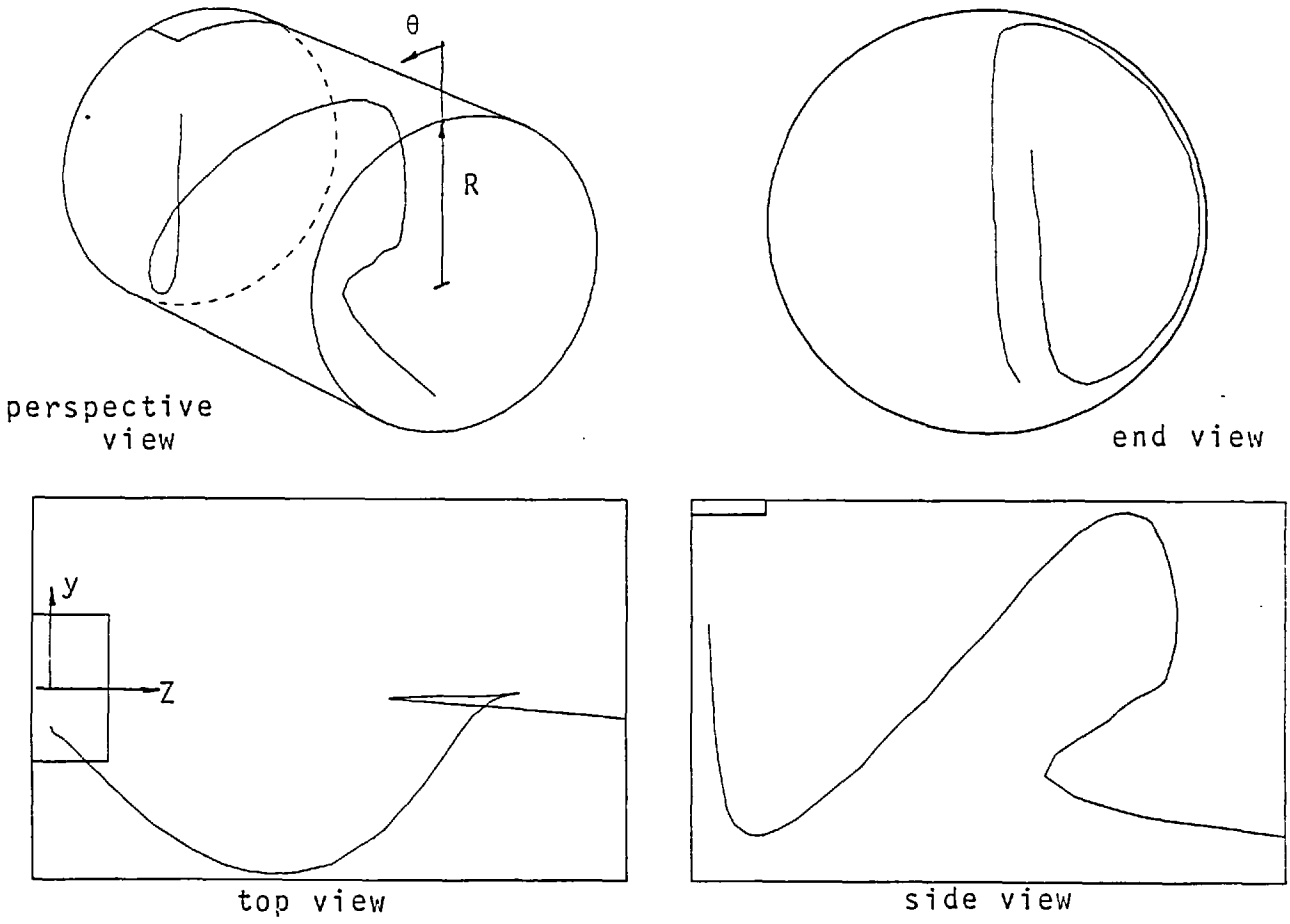

FIGURE 6.5b: VIEWS OF STREAMLINE: PARTICLE RELEASED AT Z/L(0.03), y/R(0.4), θ(.45)

system. In the figures, the inlet duct is depicted by those lines surrounding the Y-Z co-ordinate axis lines.

In Figure 6.5a, the track resulting from a particle released at Z/L=0, y/R=I and θ=I8^{o} is shown in various orthogonal views. The streamline indicates clearly the helical motion of the fluid in the horizontal leg.

In Figure 6.5b, a particle track originating at Z/L=0.03, y/R=0.04 and θ=45^{o} is shown. The distinguishing feature of this streamline is that the particle first follows the helical motion of the fluid observed in 6.5a, but is then drawn down into the recirculating zone located at the bottom of the pipe. Thereafter, the particle gets caught by the high velocity flow near the lower wall of the pipe which carries it in the downstream (down march) direction.

From the above presentation, it is clear that the flow in this particular tee-junction is different from that observed by Pollard et al (I977a). Here the recirculating zone is seen to be located towards the bottom of the pipe, while Pollard et al (I977a) show it to be located at the top. This difference could be due to either the different inlet sizes, or possibly, because Pollard et al (I977a) assumed the inlet duct conditions.

6.5 COMPARISON WITH EXPERIMENTAL DATA

In this Section, the predictions are compared to the experimental data. The predictions are obtained by using two finite-difference grid densities, the results obtained by using these grids are indicated in the figures.

The fine grid predictions (23x24x30) presented, correspond to those predictions obtained by using both the elliptic and the partially-elliptic procedures. Only in those regions where the predictions differ by more than 5% is reference made to specific procedures.

6.5.I THE SURFACE STATIC PRESSURE DISTRIBUTION

In Figures 6.6, 6.7 and 6.8, the surface pressures are compared to the experimental data. Figure 6.6 presents the pressures on the walls of the inlet duct, while Figures 6.7 and 6.8 present a comparison of the pressures on the walls of the main pipe. Note that for the comparisons, the reference pressure point has been changed from that referred to previously in Section 4.4.4, to the position indicated in Figure 6.6.

In Figure 6.6 the comparison between the predictions and the experimental data is seen to be good.

In Figure 6.7, the predictions show a moderate disagreement with the data in the near junction region, but as the junction region is left, the agreement is seen to improve. Indeed, a glance at Figure 6.8 shows that at Z/D>3, the

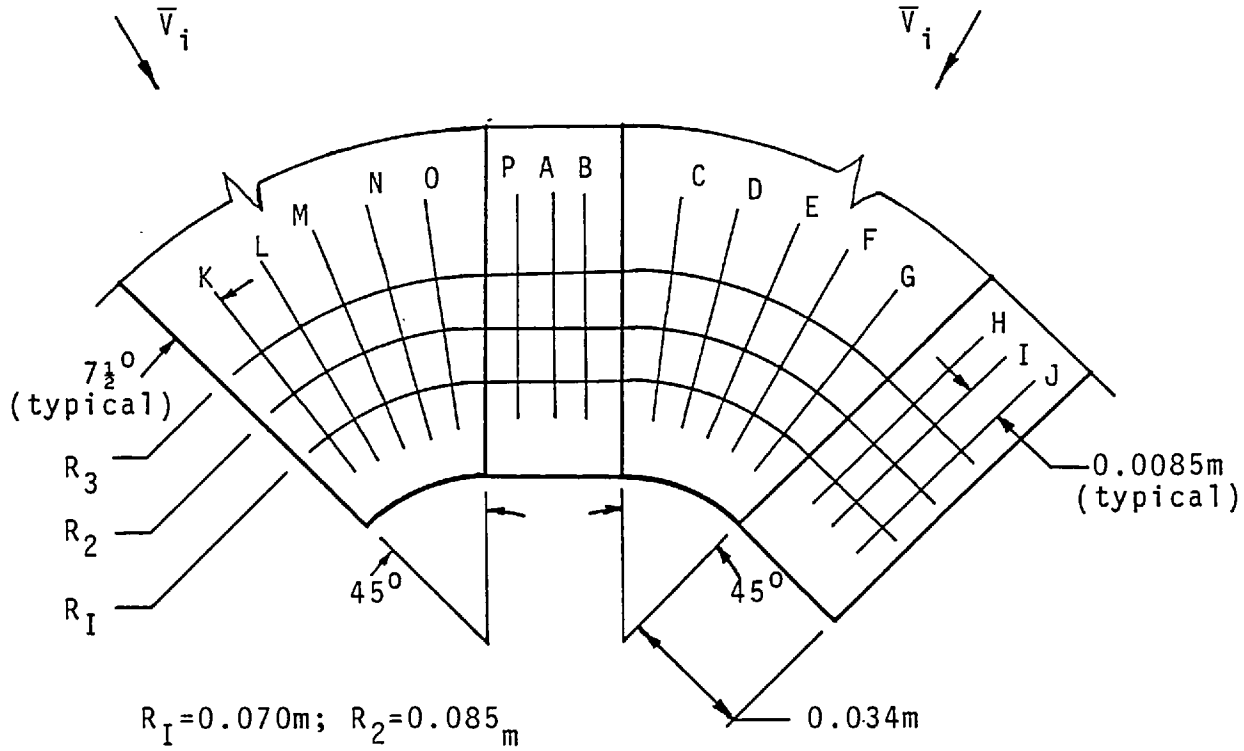

A-R_3 - LOCATION OF P_{ref}

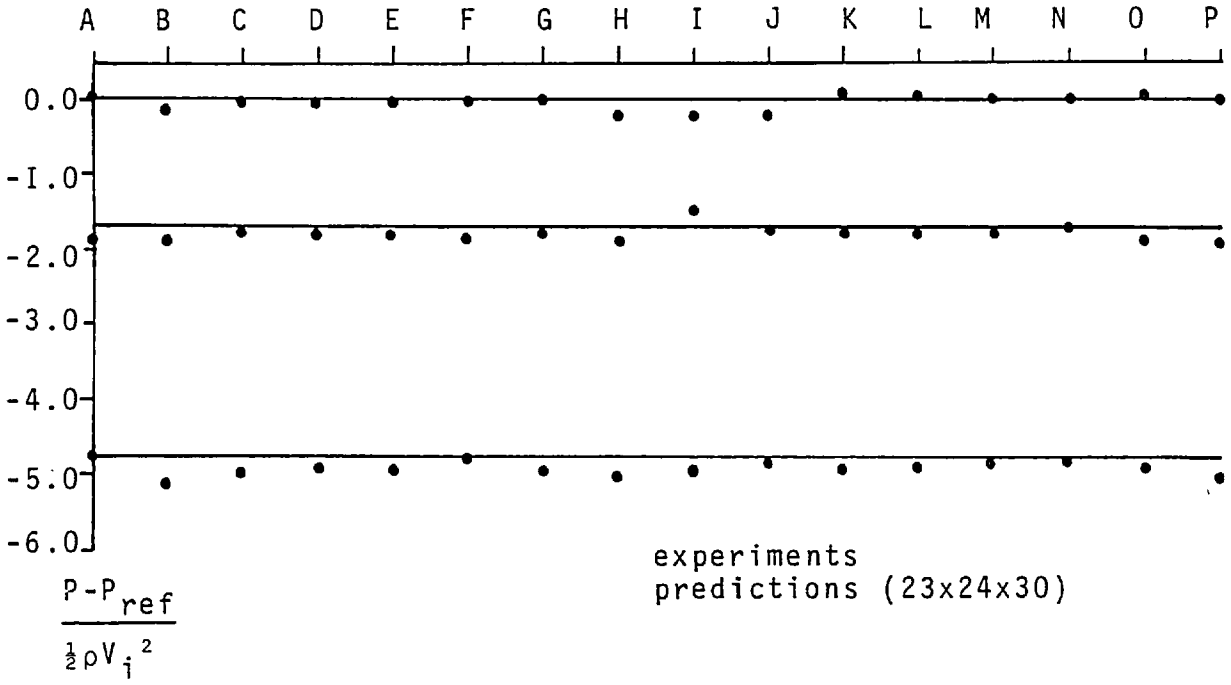

FIGURE 6.6: COMPARISON OF DATA WITH PREDICTIONS FOR PRESSURE DISTRIBUTION IN THE INLET DUCT

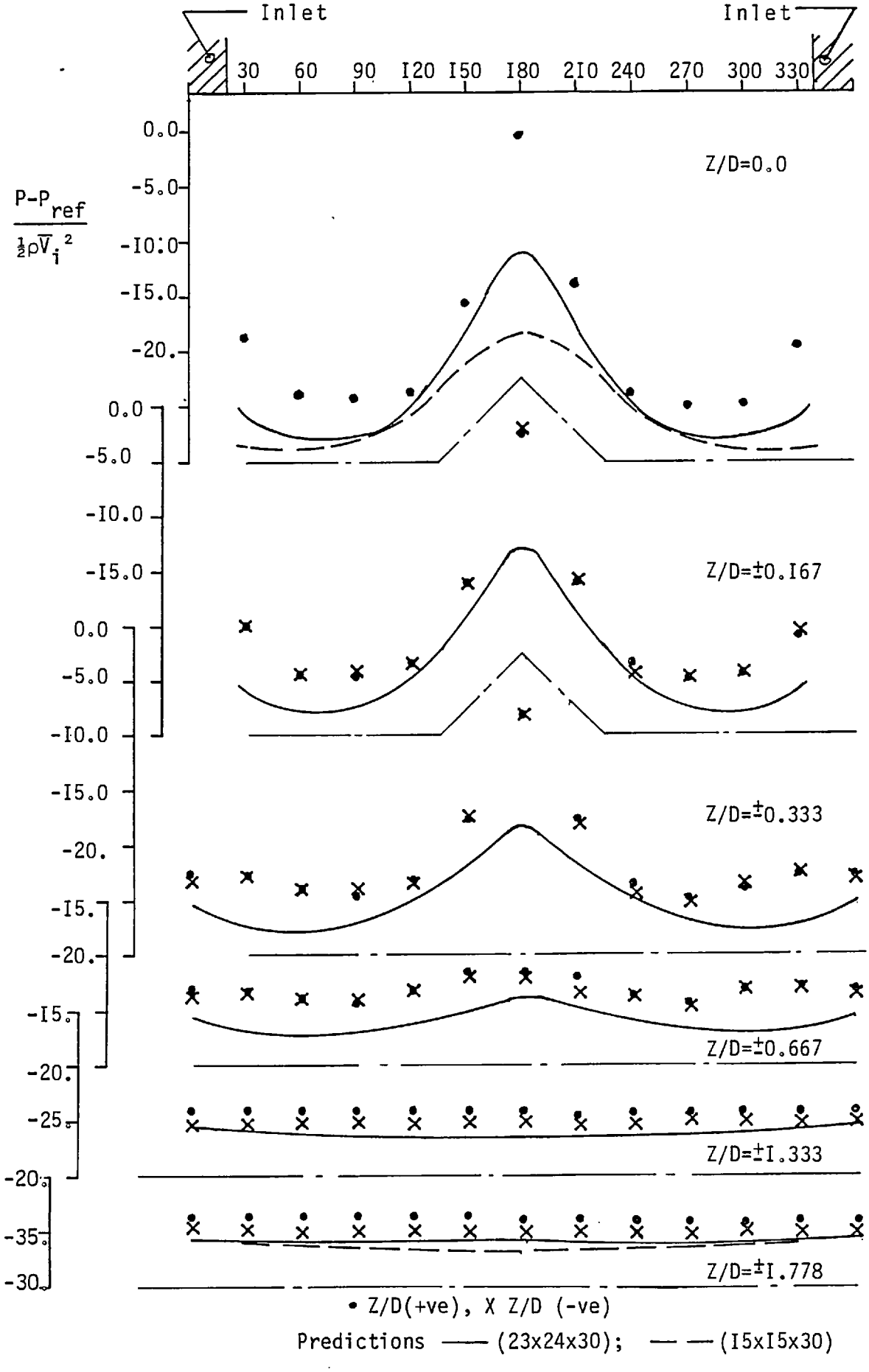

FIGURE 6.7: CIRCUMFERENTIAL WALL PRESSURE VARIATION AS A FUNCTION OF AXIAL DISTANCE DOWNSTREAM OF INLET DUCT CENTRE-LINE

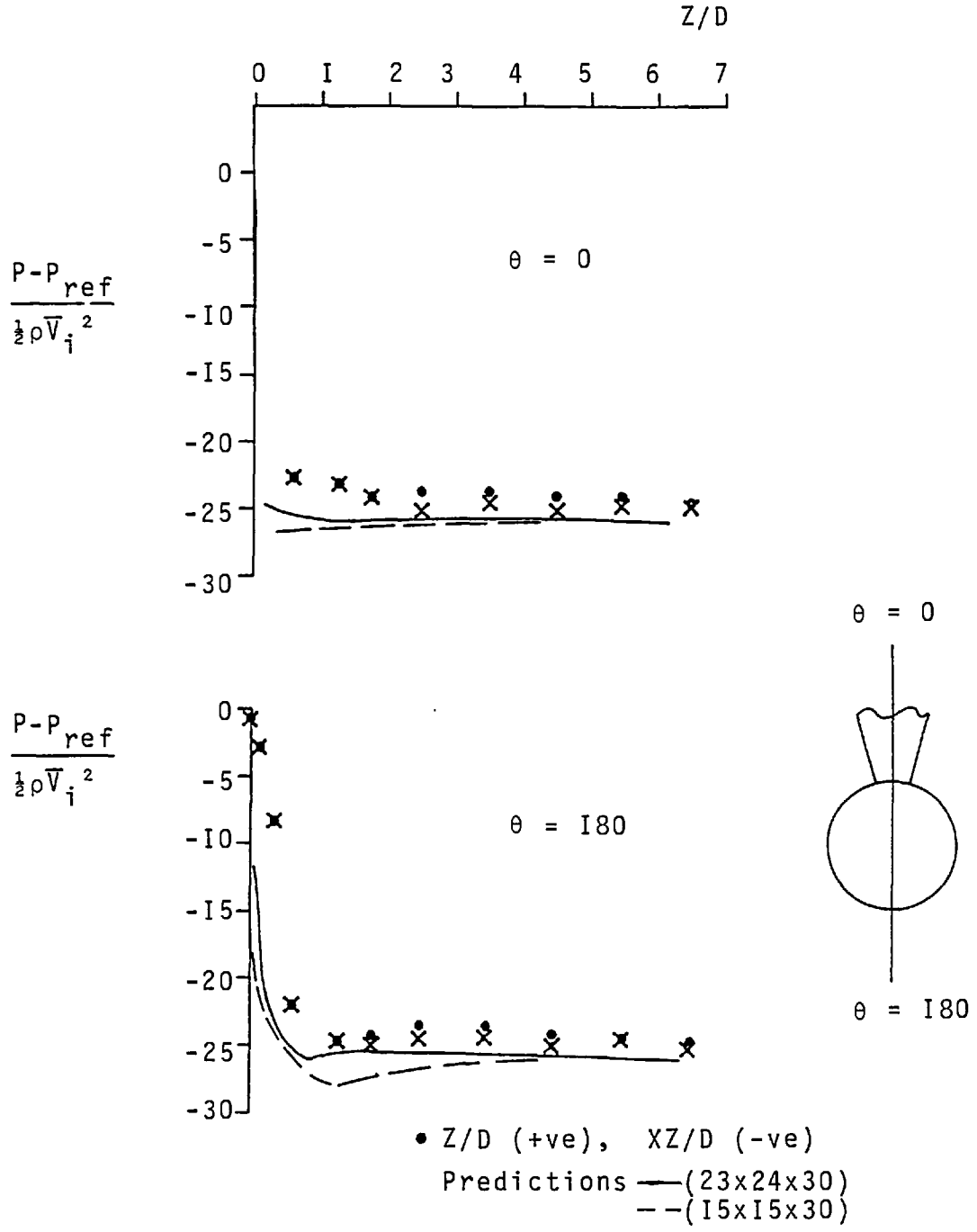

FIGURE 6.8: LONGITUDINAL WALL PRESSURE VARIATION IN MAIN LEGS DOWNSTREAM OF INLET DUCT CENTRE-LINE

predicted axial pressure gradient is seen to be in good agreement with the experimental data.

6.5.2 THE VELOCITY FIELD

In Figures 6.9 to 6.I3, the predicted velocity fields are compared with the experimental data. Specifically, Figures 6.9 to 6.I2 compare the axial profiles of velocity, while Figure 6.I3 compares at two axial locations, the velocities located on a diametral plane normal to the inlet duct axis. The orientation of each plane within the horizontal leg of the tee is shown in the sketch accompanying each figure.

In Figures 6.9 to 6.I2, the predicted axial velocity profiles are seen to be at variance with the data. Indeed, in certain regions, the flow direction is incorrectly predicted. This is particularly noticeable at axial locations less than or equal to three diameters. However, at the last axial location (Z/D=5), the agreement between the data and the predictions is seen to be good.

In Figure 6.I3, the predicted velocity normal to the horizontal diametral plane at Z/D=I and Z/D=2 is seen to be in fair agreement with the data; the predictions, particularly at Z/D=I, do not reach the peaks in the wall region indicated by the experiments.

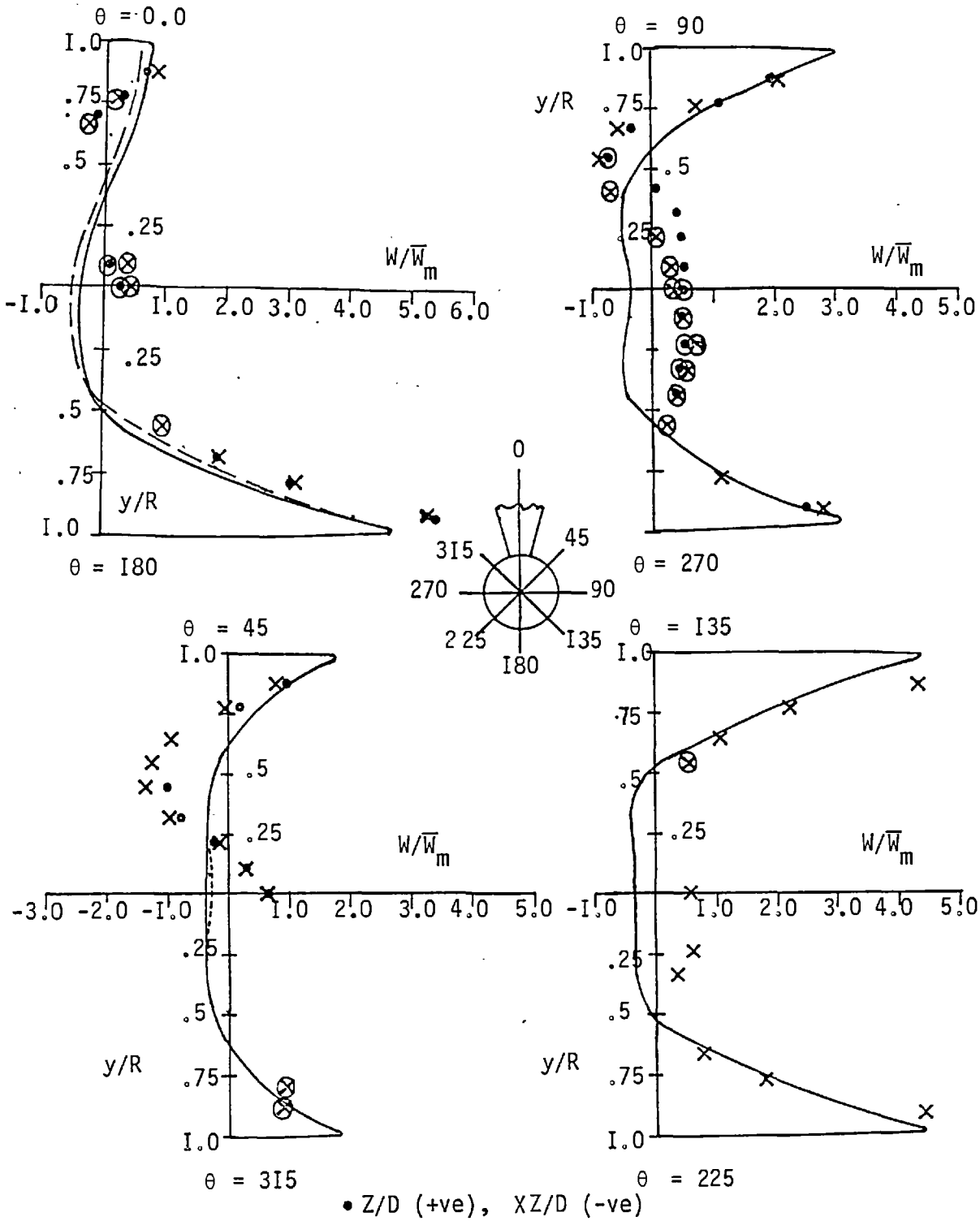

FIGURE 6.9: AXIAL VELOCITY DISTRIBUTION AT Z/D=±1.0

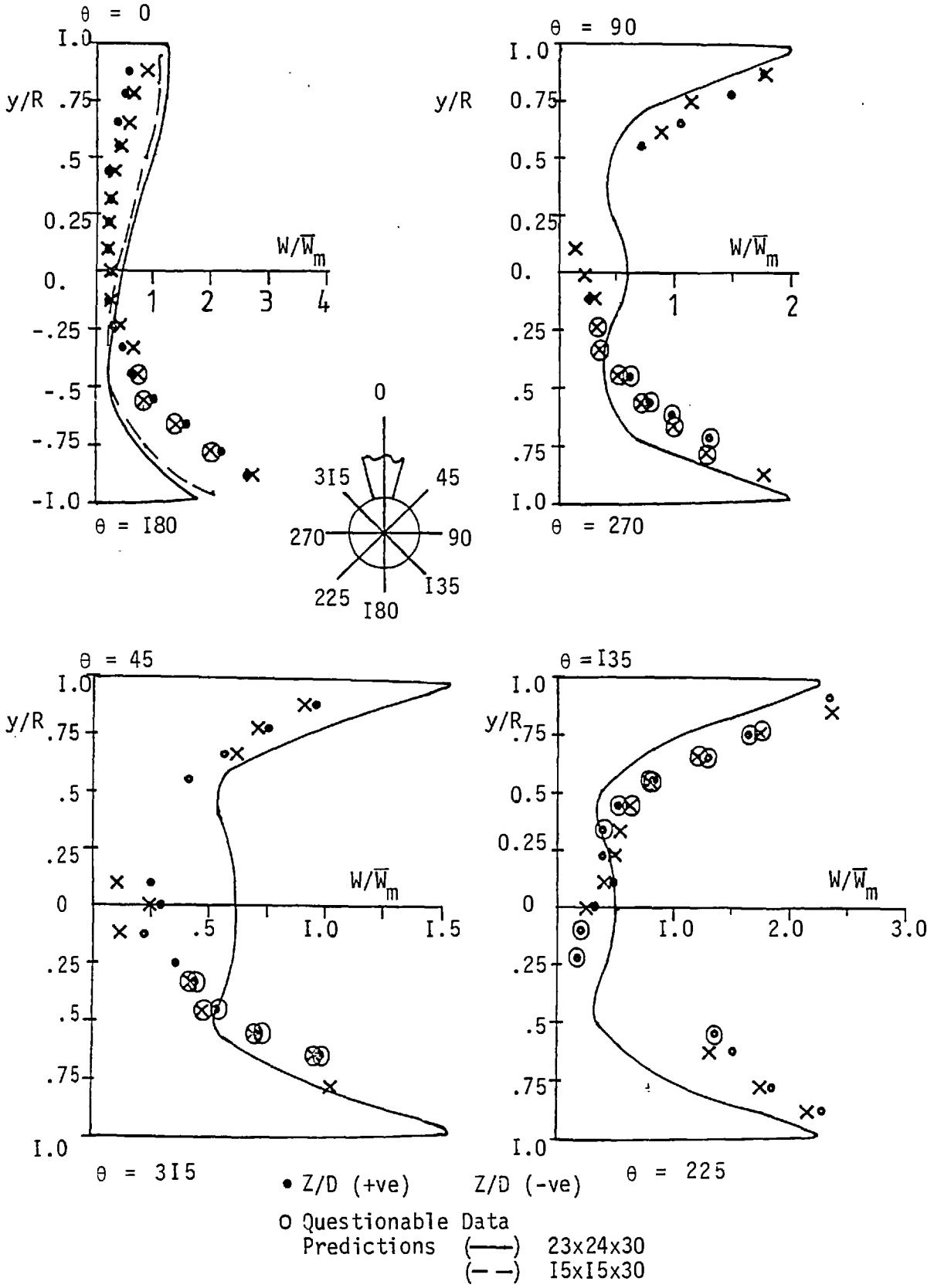

FIGURE 6.IO: AXIAL VELOCITY DISTRIBUTION AT Z/D=±2.0

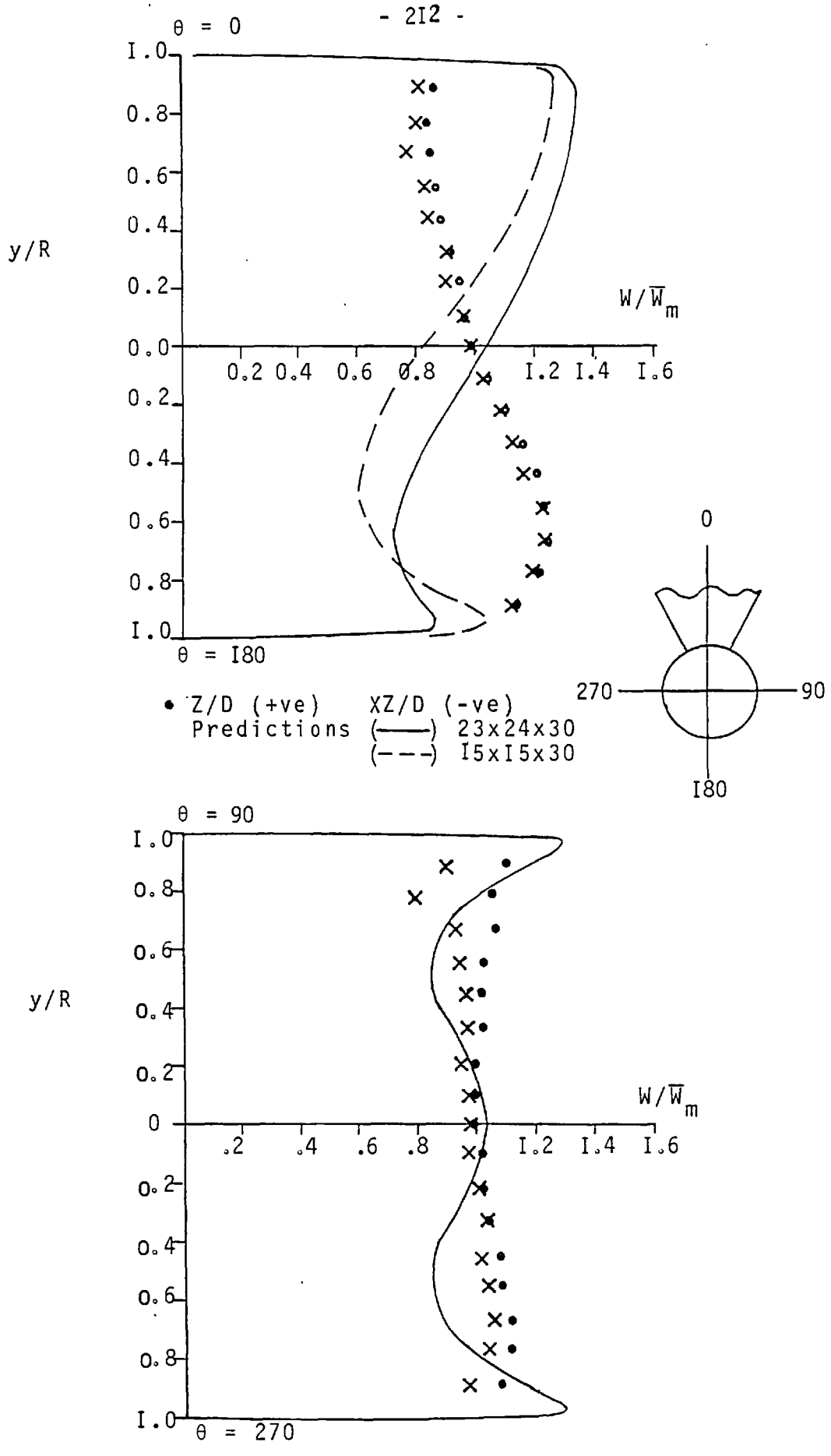

FIGURE 6.II: AXIAL VELOCITY DISTRIBUTION AT Z/D=$\pm$3.0

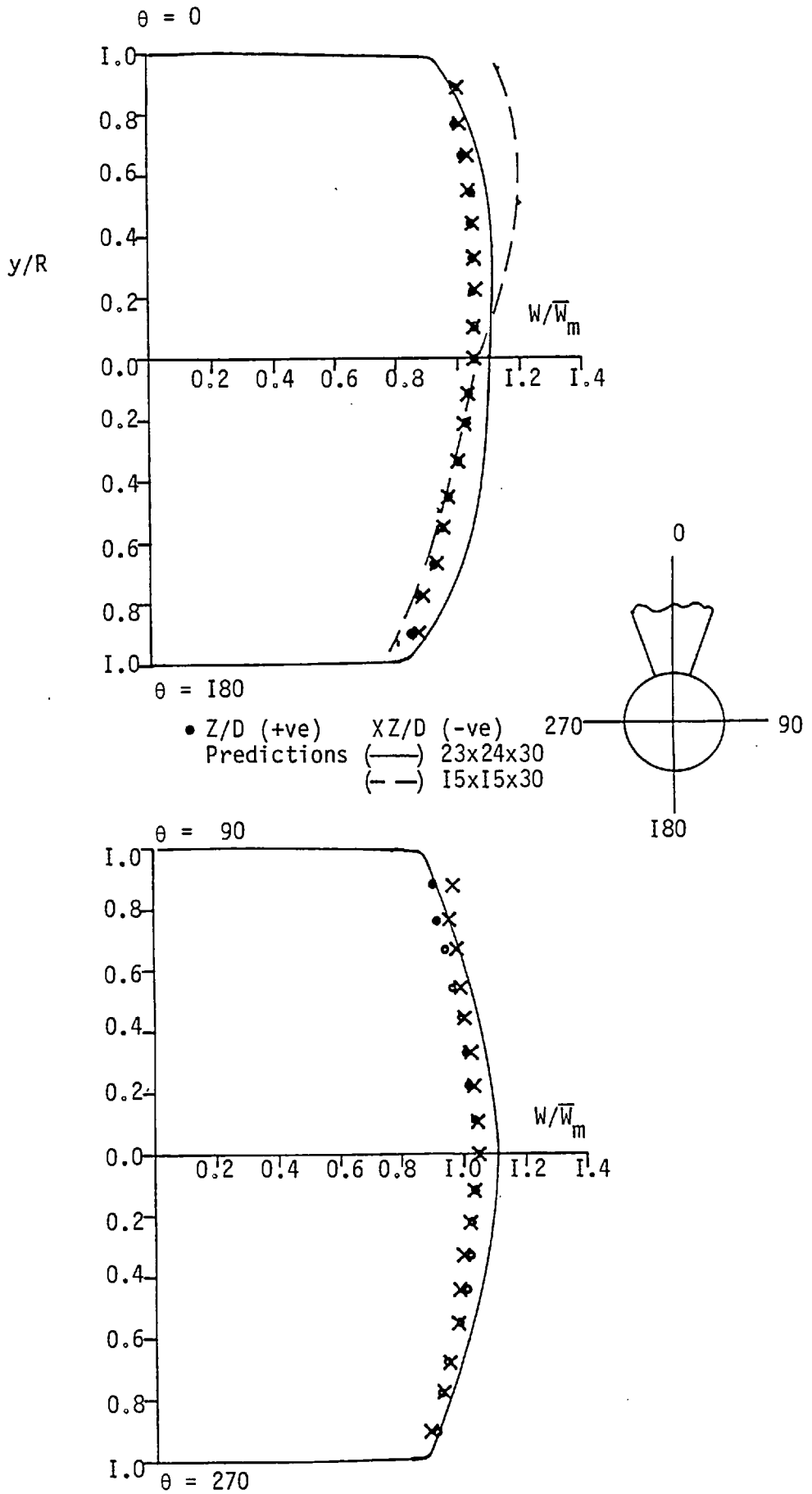

FIGURE 6.12: AXIAL VELOCITY DISTRIBUTION AT Z/D=±5.0

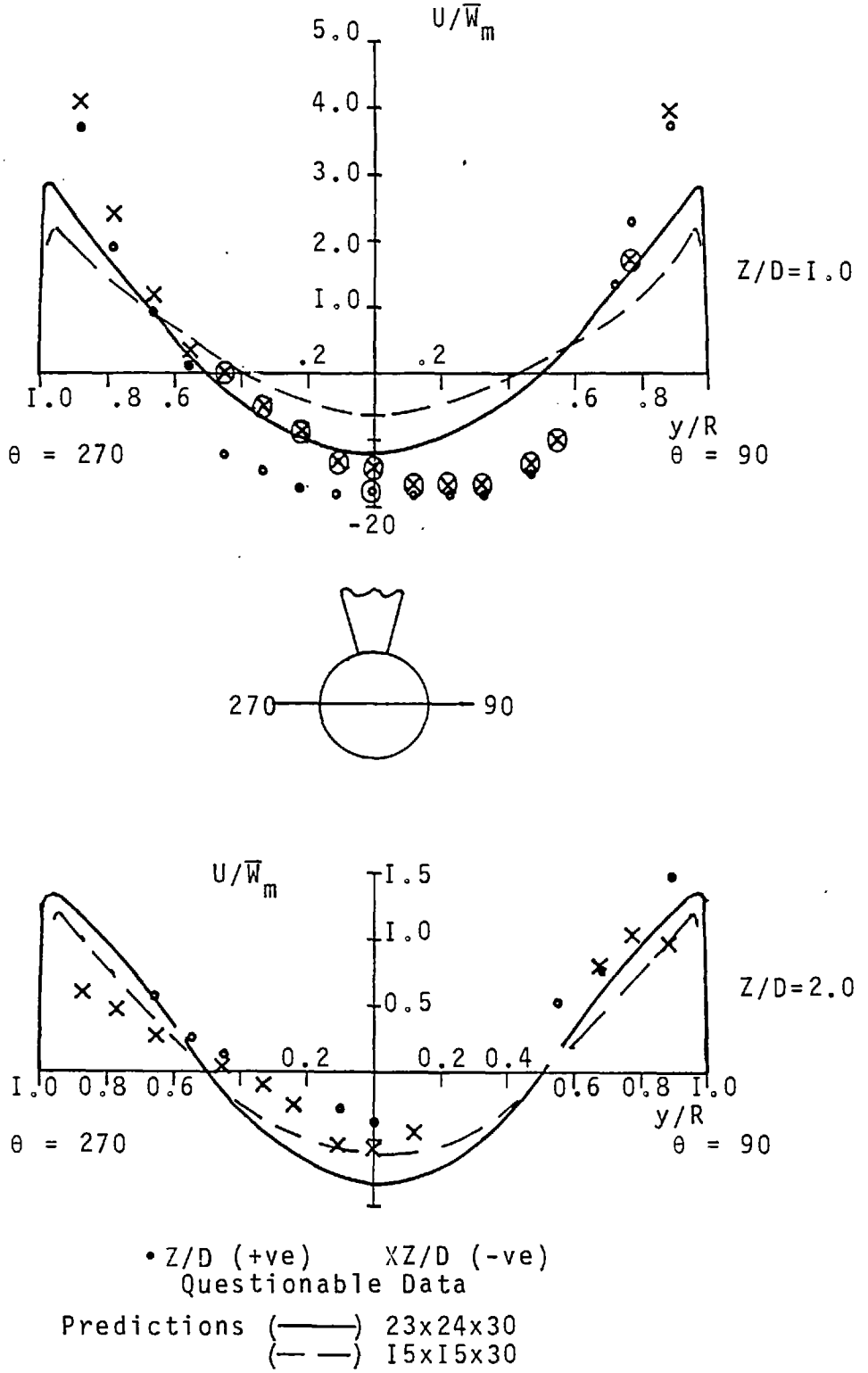

FIGURE 6.I3: VELOCITY DISTRIBUTION NORMAL TO 90-270 DEGREE PLANE AT TWO AXIAL LOCATIONS

6.5.3 DISCUSSION OF THE AERODYNAMIC RESULTS

The comparison between the data and predictions presented in the previous two sub-sections has been found to be, on average, only fair. There are three main areas in which the discrepancies between the predictions and the data are particularly large. The first is the static pressure on the walls of the main duct legs at $Z/D \leq 1$; the second is the axial velocities around the centre-line of the legs, and thirdly, the apparent opposite trend of the axial velocity at $Z/D=3.0$.

As pointed out in Chapter 4, the probe used to obtain the velocities is restricted in its range of application; in particular, as the velocity vector becomes aligned (i.e. parallel) with the probe axis, the readings become increasingly questionable. In regions where this situation occurs, (e.g. $Z/D \simeq 1$), the data must be held in doubt. Indeed, the majority of the data in this region is observed to be of a questionable nature.

At $Z/D=3$, the difference between the data and the predictions is such as to imply that the fluid is distributed incorrectly. There is more in the upper half of the pipe than there should be, and less in the lower half. The reason for this may be explained by turning our attention to the wall pressure distribution.

Returning for a quick glance at the wall surface pressures (Figure 6.7), it is noticed that the predicted pressure level is somewhat lower than the experimental data.

Because the flow in the horizontal leg is driven by these pressure gradients, the under-predicted levels imply that the fluid does not possess the correct* angular motion; therefore, it is not surprising that a shift in the velocity profile, like that illustrated in Figure 6.II, is encountered.

6.5.4 THE HEAT/MASS TRANSFER DISTRIBUTION

In Figure 6.I4, the circumferential variation of the predicted heat-transfer coefficients is compared to the mass transfer coefficient data. The comparison is seen to be fair.† There is a slight descrepancy in the ability of the predictions to reproduce the maximum and minumum values of the experimental mass-transfer coefficients, particularly in those regions close to the inlet duct. As Z/D increases, quantitative agreement becomes doubtful because of the experimental scatter.

In Figure 6.I5a and b, there is presented the longitudinal variation in the heat/mass-transfer coefficient. The predictions of Figure 6.I5a are based on a reference value of the heat-transfer coefficient evaluated using the Colburn equation (see for example, Krieth (I973)). It is:

FOOTNOTES:

*With respect to the experimental data

†Note that the line in the figures including the two graphs following connects predicted points located at angles (and axial) locations corresponding to the experiments.

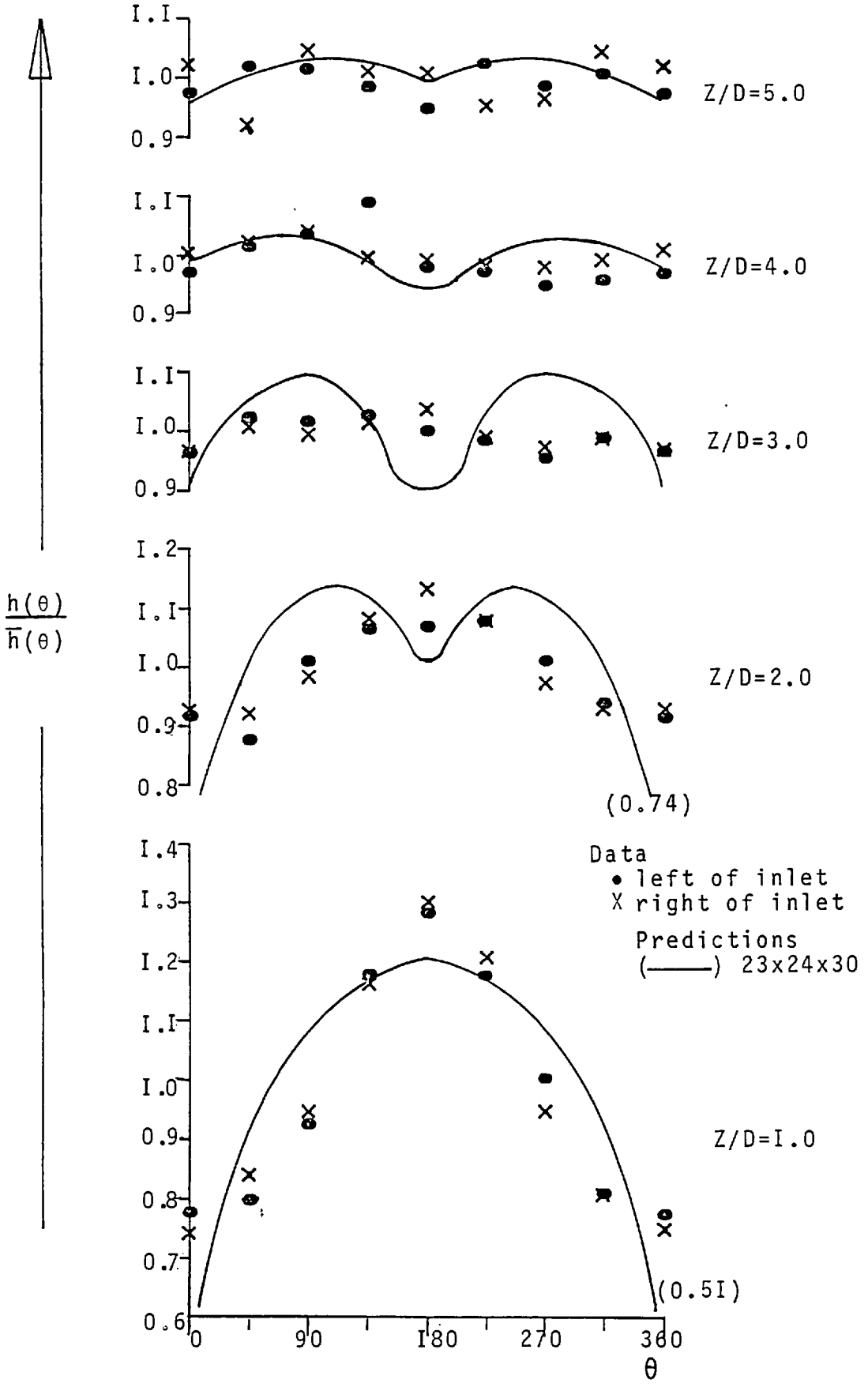

FIGURE 6.I4: CIRCUMFERENTIAL MASS/HEAT TRANSFER VARIATION

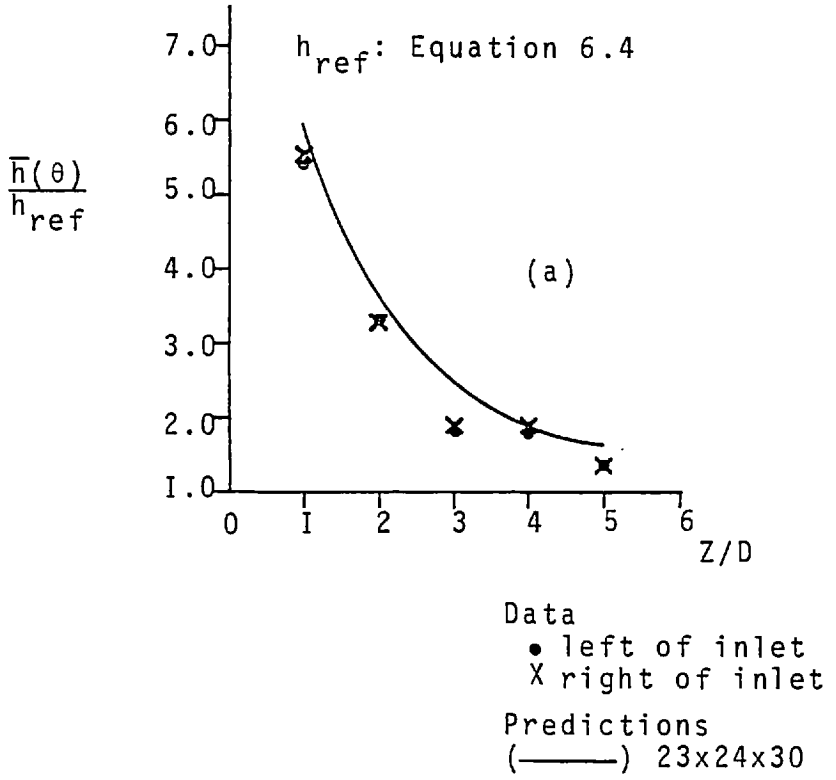

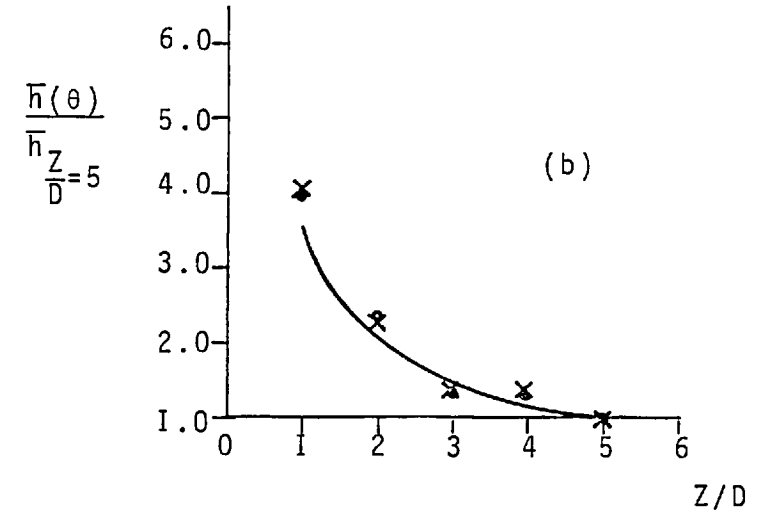

FIGURE 6.15: LONGITUDINAL AVERAGE MASS/HEAT TRANSFER VARIATION

$$St_h = 0.023\ R_e^{-.2} P_r^{-2/3} \quad , \qquad (6.4)$$

where St_h is the Stanton number based on the Nusselt and Prandtl numbers (i.e. $St_h = Nu/(R_e P_r)$). Note that this correlation is based on the heat-transfer coefficient being evaluated from the wall and bulk temperature. Since the bulk temperature or concentration in the predictions or experiment respectively is very close to the inlet temperature or concentration, its use here is considered acceptable.

In Figure 6.15a, the model used in the computations over-predicts slightly the longitudinal heat-transfer coefficient; in Figure 6.15b, the model produces a slight under-prediction. It is interesting to note that although the circumferential variation in the heat-transfer coefficient is predicted only fairly, the longitudinal variation compares in what is believed to be an acceptable manner. It is also of interest to note that the maximum heat/mass transfer coefficient is about six times larger than the corresponding fully-developed turbulent pipe flow value.

6.6 AN EXTENSION TO THE HEAT-TRANSFER RESULTS

In Figures 6.16 and 6.17, there is presented the circumferentially local and longitudinal average heat transfer distribution respectively for the aerodynamic case presented in Section 6.4. These heat transfer predictions

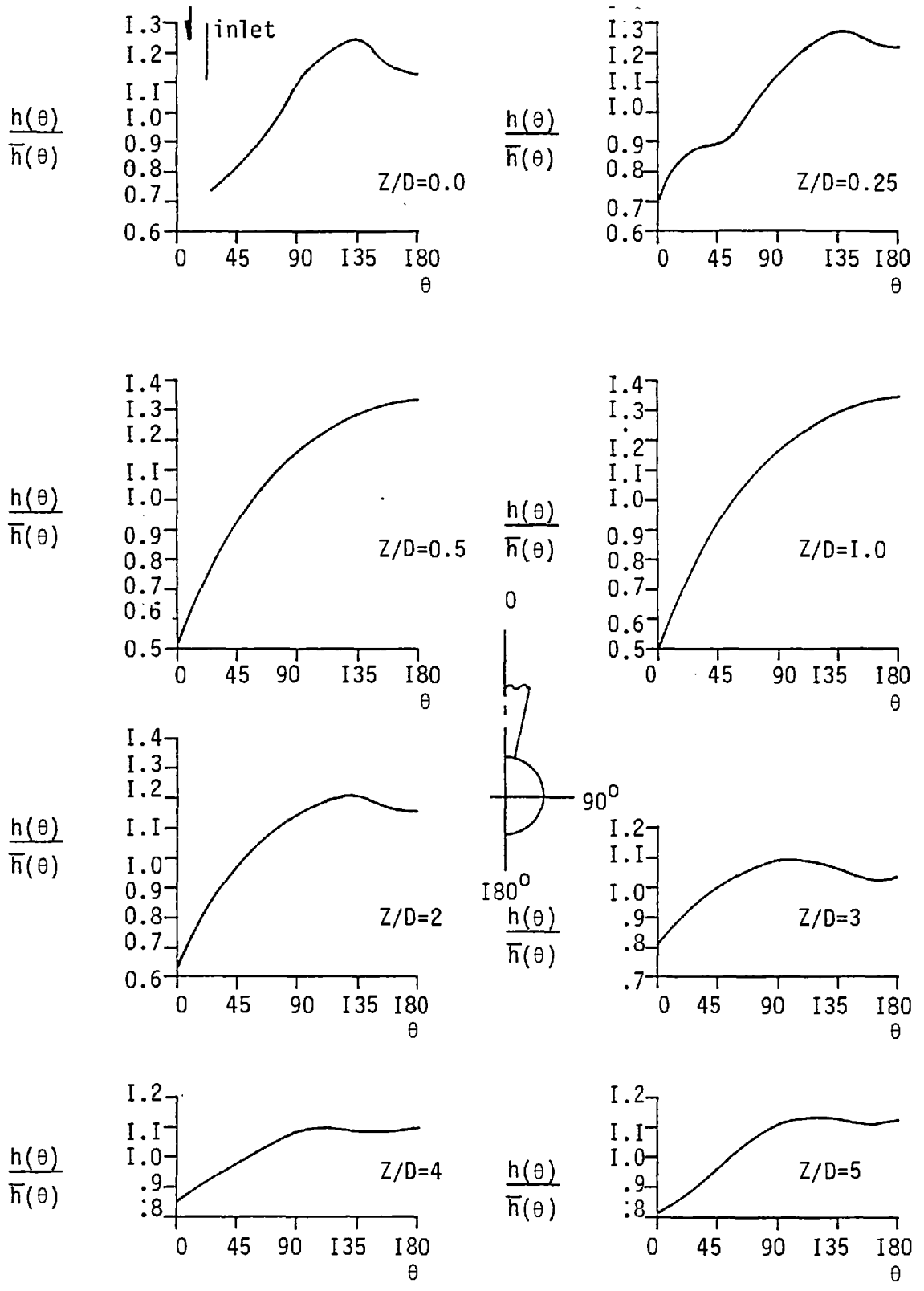

FIGURE 6.I6: PREDICTED CIRCUMFERENTIAL HEAT-TRANSFER COEFFICIENT FOR CONSTANT WALL TEMPERATURE

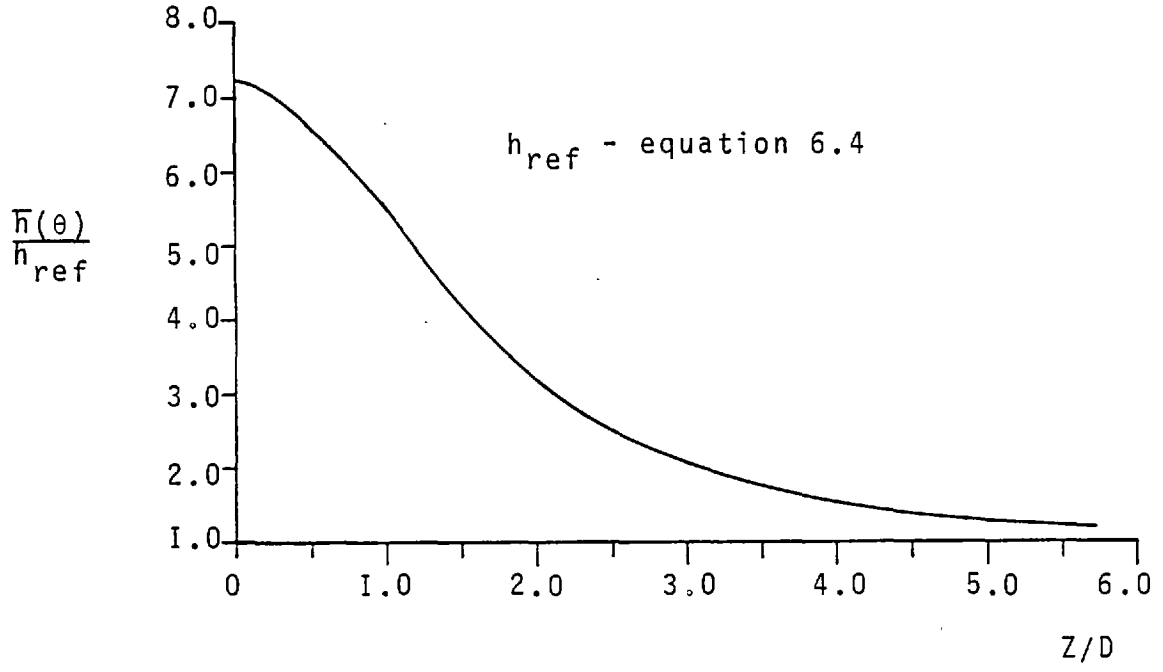

FIGURE 6.I7: PREDICTED LONGITUDINAL AVERAGE HEAT TRANSFER COEFFICIENT DISTRIBUTION FOR CONSTANT WALL TEMPERATURE

differ from those presented in the previous section in that the whole surface of the tee, including the inlet duct, is subjected to a uniform temperature boundary condition. The heat-transfer coefficient is defined in a manner that is also different from that described previously. It is:

$$h = \frac{\dot{q}''}{T_W - T_B} \qquad (6.5)$$

where the subscripts W and B refer to wall and local bulk temperatures respectively. In this manner, equation 6.4 can be used directly as a normalisation factor.

From Figure 6.I6, the circumferential variation of the heat-transfer coefficient is seen to vary quite strongly with distance around the pipe parameter. When compared to the average axial value, the minumum is seen to be consistantly at $\theta=0$ (except of course at $Z/D=0$), while the maximum varies with position but remains between $90 < \theta < 180$. The variation is a consequence of the complex velocity field in the horizontal leg. It is also of interest to note that the minimum to maximum value of $h(\theta)$ increases and then decreases with axial distance.

Turning attention to Figure 6.I7, the longitudinal average heat-transfer coefficient indicates that the maximum heat transfer occurs at $Z/D=0$. Moreover, at this point, the rate of heat transfer is about 7½ times that occuring at fully-developed conditions.

6.7 GENERAL DISCUSSION

There are two aspects of the present predictions that need discussion. Firstly, the conditions imposed at the exit of the calculation domain. In the present computations, the cross-stream velocities were set to zero and the axial gradients of other variables were set to zero. In reality, the experimental measurements indicate that a uniform pressure exists across the duct at Z/D=±6. This implies that a constant pressure (i.e. no cross-stream variation) condition should be (computationally) imposed at this location. Indeed, the predictions produced just such a condition, indicating that the assumed boundary conditions were acceptable. In any event, the effect of those exit conditions on the calculations made in regions away from the exit would be small.

Here, attention is focussed in a direction in which the most likely cause for the disagreement between the measurements and the predictions can be isolated.

Although the predictions appear to display some grid dependence, it is noticed that by increasing the grid by a factor of 2½, produces accuracy benefits that are marginal when compared to the threefold increase in computational cost. A further doubling of the grid is not expected to provide any substantial improvement.

As pointed out in Chapter 4, the data and in particular, the the pressure measurements, are estimated to be accurate to within I%. It would appear there the data is not an area where concern should be focussed.

There are two other areas that require scrutiny. The first is the numerical procedure, and the second is the models incorporated into the procedures. The first area may be denspensed with because of the success of the procedure(s) to predict other, although less complicated flows. This is evidenced by the test cases in Appendix A3 and the laminar flow in a tee-junction in Chapter 5. It would appear therefore, that it is in the direction to the applicability of the turbulence model that doubt must be cast.

6.8 SUMMARY AND CONCLUDING REMARKS

This Chapter has presented the predictions for the turbulent uniformly splitting flow in a tee-junction. The physical situation corresponded to the experimental siatuaion described in Chapter 4. The comparison between the data and the predictions revealed good agreement with the mass transfer, but only fair agreement with the aerodynamic results. The two calculation procedures were observed to produce, to within five percent, the same solutions. The computational times were found to be the same, but the partially-elliptic procedure could have employed only half the storage of the elliptic code.

The chapter provided evidence that the turbulence model is the most likely cause for the lack of agreement between the data and the predictions.

CHAPTER 7.0: CONCLUDING REMARKS

7.1 REVIEW OF THE MAIN RESULTS

The main results and the conclusions that can be drawn from the present study may be summarised as follows:-

a) Two calculation procedures, an elliptic and a partially-elliptic, have been successfully applied to predict both laminar and turbulent flow in tee-junctions.

b) The two procedures have been found to produce results that are in very good agreement with each other. Furthermore, both procedures cost about the same from the point of view of computer time expenditure; however, the partially-elliptic procedure has been found to require, for the flow situations investigated, only about one-half of the computer storage of the elliptic procedure.

c) For the laminar combining flow in square tee-junctions, the predictions show good agreement with available experimental data.

d) The capability of a two-equation model of turbulence to predict uniformly dividing turbulent flow in a tee-junction of round cross-section has been assessed. Although the grid-size effects have probably not been entirely banished, the predictions show, on average, fair agreement with the experimental data. Better agreement was found in comparing predicted heat-transfer coefficients with experimentally determined mass-transfer coefficients. It is concluded that the turbulence model is suspect when applied to uniformly dividing turbulent flow in tee-junctions of round cross-section.

e) An experimental program has been successfully completed. A rig was designed and measurements have been made of the distributions of wall static pressures and mean velocity. Furthermore, the napthalene sublimation technique has been extended so that local mass transfer rates could be obtained. These data have been useful in validating the turbulence model.

7.2 FUTURE WORK

The present work has disclosed some areas where further study is necessary in order to place the procedures upon firmer ground. These areas are outlined below; they are:

a) Computational Aspects

First, the success of the partially-elliptic procedure in reproducing the elliptic predictions should be capatalised upon by employing storage manipulations. Thus, only pressure requires full three-dimensional storage; areas outside zones of recirculating flow will require storage only in two dimensions. This will allow finer grids to be used for predicting turbulent flows in tee-junctions.

Secondly, the convergence rate of the procedure must be increased. Although the practices adopted here have been found successful, there may be other ways that could enhance convergence. In particular, attention could be concentrated upon integral conservation techniques.

Finally, the partially-elliptic procedure should be further validated. This could be done by applying it to

other flow situations that exhibit small regions of recirculating flow embedded within a predominant direction main stream.

(b) Physical Models

The implications of using models, initially applied to flows that are one and two-dimensional in character, for predicting three-dimensional, recirculating flows, have yet to be fully explored. Indeed, the effective viscosity approach to turbulence modelling, coupled with wall functions although economically justified, may be physically unrealistic when applied to tee-junctions.

Further testing of the turbulence model needs to be made to establish that the present conclusions are sound. This testing should take the form of predicting and comparing with experimental data for similar flow situations, such as a combining flow in a tee-junction of round cross-section. With the limited, but demonstrated success of the partially-elliptic procedure, a tool is now available whereby these studies can be performed relatively cheaply. If the present conclusions are confirmed, then other turbulence models such as the more complicated Reynolds Stress model should be applied.

(c) Experimental Aspects

More measurements, and in particular, those concerned with the sublimation of naphthalene and velocity, under various flow conditions, are required. It is recommended, however, that any future work directed towards obtaining velocities should be done by using other more reliable techniques, such as laser doppler anemometry.

REFERENCE LIST

BOUCHEZ, J P, GOLDSTEIN, R J (I975)
"Impingement Cooling from a Circular Jet in a Cross Flow".
Int. J Heat & Mass Transfer, I8, pp 7I9-730.

BURGRAFF, O R (I966)
"Analytical and Numerical Studies of the Structure of Steady Separated Flows".
J. Fluid Mech., 24, pp II3-I5I.

EHRLICH, L W, FREIDMAN, M H (I977)
"Paticle Paths and Stasis in Unsteady Flow through a Bifurcation"
J. Biomechanics, IO, pp 56I-568.

Engineering Sciences Data Unit (I973)
"Pressure Losses in Three-Leg Pipe-Junctions: Dividing Flow"
ESDU73022,25I Regent Street, London
and
"Pressure Losses in Three-Leg Pipe-Junctions: Combining Flow"
ESDU73023,25I Regent Street, London.

FERNANDEZ, R C, DEWITT, K J, BOTWIN, M R (I976)
"Pulsatile Flow through a Bifurcation with Application to Arterial Disease"
J. Biomechanics, 9, pp 575-580.

HARLOW, H, WELCH, J E (I965)
"Numerical Calculation of Time-Dependent Viscous Incompressible Flow of Fluid with Free Surface"
Physics of Fluids, 8, p 2I82.

HARLOW, F H, NAKAYAMA P I (I968)
"Transport of Turbulence Energy Decay Rate"
Los Almos Scientific Laboratory, University of California, Report No. LA3854.

HIETT, G F, POWELL, G E (I962)
"Three-Dimensional Probe for Investigation of Flow Patterns"
The Engineer, Jan., p I65.

HIRT, C W, AMSDEN, A A, COOK, J L (I974)
"An Arbitrary Lagrangian-Eulerian Computing Method for all Flow Speeds"
J. Computational Physics, I4, pp 227-253.

HINZE, J O (I959)
"Turbulence - An Introduction to its Mechanism and Theory"
McGraw Hill Publishers, New York.

JAYATILLEKE, C L V (I969)
"The Influence of Prandtl Number and Surface Roughness on the Resistance of the Laminar Sublayer to Momentum and Heat Transfer"
Progress in Heat and Mass Transfer, Pergamon Press, Oxford.

JONES, W P, LAUNDER, B E (I973)
"The Calculation of Low-Reynolds-Number Phenomena with a Two-Equation Model of Turbulence"
Int. J. Heat and Mass Transfer, I6, pp III9-II30.

KAMOTANI, Y, GREBER, I (I972)
"Experiments on a Turbulent Jet in a Cross-Flow"
AIAA, IO, No II, p I425.

KAMOTANI, Y, GREBER, I (I974)
"Experiments on Confined Turbulent Jets in Cross-Flows"
NASA, CR-2392, Washington DC, USA

KANDARPA, K, DAVIDS, N (I976)
"Analysis of the Fluid Dynamic Effects on Atherogenesis at Branching Sites"
J. Biomechanics, 9, pp 735-74I.

KREITH, F (I973)
"Principles of Heat Transfer"
Intext Eductional Publishers, New York (3rd Edition).

KRIED, D K, CHUNG, C-J, CROWE, C T (I975)
"Measurements of the Flow of Water in T-Junctions by the LDV Technique"
Transactions ASME, J. Applied Mechanics, p 498.

LAUNDER, B E, SPALDING D B (I972)
"Mathematical Models of Turbulence"
Academic Press, New York

LAUNDER, B E, SPALDING, D B (I974)
"Numerical Computation of Turbulent Flows"
Computer Methods in Applied Mechanics and Engineering, 3, pp 269-289.

LAUNDER, B E, REECE, G J, RODI, W (I975)
"Progress in the Development of a Reynolds Stress-Turbulence Closure"
J. Fluid Mechanics, 68, p 537.

LESLIE, D C (I973)
"Developments in the Theory of Turbulence"
Clarendon Press, Oxford

LIEPSCH, D (I974)
"Flow Conditions at 90 (DEG) Branchings as Determined in Glass Models of Small Arteries by means of a Laser Doppler Velocimeter"
Proc. 2nd New England Bioengineering Conf. Worcester Polytechnic Institute, Worcester, Mass. USA.

LOEHRKE, R I, NAGIG, H M (I976)
"Control of Free-Stream Turbulence by Means of Honeycomb: A Balance between Suppression and Generation"
Transactions ASME, J. Fluids Engineering, 76-FE-2, pp 342-353.

MACAGNO, E O, HUNG, T K (I967)
"Computational and Experimental Study of a Captive Annular Eddy"
J. Fluid Mechanics, 28, pp 43-64.

MAJUMDAR, A K, POLLARD, A (I977)
"The Graphical Representation and Analysis of Fluid Flow by Interactive Computation: GRAFFIC, a Representation of its Capabilities"
Imperial College, Dept. of Mech. Engg., Report No HTS/77/I9.

MALLINSON, G D (I977)
"GRAFFIC: The Graphical Representation and Analysis of Fluid Flow by Interactive Computation"
To be published.

MILLER, D S (I97I)
"Internal Flow: A Guide to Losses in Pipes and Duct Systems"
BHRA, London.

MILLS, A F (I962)
"Experimental Investigation of Turbulent Heat-Transfer in The Entrace Region of a Circular Conduit"
J. Mechanical Engineering Science, 4, p 63.

MOZHAROV, N A, CHIKILEVSKAYA, V I, KORMILITSYN, V I (I972)
"Experimental Investigation of the Inflow of a Water Jet into a Turbulent Confined Water Flow at a Right Angle"
Thermal Engineering, I9, No 3, pp 42-45.

NEAL, S B H C (I975)
"The Development of the Thin Film Napthalene Mass-Transfer Analogue Technique for the Direct Measurement of Heat-Transfer Coefficients"
Int. J. Heat and Mass Transfer, I8, pp 559-567.

O'BRIEN, V, EHRLICH, L W (I977)
"Simulation of Unsteady Flow at Renal Branches"
J. Biomechanics, I0, pp 623-63I.

OWEN, F K (I967)
"Heat Transfer from Plain and Finned Cylinders in Cross-Flow"
J. Institute Heating Ventilating Engineers, October, pp 2I3-226.

PATANKAR, S V, SPALDING, D B (I972)
"A Calculation Procedure for Heat, Mass and Momentum Transfer in Three-Dimensional Parabolic Flows"
Int. J. Heat and Mass Transfer, I5, pp I787-I806.

Patankar, S V (I973)
"The TRIC Program Manual"
CHAM Ltd., Wimbledon, Report No CHAM/TR/7.

PEDLEY, T J (I977)
"Pulmonary Fluid Dynamics"
Annual Review of Fluid Mechanics, 9, pp 229-274.

POLLARD, A, SPALDING, D B (I977a)
"The Prediction of the Three-Dimensional Turbulent Flow Field in a Flow-Splitting Tee-Junction"
Imperial College, Dept. of Mech. Engg., Report No HTS/77/I5, also in Comp. Meth. Appl. Mech. Eng., I3, pp 293-306 (I978)

POLLARD, A, SPALDING, D B (I977b)
"The Prediction of the Temperature Field and Heat Transfer Distribtuion in a Tee-Junction"
Imperial College, Dept. of Mech. Engg. Report No. HTS/77/I6.

POLLARD, A, THYAGARAJA, A (I978)
"A New Method for Handling Flow Problems with Body Forces"
Imperial College, Mech. Engg. Dept., Report No. HTS/TN/78/I.
Also to appear in Comp. Meth. Appl. Mech. Engg.

POPE, S B, WHITELAW, J H (I976)
"The Calculation of Near Wake Flows"
J. Fluid Mechanics, 73, p 9.

PRACHT, W E, BRACKBILL, J U (I976)
"BAAL: A Code for Calculating Three-Dimensional Fluid Flows at all Speeds with an Eulerian-Lagrangian Computing Mesh"
Los Almos Scientific Laboratory, University of California, Report no LA6342.

PRATAP, S V (I975)
"Flow and Heat Transfer in Curved Ducts"
PhD Thesis, Imperial College, Univeristy of London.

RATHGEBER, D E, BECKER, H A (I977)
"Mixing Between a Round Jet and a Transverse Turbulent Pipe Flow"
Conference Turbulent Shear Flows, Penn. State University, pp I0.I7 - I0-26.

ROACHE, P J (I976)
"Computational Fluid Dynamics"
Hermosa Publishers, New Mexico, Revised Edition.

SCHLICHTING, H (I968)
"Boundary Layer Theory"
McGraw Hill, 6th Edition.

SERAG-ELDIN, M A (I977)
"The Numerical Prediction of the Flow and Combustion Processes in a Three-Dimensional Can Combustor"
PhD Thesis, Imperial College, University of London
Also Imperial College, Mech. Engg. Dept., Report No HTS/77/2I.

SHAW, R (I960)
"The Influence of Hole Dimensions on Static Pressure Measurements"
J. Fluid Mechanics, 7, p 550.

SHERWOOD, T K, TRASS, O (I960)
"Sublimation Mass Transfer through Compressible Boundary Layers on a Flat Plate"
Transactions ASME, J. Heat Transfer, pp 3I3-324.

SIMITOVIC, R (I977)
"Turbulent Flow in a Rectangular Duct with an Obliquely-Introduced Secondary Jet"
PhD Thesis, Imperial College, University of London
also Mech. Engg. Dept., Imperial College, Report No HTS/77/I8.

SOGIN, H H (I958)
"Sublimation from Disks to Air Streams Flowing Normal to Their Surfaces"
Tansactions ASME, Heat Transfer Division, pp 6I-69.

SPALDING, D B (I972)
"A Novel Finite-Difference Formulation for Differential Expressions involving both First and Second Derivatives"
Int. J. Numerical Methods in Engineering, 4, pp 55I-559.

SPALDING, D B (I975)
"GENMIX; A General Computer Program for Two-Dimensional Parabolic Flows"
Mech. Engg. Dept., Imperial College, Report No HTS/75/I7.
Also HMT Series, I, Pergamon Press, Oxford (I977)

SPALDING, D B (I976)
"Basic Equations of Fluid Mechanics, and Heat and Mass Transfer, and Procedures for Their Solution"
Imperial College, Dept. Mech. Engg., Report No HTS/76/6.

SPALDING, D B (I978)
Private Communication (3.8.78)

SPARROW, E M (I976)
Private Communication

SPARROW, E M (I977)
"Heat Transfer in Complex Duct Flows"
ASME Paper No 77-HT-95; Heat Transfer Conference, Salt Lake City, Utah.

STOY, R L, BEN-HAIM, Y (I973)
"Turbulent Jets in Confined Cross-Flow"
Transactions ASME, J. Fluids Engineering, pp 55I-556.

Tatchell, D G (I975)
"Convection Processes in Confined Three-Dimensional Boundary Layers"
PhD Thesis, Imperial College, University of London, also Imperial College, Mech. Engg. Dept., Report No HTS/75/20.

VASILIC-MELLING, D (I976)
"Three-Dimensional Turbulent Flow Past Rectangular Bluff Bodies"
PhD Thesis, Imperial College, University of London, also Imperial College, Mech. Engg. Dept. Report No. HTS/77/I0.

VILLEMONTE, J R (I977)
"Some Basic Concepts of Flow in Brachting Conduits"
Proceedings ASCE, I03, No HY7, pp 685-697.

WESLEY, D A, SPARROW, E M (I976)
"Circumferentially Local and Average Heat Transfer Coefficients in a Tube Downstream of a Tee"
Int. J. Heat and Mass Transfer, I9, pp I205-I2I4.

WHITE, F M (I974)
"Viscous Fluid Flow"
McGraw Hill Publishers, New York.

WOLFSTEIN, M (I968)
"Numerical Smearing of One Sided Difference Approximations to the Equations of Non-Viscous Flow"
Imperial College, Dept. Mech. Engg. Report No. HTS/EF/TN/A/3.

NOMENCLATURE

SYMBOL	MEANING	LOCATION OF FIRST APPEARANCE
A	Area of napthalene plug;	Eqn. (4.2)
	Area of duct	Sec. (I.3.2)
$A_j, B_j, C_j, D_j, A'_j, B'_j, C'_j, \overline{A}_j, \overline{B}_j, \overline{C}_j$	Coefficients of tri-diagonal matrix algorithm	Eqn. (3.38)
A, B, C	Planes of interest in calculation domain (A-upmarch, B-Current, C-downmarch)	Sec. (3.3.3)
C_I, C_2	Constants in turbulence model	Eqn. (2.20)
C_μ	Constant in turbulence model	Eqn. (2.I8)
$C_P^\phi, C_E^\phi, C_W^\phi, C_N^\phi, C_S^\phi, C_H^\phi, C_L^\phi$	Coefficients of finite-difference equations	Eqn. (3.I2)
C_P	Pressure coefficient	Eqn. (4.I)
c_p	Specific heat	Eqn. (6.4)
$C_{V,W}, C_{V,O}$	Concentration of napthalene at wall (W) and free stream (O)	Eqn. (4.2)
D	Pipe diameter	Sec. (4.2.2)
d_i, D_m	Hydraulic diameters of inlet (d_i) and main (D_m) duct ($= \frac{2hl}{l+h}$, h,l lengths of sides)	Sec. (5.2.I)
E	Constant in "Log-law"	Eqn. (2.25)
$f_e, f_w, f_h, f_l, f_n, f_s$	Weighing factors in finite-difference equations	Eqn. (3.3)
G_k	Generation of turbulence kinetic energy	Eqn. (2.I9)

SYMBOL	MEANING	LOCATION OF FIRST APPEARANCE
H	Height of inlet duct	Fig. (4.II)
$h(\Theta)$	Heat/mass transfer coefficient as a function of angle	Eqn. (4.2)
$\tilde{h}(\Theta)$	Ratio of local circumfernetial heat/mass transfer coefficient ($h(\Theta)$) to average of circumferential ($\overline{h}(\Theta)$)	Eqn. (4.5)
$\tilde{h}_R$	Ratio of average ($\overline{h}(\Theta)$) to reference (h_R) mass/heat transfer coefficient	Eqn. (4.6)
$J_{\phi,j}$	Flux of ϕ in jth direction	Eqn. (2.3)
$J_{\phi,w}$	Flux of ϕ through wall	Eqn. (2.36)
k	Kinetic energy of turbulence	Eqn. (2.I5)
k_p	Kinetic energy of turbulence at near wall node "p"	Eqn. (2.28)
ℓ	Local length scale of turbulence	Eqn. (2.32)
ℓ_m	Prandtl mixing length	Eqn. (2.3I)
ℓ_i	Length of inlet duct	Sec. (2.2.2)
L_i	Length of main duct from entrance to inlet duct centre-line	Sec. (5.2.2)
L_m	Length of main duct	Sec. (5.2.2)
Δm	Mass loss	Eqn. (4.2)
$\dot{m}$	Mass flow rate	Sec. (I.3.3)
N,S,E,W, H,L,P	Finite-difference grid point locations	Sec. (3.3.4)
p	Local pressure	Eqn. (2.2)
P	Mean pressure	Eqn. (2.7)

SYMBOL	MEANING	LOCATION OF FIRST APPEARANCE
p'	Fluctuating component of pressure	Eqn. (2.10)
P	"P-function" in "log-law"	Eqn. (2.35)
Pe	Peclet Number	Eqn. (3.5)
$p_{v,w}$	Partial pressure of nathalene vapour at the wall	Eqn. (4.3)
P_{ref}	Reference pressure	Eqn. (4.1)
R	Injection ratio ($\equiv \overline{V}_i/\overline{W}_m$)	Sec. (I.3.2)
r,R	Local and overall radius of pipe	Fig. (4.12)
R	Coordinate direction	Sec. (3.3.4)
Re	Reynolds Number	Sec. (4.4.2)
R_v	Napthalene gas constant	Eqn. (4.3)
S	Split ratio ($\frac{\overline{M}_{LEG_1}}{\overline{M}_{LEG_2}}$)	Sec. (I.3.3)
S_ϕ	Source/sink of variable ϕ	Eqn. (2.3)
S_u^ϕ, S_p^ϕ	Linearised source/sink terms for variable ϕ	Eqn. (3.4)
St_h	Heat Stanton Number	Eqn. (6.4)
St_m	Mass Stanton Number	Eqn. (4.7)
Sh	Sherwood Number	Eqn. (4.7)
Sc	Schmidt Number	Eqn. (4.7)
t	Time	Eqn. (4.2)
$\overline{T}$	Temporal mean temperature	Sec. (4.5.3)
T_{IN}	Inlet air temperature	
T_{WALL}	Wall temperature	Eqn. (6.2)
T_{ij}	Local temperature	
U_i, u_j	Local velocity components	Eqn. (2.1)

SYMBOL	MEANING	LOCATION OF FIRST APPEARANCE
U_i, U_j	Mean velocity components	Eqn. (2.7)
u_i', u_j'	Fluctuating velocity components	Eqn. (2.7)
u^+	Non-dimensional velocity	Eqn. (2.25)
$\vec{U}_p$	Velocity vector parallel to wall, located at near-wall node "p"	Eqn. (2.26)
$\vec{U}_\tau$	Shear velocity vector	Eqn. (2.26)
U,V,W	Average velocity in X,Y,Z or Θ, R,Z coordinate directions respectfully	Sec. (3.3.4)
$\overline{V}_i$	Average inlet duct velocity	Eqn. (4.I)
W_{MAX}	Maximum velocity in tee-junction legs	Fig. (4.I2)
$\overline{W}_m$,W(MAIN)	Average velocity in main duct (legs) (if combining flow, at inlet)	Fig. (4.I4) Fig. (5.5)
X_i, X_j	Coordinate directions	Eqn. (2.I)
X	Coordinate direction	Eqn. (2.I)
$\Delta X, \delta X$	Lengths associated with finite-difference grid	Sec. (3.3.6)
y^+	Non-dimensional distance from wall	Eqn. (2.25)
y_p	Distance from wall to near wall grid node "p"	Eqn. (2.27)
y_c	Distance from wall to edge of near wall control volume	Eqn. (2.34)
$\Delta y, \delta y$	Lengths associated with finite-difference grid	Sec. (3.3.6)

SYMBOL	MEANING	LOCATION OF FIRST APPEARANCE
Y	Coordinate direction	Eqn. (2.I)
Z	Coordinate direction	Eqn. (2.I)
$\Delta z, \delta z$	Lengths associated with finite-difference grid	Sec. (3.3.6)
GREEK SYMBOLS		
α	Relaxation parameter	Eqn. (3.48)
ω	Momentum ratio ($\equiv \frac{M_i}{M_m} = \frac{\rho_i A_i \overline{V}_i^2}{\rho_m A_m \overline{W}_m^2}$)	Sec. (I.3.2)
ρ	Density	Eqn. (2.I)
τ_{ij}	Stress tensor	Eqn. (2.2)
τ	Shear stress	Eqn. (2.26)
ϕ^+	Non-dimensional scalar variable	Eqn. (2.35)
ϕ	Scalar variable	Eqn. (2.3)
ϕ_P, ϕ_W	ϕ at wall (W) and near wall grid node "P"	Eqn. (2.36
μ	Laminar viscosity	Eqn. (2.4)
μ_t	Turbulent viscosity	Eqn. (2.I3)
μ_e	Effective viscosity	Eqn. (A.I.I4)
σ_ϕ	Laminar Prandtl/Schmidt Number	Eqn. (2.5)
$\sigma_{t,\phi}$	Turbulent Prandtl/Schmidt Number	Eqn. (2.I4)
$\sigma_{e,\phi}$	Effective Prandtl/Schmidt Number	
$\Gamma_{t,\phi}$	Turbulent exchange coefficient	Eqn. (2.I4)
$\Gamma_{e,\phi}$	Effective exchange coefficient	Eqn. (2.I9)
ε	Volumetric rate of turbulence kinetic energy decay	Eqn. (2.I5)

GREEK SYMBOLS	MEANING	LOCATION OF FIRST APPEARANCE
ε_P	at near wall node "P"	Eqn. (2.33)
$\overline{\varepsilon}$	Average value of ε in near wall control volume	Eqn. (2.34)
κ	Constant in "Log-Law"	Eqn. (2.25)
Θ	Coordinate direction	Sec. (3.3.4)

SUBSCRIPTS	MEANING
e,w,h,l,n,s	At control volume faces
E,W,H,L,N,S	At grid nodes
e	Effective
i	Inlet
ℓ	Laminar
m	Main duct or relating to mass
P	At grid node "P", next to wall
ref	Reference value
t	Turbulent
v	Vapour
W	Wall value

SUPERSCRIPTS	
ϕ	Relating to equation under consideration
*	Approximate values
'	Corrections or fluctuating component
$\overline{\ }$	Average
$\rightarrow$	Vector quantity
+	Non-dimensionalised quantity

- PART V -

THE APPENDICES

APPENDIX AI

THE GOVERNING DIFFERENTIAL EQUATIONS

AI.1 INTRODUCTION

This appendix presents the partial-differential equations governing the steady, three-dimensional incompressible flow and heat/mass transfer phenomena in tee-junctions. The equations are expressed in the two coordinate systems mentioned in Chapter 2, namely the (x-y-z) and (θ-r-z) systems. The equation stated here are identical for laminar or turbulent flows, except that for turbulent flow situations, the shear stresses are calculated from "effective" exchange coefficients; the effective exchange coefficient is the sum of the laminar and turbulent exchange coefficients; note also that for laminar flows, the turbulence equations are not solved, i.e. those for k and ε.

The following set of equations are stated in their elliptic form; to obtain the partially-parabolic form of the equations, the terms enclosed by the boxes should be ignored. (N.B. The z coordinate direction is assumed to be the predominant flow direction).

AI.2 EQUATIONS IN (x-y-z) COORDINATE SYSTEM

The partial differential equations governing flow and heat/mass transfer phenomena in a flow situation described by the (x-y-z) coordinate system are as follows:

CONTINUITY

$$\frac{\partial}{\partial x}u + \frac{\partial}{\partial y}v + \frac{\partial}{\partial z}w = 0 \qquad ,(AI.I)$$

AXIAL MOMENTUM (z)

$$\rho\left[u\frac{\partial w}{\partial x} + v\frac{\partial w}{\partial y} + w\frac{\partial w}{\partial z}\right] = -\frac{\partial p}{\partial z} + \frac{\partial \tau}{\partial x}xz + \frac{\partial \tau}{\partial y}yz + \boxed{\frac{\partial \sigma}{\partial z}z} \qquad .(AI.2)$$

CROSS-STREAM MOMENTUM (x)

$$\rho\left[u\frac{\partial u}{\partial x} + v\frac{\partial u}{\partial y} + w\frac{\partial u}{\partial z}\right] = -\frac{\partial p}{\partial x} + \frac{\partial \sigma}{\partial x}x + \frac{\partial \tau}{\partial y}yx + \boxed{\frac{\partial \tau}{\partial z}zx} \qquad .(AI.3)$$

CROSS-STREAM MOMENTUM (y)

$$\rho\left[u\frac{\partial v}{\partial x} + v\frac{\partial v}{\partial y} + w\frac{\partial v}{\partial z}\right] = -\frac{\partial p}{\partial y} + \frac{\partial \sigma}{\partial x}xy + \frac{\partial \tau}{\partial y}y + \boxed{\frac{\partial \tau}{\partial z}zy} \qquad .(AI.4)$$

where

$$\sigma_x = 2\mu\frac{\partial u}{\partial x} \qquad ,(AI.5)$$

$$\sigma_y = 2\mu\frac{\partial v}{\partial y} \qquad ,(AI.6)$$

$$\sigma_z = 2\mu\frac{\partial w}{\partial z} \qquad ,(AI.7)$$

$$\tau_{xy} = \tau_{yx} = \mu\left(\frac{\partial v}{\partial x} + \frac{\partial u}{\partial y}\right) \qquad ,(AI.8)$$

$$\tau_{yz} = \tau_{zy} = \mu\left(\frac{\partial w}{\partial y} + \frac{\partial v}{\partial z}\right) \qquad ,(AI.9)$$

$$\tau_{zx} = \tau_{xz} = \mu\left(\frac{\partial u}{\partial z} + \frac{\partial w}{\partial x}\right) \qquad .(AI.IO)$$

KINETIC ENERGY EQUATION (k)

$$\rho\left[\frac{\partial}{\partial x}(uk) + \frac{\partial}{\partial y}(vk) + \frac{\partial}{\partial z}(wk)\right] = \frac{\partial}{\partial x}\Gamma_{e,k}\frac{\partial k}{\partial x} + \frac{\partial}{\partial y}\Gamma_{e,k}\frac{\partial k}{\partial y} + \boxed{\frac{\partial}{\partial z}\Gamma_{e,k}\frac{\partial k}{\partial z}} + G_k - \rho\varepsilon \qquad .(AI.II)$$

RATE OF DISSIPATION OF k (ε)

$$\rho\left[\frac{\partial}{\partial x}(u\varepsilon) + \frac{\partial}{\partial y}(v\varepsilon) + \frac{\partial}{\partial z}(w\varepsilon)\right] = \frac{\partial}{\partial x}\Gamma_{e,\varepsilon}\frac{\partial}{\partial x} + \frac{\partial}{\partial y}\Gamma_{e,\varepsilon}\frac{\partial \varepsilon}{\partial y} + \boxed{\frac{\partial}{\partial z}\Gamma_{e,\varepsilon}\frac{\partial \varepsilon}{\partial z}} + \frac{\varepsilon}{k}(C_I G_k - C_2 \rho\varepsilon) \quad .(AI.I2)$$

GENERAL SCALAR VARIABLE ϕ

$$\rho\left[\frac{\partial}{\partial x}(u\phi) + \frac{\partial}{\partial y}(v\phi) + \frac{\partial}{\partial z}(w\phi)\right] = \frac{\partial}{\partial x}\Gamma_{e,\phi}\frac{\partial \phi}{\partial x} + \frac{\partial}{\partial y}\Gamma_{e,\phi}\frac{\partial \phi}{\partial y} + \boxed{\frac{\partial}{\partial z}\Gamma_{e,\phi}\frac{\partial \phi}{\partial z}} + S_\phi \quad .(AI.I3)$$

where μ is the molecular viscosity for laminar flows

$$\mu = \mu_e = \mu_\ell + \mu_t \text{ for turbulent flows} \quad .(AI.I4)$$

and $$\mu_t = C_\mu \rho k^2/\varepsilon$$

Also, the effective exchange coefficient for the transport of a general variable ϕ is given by:

$$\Gamma_{e,\phi} = \frac{\mu_\ell}{\sigma_\phi} + \frac{\mu_t}{\sigma_{t,\phi}} \quad ,(AI.I5)$$

where σ_ϕ and $\sigma_{t,\phi}$ are the laminar and turbulent Prandtl/Schmidt numbers respectively.

The expression G_k in (AI.II) and (AI.I2) represents the generation of kinetic energy of turbulence; it is expressed as follows:

$$G_k = \mu_t\left[2\left\{\left(\frac{\partial u}{\partial x}\right)^2 + \left(\frac{\partial v}{\partial y}\right)^2 + \boxed{\left(\frac{\partial w}{\partial z}\right)^2}\right\} + \left\{\frac{\partial w}{\partial y} + \boxed{\frac{\partial v}{\partial z}}\right\}^2 + \left\{\boxed{\frac{\partial u}{\partial z}} + \frac{\partial w}{\partial x}\right\}^2 + \left\{\frac{\partial v}{\partial x} + \frac{\partial u}{\partial y}\right\}^2\right] \quad .(AI.I6)$$

The constants appearing in Equations (AI.II) and (AI.I2) are given in Equation 2.22.

AI.3 EQUATIONS IN (Θ-R-Z) COORDINATE SYSTEM

The equations presented in (AI.2) can be easily transformed into the (Θ-R-Z) coordinate system. The transformed equations are as follows.

CONTINUITY

$$\frac{\partial u}{r\partial\Theta} + \frac{\partial v}{\partial r} + \frac{\partial w}{\partial z} = 0 \qquad .(AI.I7)$$

AXIAL MOMENTUM (Z)

$$\rho\left[u\frac{\partial w}{r\partial\Theta} + v\frac{\partial w}{\partial r} + w\frac{\partial w}{\partial z}\right] = -\frac{\partial p}{\partial z} + \frac{\partial}{r\partial\Theta}\tau_{\Theta z} + \frac{\partial}{\partial r}\tau_{rz} + \boxed{\frac{\partial}{\partial z}\sigma_z} \qquad .(AI.I8)$$

ANGUALR MOMENTUM (Θ)

$$\rho\left[u\frac{\partial u}{r\partial\Theta} + v\frac{\partial u}{\partial r} + w\frac{\partial u}{\partial z}\right] = -\frac{\partial p}{r\partial\Theta} + \frac{\partial}{r\partial\Theta}\sigma_\Theta + \frac{\partial}{\partial r}\tau_{r\Theta} + \boxed{\frac{\partial}{\partial z}\tau_{z\Theta}} \qquad .(AI.I9)$$

RADIAL MOMENTUM (R)

$$\rho\left[u\frac{\partial v}{r\partial\Theta} + v\frac{\partial v}{\partial r} + w\frac{\partial w}{\partial z}\right] = -\frac{\partial p}{\partial r} + \frac{\partial}{r\partial\Theta}\tau_{\Theta r} + \frac{\partial}{\partial r}\sigma_r + \boxed{\frac{\partial}{\partial z}\tau_{zr}} \qquad ,(AI.20)$$

where

$$\sigma_\Theta = 2\mu\left(\frac{I}{r}\frac{\partial u}{\partial\Theta} + \frac{v}{r}\right) \qquad ,(AI.2I)$$

$$\sigma_r = 2\mu\left(\frac{\partial v}{\partial r}\right) \qquad ,(AI.22)$$

$$\sigma_z = 2\mu\left(\frac{\partial w}{\partial z}\right) \qquad ,(AI.23)$$

$$\tau_{rz} = \tau_{zr} = \mu\left(\frac{\partial v}{\partial z} + \frac{\partial w}{\partial r}\right) \qquad ,(AI.24)$$

$$\tau_{\Theta z} = \tau_{z\Theta} = \mu\left(\frac{\partial u}{\partial z} + \frac{\partial w}{r\partial\Theta}\right) \qquad ,(AI.25)$$

$$\tau_{r\theta} = \tau_{\theta r} = \mu\left[r\frac{\partial}{\partial r}\left(\frac{u}{r}\right) + \frac{I}{r}\frac{\partial v}{\partial \theta}\right] \qquad .(AI.26)$$

KINETIC ENERGY EQUATION (k)

$$\rho\left[\frac{\partial}{r\partial\theta}(uk) + \frac{\partial}{\partial r}(vk) + \frac{\partial}{\partial z}(wk)\right] = \frac{I}{r}\frac{\partial}{\partial r}\Gamma_{e,k}\, r\frac{\partial k}{\partial r}$$

$$+ \frac{I}{r}\frac{\partial}{\partial\theta}\Gamma_{e,k}\frac{\partial k}{r\partial\theta} + \boxed{\frac{\partial}{\partial z}\Gamma_{e,k}\frac{\partial k}{\partial z}} + G_k - \rho\varepsilon \qquad .(AI.27)$$

RATE OF DISSIPATION OF k (ε)

$$\rho\left[\frac{\partial}{r\partial\theta}(u\varepsilon) + \frac{\partial}{\partial r}(v\varepsilon) + \frac{\partial}{\partial z}(w\varepsilon)\right] = \frac{I}{r}\frac{\partial}{\partial r}\Gamma_{e,\varepsilon}\, r\frac{\partial \varepsilon}{\partial r}$$

$$+ \frac{I}{r}\frac{\partial}{\partial\theta}\Gamma_{e,\varepsilon}\frac{\partial\varepsilon}{r\partial\theta} + \boxed{\frac{\partial}{\partial z}\Gamma_{e,\varepsilon}\frac{\partial\varepsilon}{\partial z}} + \frac{\varepsilon}{k}(C_I G_k - C_2\rho\varepsilon) \qquad .(AI.28)$$

GENERAL SCALAR VARIABLE ϕ

$$\rho\left[\frac{\partial}{r\partial\theta}(u\phi) + \frac{\partial}{\partial r}(v\phi) + \frac{\partial}{\partial z}(w\phi)\right] = \frac{I}{r}\frac{\partial}{\partial r}\Gamma_{e,\phi}\, r\frac{\partial\varepsilon}{\partial r}$$

$$+ \frac{I}{r}\frac{\partial}{\partial\theta}\Gamma_{e,\phi}\frac{\partial\phi}{r\partial\theta} + \boxed{\frac{\partial}{\partial z}\Gamma_{e,\phi}\frac{\partial\phi}{\partial z}} \qquad .(AI.29)$$

where the expressions for the viscosities are as before, (i.e. equations AI.I4 and AI.I5).

The expression for the generation of kinetic energy G_k, is given by the following expression:

$$G = \mu_t\Bigg[2\{\boxed{\left(\frac{\partial w}{\partial z}\right)^2} + \left(\frac{\partial v}{\partial r}\right)^2 + \left(\frac{\partial u}{r\partial\theta} + \frac{v}{r}\right)^2\}$$

$$+ \left(\frac{\partial w}{\partial r} + \boxed{\frac{\partial v}{\partial z}}\right)^2 + \left(\boxed{\frac{\partial u}{\partial z}} + \frac{\partial w}{r\partial\theta}\right)^2$$

$$+ \left(\frac{\partial v}{r\partial\theta} + \frac{\partial u}{\partial r} - \frac{u}{r}\right)^2\Bigg] \qquad .(AI.30)$$

The constants appearing in the equations for k and ε are given in Equation 2.22.

APPENDIX A.2

EXPERIMENTAL INFORMATION

A2.I DETAILS OF EQUIPMENT USED

Below are listed the specific items used in the experiments.

i) CONSTANT SPEED BLOWER

BLACKMAN 8HP SER. NO. 034907

ii) DIGITAL VOLTMETER

SOLATRON (LM I4202) SER. NO. I57278

iii) MICRO-MANOMETER

FURNISS CONTROLS NO. 575 HT

iv) DISA - TYPE 52830 TRUE INTEGRATOR NO. 80I HT

v) BALANCE

METTLER TYPE H6 SER. NO. 205623.

A2.2 CALIBRATION

A2.2.I MICRO-MANOMETER CALIBRATION

To calibrate the micro-manometer, a total head pressure probe was located within the potential core of a round free jet. By reference to a Betz-type water monometer, with a sensitivity of less than 0.02mm water, the micro-manometer was calibrated. The result of this calibration is shown in Figure A2.I.

A2.2.2 TRANSVERSE CYLINDER PROBE CALIBRATION

The probe was calibrated in the potential core of a 4cm diameter round jet; the jet velocity could be controlled

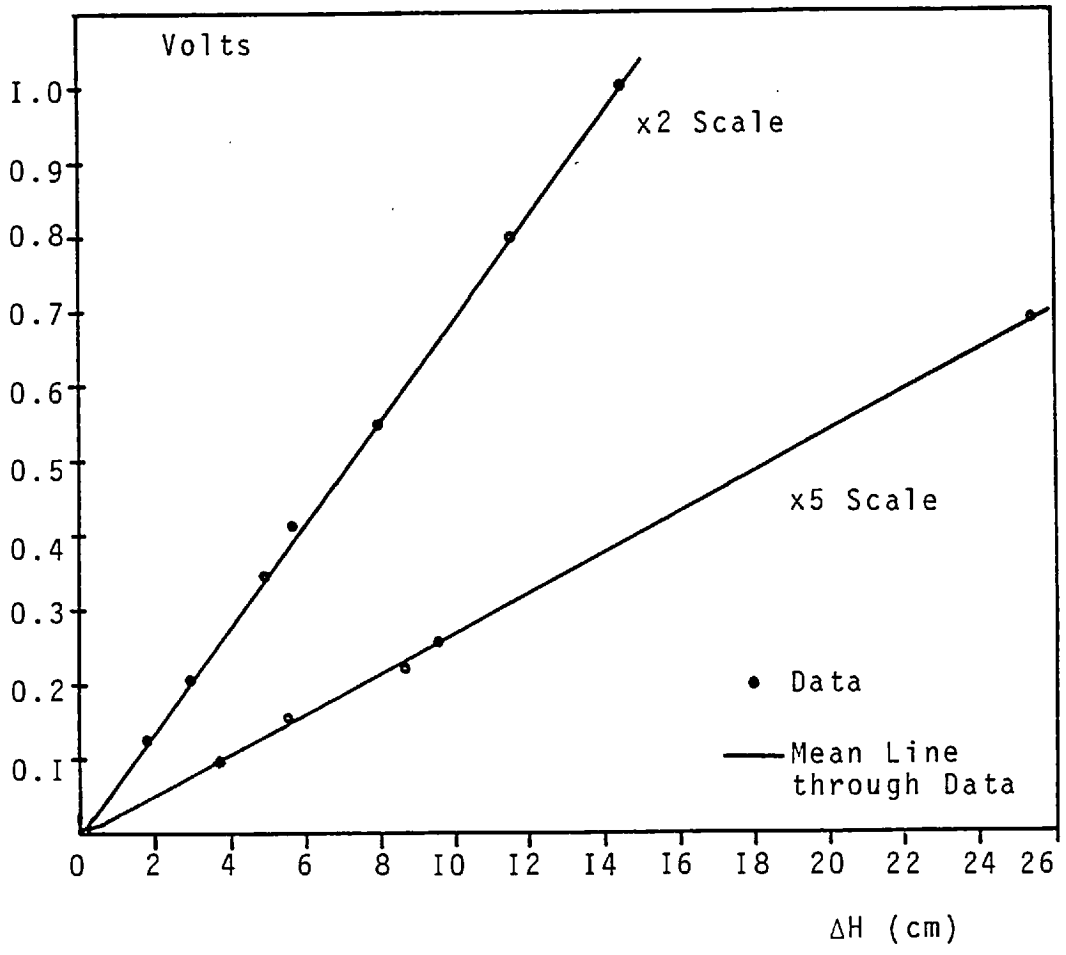

FIGURE A2.I: CALIBRATION CURVES FOR MICRO-MANOMETER

to give mean velocities up to about 35m/sec. The probe during calbiration was subjected to a range of velocities; a separate set of calibration curves for each jet velocity being obtained. The resulting calibration curves, shown in Figures A2.2 and A2.3 depict the average of the separate calibration curves.

Figure A2.2 presents the pressure ratio-pitch angle calibration curve; the curve is continuous between 40^{o} and 135^{o}. Figure A2.3 presents the pressure coefficient-pitch-angle calbiration curve. The two curves are used together: with a given pressure ratio $(\frac{P_I - P_3}{P_I - P_2})$, the pitch angle is obtained from Figure A2.2; using this pitch angle, the pressure coefficient is obtained from A2.3, hence the magnitude of the velocity vector.

In obtaining these calibration curves, the data exhibited large amounts of scatter particularly below pitch angles of 70^{o} on the (Figure A2.3) curve. Since the other curve (Figure A2.2) did not exhibit data scatter at this point (but it did around the 45^{o} pitch angle mark), the reliability of the curves is governed by the pressure-coefficient-pitch-angle calibration.

In examining the experimental data, any point that indicated a pitch angle of less than 60^{o} was discarded; if however, the pitch angle was in the range of 60^{o} to 70^{o} the data was kept, but the data is considered to be questionable; this questionable data is enclosed by a circle (0) in all references to the data. Data indicating a pitch angle of between 70^{o} and 130^{o}, is considered to be reliable.

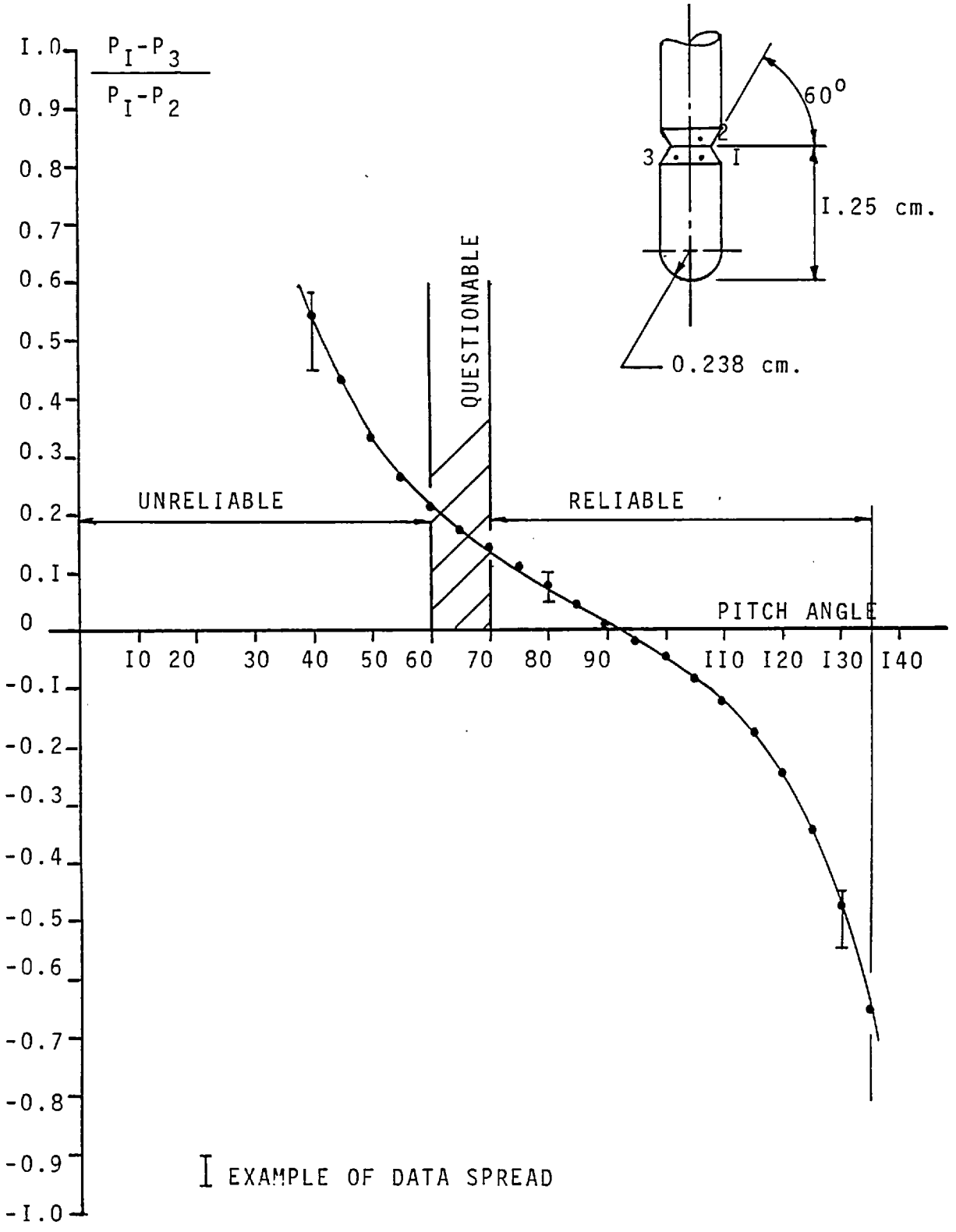

FIGURE A2.2: 3-HOLE TRANSVERSE CYLINDER PROBE
CALIBRATION CURVE
PRESSURE RATIO vs PITCH ANGLE

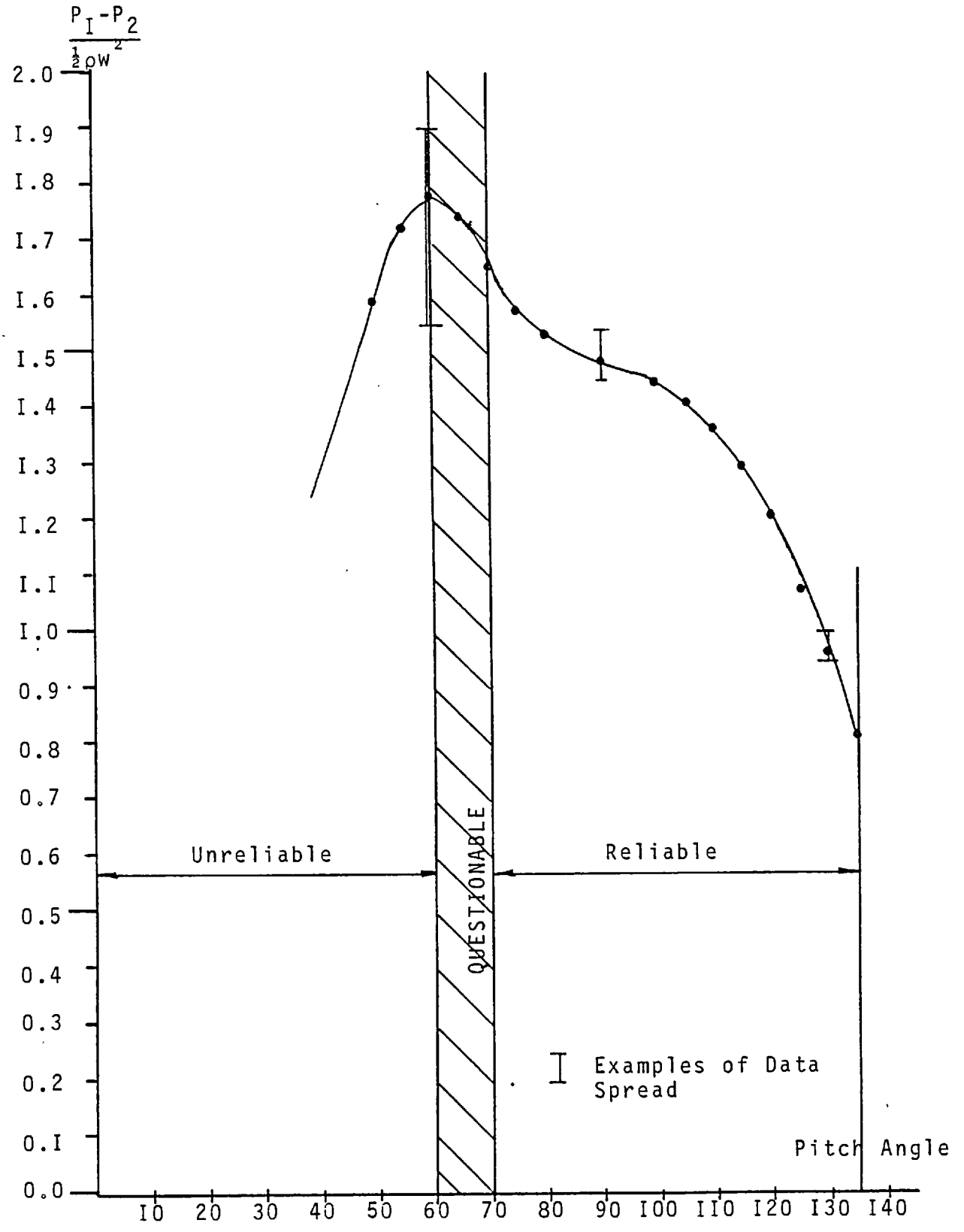

FIGURE A2.3: 3-HOLE TRANSVERSE CYLINDER PROBE CALIBRATION CURVE PRESSURE COEFFICIENT vs PITCH ANGLE

As mentioned above, the cylinder probe was calibrated in a free-jet. In practice however, it is employed in an enclosed space and therefore some doubts may arise regarding the validity of the calibration. Before being employed to obtain data in the tee-junction, the data obtained using the cylinder probe was checked using a pitot probe (d=2.2mm); the data for each probe was obtained both in the inlet duct and at the reference locations where three-dimensional effects are neglible. As shown in Figures 4.II and 4.I2 (Chapter 4), the results obtained by both probes are in good agreement.

APPENDIX A3

VERIFICATION OF THE NUMERICAL PROCEDURE - A FEW EXAMPLES

A3.I INTRODUCTION

Here, four test cases are presented so as to indicate the validity of the computer codes used in the present work. All four test cases employed the "elliptic" version of the code; the flow in a square duct was also calculated using the "partially elliptic" version. The predictions are compared to either analytical results or to data obtained from experiments. In all the cases tested, grid independence tests have not been performed; however, in some cases, various grids have been used to demonstrate that the results improve with grid refinement.

A3.2 THE TEST CASES

CASE I: LAMINAR DEVELOPING FLOW IN A PIPE

THE PROBLEM: It is desired to predict the steady, fully developed laminar flow profile in a round pipe; the fluid at the entrance to the pipe is uniform in profile.

THE GEOMETRY AND FINITE-DIFFERENCE GRID

A sector of a pipe of radius 0.Im and of length 8m was mapped using a 6x6xI0 and a 6xI0xI0 finite-difference grid distributed in a non-uniform manner in the θ, R and Z coordinate directions respectfully.

BOUNDARY CONDITIONS

The boundary conditions for this problem were specified as:

$Z = 0$	W specified; u,v=0 (Re=I000)
$Z = 8$	$u,v=0;\ \frac{\partial w}{\partial z} = 0$
$R = 0$	$\frac{\partial w}{\partial r} = 0,\ u,v=0$
$R = .I$	w,u,v=0
$\Theta = 0, \Theta=90^{o}$	$u=0,\ \frac{\partial v}{\partial \Theta} = \frac{\partial w}{\partial \Theta} = 0$

THE RESULTS

The results of the computations are illustrated in Figure A3.I The predictions show good agreement with the well known analytical solution; the agreement increases as the grid is refined. The maximum discrepancy is observed to be at the centre-line and is of the order of 5% for the coarse grid.

CASE 2: LAMINAR FLOW IN A SQUARE CAVITY WITH MOVING LID

THE PROBLEM: To predict the steady velocity field in a square cavity filled with an incompressible fluid which is acted upon by a lid moving at a constant speed U_{TOP}.

THE GEOMETRY AND FINITE-DIFFERENCE GRID

A square, two dimensional box is overlaid with a uniform I5 x I5 finite-difference grid; 3 grid nodes in the longitudinal direction are used. The box has sides of length H.

THE BOUNDARY CONDITIONS

X=0, X=H	u,v,w=0
Y=0	u,v,w=0
Y=H	$u=U_{TOP};\ v,w=0$
Z=0, Z=H	$\frac{\partial \phi}{\partial z} = 0$

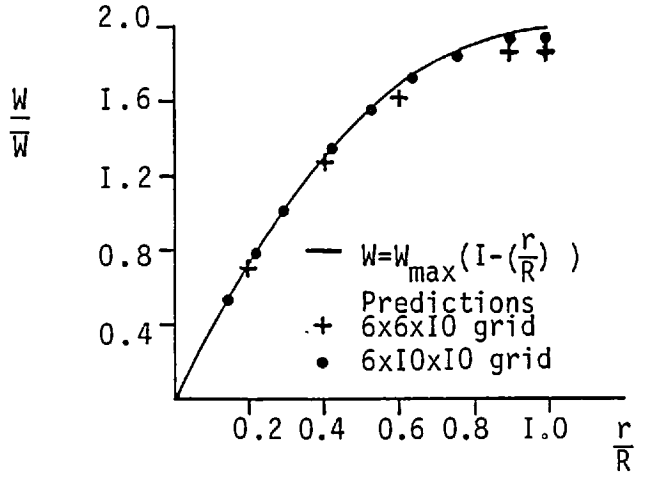

FIGURE A3.I: LAMINAR FULLY-DEVELOPED PIPE FLOW, PREDICTION vs ANALYTICAL SOLUTION

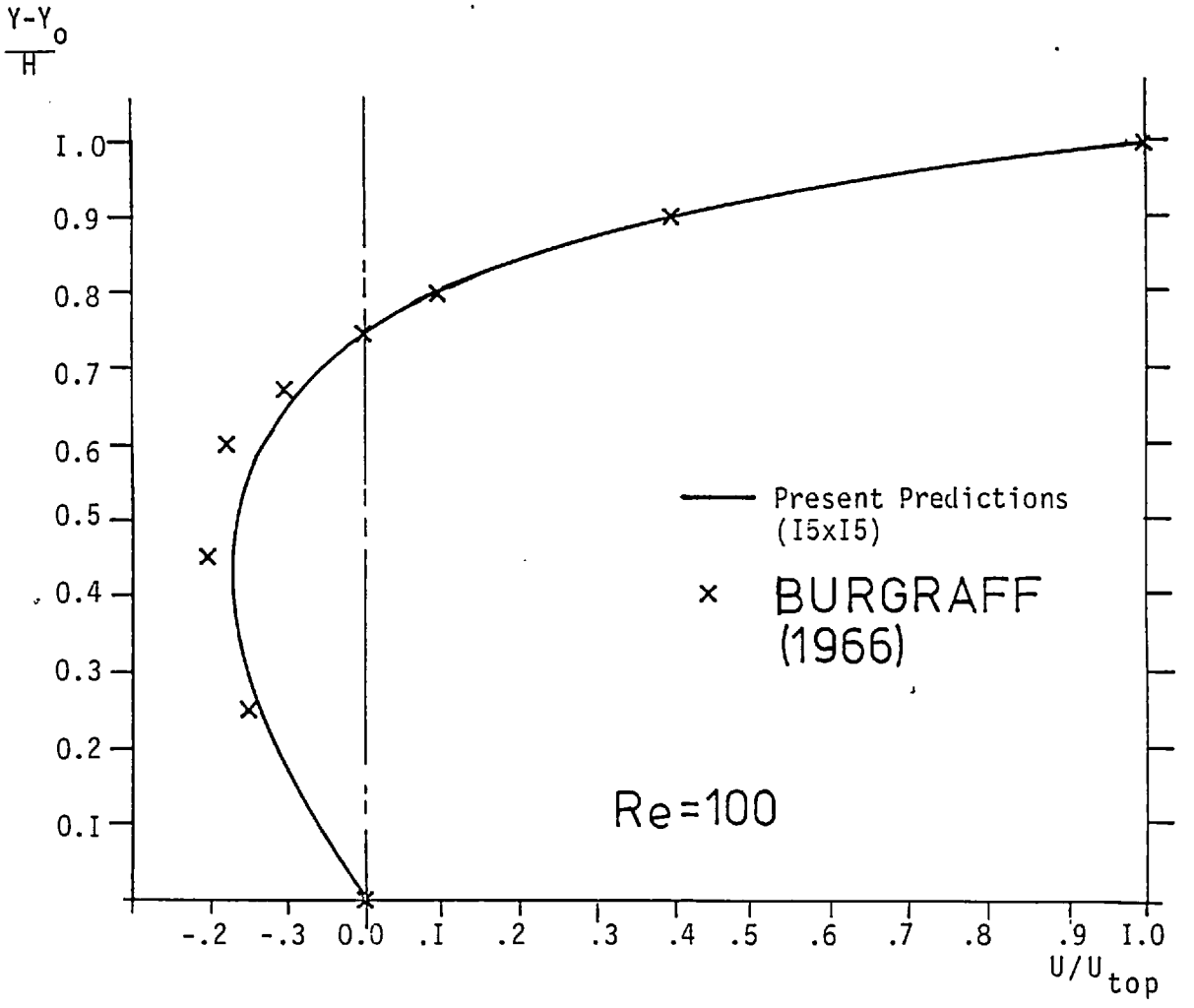

FIGURE A3.2: SQUARE CAVITY WITH SLIDING TOP PRESENT PREDICTIONS vs BURGRAFF (I966)

Reynolds Number ($\equiv \frac{\rho U_{TOP} H}{\mu}$) is 100.

THE RESULTS

In Figure A3.2 is the distribution of the horizontal velocity (U) along the vertical centre plane (H/2) of the square cavity. The figure is taken from Pollard and Thyagaraja (1978); here, y_0 in the figure is zero. The predictions are compared to the predictions of Burfraff (1966). The agreement is seen to be good especially since Burgraff used a 51x51 grid.

CASE 3: LAMINAR FLOW IN A SUDDEN ENLARGEMENT

THE PROBLEM: To predict the re-attachment length - Reynolds number characteristics of the laminar flow in sudden enlargement of round cross-section.

THE GEOMETRY AND FINITE-DIFFERENCE GRID

The geometry is shown in Figure A3.3 This geometry was overlaid with a 10x10x10 uniformly distributed grid.

THE BOUNDARY CONDITIONS

Z=0	u,v=0, $W=W_{MAX}\ (1-(\frac{a}{r})^2)$; u,v,w=0 on wall
Z=10d	u,v=0 $\frac{\partial w}{\partial z} = 0$
r=0	$\frac{\partial w}{\partial r} = 0$, u,v=0
r=2r	u,v,w=0
Θ=0,Θ=90	u=0, $\frac{\partial v}{\partial \Theta} = \frac{\partial w}{\partial \Theta} = 0$

THE RESULTS

In Figure A3.3 the re-attachment length of the separated flow is plotted versus inlet Reynolds number. The predictions

are compared with the data of Macagno and Hung (I967). The agreement is seen to be satisfactory for the range of Reynolds numbers tested.

CASE 4: THE LAMINAR FLOW IN A SQUARE DUCT

THE PROBLEM: To predict the laminar developing flow in a square duct using two computational procedures.

THE GEOMETRY AND FINITE-DIFFERENCE GRID

A half section of a square duct of sides H and length $6D_H$ ($D_H = \frac{2H^2}{H+H}$) is mapped using a 6xI2xIO finite-difference grid. The grid is uniform in the cross-stream (x(6), y(I2)) and non-uniform in the axial direction.

THE BOUNDARY CONDITIONS

x=0:	$u=0;\ \frac{\partial v}{\partial x} = \frac{\partial w}{\partial x} = 0$
x=H/2:	u=v=w=0
y=0,y=H:	u,v,w=0
z=0:	w=constant; u=v=0
$z=6D_H$:	$u=v=0;\ \frac{\partial w}{\partial z} = 0.$

THE RESULTS

Plotted in Figures A3.4 (a) and (b) is the axial dependence of the square duct centre-line velocity ($W_{\mathbb{C}}$) and the centre-line pressure drop respectively. The data is from Tatchell (I975), and the solid curve in each figure is the prediction obtained using both versions of the code. The agreement is seen to be acceptable considering the grid distribution. It is also observed that both versions of the code produce the same results (to within I%).

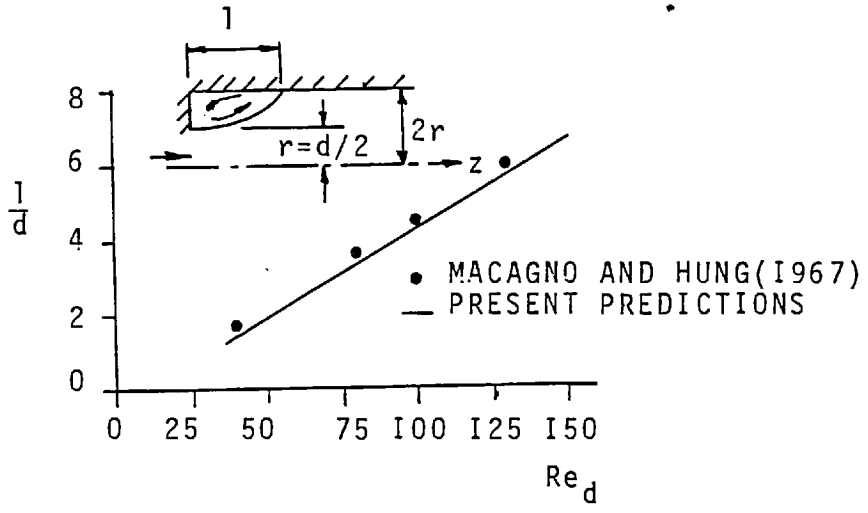

FIGURE A3.3: RE-ATTACHMENT LENGTH vs REYNOLDS NUMBER, PREDICTIONS vs EXPERIMENT

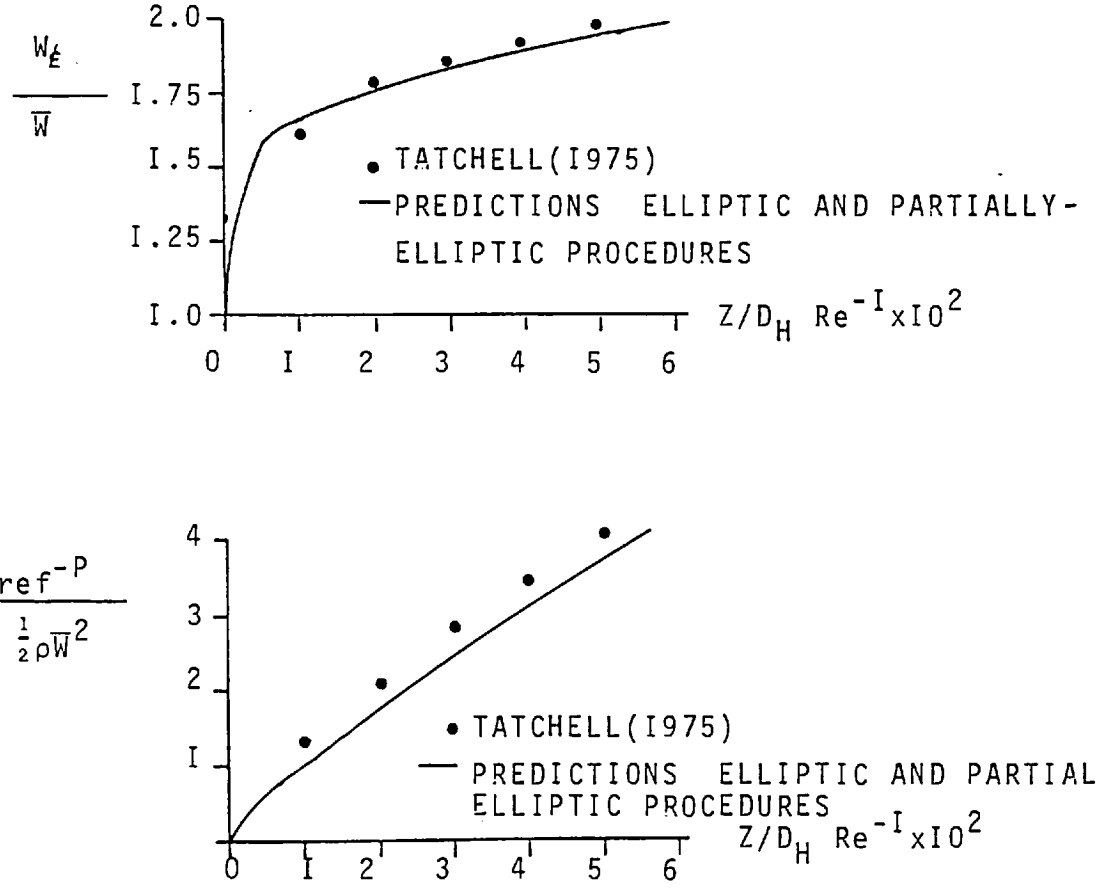

FIGURE A3.4: AXIAL VELOCITY AND PRESSURE DEVELOPMENT IN A SQUARE DUCT : A COMPARISON OF PROCEDURES

A.3.3 CONCLUDING REMARKS

The test cases presented above indicate that the numerical procedures are capable of producing physically realistic results that compare well with data from other sources for a variety of flow situations.